23

The Erosion of Materials

by

Zheng Feng

A thesis submitted to the Faculty of Engineering, University of Cape Town in fulfilment of the degree of Doctor of Philosophy

Department of Materials Engineering
University of Cape Town
December 1998

ABSTRACT

Solid particle erosion tests of glass, stainless steel, WC-Co and sintered alumina, have been performed with seven erodents using a range of particle diameters D (63 μm - 1000 μm), velocities V (33 $m.s^{-1}$ - 131 $m.s^{-1}$) and impact angles α (30° - 90°). The seven erodents are steel shot, glass beads, silica, alumina, tungsten carbide, silicon carbide and diamond particles. In addition, the target materials have been subjected to cavitation erosion using a conventional ultrasonic horn in distilled water. Systematic studies of the influence of the impact variables on the erosion rate have been made. Scanning electron microscopy of the eroded surfaces and the erodents after impact has been performed. Empirical correlations between erosion rate and the parameters of erosion and the erodents were obtained and are discussed in terms of the modes and mechanisms of erosion. A semi-quantitative theoretical model has been developed to explain the empirical correlations for brittle and ductile materials.

The mode of erosion of glass impacted by irregularly shaped particles is associated with the formation and interaction of lateral cracks over all impact velocities and angles used in this study. The erosion of glass by spherical particles is determined by particle size, impingement velocity and angle. An erosion map, in which the erosion of glass is mapped against velocity and particle size, has been constructed to categorise the types of damage observed in glass for impingement angles between 90° and 30°. The erosion behaviour of 304 stainless steel is associated with cutting or ploughing and plastic accumulation processes. The erosion of WC-Co is associated with a combination of ductile and brittle modes of erosion. The erosion of alumina is brittle and associated with intergranular spallation and grain-crushing.

An analysis of the results reveals that for the brittle materials, glass and alumina, the erosion rate is determined by kinetic energy, particle size and the relative hardness and toughness of the erodents. However, for ductile materials, the shape and kinetic energy of erodents are the most important factors determining the erosion rate. There is no significant effect of hardness and toughness of erodents on erosion. Surprisingly, the erosion resistance of the softer 304 stainless steel is better than that of alumina and WC-Co when hard erodents are used at impact angle greater than 40°. On the other hand the erosion resistance of the harder WC-Co and alumina is better than that of 304 stainless steel for softer erodents like silica erodents. Glass always exhibits poor erosion resistance.

In cavitation erosion, stainless steel exhibits better cavitation erosion resistance than glass, alumina and WC-Co. The cavitation erosion resistance of WC-Co is dependent upon the cobalt content. An attempt to rationalise the results in terms of mechanisms has been made. Both solid particle and cavitation erosion rate for the as received glass is higher than that for the tempered glass due to introduction of residual compressive stresses into the surface by the tempering process. Particularly, it reveals that compressive stresses are more efficient in preventing the formation and propagation of Hertzian cracks. These findings will assist in the choice and design of materials that undergo both particle and cavitation erosion under specified conditions.

ACKNOWLEDGEMENTS

I would like to thank all those who assisted me during the course of this project, in particular:

Professor A Ball, my supervisor, for his guidance and encouragement.

Dr. C. Lang and Dr. K. Marcus for their advice. Mr. David Dean and Mr. Glen Newins for their help with the construction of the equipment for velocity measurement and for the assistance in the workshop. Mr. Bernard Greeves, Mr. James Petersen and Mr. Adriaan Loedolff for all the photographic work. Mrs. Mira Topic for her technical assistance. Mrs. Jullie Henry for her administrative support.

The staff and students in the Department of Materials Engineering for their support and encouragement.

Boart International Industrial Division for the provision of specimens.

The financial assistance of the department is gratefully acknowledged

Dedicated to my family

TABLE of NOMENCLATURE

- α: incidence angle
- M: particle's mass
- V: particle's velocity
- σ: flow stress of target
- $f(\alpha)$: function for incidence angle α,

  $f(\alpha) = \sin 2\alpha - 3\sin^2\alpha \qquad \alpha \leq 18.5°$

  $f(\alpha) = \cos^2\alpha \qquad \alpha \geq 18.5°$
- Ev: erosion in units of volume loss
- K′: constant
- ε': energy needed to remove a unit volume of target during deformation wear
- U_p: horizontal component of particle velocity
- ϕ: energy needed to remove a unit volume of target during cutting wear
- p_0: mean indentation pressure
- P: load
- a: surface dimension of the plastic impression
- Λ: shape factor of erodent
- H: hardness of materials
- π: 3.14
- C: radius of lateral crack
- h: depth of the lateral crack below surface
- Us: total surface energy
- Um: total strain energy
- Γ: fracture surface energy
- E: Young's modulus of target
- E′: Young's modulus of indenter
- β: dimensionless factor determined by zone geometry
- ρ: density of the particle
- z: distance of mutual approach of the deforming solids

- P(z): load corresponding to the distance z
- R: radius of indenter
- γ: Poisson's ratios of the target materials
- γ': Poisson's ratios of the indenter
- k: $(9/16)[(1-\gamma^2)+(1-\gamma'^2)E/E']$
- Pm: maximum load
- β': dimensional parameter
- Uk: impacting kinetic energy
- n: number of grains included in a pit
- d: average grain diameter
- γ_1: grain boundary fracture energy
- Hp: hardness of particle
- Ht: hardness of target
- ε: strain rate
- ε_t: true strain
- σ_t: true stress
- Eg: volume loss per gram of erodent
- Ep: volume loss per particle
- NE: normalised erosion rate which means erosion rate multiplied by the correction factor
- NE_p: normalised erosion rate per particle
- K_p: toughness of erodent
- K_t: toughness of target
- D: diameter of erodent
- a_m: maximum contact radius
- Fm: maximum mean pressure
- T: contact time of the elastic impact
- x: velocity exponent
- y: size exponent
- d': depth of cut of target

1. INTRODUCTION

Erosion usually refers to the deterioration of a target material as a result of continued impingements by solid particles or liquid droplets that are carried in a fluid stream[1]. Solid particle erosion is an important material degradation mechanism encountered in a number of engineering systems[2, 3, 4, 5, 6, 7] such as pulverised coal combustion systems, the petrochemical industry, gas turbine engines and the pneumatic transport of powders. It is also encountered by space vehicles[8, 9, 10].

Many mechanisms have been proposed which attempt to relate erosion rate to the properties of erodent particles and targets[11, 12, 13 14, 15, 16, 17, 18, 19, 20, 21, 22, 23, 24, 25, 26]. However, no universal correlation using a single property or a combination of properties has been established. This is attributed to the complexity of erosion which depends on the combination of the type of impact event, the impact parameters and the structural and mechanical properties of the solid particles and the target. Since the fracture behaviour of brittle materials is better understood than that of ductile materials, glass, as a typical brittle material, has commonly been used as the target in past years due to it being elastically isotropic. Attempts have been made to correlate the erosion of glass with properties of erodent particles and targets[27, 28, 29, 30].

Previous work by Finnie, Wolak and Kabil[27] indicated that the velocity exponent is about 6 for glass impacted with steel shot. Verspui[31] indicated that the experimental velocity exponent is 4.36 and 3.86 for glass impacted by spherical glass beads and angular alumina erodents respectively. However, Buijs and Pasmans[28] indicated that the value of velocity exponent is 7/3 for glass impacted with alumina particles. Recently Slikkerveer, Bouten and Scholten[32] indicate that the velocity exponent and particle size exponent are 2.46 and 3.69 respectively for glass impacted with alumina particles. Several mechanisms[29, 30] of erosion of glass were proposed which relate erosion rate to particle size and impact angle. Sparks and Hutchings[33] investigated the mechanisms of material removal during the erosive wear of a glassy ceramics. They proposed that the brittle - ductile transition modes that occurred depended on the particle shape, impact velocity and impact angle. Sheldon and Finnie[29] investigated the erosion of glass eroded by silicon carbide particles of three different sizes. They showed that on reducing the size of the silicon carbide erodent particles from 125 μm

to 9 μm, the angle of maximum erosion for glass shifted from close to 90^0 to a much lower angle; the behaviour had changed from 'brittle' to 'ductile'. More recently, Ballout, Mathis and Talia[30] studied the erosion mechanism of glass when impacted with alumina particles and glass beads with various sizes and velocities. The mechanism of erosion of glass is predominately controlled by the formation and propagation of lateral cracks.

Verspui and Slikkerveer[17] investigated the modes of erosion of glass by single impacts of Zirblast beads. An erosion map where the velocity of a particle is depicted versus the diameter of particle is derived[17]. In this map, the transition of modes is noted. However, no systematic work on the effect of different erodent particles on the erosion of glass has been made to understand the relationship between erosion rate and particle size, hardness and velocity of erodent particles. A proper understanding of mode and mechanism of solid particle erosion of glass is a prerequisite for providing guidelines for optimum material selection for particular components in industrial equipment and the reduction of wear in machinery.

1.1. Research objectives

The research work primarily deals with quantifying the erosivity of glass as a function of erodent and target parameters in an attempt to understand the mode and mechanism of the erosion. The solid particle erosion and cavitation erosion tests were conducted on WC-7%Co, **AISI** 304 stainless steel, a high-nitrogen Cr-Mn stainless steel (Cromanite™), alumina and glass in the thermally tempered condition for comparative purposes. The research objectives are as follows:

1. To characterise the relative erosion resistance of glass in as received and thermally tempered condition, WC-7%Co, 304 stainless steel, Cromanite™ and alumina under identical erosion test conditions.
2. To characterise the nature of eroded surface and erodent particles before and after impact.

3. To obtain quantitative empirical equations which relate the particle erosion resistance of these materials with their properties, the erodent properties and the impingement variables, in an attempt to correlate the modes and mechanisms of the different erosion processes.
4. To assess the effectiveness of the compressive stress which was introduced into the surface of glass in inhibiting erosion.
5. To characterise the damaged surface produced by cavitation erosion in order to understand the mode and mechanism of cavitation erosion.
6. To provide useful information for optimum material selection for particular components in industrial equipment.

1.2. Experimental approach

The experimental work concerns the effect of different erodent particles and their size on the mass loss of the target materials under various test conditions. The seven erodent particles selected for solid particle erosion were steel shot, glass beads, silica, alumina, tungsten carbide, silicon carbide and diamond particles with different size, shape, hardness, toughness and density. The target materials, the glass in the as-received and thermally tempered conditions, WC-7%Co, **AISI** 304 stainless, Cromanite™ and alumina, have also been subjected to cavitation erosion using a conventional ultrasonic horn in distilled water.

Optical and scanning electron microscopy (SEM) techniques were used to examine the erodent particles and target topographies before and after impact.

A Malvern Mastersizer apparatus was employed to determine the size distribution of the erodents before and after impact. Energy dispersive x-ray spectroscopy (EDS) techniques was used to measure compositional variation of surface due to erodent particle embedment and fragmentation. Uniaxial tensile tests were conducted on the 304 stainless steel and Cromanite™ in order to characterise their mechanical behaviour. The erosion test results are discussed in terms of the mechanical properties and the erosion damage characteristics of these materials and properties of erodents.

2. LITERATURE REVIEW

2.1. Modes of erosion

Finnie et al[27] indicated that there is a dramatic difference in the response of ductile and brittle materials when the weight loss in erosion is measured as a function of the angle of impact as shown in the trends for ductile and brittle materials (fig. 2.1 after Finnie et al[27]). Various mechanisms[11, 12, 13, 14, 15, 16] have been proposed to explain these trends in terms of material removal. Although these mechanisms differ, there is general agreement that materials are often characterised as responding in either a ductile or brittle mode.

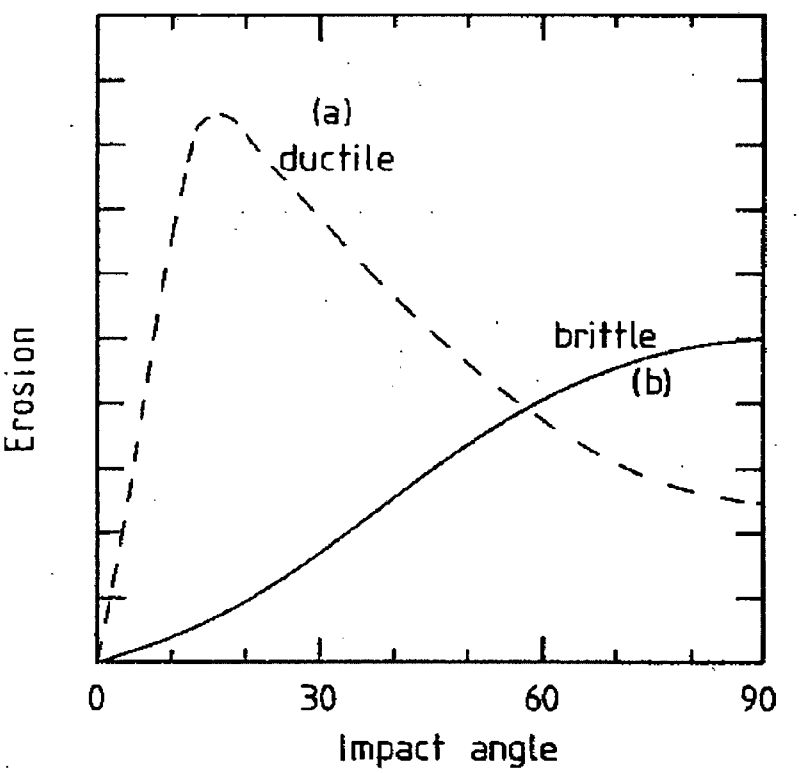

Figure 2.1 Typical trend curves showing the variation of erosion loss with impact angle and agree well with the experimental trend: (a) for a ductile metal; (b) for a brittle material eroding by fracture (after Finnie et al.[27])

2.1.1. Ductile mode of erosion

A ductile plastic shear mode of erosion generally occurs in ductile materials[11]. Solid particle erosion of metallic materials at room temperature has been extensively studied[34, 35, 36]. Several different mechanisms of erosion of ductile metals have been proposed through the years.

2.1.1.1. Cutting mechanism

The "cutting" or "micromachining" model of Finnie and co-workers[11, 12, 37] represents the pioneering effort in the explanation of erosion of metallic materials. This model computed the volume of the crater generated in the eroding material when it is impacted by a hard angular particle at a given velocity and angle of incidence; it is assumed that this crater volume or a proportion of it is removed causing weight loss. The basic equation (2.1) attempts to predict erosion weight or volume loss per individual particle impact as being directly proportional to the total available kinetic energy of the particle ($\propto MV^2$) and inversely proportional to shear stress (σ) of the target material.

$$\text{Erosion loss} \approx f(\alpha)\, MV^2/\sigma \qquad (2.1)$$

where

$f(\alpha)$ is function for incidence angle, α

$f(\alpha) = \sin 2\alpha - 3\sin^2\alpha \qquad \alpha \leq 18.5°$

$f(\alpha) = \cos^2\alpha \qquad \alpha \geq 18.5°$

M is particle's mass

V is particle's velocity

σ is flow stress of target material surface at test temperature.

The material removal was predicted to vary with the impingement angle. Finnie indicated that the maximum erosion rate occurs at an impingement angle of 17° for aluminium eroded by silicon carbide particles. The cutting model is capable of explaining the experimentally observed maximum erosion rate at low angles and agrees very well with experimental results as shown in fig.2.1. However, the cutting model predicted a zero erosion rate at 90°

incidence. This is incorrect and contradicts the observed results as shown in fig.2.1 where erosion loss is not zero at 90° incidence. Recently, Finnie, Stevick and Ridgely[38] proposed that surface roughening plays an important role in the erosion of ductile metals at 90° incidence. Once the surface is roughened, particles strike the surface locally at a variety of angles and at grazing angles volume is removed, which may predict the value of erosion for 90° incidence.

Hutchings[13] used high-speed photography to observe erosion by cutting. Erosion loss is as a result of a sharp cornered projectile machining a chip of material from the target surface. Each impact, causing the removal of a chip, is considered to be independent and the total amount of erosion is the sum of the contributions from each micro-machining impact. This theory is quantitatively successful. However, not all eroding particles are angular and not all impacts give rise to detached chips of material. This theory appears to be unable to deal with these exceptions. The controlled single particle impact experiments carried out by Hutchings and co-workers [39, 40] reveal that with angular particles the classical cutting removing material by scraping it out from the target surface in the form of a chip occurs rarely. On the other hand, the plowing, or flow localisation mechanism causes the extrusion of a lip at the exit side if the crater was found to be the dominant material removal mechanism.

In order to account for the substantial erosion loss as observed in the experimental trends shown in fig.2.1, several forms of a damage accumulation mechanism have been proposed. These include, melting[41, 42, 43, 44], microforging or extrusion (platelet) processes[45], delamination[46] wear, deformation wear[3], fatigue[29, 47] and adhesion[48]. The cutting model dominates at the lower angles of impact while damage-accumulation dominates at 90° incidence[3, 4]. The micrographic observations in the literature[49, 50, 51, 52] support the suggestion that the erosion loss does not result from a single mechanism.

2.1.1.2. Melting mechanism

The mechanism of target melting has been proposed by many authors[41, 42, 43, 44]. Uetz and Gommel[53] were able to measure directly the temperature rise produced by the impact of

hardened steel balls of diameter 1 to 2 mm on a steel surface. The speed of the balls was in the range 45-70 $m.s^{-1}$ and the resulting temperature rise was between 185-510 K, with the highest temperature generated by the smallest ball travelling at 70 $m.s^{-1}$. Andrews and Field[54] indicated that evidence for melting was found over the temperature range 70–1350 K for annealed copper target impacted by 5mm diameter hardened steel spheres at 20° impact and an impingement velocity of 130 $m.s^{-1}$. At low temperatures melting was insufficient to produce detectable mass loss and was only found in localised shear bands. At temperatures within 200 K of homogeneous melting, evidence of considerable melting was observed in craters, and deposits of molten copper were found attached to the spheres.

Hutchings and Winter[55] observed coloured oxide films on the surfaces of craters on steel targets impacted by steel spheres. The colours suggested temperature rise in excess of 500 K. Hutchings and Winter[56] estimated a temperature rise of 3000 K in an adiabatic shear band produced during impact. In addition, Hutchings and Levy[57] suggested that heat conduction is found to play an important role in reducing the maximum temperature rise in all practical cases of erosion and the cumulative effect on the temperature rise of successive impacts is shown to be negligible. The maximum temperature rises are rather lower than that estimated from adiabatic model.

Doyle and Ball[58] applied the analysis of Hutchings and Levy[57] to the erosion of alumina, steel and ultrahigh molecular weight polyethylene by 100 μm SiC erodent particles at a feed rate of $0.1 g.s^{-1}$ travelling at 40 $m.s^{-1}$. Figure 2.2 (after Doyle and Ball[58]) shows a plot of the isothermal-adiabatic boundary for various conditions of indentation hardness and target thermal diffusivity. It suggested that thermomechanical effects are expected during the impact of small hard particles on solid targets. The extent of these thermal effects is determined by the competition between heat generation and heat dissipation.

Smeltzer, Gulden and Compton[6] have also suggested that melting of the target can occur during impact and that material is thrown out in the form of molten droplets. However, these qualitative observations which indicate that melting has occurred have been restricted to scanning electron microscopy of eroded target surfaces. This kind of evidence cannot be accepted as proving that melting is a dominant mechanism of erosion. Although all researchers agree on the existence of a substantial temperature rise in the target during an

impact, there is little agreement on the role that this temperature rise plays in determining material loss.

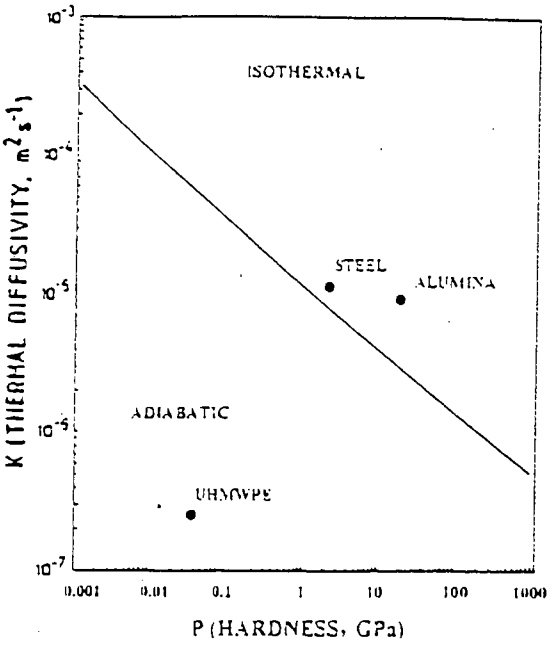

Figure 2. 2 The isothermal-adiabatic boundary appropriate for the experimental conditions used for the various values of thermal diffusivity and hardness. The values for various materials are plotted on the diagram (after Doyle and Ball[58]).

2.1.1.3. Platelet mechanism

Levy [59]suggested that in the initial phase, an impacting particle forms a crater, and material is extruded or displaced from the crater to form a raised lip. In the second phase the displaced metal is deformed by subsequent impacts; this may lead to lateral displacement of the material and can be accompanied by some ductile fracture in heavily strained regions. Finally, after a relatively few impacts, the displaced material becomes so severely strained that it is detached from the surface by ductile fracture. However, Brown, Jun and Edington[60] observed that the flake -and platelet - type structures occurred in materials eroded by spherical particles and not for angular particles.

2.1.1.4. Delamination wear mechanism

Suh[46] indicated that the delamination wear mechanism which was initially developed for sliding wear of metals may apply to solid particle erosion of metals. The target is considered to be composed of a matrix containing harder inclusions. The projectile interacts with the surface by sliding across it but not directly removing material. Delamination can only occur when subsurface cracks start to extend parallel to the target surface. These cracks are nucleated by voids that can form at the interface between the matrix and the inclusions. However, Jahanmir[61] discusses delamination in terms of a projectile sliding across a surface and sliding is impossible at normal impingement.

2.1.1.5. Deformation mechanism

Bitter[3] proposed that the removal of material from the surface of a target occurs by the joint action of two mechanisms: cutting, which only occurs when the projectile strikes the target at a grazing incidence; and deformation wear, which predominates at normal impingement. Bitter's equation (2.2) given below is based solely upon an analysis of brittle type of wear. The erosion loss predicted by this equation increases systematically with increasing impingement angle. Unfortunately he did not explain clearly how material was removed by deformation wear. Neilson and Gilchrist[7] have extended the Bitter's equation (2.2) to include the contribution of the horizontal force component of the particle that is theoretically associated with the ductile or "cutting" mode of erosion. The erosion loss predicted by this function decreases with increasing impingement angle (see equation 2.3). Neilson and Gilchrist assume that the total erosion obtained is as a result of combination of brittle and ductile contributions, and therefore, the maximum in erosion loss at an intermediate impingement angle can be predicted. However, this equation (2.3) is very complex due to the difficulty in measuring quantities such as ε, K, U_p and ϕ.

$$Q = \tfrac{1}{2} M(V\sin\alpha - K)^2 / \varepsilon' \qquad (2.2)$$

$$Ev = 0.5\,(MV^2\cos^2\alpha - U_p^2)/\phi + 0.5\,(MV\sin\alpha - K')^2/\varepsilon' \qquad (2.3)$$

Where

Ev is erosion in units of volume loss

M is total mass of eroding particle

V is velocity of eroding particle

α is impingement angle

K′ is constant, related to a threshold velocity below which erosion stops

ε' is energy needed to remove a unit volume of target material (repeated deformation wear)

U_p is horizontal component of particle velocity

ϕ is energy needed to remove a unit volume of target material (cutting wear)

2.1.1.6. Fatigue wear mechanism

Mamoum[47] proposed a fatigue wear model in which the material is assumed to be removed when it reaches a critical strain. The model assumes that each event of impact constitutes a strain cycle and that a critical number of such cycles result in material removal by fatigue failure. Hutchings[13] also proposed that there exists a criterion of a critical plastic strain at which material will be removed. Ball[62] has demonstrated the advantage of materials with high work-hardening rates. Material removal during erosive and abrasive wear occurs once a critical strain for fracture is attained and consequently a material which delays the attainment of the critical strain for fracture will exhibit superior wear resistance.

2.1.1.7. Adhesion mechanism

Salik and Buckly[48] proposed that the erosion is a result of the adhesion of the target material to the impacting particle. However, evidence continues to support the mechanism involving platelet formation and removal.

In summary, a single mechanism cannot fully account for the total material erosion loss for all shapes and sizes of impinging particles. It is understood that two or three mechanisms can better explain the erosion process with different shapes and sizes of particles[39, 49, 50, 63]. However, recently, Finnie, Stevick and Ridgely[38] observed that the curves shown in fig.2.1, of erosion loss as a function of angle, are similar for ductile metals with a wide range of thermal and mechanical properties. This is so even experimentally for glass and untempered martensite materials when eroded with small enough particles. They suggest that a simple basic mechanism may be sufficient to explain erosion at large angles of incidence. The measurements of surface profile may be combined with the analysis of a particle striking a smooth surface to predict the value of erosion for 90^0 incidence.

2.1.2. Brittle mode of erosion

Erosion of brittle materials such as glass and ceramics has generally been viewed as a brittle fracture process. The erosion of brittle materials by solid particle impact has been the subject of increasing interest because ceramic materials are increasingly specified for tribological applications, such as in the gas turbine engines[64], cutting tools[65, 66, 67]and other applications in which wear is a problem. In fact ceramic materials or coatings are the only solution to some wear problems, particularly those used at high temperature and in severe chemical environments. The damage resulting from erosion can cause a serious degradation of strength and may ultimately lead to failure. Their response to potential impacts during operation must be evaluated. A clear understanding of the erosion processes of brittle materials is therefore important.

Investigations have shown that a number of erosion mechanisms for ceramics can exist and that erosion is a complex process[68]. The earlier elastic model[12] was based on elastic interaction between target and particle and predicted that material removal occurs by the intersection of ring cracks on the target surface. Later analysis[15, 16] has treated static and dynamic plastic indentation, which is characterised by inelastic or plastic deformation of the contact area between the particle and the target. Radial cracks propagate outward from the contact zone and subsurface lateral cracks propagate outward on planes nearly parallel to the surface.

Field and Hutchings[69] indicated that the modes of fracture and deformation depend on the particle velocity, shape and mechanical properties relative to those of the target material. Low velocity, blunt particles set up elastic Hertzian stress fields in the target which initiate cone cracking. Material removal will depend on the propagation of the fracture into the material and its interaction with other fractures. Sharp particles impacting at high velocities produce inelastic deformation zones and initiate median and lateral cracking.

Recently, Ritter and Jakus[70] indicated that for soda-lime glass under sharp indentation or particle impact, the radial crack controls strength degradation. Under blunt indentation or particle impact, the cone cracks control strength degradation. For fused silica the radial crack is strength controlling under both sharp and blunt indentation or impact as fused silica can densify under indentation.

2.1.2.1. Elastic model

The problem of elastic contact between a solid spherical indenter and a flat solid surface was first analysed by Hertz[71] and since then it has been the subject of numerous experimental and theoretical investigations. Routbort, Scattergood and Turner[72] modified Hertz's theory to take into account interfacial frictional stresses and showed that if there is a mismatch in the elastic constants of the solids, the maximum of the radial tensile stress occurs outside the circle of contact. This explains the observation that the radius of the ring crack that forms on the surface for a critical load on the indenter is greater than the radius of the contact circle if the modulus of the indenter is greater than that of the flat specimen.

Sheldon and Finnie[29] also assumed that particle-target interactions were perfectly elastic. The extent of damage or volume removed was described on the basis of a classical Hertzian analysis of fracture beneath a spherical indenter. Finnie[11] indicated that on the loading cycle, surface ring cracks would form at the edge of contact area. On continued loading, these surface traces formed fully developed cone cracks as shown in fig.2.3. This elastic/brittle treatment leads to the conclusion that the erosive wear of a brittle material depends on the fracture toughness[73] and on the size and distribution of pre-existing flaws[74].

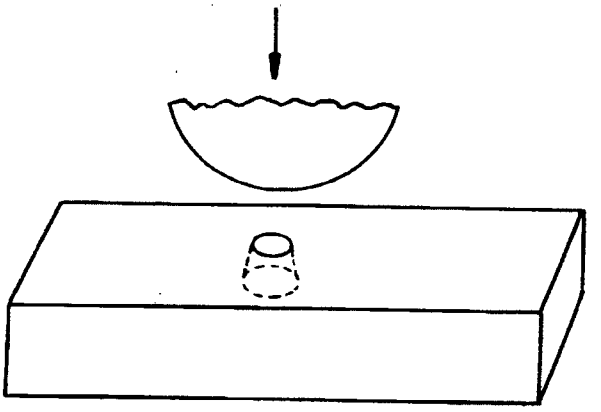

Figure 2. 3 A schematic diagram of a Hertzian cone crack formed by the impact of a steel ball against a glass specimen (after Finnie[11]).

2.1.2.2. Inelastic model

In most practical situations, surfaces are subjected to impact by irregularly shaped particles. Erosion of brittle materials by hard, sharp particles is generally thought to result from elastic/plastic fracture[15, 68, 74, 75, 76]. This type of fracture is characterised by plastic or crushing deformation of the contact area between the impacting particle and target[77]. Lawn and Wilshaw[73] indicated that typical contact situations resemble quasi-static indentation with indenters of small radius of curvature as shown schematically in fig. 2.4. During the loading cycle the sharp indenter produces inelastic or plastic deformation until the contact area is large enough to support the load. Sub-surface radial or median cracks are produced by tensile stresses on median planes and propagate radically from the centre of the impact site. On unloading, the median cracks close up and further unloading produces lateral cracks which propagate parallel to the surface of the target material due to the incompatibility between the plastic deformation and elastic deformation around it.

The lateral cracks are considered to be responsible for material removal and the radial cracks are a source of strength degradation. The intersection of lateral cracks with the surface produces saucer-shaped flakes of material which are subsequently removed and account for the major loss of material by erosion. Analyses of the contact mechanics between impacting particles and brittle materials have been the basis for several models of erosion[15, 74, 75, 77, 78, 79,

[80, 81, 82]. Two elastic-plastic theories proposed by Wiederhorn and Lawn[16] and Evans, Gulden and Rosenblatt[15] have been developed to explain the erosion of brittle materials. Both are based on the assumption that lateral cracks grow in a quasi-static manner as a result of residual stresses introduced by the impact event. In both theories, the erosion volume is determined from the size of the lateral crack and the depth of the crack beneath the target surface. The lateral cracks are assumed to be caused by the normal load[74]. These two elastic-plastic theories [15, 16] differ in their assumed impact load.

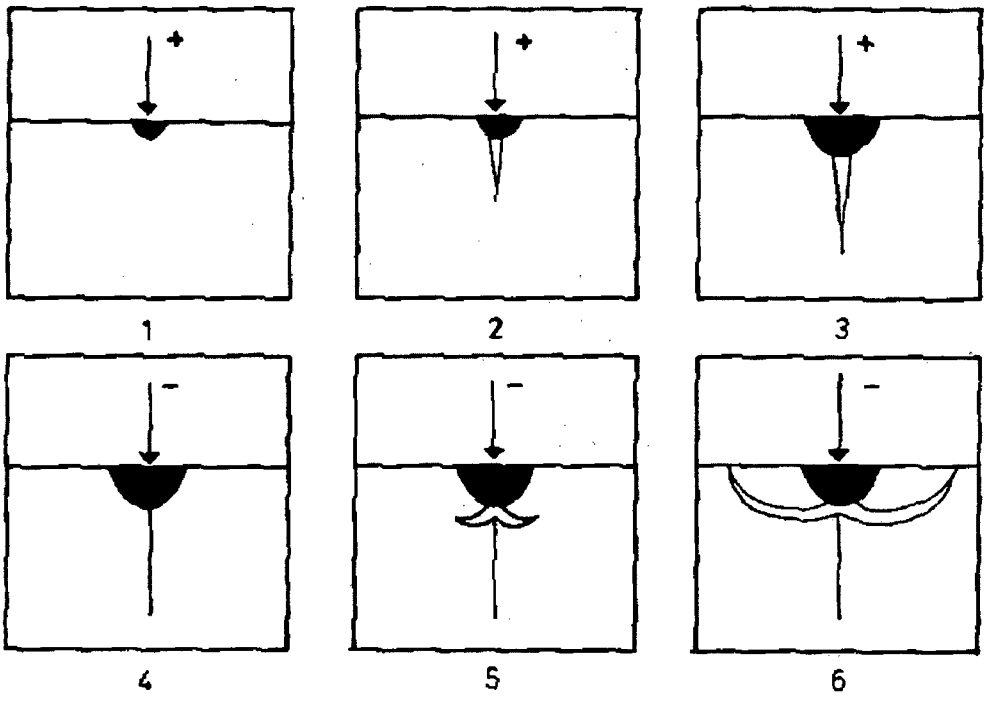

Figure 2. 4 A schematic diagram of the loading cycle under a sharp indenter. Cross-sectional view of the formation of a radial crack during the loading cycle(+) and of the formation of cracks during the unloading cycle(-). The dark region represents the zone of plastic deformation (after Lawn and Wilshaw[73]).

The deformation and cracking patterns produced by quasi-static Vickers-indentation are schematically represented in fig. 2.5. Evans et al.[15] and Wiederhorn et al. [16] indicated that the mean indentation pressure at any stage of the contact may be expressed in terms of the load.

$$p_0 = P/\Lambda\pi\, a^2 \equiv H \qquad (2.4)$$

where

P is load

a is a surface dimension of the plastic impression

Λ is shape factor of erodent

H is the hardness of materials.

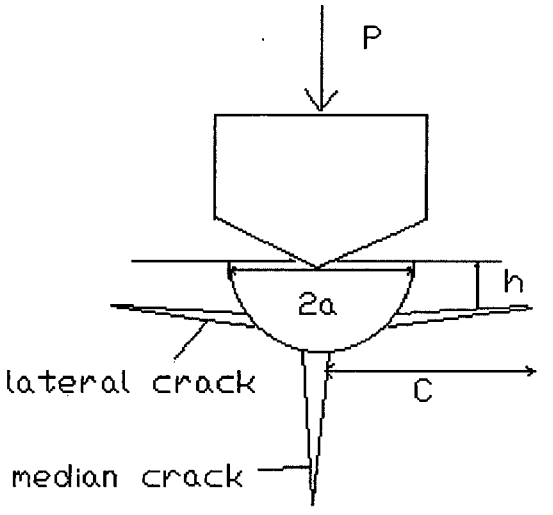

Figure 2. 5 Schematic diagram of indentation caused by a sharp erosive particle

Evans et al.[15] performed erosion tests on MgF_2, Si_3N_4 and alumina materials and observed that the lateral fractures from adjacent impacts intersect with little interaction, thus the material removal process may be considered as a simple summation of the material removed per impact.

$$\Delta V \propto \pi C^2 h \qquad (2.5)$$

Where

h is depth of the lateral crack below surface

C is radius of lateral crack.

According to the assumption made by Griffith[83], the energy–balance condition for crack extension is that the rate of increase of total surface energy (Us) just balances the rate of decrease of total strain energy (Um) as the crack expands (applied to glass and brittle materials) i.e. d(Um -Us)/dC =0. Lawn and Fuller[84] indicated that since the area of crack surface must scale with the square of the characteristic crack dimension, C, the total surface energy must be of the form:

$$Us \propto \Gamma C^2 \qquad (2.6)$$

where Γ is the fracture surface energy. The intensity of the indentation stress field will be determined by the point load divided by a characteric area ($\propto P/C^2$). The strain energy density will be given by the square of the stress divided by an elastic modulus [$\propto (P/C^2)^2 /E$, where E is Young's modulus of material].

The volume of stressed material associated with the field of the crack will scale with the cube of the crack dimension ($\propto C^3$) so that the total strain energy may be written

$$Um \propto P^2 /E\, C, \qquad (Um = \text{strain energy density x volume}) \qquad (2.7)$$

The energy-balance requirement, dUs/dC=dUm/dC, then gives

$$P^2/C^3 = \text{Const.}\ \Gamma E \qquad (2.8)$$

The equation (2.8) can be rewritten into the equation (2.9)

$$P/C^{3/2}=\beta K_t, \qquad (2.9)$$

where β is a dimensionless factor determined by zone geometry.

Evans et al.[15] performed a series of erosion tests on ZnS using WC and glass erodents and observed that the depth of the lateral crack below the surface is proportional to the radius of contact area.

$$h \propto a \qquad (2.10)$$

Substituting for C, h from the equations (2.9) and (2.10) into equation (2.5) gives

$$\Delta V \propto \pi(P/\beta K_t)^{4/3}\, a \qquad (2.11)$$

substituting for a from equation (2.4) into equation (2.11) gives

$$\Delta V \propto P^{11/6} K_t^{-4/3} H^{-1/2} \qquad (2.12)$$

The quasi-static theory developed by Wiederhorn et al.[16] assumed that the kinetic energy of the particle is absorbed completely by plastic flow when a particle impacts the surface. Eq.(2.13) holds for both elastic and plastic deformation.

$$0.5\,[4\pi R^3\,\rho/3]\,V^2 = \int_0^z P(z)\,dz \qquad (2.13)$$

where

ρ is the density of the particle

V is the impact velocity

P(z) is the load corresponding to the distance of mutual approach of the deforming solids z.

Timoshenko and Goodier[85] indicated that for the purely elastic case, the radius a of the circle of contact between the indenter of radius, R, and the flat solid surface is given by

$$a^3 = 4kPR/3E \qquad (2.14)$$

$$z = [4k/3E]^{2/3}\,P^{2/3}\,R^{-2/3} \qquad (2.15)$$

where

$k = (9/16)[(1-\gamma^2)+(1-\gamma'^2)E/E']$

γ and γ' are the Poisson's ratios of the target materials and the indenter

E and E′ are the Young's moduli of the target and the indenter

z is the distance of mutual approach of the deforming solids

Integration of equation (2.13) gives the maximum load,

$$P_m = [5\pi\rho/3]^{3/5}\,[4k/3E]^{-2/5}\,R^2\,V^{6/5} \qquad (2.16)$$

Substituting for P_m from the equation (2.16) into equation (2.12) gives

$$\Delta V \propto P^{11/6}\,K_{IC}^{-4/3}\,H^{-1/2} \propto \rho^{1.1}R^{3.7}V^{2.2}K_t^{-1.3}\,H_t^{-0.5} \qquad (2.17)$$

where

ΔV is erosion rate per particle

R is particle radius

ρ is particle density

V is the particle velocity

H and K are the hardness and toughness of target respectively

The dynamic elastic-plastic theory developed by Evans et al.[15] considered the dynamic elastic-plastic response of a sharp particle at normal incidence and included dynamic stress wave effects in the calculation of impact load. The contact pressure is assumed to be equal to the dynamic pressure that occurs when the particle first hits the target surface. The depth of penetration is determined from the time of contact and the mean interface velocity, both of which are calculated from a one-dimensional analogue. The erosion expression is as follows.

$$\Delta V \propto \rho^{1.3} R^{3.7} V^{3.2} K_t^{-1.3} H_t^{-1.25} \qquad (2.18)$$

Despite the differences in physical assumptions, the two elastic-plastic theories predict erosion rates that have similar functional dependence on the particle velocity, size, density and on the mechanical properties of the target.

Particular attention was drawn to the paper written by Evans and Wilshaw[77]. They performed indentation tests using sapphire, spinel, silicon nitride and zinc sulphide. The indenter is WC. They found the empirical relationship between P and C is as follows. β is supposed to be dimensional in order to keep Eq.(2.19) dimensionally correct although Evans et al[77] did not mention whether or not it is dimensional.

$$P/C^{4/3}=\beta' K_t \qquad (2.19)$$

substituting for C, h from the equation (2.19) and (2.10) into equation (2.5) gives

$$\Delta V \propto \pi(P/K_t)^{3/2} a \qquad (2.20)$$

substituting for a from equation (2.4) into equation (2.20) gives

$$\Delta V \propto P^2 K_t^{-3/2} H_t^{-1/2} \qquad (2.21)$$

Substituting for P_m from the equation (2.16) into equation (2.21) gives

$$\Delta V \propto P^2 K_t^{-3/2} H_t^{-1/2} \propto \rho^{6/5} R^4 V^{12/5} K_t^{-3/2} H_t^{-1/2} \qquad (2.22)$$

The only discrepancy between equation (2.17) and (2.22) is that the assumption of relationship between P/C and K_t differs. The equation (2.17) is derived by assuming that $P/C^{3/2} \propto K_t$. The equation (2.22) is derived by assuming that $P/C^{4/3} \propto K_t$. It reveals different assumption for impact loading condition results in different erosion loss equations (2.17), (2.18) and (2.22). Later Wiederhorn and Hockey[74] performed the erosion tests on a series of brittle materials like MgO, glass, silica, sapphire and alumina using SiC erodent impacts. The empirical equation of erosion is given below (equation 2.23). It shows that the dependence of erosion rate on these parameters is different from that predicted by these models mentioned above. They attribute these discrepancies primarily to microstructural aspects of erosion that are not modelled by these models.

$$\Delta V \propto \rho^{1.4} R^{3.9} V^{2.8} K_t^{-1.9} H_t^{0.48} \qquad (2.23)$$

Routbort, Scattergood and Turner[72] investigated the impact erosion of commercial reaction-bonded SiC by angular Al_2O_3 particles with a range of median particle sizes, velocities and angles. They suggested these theories mentioned above do not predict the empirical result that the steady state erosion rate is given by

$$E_g \propto R^{0.7\text{-}0.95} V^{2.0\text{-}2.5} \qquad (2.24)$$

where R is the impacting particle radius and V is the velocity.

Recently, Ritter and Jakus[70] performed the particle impact test on fused silica using hyperveloicty (greater than 3 km/s) and indicated that the volume loss of the pit is proportional to the impacting kinetic energy of the particle only. Slikkerveer et al.[32] performed the erosion tests on a boro-silicate glass using angular alumina particles. They indicated that erosion rate is proportional to erosion efficiency and the impingement velocity raised to power 2. Erosion efficiency is defined as the amount of removal target per amount of energy in the incoming particles. The erosion efficiency is proportional to the kinetic energy of impacting particle raised to power 7/6 and the parameters of target. So systematic studies on the influence of the impact variable and material parameters on the erosion rate are needed to understand the modes and mechanisms of erosion of glass. This is the major objective of this thesis.

2.1.3. Erosion of glass

Ballout, Mathis and Talia[30] studied the erosion mechanism of glass with impact of alumina particles and glass beads as a function of particle velocity and size. They showed that the tangential impact forces dominate in the process of the material removal at low angles, while the normal impact forces lead to the material removal at high angles. The mechanism of erosion of glass is associated with the formation and propagation of lateral cracks. Sparks and Hutchings[33] investigated the mechanisms of material removal during the erosive wear of a glassy ceramics. They proposed that the brittle - ductile transitions modes that occurred depended on the particle shape, impact velocity and impact angle. The modes of material removal caused by rounded silica sand changed from fine-scale fracture and plastic processes below a transition point to large-scale cracking of the surface above the transition. The mechanism of material removal is dominated by lateral fracture and flake formation for angular silica particles. In addition, erosion by glass beads showed features of a fatigue-dominated erosion mechanism with much less plastic flow.

Sheldon and Finnie[29] investigated the erosion of soda-lime glass eroded by silicon carbide particles of three different sizes. They showed that on reducing the size of the silicon carbide erodent particles from 125 μm to 9 μm, the angle of maximum erosion for soda-lime glass shifted from close to 90^0 to a much lower angle. The erosion mode had changed from 'brittle' to 'ductile'. Buijs and Pasmans[28] also investigated the erosion of glass impacted by alumina particles (30μm) and observed two transitions: at low velocities the removal process changes from ductile to brittle, while at high velocities fragmentation of the alumina particles occurs. They indicated that the erosion can be well described using indentation fracture mechanics. The exponent of the velocity-dependence of the removal rate was found to be in good agreement with the value of 7/3 which is predicted by quasi-static indentation theory[16]. However, previous work by Finnie et al.[27] indicated that the velocity exponent is about 6 for glass impacted with steel ball. Verspui[31] indicated that the experimental velocity

exponent is 4.36 and 3.86 for glass impacted by spherical glass beads and angular alumina erodents respectively. Recently, Slikkerveer et al.[32] performed the erosion of glass using alumina erodents with a range of particle sizes (9-200μm) and particle velocities (20-300m/s). They found that the velocity exponent and particle size exponent are 2.46 and 3.69 respectively. In addition, the velocity exponent appears to decrease systematically with increasing size of the impacting particle[86].

Verspui and Slikkerveer[17] investigated the modes of erosion of glass by single impacts of Zirblast beads. An erosion map where the velocity of a particle is depicted versus the diameter of particle is derived. In this map, the transition of modes is noted. At low impact velocities, the glass behaves elastically. The plastic deformation occurs above certain impact velocity. In the plastic regime a transition takes place to the development of radial and lateral cracking. The evidence of ring and cone cracks in the plastic region is observed.

2.1.4. Erosion of stainless steel

The room temperature solid particle erosion behaviour of various types of stainless steel has been characterised by a number of investigators over the last decade[36, 87, 88, 89, 90, 91]. Singh, Tiwariand and Sundararajan[87] investigated the room temperature erosion behaviour of three stainless steels eroded by silicon carbide at three impact angles and at two impact velocities for each angle. The impact angle and velocity dependence of the erosion rates of 304 stainless steel are consistent with a ductile erosion response. The formation of lips and platelets and their fracture are responsible for material removal. The depth of the plastic zone beneath the eroded surface increases with increasing impact angle and increasing impact velocity. Similar results are also found by Foley and Levy[36]. They investigated room temperature erosion of 304 stainless steel using alumina particles with an average size of 140 μm. It was found that the platelet mechanism of erosion occurred in all the steels. Platelets of metal formed in the immediate surface region were subsequently highly deformed by continuing particle impacts and were eventually knocked off the surface when their local fracture strain was exceeded. Beneath the highly deformed surface region a cold-worked zone was developed that enhanced the ability of the impacting particles to form,

deform and knock off platelets. Soderberg, Hogmark and Swahn[90] performed the solid particle erosion tests of an austenitic stainless steel and found that cutting and deformation mechanisms operate in the process of erosion.

Sundararajan and Shewmon[14] indicated that localised lip formation and subsequent lip fracture is the dominant mechanism by which material is removed during the normal incidence of single spherical particles on 304 stainless steel. The lip formation is the result of localisation of deformation in the near-surface regions of the target and that the lip is removed once a critical strain is exceeded. Ball[62] has demonstrated the advantage of materials with high work-hardening rates. Material removal during erosive and abrasive wear occurs once a critical strain for fracture is attained and consequently a material which delays the attainment of the critical strain for fracture will exhibit superior wear resistance. Finnie et al.[37] and Hutchings[13] indicated that cutting mechanism is operative at oblique angle impact for ductile materials. Morrison and Scatttergood[88] however indicated that a single mechanism, that is, shear deformation is operative for 304 stainless steel eroded by sharp alumina particles at different angle incidence. They found the velocity and the particle size dependence of the erosion rates were similar at all angles of impact between 10^0 and 90^0. SEM observations of the steady state erosion surfaces disclosed similar morphologies for low and high angles of impact. The surfaces display a peak and valley topology together with attached platelets of material.

2.1.5. Erosion of tungsten carbide - cobalt

The severity of the wear encountered in valves in industrial pumps and other components exposed to erosive fluids has led to the application of hard, wear-resistant materials like cemented carbide[92, 93, 94]. Owing to cobalt's excellent wetting and adhesion to metallic carbides and adequate mechanical properties, it is the most common binder metal for cemented carbide applications. Several mechanisms have been proposed to relate the erosion rate to the properties of WC-Co.

Ball, Willmott and Resente[95] indicated that the dominant mode of erosion is extrusion of the binder phase with subsequent smearing over the WC grains. The removal of the carbide particles occurs when there is not sufficient binder present to retain these particles. Ball and Paterson[96] indicated that the cobalt content is important to erosion rate. They observed that below 10 wt% cobalt the erosion is controlled by the WC skeleton. Above 10 wt% cobalt, erosion is controlled by the strength and microtoughness of the binder. At 10wt% the cobalt has low toughness and the WC skeleton is fragile and discontinuous. Wright, Shetty and Clauer[97] also observed a trend of decreasing erosion with decreased binder content to a minimum binder level of 7.1%. For high binder levels, erosion appears to occur mainly by preferential removal of the binder phase, while the WC grains undergo only minor erosion that results in blunting of sharp corners or edges. This type of erosion response is characterised as ductile erosion. For the low binder types, the contiguity of carbide particles increases rapidly with decreasing binder content, and the fracture toughness decreases accordingly. Cracking of the carbide/carbide interfaces and intergranular failure is a likely failure mode. This type of erosion response is characterised as brittle erosion. They suggested that the erosion of cemented tungsten carbide occurs by a mixture of modes, the larger particles produce erosion of the tungsten carbide by chipping while the smaller size particles erode by ductile cutting and extrusion of the binder.

Conrad, Shin and Sargent[98] investigated the effect of WC grain size in the range of 0.9-3.0μm and cobalt contents of 4.5 to 11.3 wt% on the erosion of sintered WC-Co alloys with 240 grit Al_2O_3 particles at velocities of 30-100 m. s^{-1} and impact angles of 20^0-90^0. The erosion of the sintered WC-Co alloys considered may obey a rule of mixtures, the erosion of the WC phase occurring by a Hertzian elastic fracture mechanism and that of the cobalt phase by a combined cutting and deformation wear mechanism. They indicated that maximum erosion occurred at 90° impact for all cobalt contents tested. This appears to indicate that a brittle mode of erosion occurs in WC-Co alloys. However, Shetty, Wright and Stropki[99] observed that the impingement angle dependence of erosion rates was similar for 5.1 wt% and 36.9 wt% cobalt alloys. The erosion rates were maximum and approximately constant in the impingement angle range 50° to 90°. It reveals that angular dependence tests tend to be independent of the modes of erosion of WC-Co alloy.

2.1.6. Erosion of alumina ceramics

The modes of material removal for alumina ceramics are categorised as lateral cracking, transgranular fracture or intergranular fracture in terms of the properties of targets and erodents. Shetty, Wright and Stropki[100] carried out the slurry erosion of alumina, slurry consisting of 8 weight percent fused silica particles with silica particle size range 10-15 μm dispersed in a petroleum-based oil. They found that polycrystalline ceramics could be classified into two groups based on their erosion response. Hot-pressed alumina exhibited a transgranular wear mechanism and the resulting wear rates were low. Material removal was by a micro-flaking or a delamination mechanism. The wear rate showed an approximate inverse correlation with target hardness. Sintered alumina exhibited a brittle intergranular fracture mechanism and relatively high wear rates. The mode of erosion for alumina appears to be determined by the erodent properties.

Murugesh and Scattergood[101] investigated the effect of erodent particle properties for solid particle erosion in a series of alumina ceramics using alumina and SiC erodents. They indicated that the steady state erosion surfaces display lateral crack controlled morphology when the erodents are harder than the target while plastic deformation is produced when the erodents are softer than the target. Multiple plastic deformation impacts build up the requisite critical penetration depth needed to generate lateral cracks. Vaughan and Ball[102] performed the erosion tests on six ceramics and indicated that the fragile and defective alumina materials suffer massive damage by the process of lateral spallation, while the tough zirconias absorb energy by plastic processes and provide good erosion resistance.

Ritter, Rosenfeld and Jakus[103] performed erosion tests on sintered alumina target using angular SiC erodent impacts. They observed the damage morphology in sintered alumina and assumed that the kinetic energy of the impacting particles goes into grain boundary cracking and subsequent grain fallout creates a hemispherical pit with an annular crack equal to about a grain diameter, contrary to predictions based on elastic-plastic fracture. Thus, the impacting energy will be proportional to the grain boundary fracture energy γ_i

$$U_k \propto n \gamma_i d^2 \qquad (2.25)$$

Where

n is the number of grains included in a pit

d is the average grain diameter.

Since the number of grains per pit is proportional to the ratio of the pit volume over the average grain volume, the pit volume given below will vary with the kinetic energy of the impacting particles U_k. They indicated that this model can well explain the experimental data.

$$\text{Pit volume} \propto (d\, U_k)/\gamma_1 \qquad (2.26)$$

Where γ_1 is the grain boundary fracture energy.

2.2. Variables affecting erosion

According to Finnie[104] erosion is affected by a number of factors which fall into three major categories: impingement considerations (angle of impingement, particle velocity), eroded material properties (microstructure, hardness and toughness) and erodent characteristics (particle size and its density, shape, hardness and toughness).

This section surveys and analyses literature on the effect of a variety of factors on the solid particle erosion, which is relevant to the present work.

2.2.1. Target material variables

2.2.1.1. Target hardness

Hardness is a measure of a material's resistance to plastic flow. There are many different views of its influence on the erosion rate. Finnie[12] observed that the erosion rate is inversely proportional to hardness for annealed face centred cubic materials. Levy[105] also showed that the erosion rate of a 1075 steel and the two harder 1020 steel samples varied inversely with hardness. However, other researchers have found that erosion rate shows no significant

increase with hardness although heat treatments of steel and aluminium alloys result in a threefold increase in bulk hardness[27, 39 106]. Wilson and Ball[107] investigated the solid particle erosion of aluminium matrix composites and indicated that mass losses were not dependent on resistance to indentation hardness, but rather on each material's ability to accumulate strain followed by shear failure of the matrix.

Shewmon and Sundararajan[35] correlated the erosion rate of a metal or alloy with various parameters such as velocity, angle of impact, size and shape of the impinging particle, hardness and therm-physical properties of the material being eroded. They indicated that erosion rate is strongly dependent on velocity, impact angle and shape of the erodent but is insensitive to particle size as well as hardness increase achieved in the eroding material through cold-work and heat treatment. Budinski[108] conducted erosion tests on tool steels and carbon steels and also confirmed that under steady state conditions hard and soft metals have similar erosion rates when particles are significantly harder than the target. The independence of erosion rate to hardness changes has been explained by a thermal softening mechanism[106] or by the high strain rate of the erosive process ($10^5 - 10^7$ sec^{-1})[39].

For brittle materials, Srinivasan and Scattergood[109] noticed that the relative hardness values of the erodent particles and the target sample might play a significant role during erosion. In steady state, the lateral-crack-based erosion mechanisms operate for harder erodents but for softer erodents damage accumulation is necessary to build up the requisite stresses to produce lateral cracks. In particular, the erosion rates can increase significantly when the erodent particle-to-target hardness ratio H_p/H_t increases above $H_p/H_t=1$ [110]. Vaughan and Ball[102] also showed that the ease of lateral crack initiation is the controlling factor in erosion of ceramic and ultrahard materials when the erodent hardness is similar to the target hardness. When the erodent particles are much harder than the target material lateral crack initiation is inevitable.

Hutchings[13] indicated that dynamic hardness is probably a more appropriate variable for characterising the erosion of either ductile or brittle materials and suggested that dynamic hardness should be used in the basic erosion rate equation.

2.2.1.2. Target toughness

Fracture toughness is a measure of a material's resistance to fracture propagation. Several attempts to correlate the erosion rates of brittle materials with experimental and material parameters can be found in the literature[15, 16]. In these models, the hardness and the fracture toughness emerge as the main material parameters for erosion control. Because erosion of brittle materials occurs by formation and propagation of lateral cracks under driving forces imposed by the particle impact event[15], increasing K_t should result in an improved erosion resistance. Sykes, Scattergood and Routbort[111] have shown that the erosion resistance of an Al_2O_3-SiC composite increases with additions of up to 25wt% SiC which raises K_t in accordance with theoretical expectations. However, Morrison, Routbort and Scattergood[112] have shown that for Si_3N_4 materials, the erosion behaviour remains independent of whisker content although the additions of SiC increased its toughness.

For ductile materials, Foley and Levy[113] investigated the erosion behaviour of a plain carbon steel, an austenitic stainless steel and a low alloy steel in various heat-treated conditions using 140 μm average size alumina particles and indicated that the hardness, strength, fracture toughness and impact strength of these materials had little effect on erosion behaviour.

2.2.1.3. Dynamic properties

The strain rate during an erosive strike on metals has been estimated by Hutchings and Winter [114] as being in the range of 10^5-10^7 sec^{-1}. Winter and Hutchings[115] indicated that the high strain rates associated with particle erosion may lead to different deformation modes in different materials. Ball[62] and Foley and Levy[113] showed that the erosion resistance of ductile materials increases as the work-hardening exponent increases. However,

Sundararajan[116] indicated that there is no consistent correlation between work-hardening exponent and the erosion rate.

2.2.2. Erodent variables

2.2.2.1. Particle hardness

Hardness is often used as a measure of the strength and integrity of a particle[117]. Soft particles are prone to blunting and there is a decreased tendency for plastic deformation beneath blunt indenters, making lateral crack initiation less likely and favouring Hertzian fracture for brittle targets. Harder particles are more likely to maintain their integrity on impact and are more able to concentrate energy in a surface. Wada, Watanabe and Tani[110] and Head, Lineback and Manning[118] have shown that the properties of the erodent particles affect the erosion rates and crack morphologies of brittle materials and that the erosion rates increase with increasing particle hardness. However, Evans et al.[15] observed little effect of particle hardness on the erosion of brittle materials at 90^0 incidence.

For ductile materials, Levy and Chik[117] reported that above a particle hardness of 700 HV, mild steel erodes at approximately the same erosion rate regardless of the hardness-strength characteristics of the particle composition. Finnie[11] also suggested that the relative wear rate of different metallic materials should show less variation as the particle hardness increases. He however indicated that when the particle is softer than the metal the wear would be expected to decrease greatly.

2.2.2.2. Particle density

Particle density is an essential factor of all theoretical and empirical analyses during erosion as the particle density determines the kinetic energy of impacting particles and thus affects the loading conditions. A denser particle has higher kinetic energy, which leads to greater potential for surface damage. For ductile materials, the value of density exponent derived by

Finnie[11] is 1. For brittle materials, Ritter and co-workers[70, 103] performed the particle impact test on fused silica using hyperveloicty (greater than 3 km/s) and sintered alumina target using angular SiC erodent impacts. They indicated that the volume loss of the pit is proportional to the impacting kinetic energy of the particle. This means that the value of density exponent is 1. However, the values of density exponent derived theoretically by Evans et al.[15] and Wiederhorn et al.[16] are 1.2 and 1.3 respectively. The effect of particle density on the erosion has not been extensively investigated in any systematic manner, so that there is no way of knowing if the density exponents given in these two models by Evans et al.[15] and Wiederhorn et al.[16] are correct.

2.2.2.3. Shape

The particle shape is one of factors affecting the damage morphology and erosion rate. For brittle materials, blunt projectiles at low velocities produce ring crack formations that develop into cone and radial cracks at higher impact velocities[11]. Sharp projectile damage involves local inelastic or plastic deformation and median/lateral crack formation[11, 16]. In general, sharp angular particles will produce more erosion than spherical particles if all other properties are the same[11]. Wiederhorn et al.[16] explained that sharp particles have a greater capacity to concentrate stresses and induce irreversible deformation and subsequent lateral cracking, which is associated with higher erosion rates.

Sparks and Hutchings[33] investigated the effect of impact velocity, angle and particle shape on the erosion of a silicate glass-ceramic. They observed the variation of erosion rate with impact velocity for the two types of silica particles at 30° impact angle. With the rounded particles, there was a sharp increase in erosion rate at velocities between 44 and 52 $m.s^{-1}$, while with the angular particles a constant velocity exponent applied. Above 52 $m.s^{-1}$, the erosion rate due to the angular silica was about 1.5 times that measured with the rounded silica, but below the transition point the ratio was about 10:1. Above the transition, material was removed in the form of relatively large flaky fragments that were formed by lateral fractures associated with the particle impact sites. Below the transition, material removal by the rounded particles involved much less extensive fracture.

For ductile materials, this effect has been studied in detail by Winter and Hutchings[119] who introduced the term "rake angle" that denotes the angle between the front face of the particle to the normal to the target surface. This angle is dependent on the particle shape. For a spherical particle, the rake angle is always large and negative. They showed that a difference in rake angle caused a change in erosion mechanism-from a ploughing or smearing type of impact crater with large rake angles to a cutting mechanism at small rake angles. Angular particles are generally found to cause a greater proportion of cutting type of material removal. Budinski[108] performed the single impact tests on copper and steel materials using angular particles (alumina, SiC and silica) and spherical particles (glass beads) and indicated that the particle shape is not important. Angular particles, spherical particles and blocky shaped particles will produce impact craters of similar area if the particle diameters are the same.

2.2.2.4. Size

General agreement has been reached on the particle size threshold effect for ductile materials, where erosion increases for increasing particle size up to about 100 μm in diameter[120, 121, 122, 123]. The explanations for this phenomena are proposed by some researchers[120, 120, 124,]. Hutchings[124] investigated solid particle erosion and concluded that the size effect in erosion is due to the strain rate sensitivity of the target material. For purely elastic loading the strain rate is inversely proportional to particle radius and only varies slightly with velocity. The strain rate (ε) for perfectly plastic impact is given by Hutchings[124].

$$\varepsilon = (2^{2/3}V^{1/2}(3P/2\rho)^{1/4})/5\pi R$$

where

V is the particle velocity

P is the mean pressure acting on the sphere during indentation

ρ is the erodent density

R is the sphere radius

It shows that the small particle caused high strain rate of target. This results in an increase in the flow stress of the target material, thus showing a size effect. However, Misra and Finnie[120] indicated that the size effect can not be entirely due to strain rate, which only changes the magnitude of the wear resistance. They suggested that the only explanation for the size effect is that shallow surface layers work harden more than that of the bulk material when they are eroded or abraded. They concluded that the hardness gradient near the surface is formed by the impact particle, small particles do not penetrate this layer, hence removing less material. However, sufficiently large particle which can penetrate the hard layer will plastically deform a material which is softer than that encountered by the small particles. Thus after some critical size the influence of this hard layer on material removal will be slight. However, this explanation has difficulties since it has been shown that heat treatment of the bulk material to a range of hardness and various degrees of cold work have no effect on the erosive performance of the material[105].

Tilly and Sage[122] proposed a two stage mechanism of erosion of ductile materials. Experiments showed that under certain conditions particles shatter into smaller fragments upon striking a surface. The fragments move radically outward, their circumferential distribution depending on the impact angle. The particle size effect can be explained by this mechanism, since smaller particles will be less likely to break up on impact. Apparently, each pair of materials has a threshold size below which fragmentation does not occur. Some materials also have a saturation level, beyond which fragmentation becomes independent of particle size.

For brittle materials, a strong dependence of erosion rate and strength degradation on particle size is predicted. Routbort, Helberg and Goretta[125] investigated the erosion of whisker-reinforced ceramic using SiC erodent whose size and velocity varied from 42 to 390 μm in diameter and 40 to 100 $m.s^{-1}$ respectively. The steady-state erosion rate tends to level off with increasing erodent size. This effect is considered to be due to greater fragmentation of larger erodents. However, no systematic studies of erodent fragmentation distributions and erosion rate behaviour in ceramic systems have been made, and more explicit confirmation of the effect is needed.

2.2.3. Impingement variables

2.2.3.1. Velocity

Particle velocity is considered to be a prime controlling variable in erosion. Researchers are in general agreement that erosion rate varies as: $Ep \propto V^x$ where n is velocity exponent. Finnie, Wolak and Kabil[27] eroded a variety of metals with silicon carbide particles at an angle of 20^0 and concluded that the velocity exponent ranged from 2.05 to 2.44. In general, the velocity exponent n has been placed in the range 2 to 3. The values of the velocity exponent for 90^0 impingement of ductile materials have been reported to be higher than that for low angle incidence[126, 127]. However, the general appearance of the eroded surface does not depend very strongly on the particle velocity or impact angle[128]. Examination of micrographs showed little difference for surfaces of 1020 steel eroded with 250μm silicon carbide particles at two impact angles (30^0 and 90^0) and two velocities (30 and $130 m.s^{-1}$) although they have large differences in erosion rates.

Gulden[129] investigated the erosion of a series of ceramics such as hot-pressed silicon nitride(Si_3N_4), reaction-bonded Si_3N_4, a glass-bonded aluminium oxide (Al_2O_3) and hot-pressed magnesium fluoride (MgF_2). She indicated that the velocity exponent ranges from 1 to 4. Finnie, Wolak and Kabil[27] indicated that the velocity exponent is about 6 for glass impacted by steel shots. However, Buijs et al.[28] indicated that the value of velocity exponent is 7/3 for glass eroded by alumina erodents. The reasons for such variations in exponents between researchers remain unclear.

2.2.3.2. Angle

It has been determined that the erosion of ductile alloys depends markedly on the particle velocity and on the impingement angle as shown in fig. 2.1. Ductile erosion occurs most effectively at glancing impact angles while brittle erosion occurs most effectively at normal impact angles. The difference in behaviour has been attributed to the differences in the

underlying mechanisms governing erosion. The shape of the curves obtained has been shown not to vary significantly with the changes in particle size or particle velocity[7].

2.3. Cavitation erosion

Cavitation erosion is caused by the collapse of bubbles at or near the solid boundaries guiding high speed flow[130] and is one of the major problems confronting the designers of modern high-speed hydrodynamic systems[131] such as hydraulic turbines, pumps, ship propellers, hydrofoils, bearings, diesel engine cylinder liners and torque converters. The damage caused to the component is argued to be either due to the shock wave generated by the symmetrical collapse of the cavity, as originally proposed by Rayleigh[132] or liquid jet impingement, first suggested by Kornfeld and Suvorov[133]. The damage is most likely to be caused by a synergistic effect of the two, with the relative contribution being dependent on the distance of the bubble from the surface of the material and the radius of the bubble[134].

A number of theories on the mechanism of cavitation damage have been proposed to relate the material removal to material property[134, 135, 136, 137, 138, 139, 140, 141, 142]. Woodford[141] investigated cavitation erosion performance of Stellite 6B and several transformation-induced plasticity steels and the effect of ageing on the performance of Stellite 6B. Better performance of cavitation resistance of Stellite 6B is ascribed to lower stacking fault energy (S.F.E.) and the material's planar slip mode of deformation which delays the development of localised stresses required to initiate fracture. However, Karimi and Martin[134] found that Stellite 6B has good cavitation resistance due to its ability to transform to strain induced martensite.

Heathcock, Protheroe and Ball[142] investigated the cavitation erosion performance of a large number of engineering materials using standard vibratory apparatus. Stellites and 304 stainless steel showed superior resistance. Their superior performance was ascribed to their ability to accommodate fatigue-like strain and to limit dislocation build-up by undergoing a stress-induced phase transformation. The fine lath-like transformation product also improved the fracture toughness and cavitation erosion resistance by inhibiting the

propagation of microcracks which lead to material loss. Ultra high molecular weight polyethylene and nylons have relatively high erosion resistance. Their exceptional performances are due to a high strain to fracture and high yield strength respectively. They concluded that factors which promote resistance to cavitation erosion are identified as follows: (1) a high work hardening rate, (2) a high starting hardness or yield strength and (3) a stress-induced phase transformation which accommodates the imposed strain and delays fracture to higher stress levels.

3. MATERIALS AND EXPERIMENTAL METHODS

3.1. Specimen preparation

Glasses are fused mixtures of inorganic oxides. They are commonly considered in three main groups: the soda-lime-silica, the borosilicate and the lead silicate glasses. The glass used in this study is soda-lime silica. Soda-lime-glass termed "as received" condition mainly consists of the SiO_2, Na_2O and CaO. Values obtained from the scientific literature for selected room temperature mechanical properties of soda-lime-glass are shown in Table 3.1. The following materials were selected for comparative testing: 304 stainless steel, high-nitrogen Cr-Mn stainless steel (Cromanite™), WC-Co and sintered alumina. The microstructure of these target materials is shown in fig. 3.1. Their Vickers hardness (HV) is 210, 497, 1036, 1344 for 304 stainless steel, glass, alumina and WC-7%Co respectively. The toughness of WC-7% Co and alumina is 13.7MPa$^{0.5}$ and 5.0MPa$^{0.5}$ respectively. The grain size of alumina and WC is 3.5μm and 2.3μm respectively.

The stainless steel, cobalt based tungsten carbide hardmetal and alumina were ground down to a 600 grit finish before testing. A number of specimens of the as received soda-lime glass were heated to a temperature of about 650^{0}C for a half hour. It is then rapidly taken from the furnace followed by air fan cooling, termed the "as tempered" condition in this thesis. The 304 stainless steel was received as 16 mm extruded rod. Cromanite™ was supplied by *Columbus Stainless* in annealed condition. Their compositions are given in Table 3. 2. Nickel (Ni) and manganese (Mn) are elements of austenite stabilisers. These elements hinder any transformation of the desirable austenite phase to ferrite or martensite.

Table 3.1. Mechanical properties of soda-lime-glass (after Rawson[143] and Holloway[144]).

Property	Value
Density(g/cm^3)	2.48
Poisson's ratio	0.22
Vickers hardness(HV)	540
Young's modulus(GPa)	70.7
Toughness (MPa m$^{0.5}$)	0.2-0.7

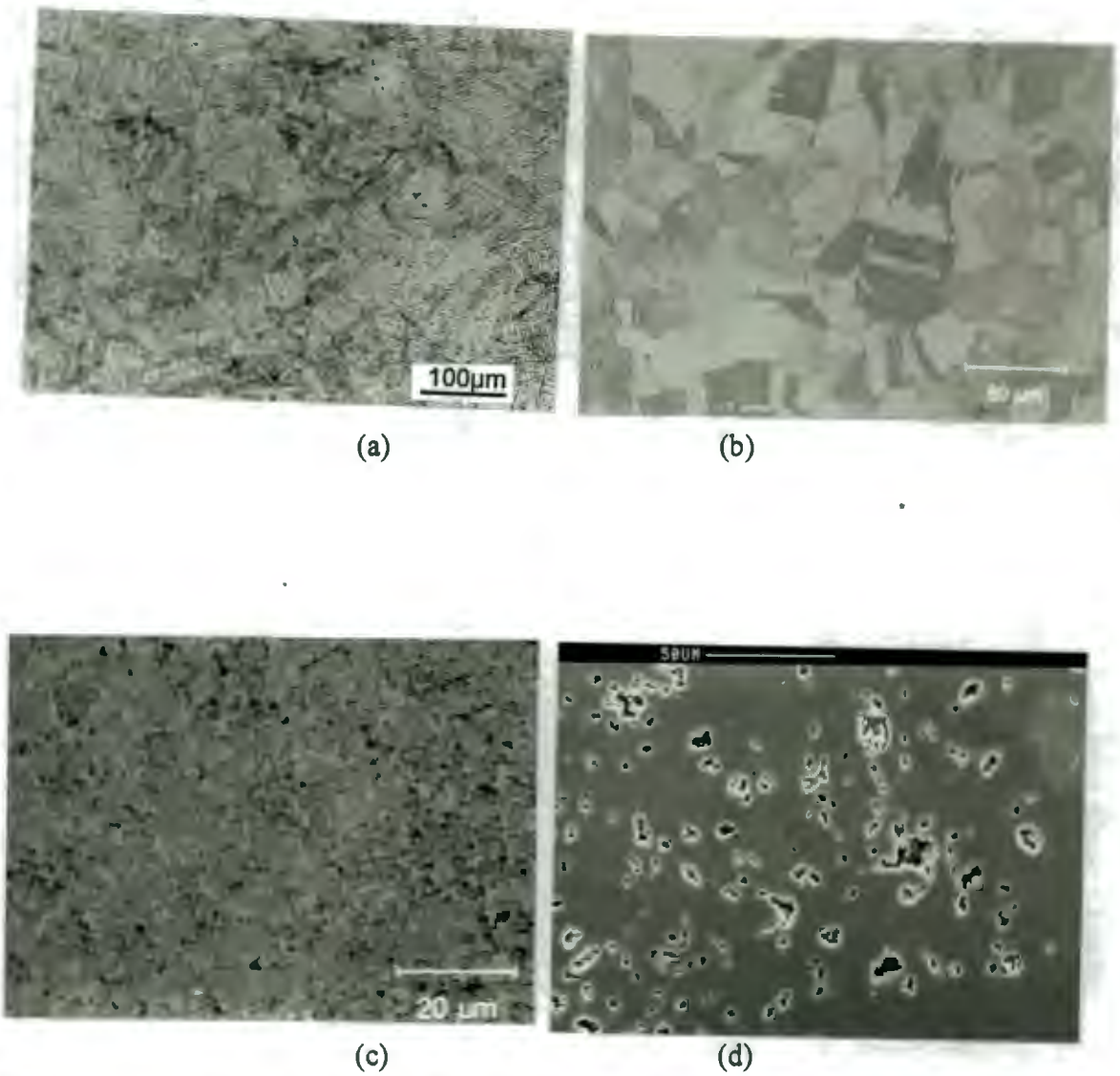

Figure 3. 1 Micrographs of the target materials (a) 304 stainless steel (b) Cromanite™ (c) WC-7%Co (d) sintered alumina, showing porosity on the polished cross section surface

Table 3. 2 The composition of the stainless steel used in the study in wt%

Alloy	Cr	Mn	Si	Ni	N	C
AISI 304	18.36	1.8	0.41	7.77	0.02	0.049
Cromanite™	18.09	9.74	0.004	0.59	0.511	0.036

WC-Co was supplied by *Boart Hardmetals* in the hot-isostatically-pressed and sintered condition. WC-Co is a mixture of hard constituent tungsten carbide (WC) and ductile metal cobalt (Co). The crystal structure of tungsten carbide is a simple hexagonal as shown in fig. 3.2, with the lattice constants a=2.91A^0 and c=2.84A^0.

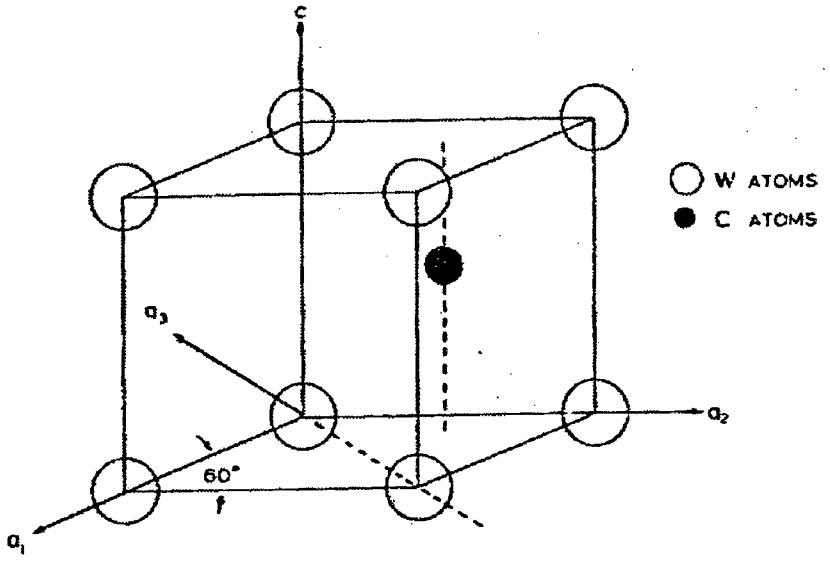

Figure 3. 2 Crystal structure of tungsten carbide (after reference[145, 146, 147]).

The physical properties of cemented carbides are influenced by many factors. Microstructural features such as mean free path, contiguity and average WC grain size are determined by the nature and volume fractions of the initial powders and the sintering process parameters[148]. The relationship between structure and properties of WC-Co composites has been the subject of extensive research[149, 150, 151, 152, 153]. In general, hardness has been found to decrease with increasing cobalt content whereas the transverse rupture strength (TRS) increases and shows a maximum around 20-25% Co. Contiguity has been used as a quantitative measure of WC skeleton formation and has been reported to vary with cobalt content, sintering time and temperature. Increasing contiguity generally results in increased hardness and a decrease in TRS. The fracture toughness, as measured by the critical stress intensity factor (K_c), increases with increasing cobalt content and increasing WC grain size.

Sintered alumina was supplied by *Multotec Wear Linings (Pty) Ltd.* Alumina is a solid in which the atoms or ions are arranged in regular arrays as shown in fig. 3.3. The type of bonding and the atomic arrangements affect a wide range of mechanical properties including strength, hardness, and plastic properties.

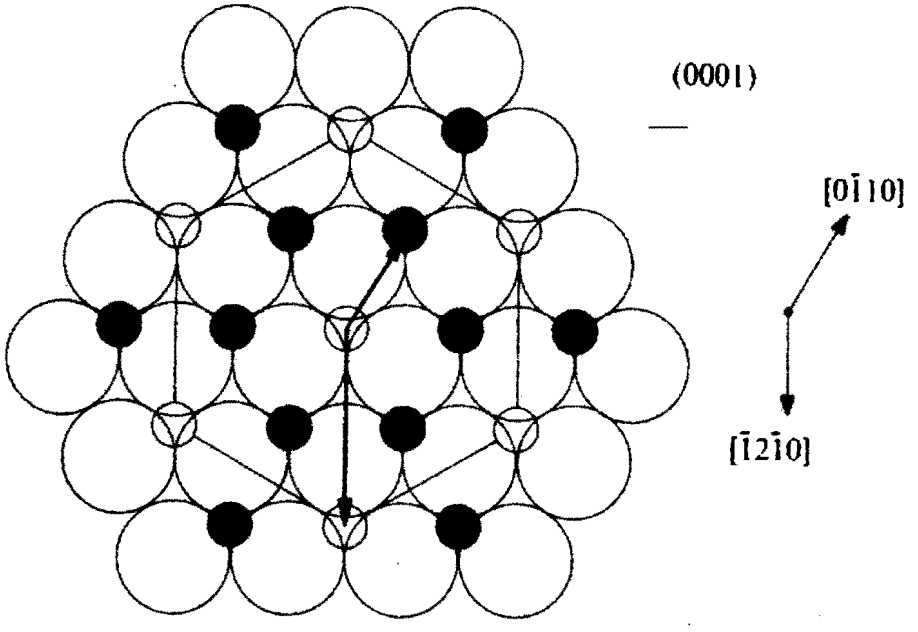

Figure 3. 3. Atomic arrangements in basal planes of alumina. Large circles: O; small filled circles: Al; small open circles: vacant Al sites; hexagonal layers of oxygen atoms are sited between the Al layers (after Kronberg [154]).

The strength of alumina is largely dependent upon the purity, porosity, grain size and surface conditions[155]. In general, cracks originate from the inhomogeneous regions such as pores, grain boundaries, impurity inclusions and surface damaged layers caused by machining operations. For alumina with about 10% porosity, the possibility of flaw linking prior to catastrophic failure is small, while a sub-surface flaw for alumina with 50% porosity is found to link up with a surface-flaw at a stress approximately 75% of the stress to extend the isolated surface flaw[156].

3.2. Erodent preparation

The seven erodents chosen for this particle erosion study are steel shot, glass beads, silica, alumina, tungsten carbide, silicon carbide and diamond. Table 3.3 presents the measured hardness, particle size range, densities and the shapes of the erodents as seen in the scanning electron micrographs (SEM) of fig. 3.4. It shows the erodent particles in order of increasing hardness. However, the toughness data for the erodent particles are not available because the particles are too small to be measured quantitatively. The bulk material values are presented.

The steel shot erodents are spherical in shape. The glass beads were obtained from the *Jencons Ltd. England* and are spherical. Silica erodents were supplied by the *Consolidated Glassworks quarry, Phillipi, Cape Town.* It is noted that they have a large amount of porosity. The alumina erodent particles were obtained from the *Colbern Abrasive, Cape Town.* The particles exhibit angular and are elongated. The tungsten carbide erodent particles were supplied by *Boart Industrial Division, South Africa.* The particles show irregular shape. The silicon carbide particles were supplied by *Colbern Abrasive* and have irregular shape with surface asperities and exhibit fracture facets. The synthetic diamond erodent particles are manufactured by *De Beers Industrial Diamond Division (Pty) Ltd.* The particles are of blocky shape and have the inherent crystal growth planes. The synthetic diamond erodent particles exhibit the highest hardness, followed by silicon carbide, tungsten carbide, alumina, silica, glass beads. The steel shot has the lowest hardness. However, the steel shot exhibits the highest toughness, followed by diamond, tungsten carbide, silicon carbide, alumina, silica and the glass bead erodents. Particular attention should be drawn to tungsten carbide erodents which have the highest density among all the particles. The glass and silica erodents have low densities.

Table 3. 3. Summary of properties of the erodent particles based on bulk material values given in the literature[102, 157]

Erodent Particle	Hardness (HV_{500})	Toughness (MPa $m^{0.5}$)	Density ($g.cm^{-3}$)	Shape	Size(μm) Range
Steel shot	340	50	7.8	Spherical	400-500
Glass Beads	498	0.2-0.7	2.55	Spherical	63-106, 106-125 180-250, 400-500 600-700, 800-1000
Silica	1078	1.2	2.67	Irregular	63-106, 106-125 180-250, 400-500 600-700, 800-1000
Alumina	1612	3.0-3.5	3.99	Irregular	63-106, 106-125 180-250, 400-500 600-700, 800-1000
Tungsten Carbide	2169	4.0-5.0	15.9	Irregular	125-180, 212
Silicon Carbide	2580	3.4-4.5	3.2	Irregular	63-106, 106-125 180-250, 400-500 600-700, 800-1000
Diamond	8000	7.0-11	3.5	Blocky	126,151,181

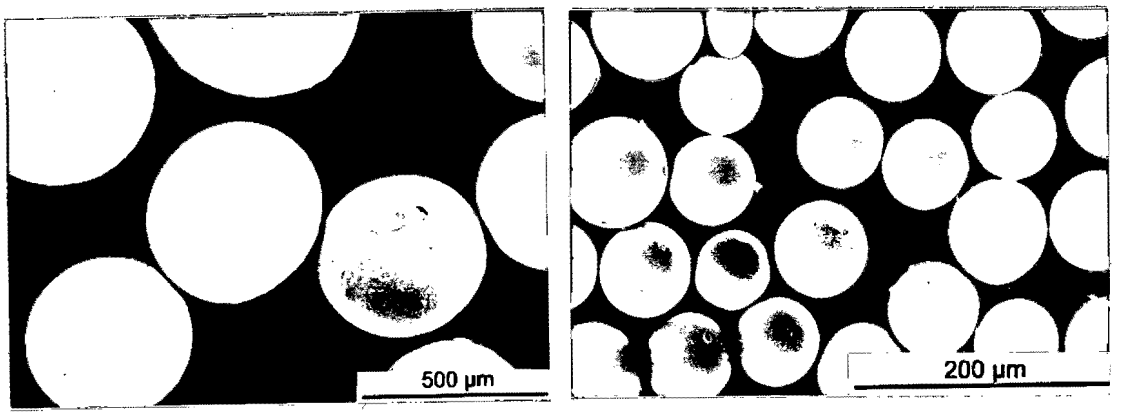

(a) (b)

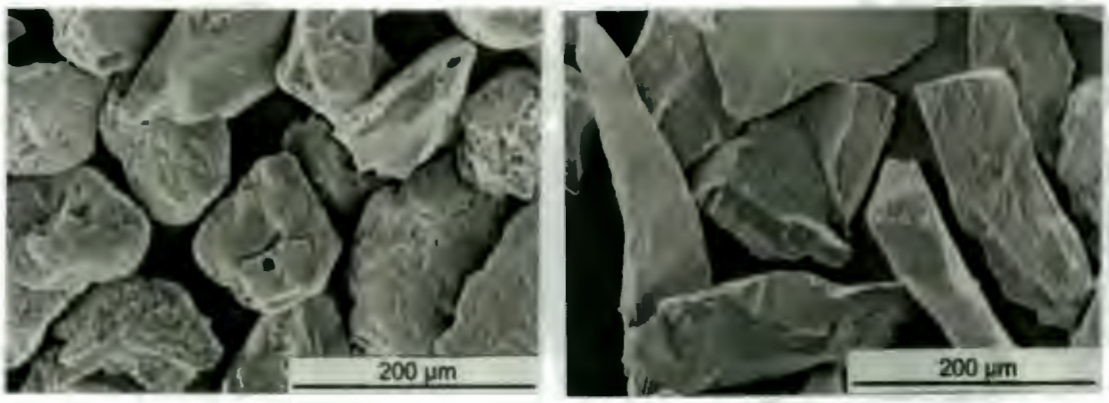

(c) (d)

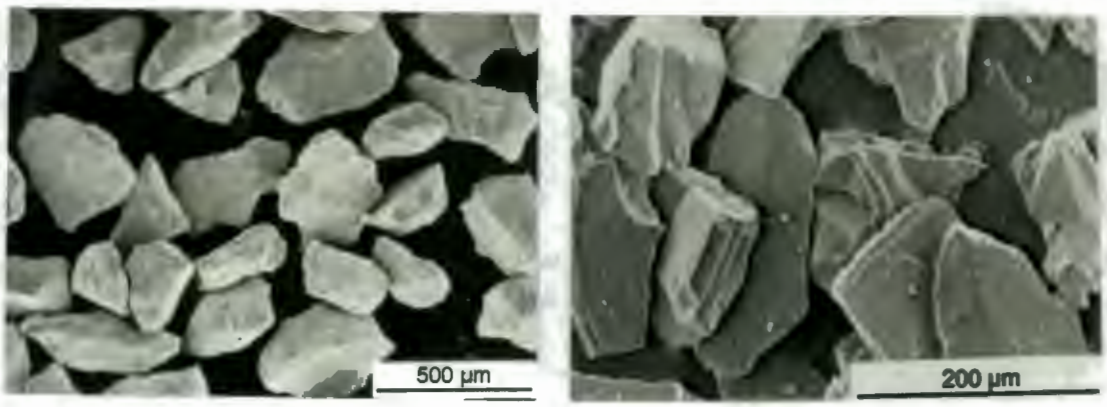

(e) (f)

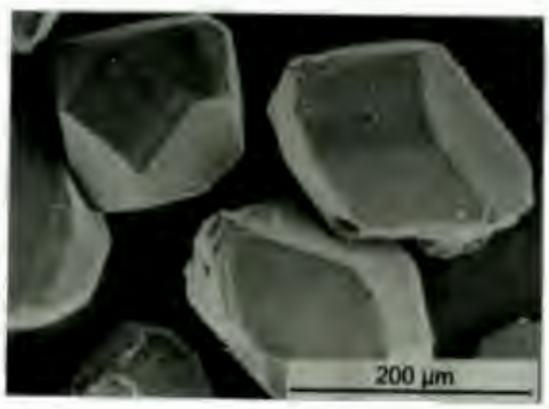

(g)

Figure 3. 4. SEM micrographs of erodents: (a) Steel shot (400-500 µm) (b) Glass beads (63-106 µm) (c) SiO_2 (106-125 µm) (d) Al_2O_3 (106-125 µm) (e) WC (212 µm) (f) SiC (106-125 µm) (g) Diamond (106-125 µm).

3.3. Solid particle erosion

Solid particle erosion tests were performed using a modified air blast similar to that described by Shipway and Hutchings[158]. A schematic diagram and photograph of the erosion testing rig are shown in figs. 3.5 and 3.6. The equipment is designed to feed abrasive particles into a high velocity air stream which propels the particles against the specimen surface. The particles are accelerated by passing them through a 304 stainless steel tube with a diameter of 16 mm.

The average velocity in the air stream at the specimen was measured by means of the rotating-disk method[159]. An opto-electronic flight timer[160] (fig. 3.7) was constructed to calibrate the velocity measured by the rotating-disk method. A stream of airborne particles pass through a glass-tube. Two optical transducers with a collimated 1 mm light beam are placed 13.3 mm apart. A particle has to pass through both beams to record a measurement. A computer program was written to calculate the probabilities of recording flight-times of particles since the particle that started the counter may not be the one that stopped it. The relationship between the velocities measured by the two different methods is shown in figs. 3.8 to 3.11. Compared to the values by the opto-electronic flight timer, the double rotating disk method indicates values that are lower at low velocity and higher at high velocity for most particles.

The test parameters for the erosion tests are summarised in Table 3.4. A list of parameters used for solid particle erosion is presented in Table 3.5. The erosion procedure is as follows. The specimens of 14 mm diameter were initially cleaned ultrasonically in alcohol, dried and then weighed using an electrical balance with a resolution of 0.01 mg. The particle velocity, particle size and angle of impingement were set. After erosion the specimens were again cleaned in alcohol and reweighed. A plot of weight loss versus gram of erodent is constructed and the steady state erosion rate is defined as the slope of the straight line and given as mass loss per gram of erodent in g/g. The mass loss per gram of erodent is then converted to volume loss per gram of erodent (Eg) in cm^3/g to facilitate comparison of target materials with different densities. If the interaction of particles during impact is assumed to be negligible, the volume loss per particle (Ep) in cm^3/particle at constant flux of particles is then calculated by dividing the volume loss per gram of erodent (Eg) by the number of

particle in a gram erodent that is assumed spherical in shape. This term is introduced in order to understand the effect of individual erodents on the erosion process. A specimen holder which exposed a circular area of 8 mm diameter was used. This necessitated the normalisation of the erosion rates since some of the erodent particles strike the holder rather than the specimen and the number of particles striking the surface decrease as the angle of erosion decreases. In order to calculate a true erosion rate as the ratio of volume of material loss to mass of erodent used, the amount of erodent striking the surface must be known for each erosion angle. The correction factor was determined from the ratio of erosion rate of the completely exposed specimen to the erosion rate of the partially covered specimen. Each measured erosion rate was multiplied by the correction factor to give a normalised erosion rate (NE). NEp is defined as normalised volume loss per particle (NE/particle).

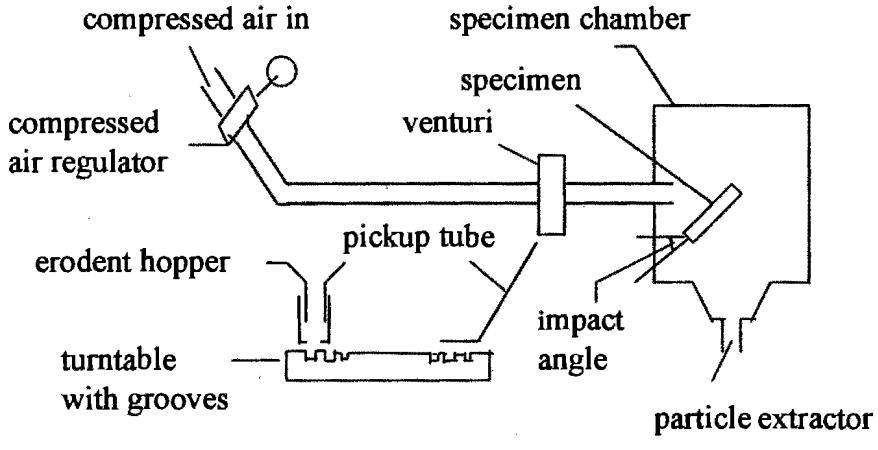

Figure 3. 5. Schematic diagram of the room temperature solid particle erosion apparatus.

Table 3.4. Summary of test parameters for room temperature particle erosion apparatus

Parameters	Values
Acceleration tube length	250 mm
Acceleration tube diameter	6 mm
Impact angles	30^0, 60^0, 90^0
Particle velocity range	33 $m.s^{-1}$-131 $m.s^{-1}$
Specimen stand-off distance	26 mm
Feed rate	0.17 $g.s^{-1}$
Exposed target area	50.3 mm^2

Figure 3. 6. Photograph of the room temperature solid particle erosion apparatus showing the particle extractor (a), the specimen chamber (b), the venturi (c), the pickup tube (d), the erodent hopper (e) and the turnable with grooves (f).

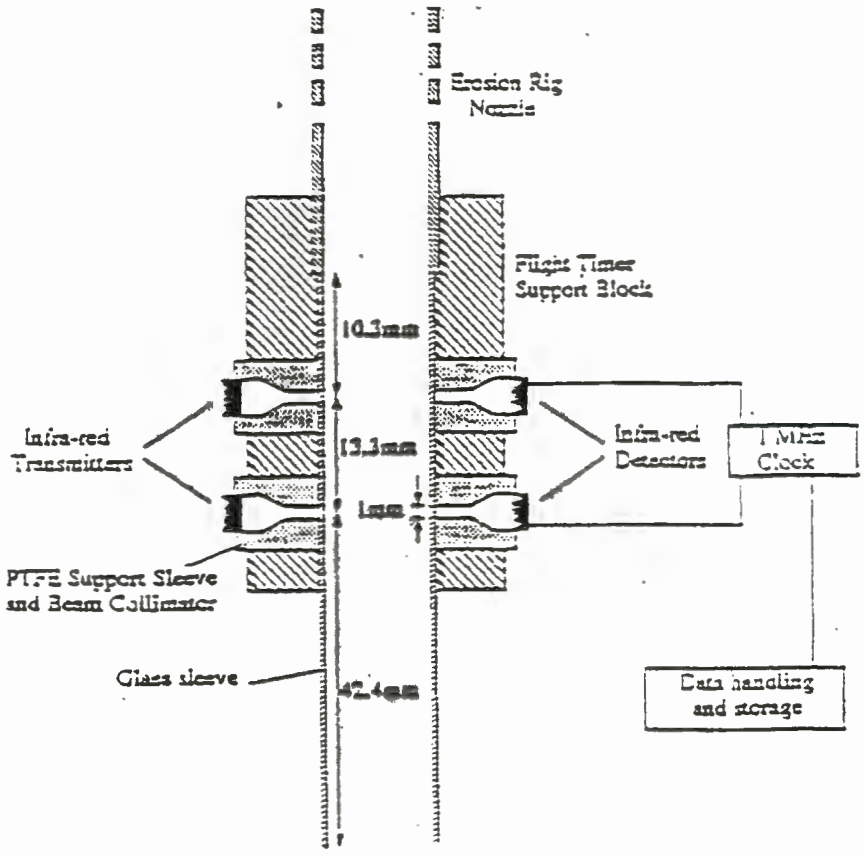

Figure 3. 7. Schematic diagram of the particle flight-timer (after Shipway and Hutchings [160]).

Table 3.5. Parameters below are used for solid particle erosion

Materials	Erodents	size(μm)	angle			V(m/s)											
			90°	60°	30°	25	30	33	39	45	51	57	65	71	99	119	131
as-rec.glass	steel shot	400-500	x			x	x	x	x	x							
	glass bead	63-106	x	x	x					x	x	x	x	x	x	x	x
		106-125	x	x	x					x	x	x	x	x	x	x	x
		180-250	x	x	x					x	x	x		x	x	x	x
		400-500	x	x	x			x	x	x	x	x					
		600-700	x	x	x			x	x	x	x	x					
		800-1000	x	x	x			x	x	x	x	x					
	silica	63-106	x	x	x					x	x	x		x	x		
		106-125	x	x	x					x	x	x		x	x		
		180-250	x	x	x					x	x	x		x	x		
		400-500	x	x	x			x	x	x	x	x					
		600-700	x	x	x			x	x	x	x	x					
		800-1000	x	x	x			x	x	x	x	x					
	alumina	63-106	x	x	x					x	x	x		x	x		
		106-125	x	x	x					x	x	x		x	x		
		180-250	x	x	x					x	x	x		x	x		
		400-500	x	x	x			x	x	x	x	x					
		600-700	x	x	x			x	x	x	x	x					
		800-1000	x	x	x			x	x	x	x	x					
	WC	181	x							x	x	x		x	x		
		215	x							x	x	x		x	x		
	SiC	63-106	x	x	x					x	x	x		x	x		
		106-125	x	x	x					x	x	x		x	x		
		180-250	x	x	x					x	x	x		x	x		
		400-500	x	x	x			x	x	x	x	x					
		600-700	x	x	x			x	x	x	x	x					
		800-1000	x	x	x			x	x	x	x	x					
	diamond	126	x	x	x					x	x	x		x	x		
		151	x	x	x					x	x	x		x	x		
		181	x	x	x					x	x	x		x	x		
tem.glass	glass bead	63-106	x									x		x	x	x	x
		106-125	x									x		x	x	x	x
		180-250	x								x	x		x	x	x	
		400-500	x					x	x	x	x	x					
		600-700	x					x	x	x	x	x					
		800-1000	x					x	x	x	x	x					
	SiC	63-106	x							x	x	x		x	x		
		106-125	x							x	x	x		x	x		
		180-250	x							x	x	x		x	x		
		400-500	x					x	x	x	x	x					
		600-700	x					x	x	x	x	x					
		800-1000	x					x	x	x	x	x					

Materials	Erodents	size(μm)		angles					velocit			
			90	60	30	33	39	45	51	57	71	99
304ss	silica	180-250	x		x			x	x	x	x	x
	alumina	180-250	x		x			x	x	x	x	x
	WC	181	x		x			x	x	x	x	x
	SiC	63-106	x		x			x	x	x	x	x
		106-125	x		x			x	x	x	x	x
		180-250	x	x	x			x	x	x	x	x
		400-500	x		x	x	x	x	x	x		
		600-700	x		x	x	x	x	x	x		
		800-1000	x		x	x	x	x	x	x		
	diamond	181	x		x			x	x	x	x	x
WC-Co	silica	180-250	x		x			x	x	x	x	x
	alumina	180-250	x					x	x	x	x	x
	WC	181	x					x	x	x	x	x
	SiC	63-106	x					x	x	x	x	x
		106-125	x					x	x	x	x	x
		180-250	x	x	x			x	x	x	x	x
		400-500	x			x	x	x	x	x		
		600-700	x			x	x	x	x	x		
		800-1000	x			x	x	x	x	x		
	diamond	181	x					x	x	x	x	x
alumina	silica	180-250	x		x			x	x	x	x	x
	alumina	180-250	x					x	x	x	x	x
	WC	181	x					x	x	x	x	x
	SiC	106-125	x					x	x	x	x	x
		180-250	x	x	x			x	x	x	x	x
		400-500	x			x	x	x	x	x		
		600-700	x			x	x	x	x	x		
		800-1000	x			x	x	x	x	x		
	diamond	181	x					x	x	x	x	x

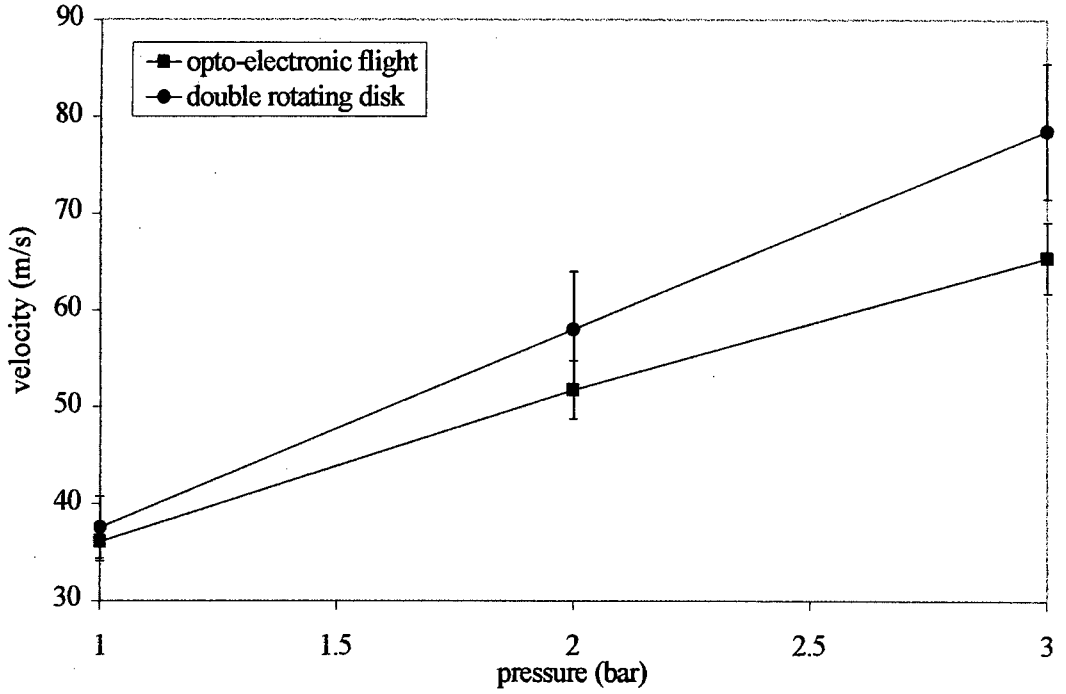

Figure 3. 8. Comparison of velocities measured with an opto-electronic flight-timer and a double rotating disk for glass beads (180-250μm).

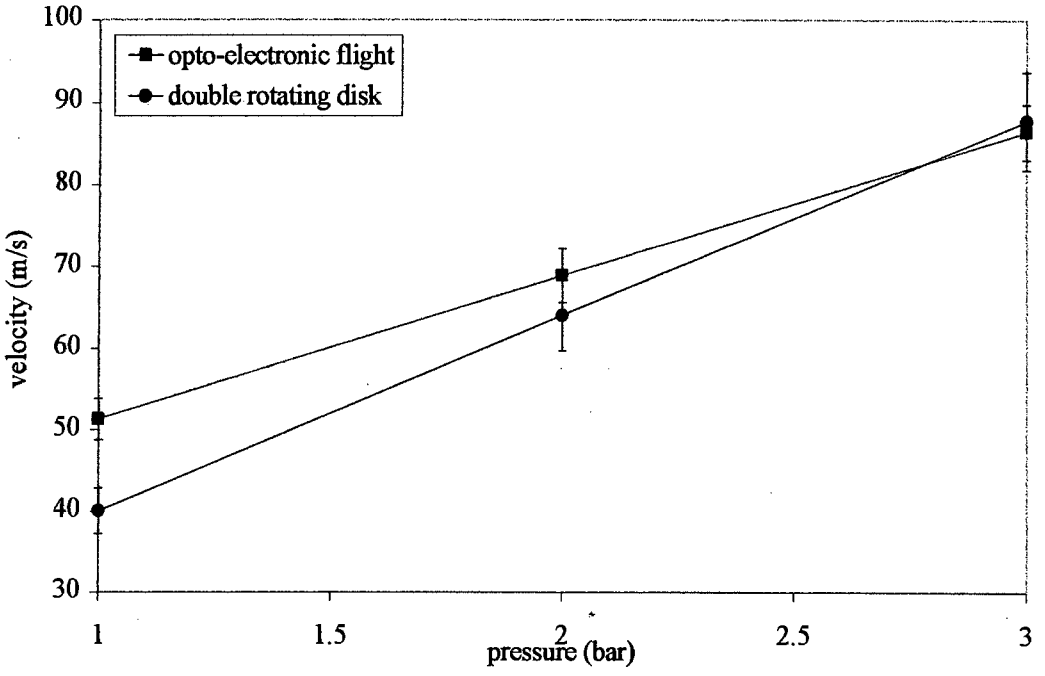

Figure 3. 9. Comparison of velocities measured with an opto-electronic flight-timer and a double rotating disk for silica particles (180-250 μm).

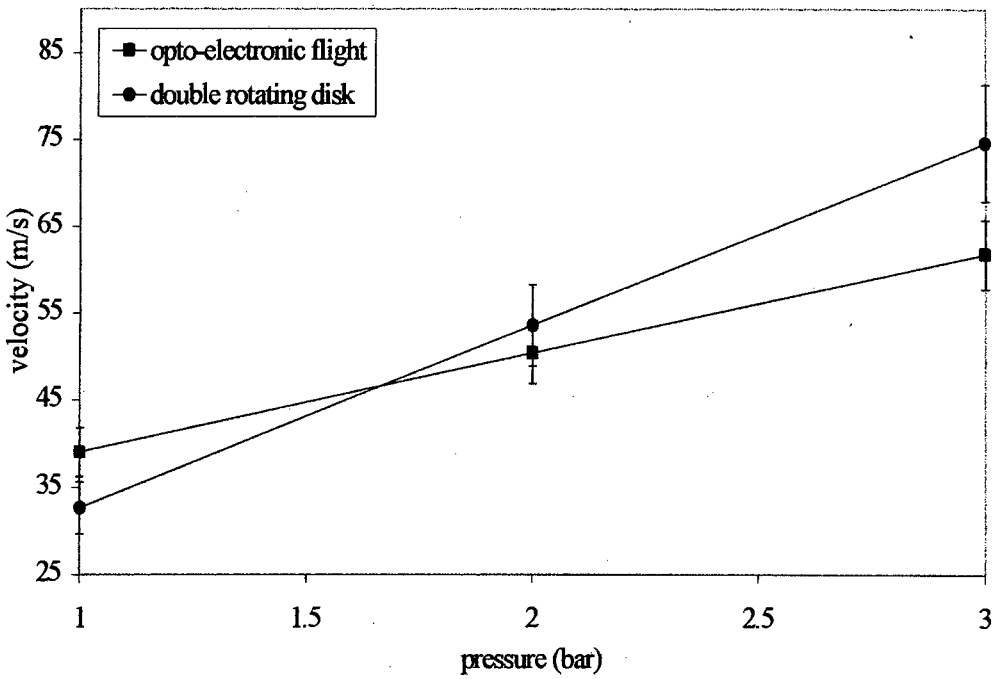

Figure 3. 10. Comparison of velocities measured with an opto-electronic flight-timer and a double rotating disk for alumina particles (180-250μm).

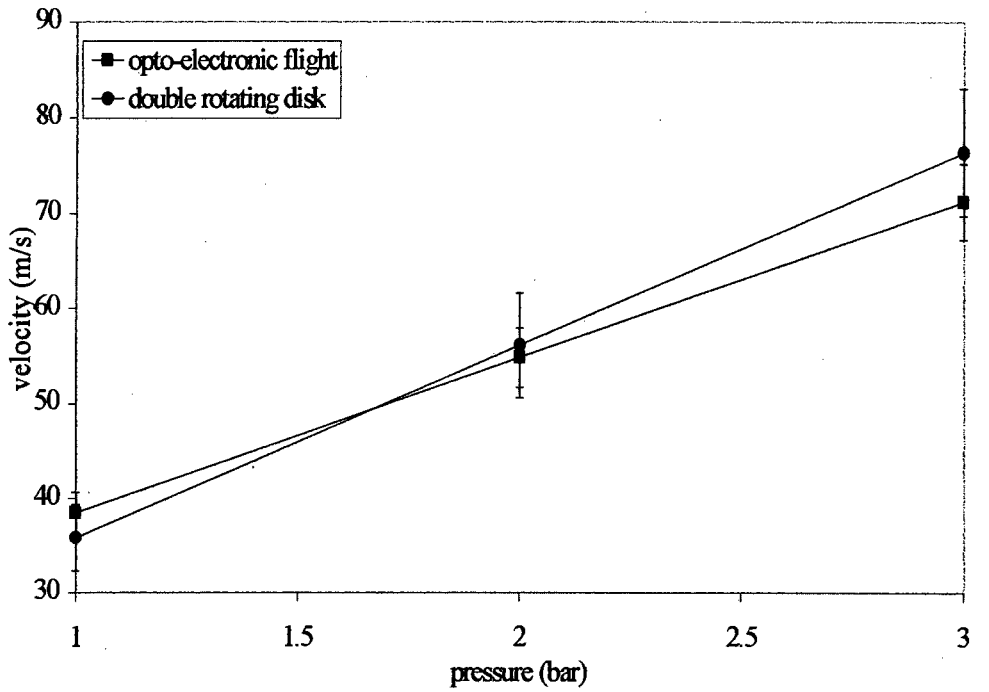

Figure 3. 11. Comparison of velocities measured with an opto-electronic flight-timer and a double rotating disk for SiC particles (180-250 μm).

3.4. Source of experimental error

Many factors contribute to the sources of errors in measurements. The particle velocity is probably the most important single variable introducing errors in the measurements of erosion rates. The velocities in this study were measured using two different apparatus described in section 3.3. The main error in the method of double rotating disk is in the measurement of the angular separation of the wear scars. It can be measured to at a level of precision of about 10% [159]. Particularly, the wear scar caused by bigger particle impact is too broad to measure accurately. An infrared detector was therefore employed to measure the velocity of bigger particles.

The velocity for small particles is still measured by double rotating disk because of the limitation of infrared detector that can only detect particle size bigger than 100μm. It is noted that there was up to 10-15% difference between the velocities of erodents (180-250μm) measured with double rotating disk and infrared detector as shown in figs. 3.8-3.11. In order to obtain more accurate results, a reliable apparatus for velocity measurement needs to be developed. The other factors which decrease the test accuracy are error in feed rate control, specimen mass loss weighting and particle size distribution. Although the particle size ranges for different erodents are well controlled, the size distribution in this range is very different and broad for different erodents.

3.5. Cavitation erosion

A cavitation environment was created by using an ultrasonic drill. The drill was originally supplied by KLN Ultraschall Gesellschaft of Germany and then assembled by Heathcock, Protheroe and Ball[142]. A schematic diagram and photograph of the cavitation testing rig are shown in figs. 3.12 and 3.13. The specimen and drill tip are contained in a test bath filled with distilled water. The temperature of the water in the test bath is controlled by a heat exchanger coil through which water from a temperature regulated reservoir is pumped. To ensure that there is no localised heating of the distilled water in the test bath during cavitation testing; the water is continually stirred by a magnetic stirrer. The test conditions employed are given in Table 3.6. The distance between drill tip and specimen of 0.35 mm is

selected as the maximum erosion loss occurs at this distance[142]. Erosion was monitored by cleaning, drying and weighing the specimen at regular intervals during each test. The steady state cavitation erosion rate was measured as the volume of material loss per hour of erosion. The incubation period (the period before the onset of steady state erosion) was defined as the intercept on the time axis of a straight line extension of the steady state line[161]. The definition of the steady state erosion rate and the incubation period used in the present study are shown in fig. 3.14.

Table 3.6 The test condition used for the cavitation test

Drill tip frequency	20kHz
Distance between drill tip and specimen	0.35 mm
Drill tip diameter	10 mm
Temperature	25^0
Specimen geometry	13 mm x 13 mm blocks

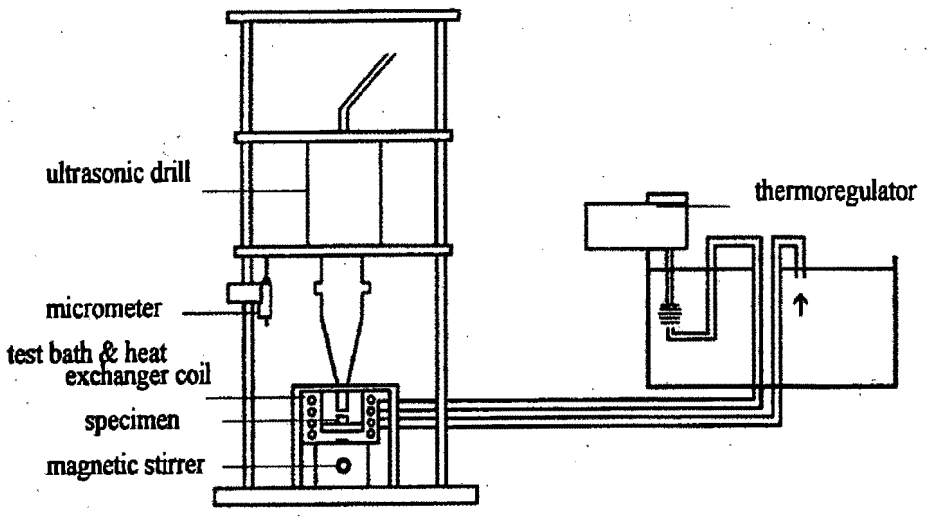

Figure 3. 12. Drawing of the vibratory cavitation erosion test apparatus (after Heathcock et al.[142]).

Figure 3. 13. Photograph of the vibratory cavitation erosion test apparatus.

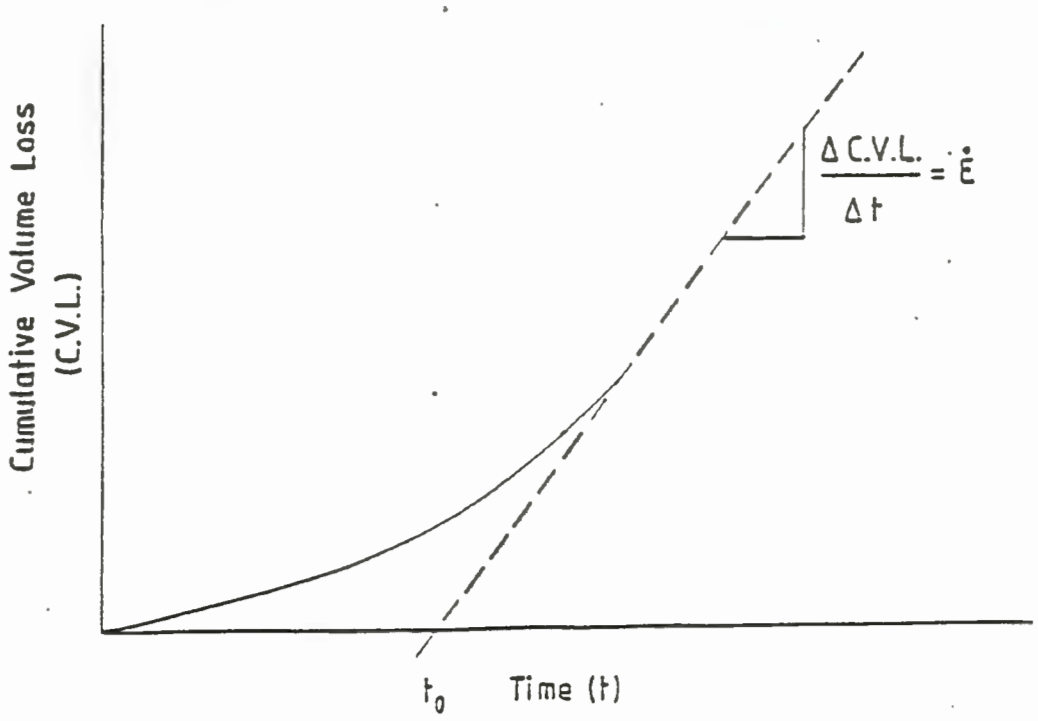

Figure 3. 14 A plot of the cumulative volume loss against cavitation erosion time. The incubation volume (t_0) and the steady state erosion rate E are indicated on the graph.

3.6. *Microscopy*

Optical microscopy was performed using a *Reichert MeFsA* metallurgical microscope to characterise the initial microstructures of all the targets and the eroded surfaces of the glass target after single particle impact.

A *Cambridge Stereoscan 200* scanning electron microscope (SEM) equipped with a *Tracor Northern Tn5400* energy dispersive x-ray microanalysis system and a back scattered electron detector was used for microstructure examination and semi-quantitative element analysis of both targets and erodents. Operating conditions were set at an accelerating voltage of 20 kV.

3.7. *Tensile testing*

The tensile tests were performed on the AISI 304 stainless steel and Cromanite™ at room temperature. A computer interfaced Zwick 1484 Universal Testing Machine with an extensometer arm extension was used for all the tests. The tests were performed at an initial strain rate of 1×10^{-3} s^{-1}. The resulting load versus extension data obtained from the tensile testing machine was converted to true stress (σ_t) versus true strain (ε_t) data using Quatro Pro spreadsheet facilities. The work hardening rate at a given strain was obtained by plotting the slope of the true stress versus true strain curve against strain. The following equation was used to calculate the work hardening rate[8]:

$$d\sigma_t / d\varepsilon_t = \sum \varepsilon_t \sigma_t - n\varepsilon_t^* \sigma_t^* / \sum \varepsilon_t^2 - n\varepsilon_t^{*2}$$

where ε_t^* and σ_t^* are average values for ε_t and σ_t respectively and n is the number of data points (ε_t, σ_t) over which the averages are taken. Typical tensile stress/strain curves for 304 stainless steel and Cromanite™ are shown in figs. 3.15 and 3.16. Test results are summarised in Table 3.7. Graphs of work hardening rate versus true strain are shown in figs. 3.17-3.18. The work hardening rate of Cromanite™ is considerably higher than that of 304 stainless steel. Recent developments[162] indicated that austenitic high-nitrogen Cr-Mn

stainless steels (Cromanite™) exhibit high strength without significant reduction in fracture toughness due to the effect of high nitrogen contents in solid solution.

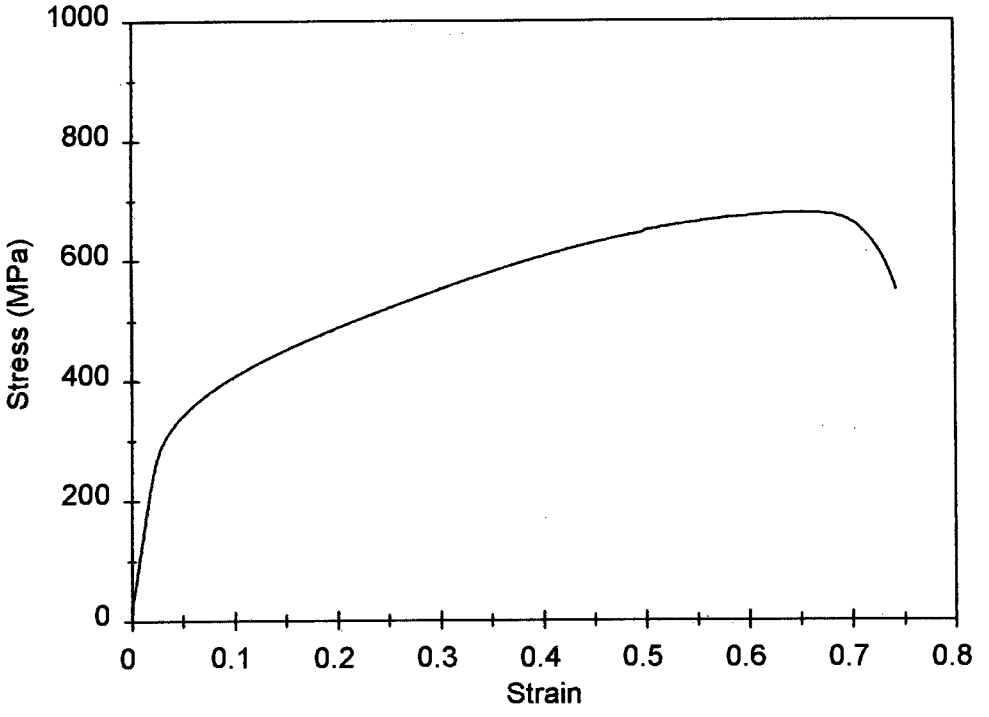

Figure 3. 15. Tensile stress versus strain curve for 304 stainless steel.

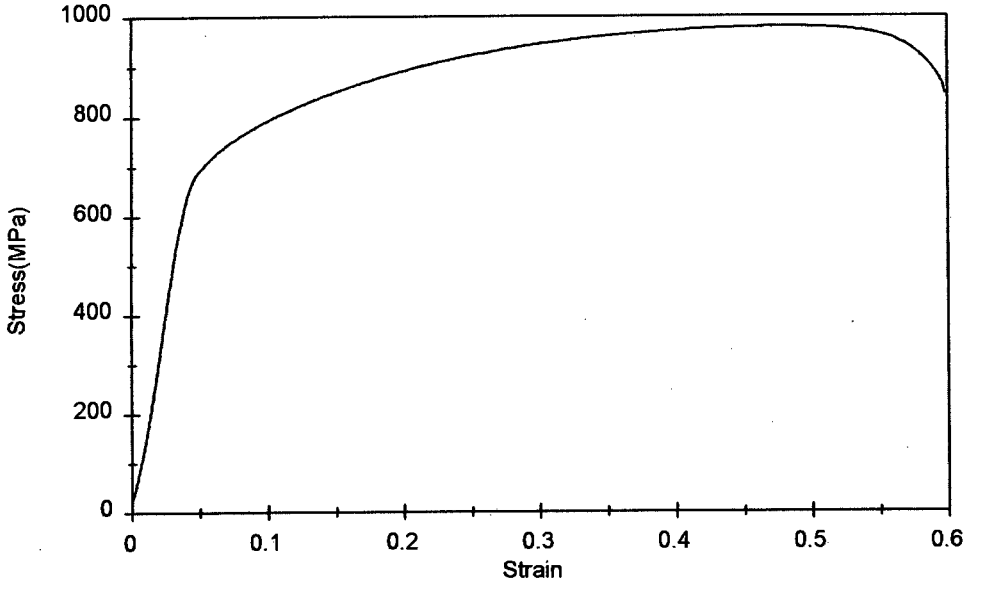

Figure 3. 16. Tensile stress versus curve for Cromanite™.

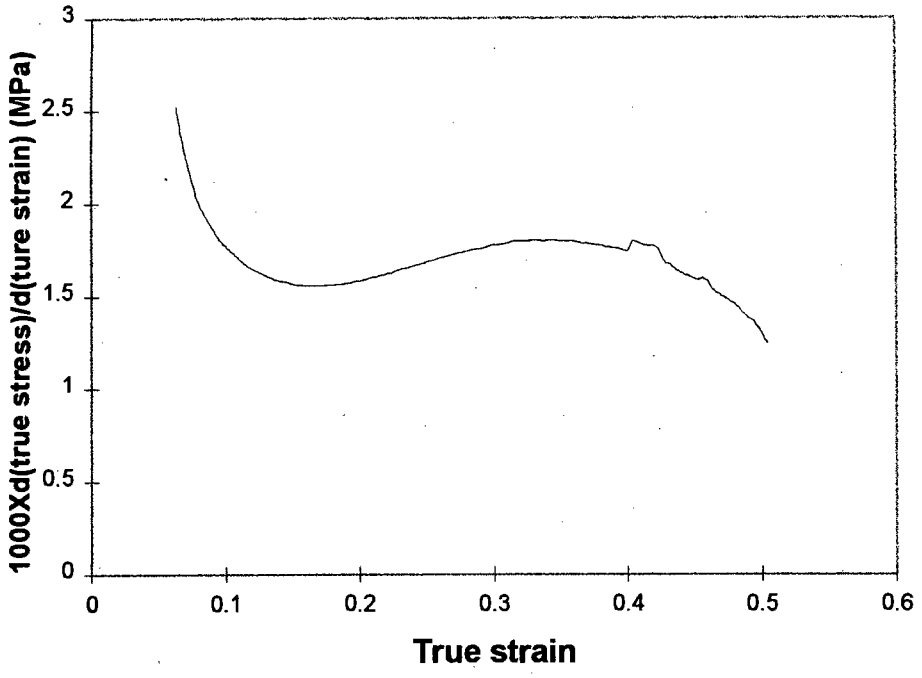

Figure 3. 17. Graph of work hardening rate, dσ/dε, versus true strain for 304 stainless steel.

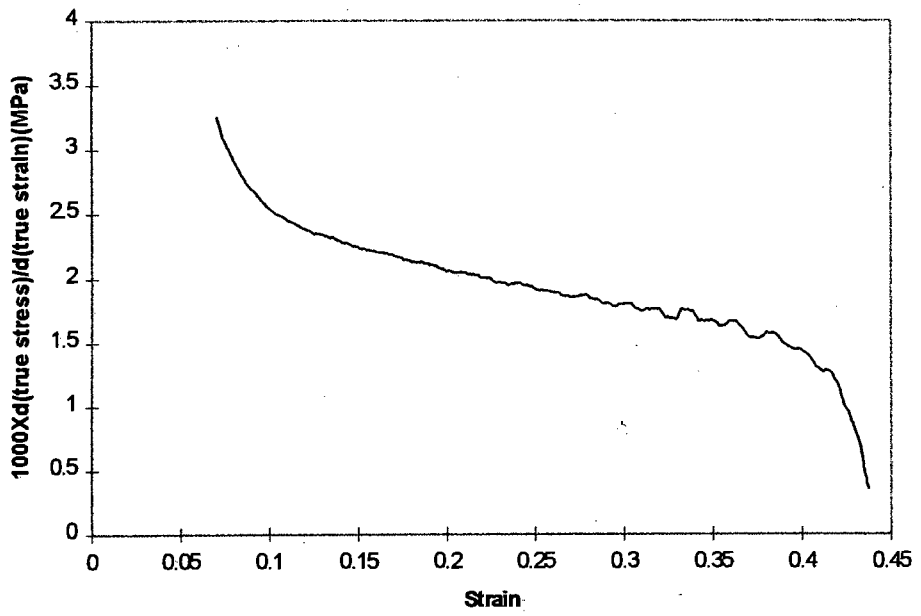

Figure 3. 18. Graph of work hardening rate, dσ/dε, versus true strain for Cromanite.

Table 3.7. Tensile test results for stainless steel and Cromanite™

Material	σ uts (MPa)	ε (%)	Yield strength (MPa)
304 stainless steel	660	63	265
Cromanite™	980	44	580

3.8. Microhardness tests

The subsurface work hardening produced by erosion was evaluated from the microhardness reading taken on the cross sections of the eroded specimens using a Matsuzawa tester. A Vickers diamond pyramid indenter with a load of 25gf, applied for 10 seconds, was used to produce indents on a polished cross sectioned surface of 304 stainless steel. The hardness of target materials are measured with a load of 500gf. At least five hardness indentations were made and from this an average of the microhardness was calculated.

3.9. Analysis of erodent fragmentation

To quantify the amount of fragmented erodent after impact, a Malvern Mastersizer apparatus was employed to determine the size distribution of the erodents before and after impact. The principle[163] used is based on the diffraction of a coherent light beam by the grains of the erodent. The erodent to be examined is dispersed in a liquid which is then circulated through a glass cell by means of a mechanical stirrer. An ultrasonic generator deflocculates the powder. A parallel beam from a low-power helium-neon laser lights up the cell, and the beam which leaves is focused by means of a convergent optical system. The values of illumination with and without sample are read by an electronic detector and fed into a programmed processor, which then displays the results as cumulative percentage undersize compared to before testing.

4. RESULTS

4.1. Solid particle erosion

4.1.1. As received glass

4.1.1.1. As received glass impacted by steel shot

The particle impingement erosion was measured at five velocities for steel shot (400-500 μm) with an impingement angle of 90^0. Fig. 4.1 shows a plot of the logarithm of the erosion rate versus the logarithm of impingement velocity. It is noted that the erosion rate increases with increasing impingement velocity.

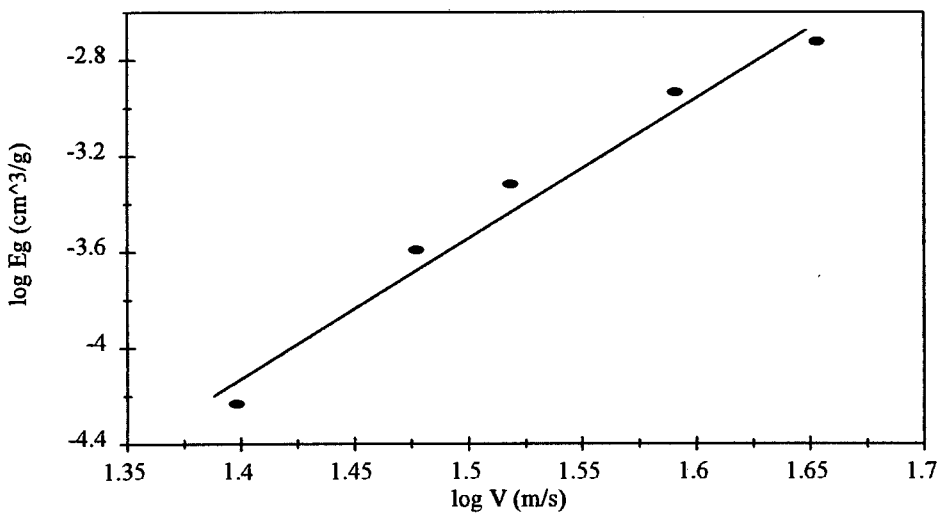

Figure 4. 1 Graph of the erosion rate (Eg) of as received glass versus velocity of steel shot erodents using 400-500 μm size ranges at an impingement angle of 90^0 incidence.

4.1.1.2. As received glass impacted by glass beads

The variation of the erosion rates as a function of the impingement velocity of glass beads is plotted on a log-log scale in figs. 4.2 to 4.4 for the impingement angles of 90^0, 60^0 and 30^0 respectively. It is seen that the erosion rate increases with increasing impingement velocity and particle size. There is a sharp increase in erosion rate at a critical threshold velocity. The threshold velocity increases with decreasing impingement angle and increasing particle size.

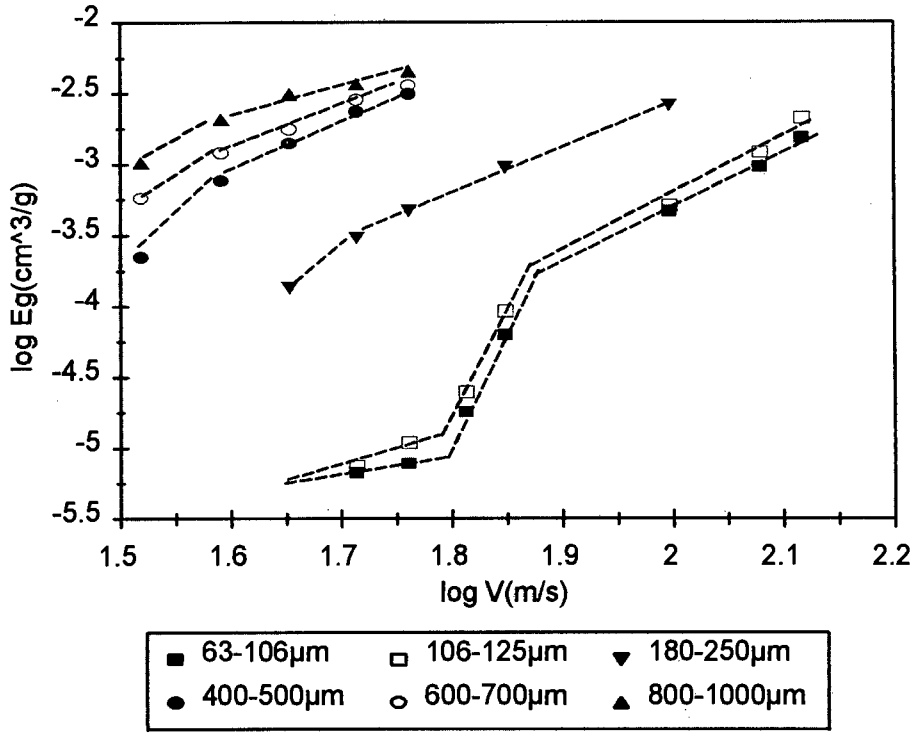

Figure 4. 2 Graph of the erosion rate (Eg) of as received glass versus velocity of glass beads using different sizes at an impingement angle of 90^0 incidence.

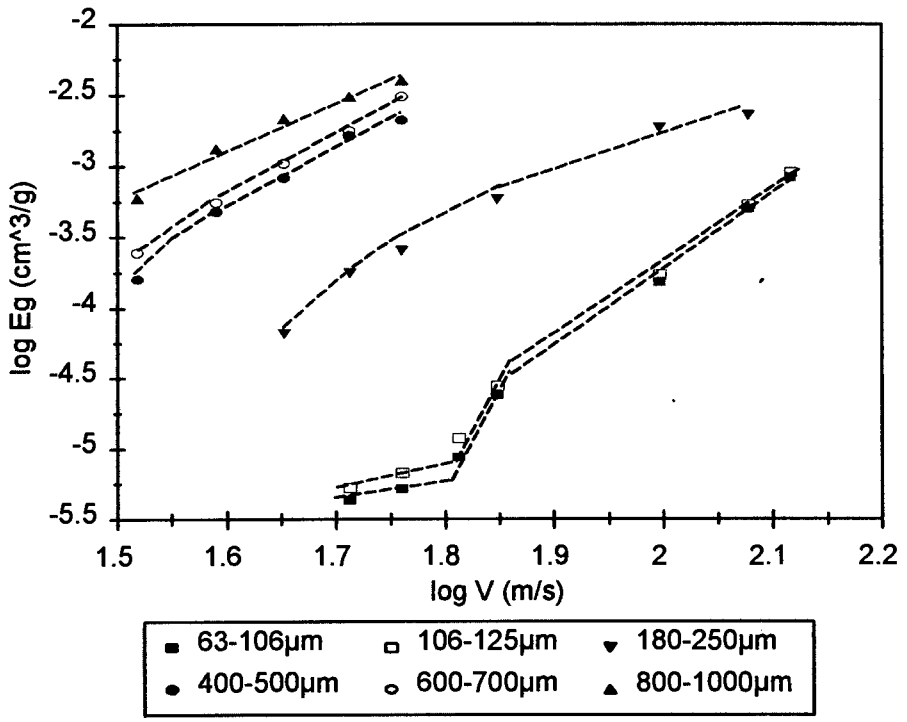

Figure 4. 3. Graph of the erosion rate (Eg) of as received glass versus velocity of glass beads using different sizes at an impingement angle of 60^0 incidence.

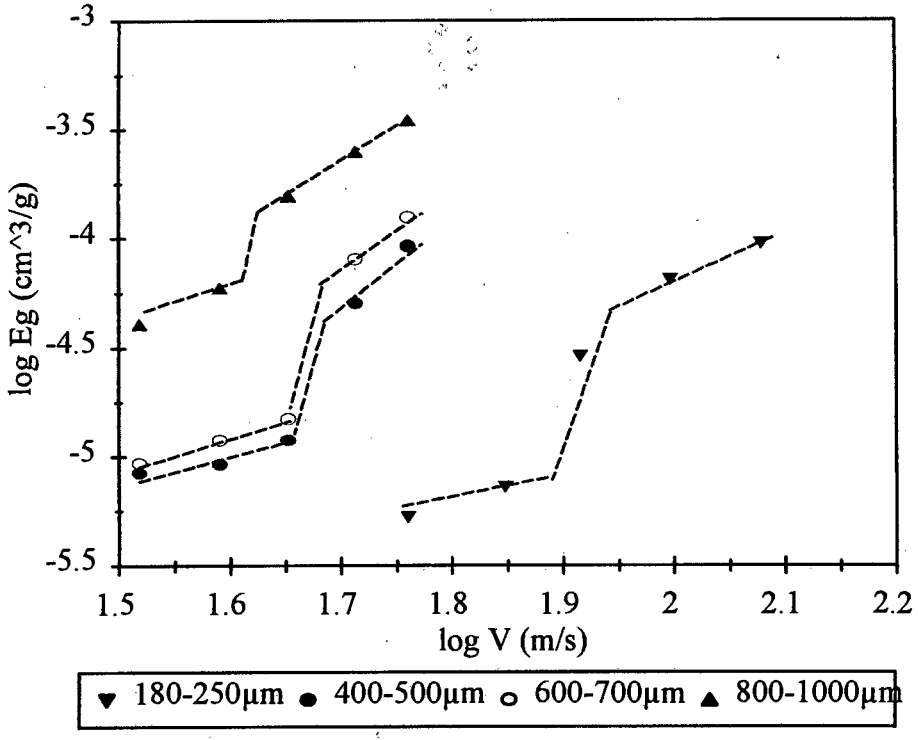

Figure 4. 4. Graph of the erosion rate (Eg) of as received glass versus velocity of glass beads using different sizes at an impingement angle of 30^0 incidence.

4.1.1.3. As received glass impacted by silica erodent particles

The variation of the erosion rates as a function of the impingement velocity of silica erodents is plotted on a log-log scale in figs. 4.5, 4.6 and 4.7 for the impingement angles of 90^0, 60^0 and 30^0 respectively. It is noted that the erosion rate increases with increasing impingement velocity and particle size. Unlike the case of glass beads, there is no observed threshold velocity with the silica erodent.

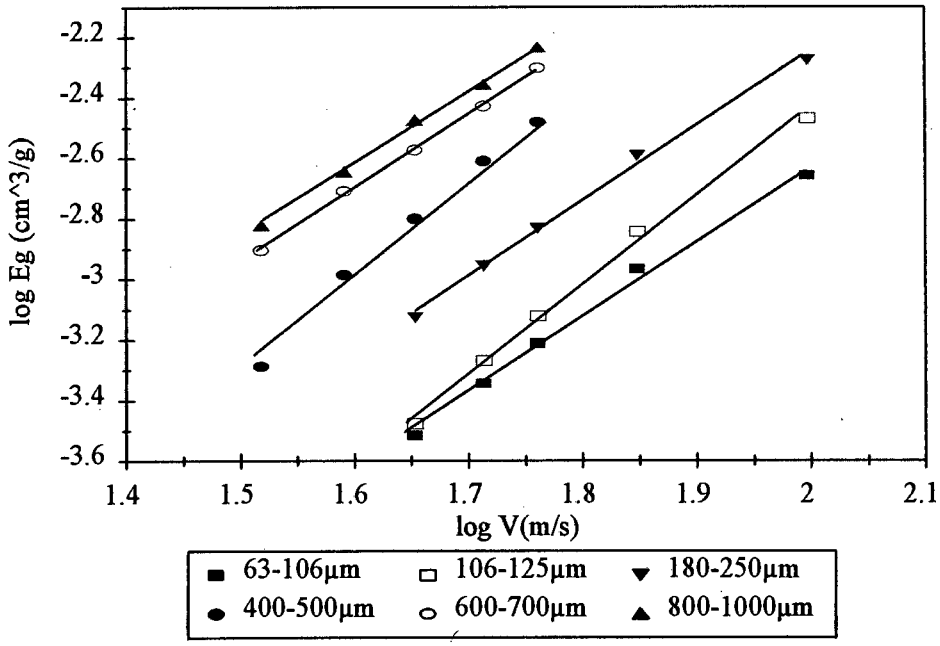

Figure 4. 5 Graph of the erosion rate (Eg) of as received glass versus velocity of silica erodents using different sizes at an impingement angle of 90° incidence.

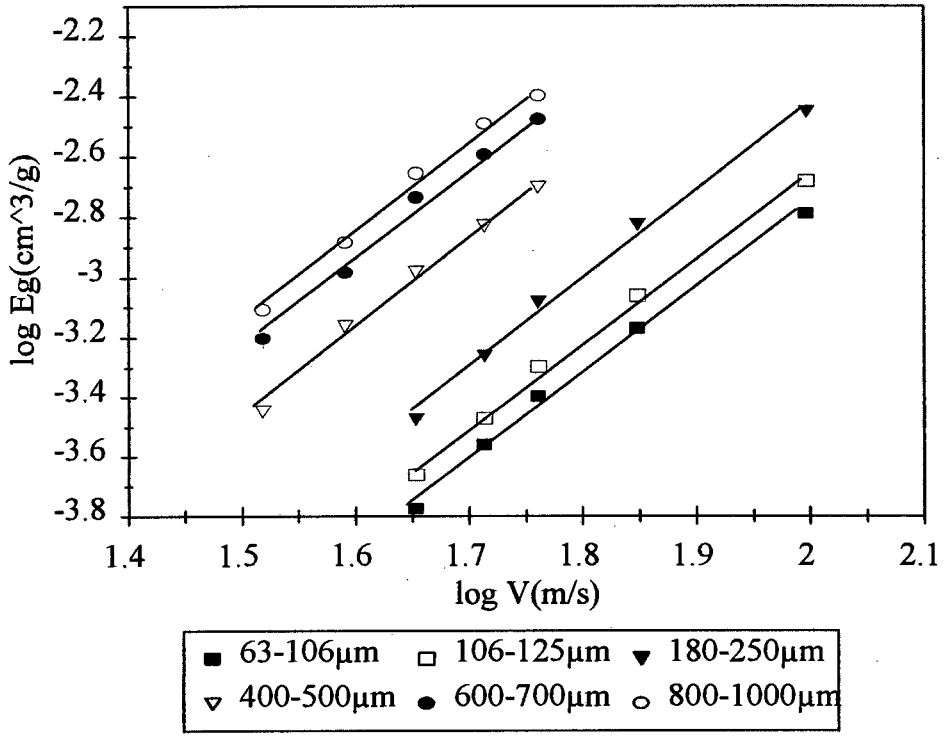

Figure 4. 6 Graph of the erosion rate (Eg) of as received glass versus velocity of silica erodents using different sizes at an impingement angle of 60° incidence.

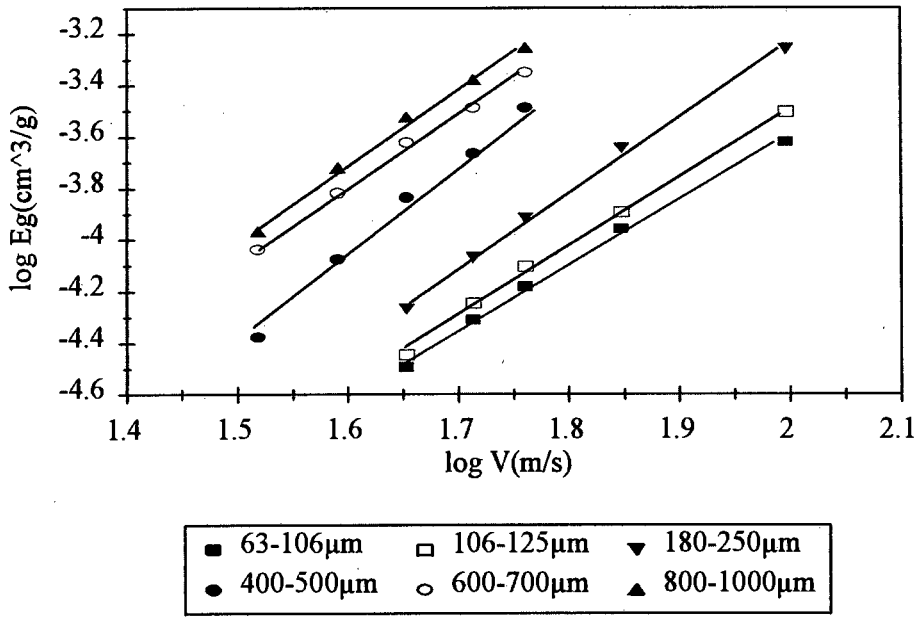

Figure 4. 7 Graph of the erosion rate (Eg) of as received glass versus velocity of silica erodents using different sizes at an impingement angle of 30° incidence.

4.1.1.4. As received glass impacted by alumina erodent particles

The variation of the erosion rates as a function of the impingement velocity of alumina erodents is plotted on a log-log scale in figs. 4.8 to 4.10 for the impingement angles of 90^0, 60^0 and 30^0 respectively. It is noted that the erosion rate increases with increasing impingement velocity and particle size.

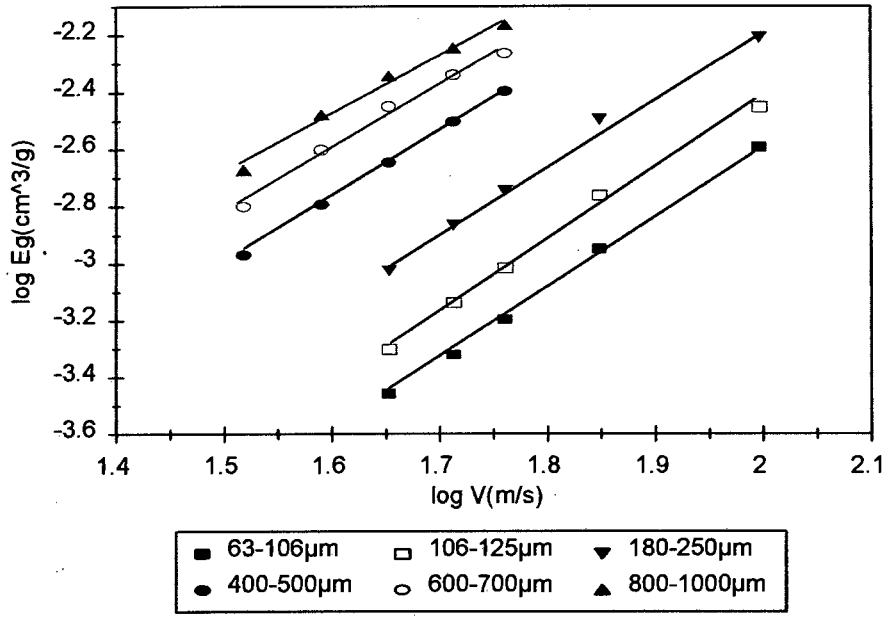

Figure 4. 8 Graph of the erosion rate (Eg) of as received glass versus velocity of alumina erodents using different sizes at an impingement angle of 90^0 incidence.

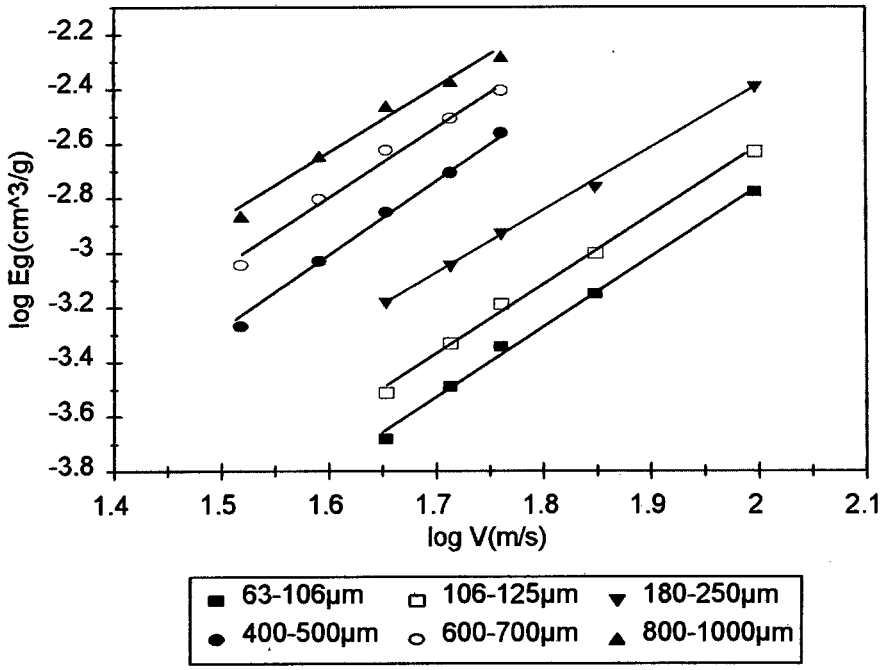

Figure 4. 9 Graph of the erosion rate (Eg) of as received glass versus velocity of alumina erodents using different sizes at an impingement angle of 60^0 incidence.

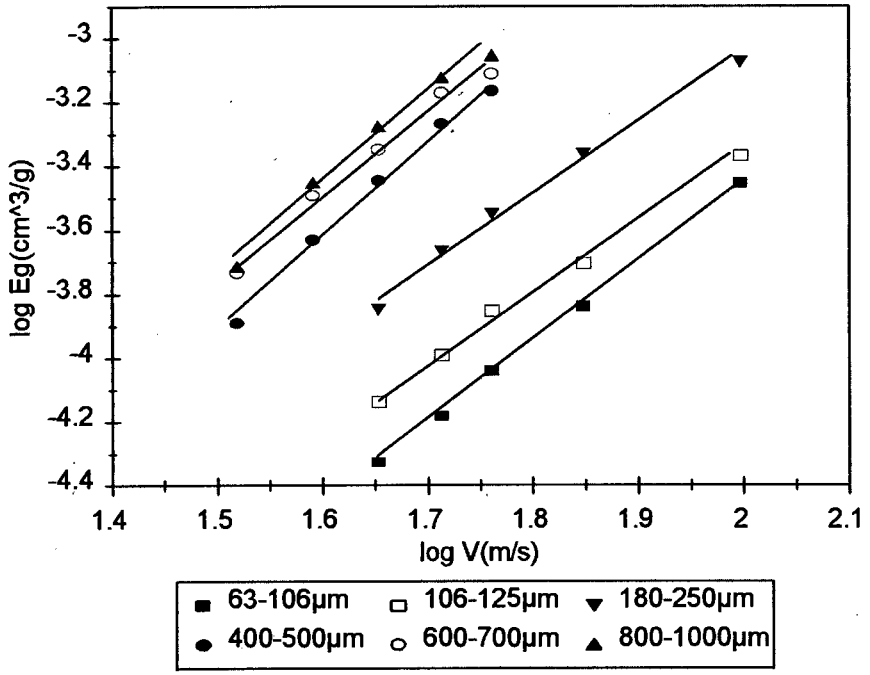

Figure 4. 10 Graph of the erosion rate (Eg) of as received glass versus velocity of alumina erodents using different sizes at an impingement angle of 30° incidence.

4.1.1.5. As received glass impacted by tungsten carbide erodent particles

The variation of the erosion rates as a function of the impingement velocity of tungsten carbide erodents is plotted on a log-log scale in fig. 4.11 for an impingement angle of 90^0. It is noted that the erosion rate increases with increasing impingement velocity and particle size.

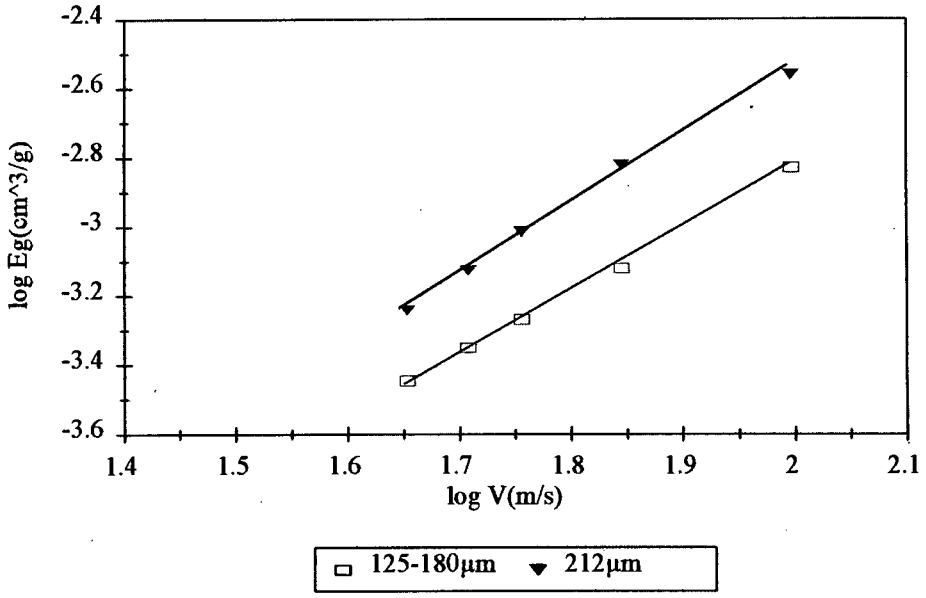

Figure 4. 11 Graph of the erosion rate (Eg) of as received glass versus velocity of tungsten carbide erodents using different sizes at an impingement angle of 90^0 incidence.

4.1.1.6. As received glass impacted by silicon carbide erodent particles

The variation of the erosion rates as a function of the impingement velocity of silicon carbide erodents is plotted on a log-log scale in figs. 4.12 to 4.14 for the impingement angles of 90^0, 60^0 and 30^0 respectively. It is noted that the erosion rate increases with increasing impingement velocity and particle size.

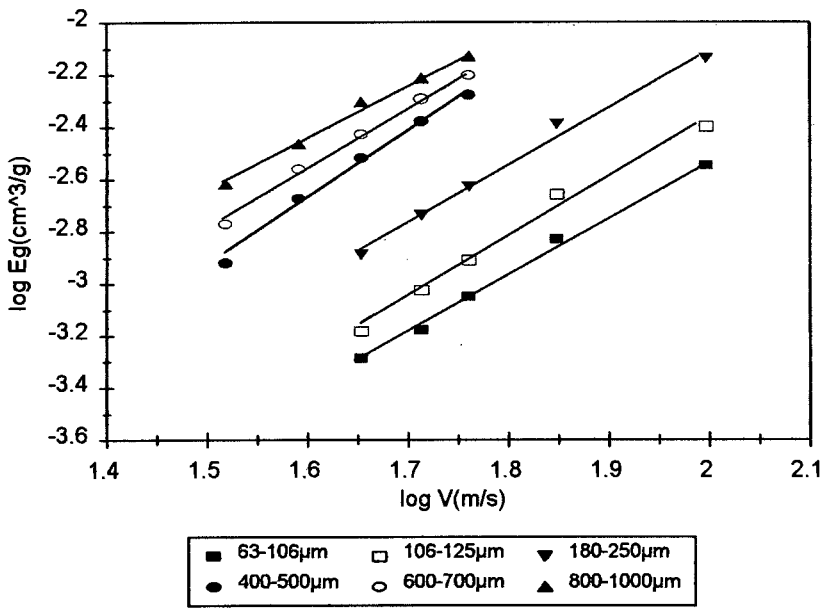

Figure 4. 12 Graph of the erosion rate (Eg) of as received glass versus velocity of silicon carbide erodents using different sizes at an impingement angle of 90° incidence.

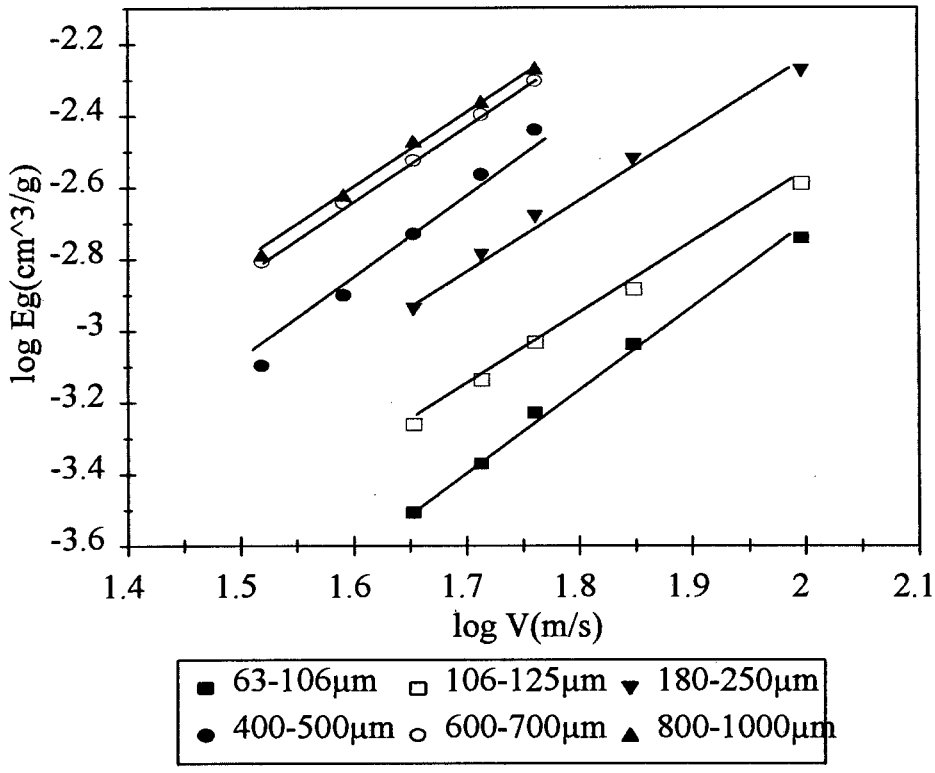

Figure 4. 13 Graph of the erosion rate (Eg) of as received glass versus velocity of silicon carbide erodents using different sizes at an impingement angle of 60^0 incidence.

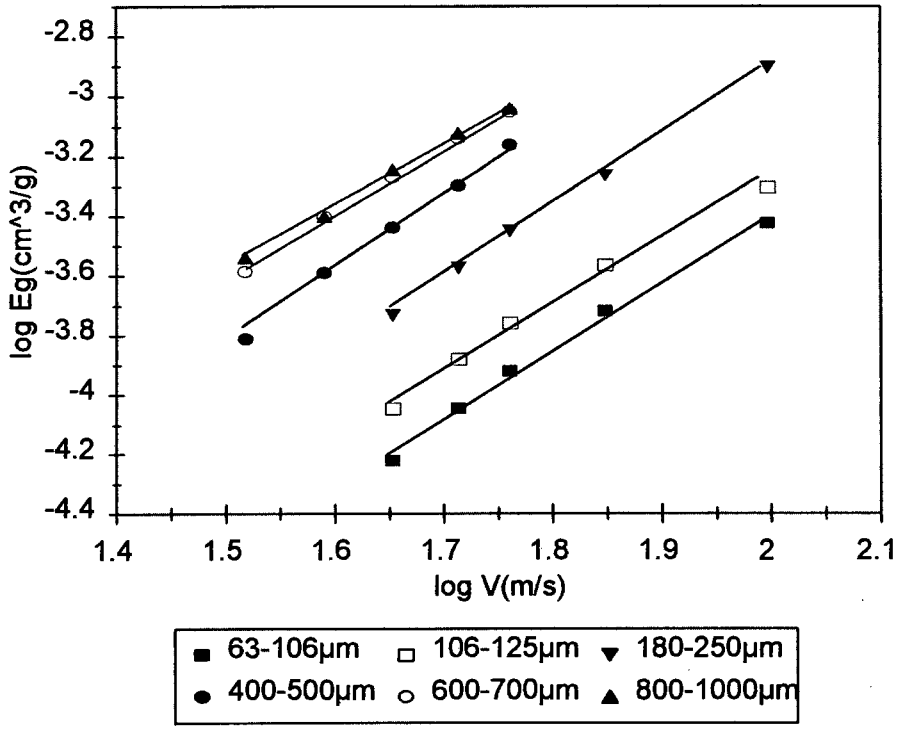

Figure 4. 14 Graph of the erosion rate (Eg) of as received glass versus velocity of silicon carbide erodents using different sizes at an impingement angle of 30^0 incidence.

4.1.1.7. As received glass impacted by diamond erodent particles

The variation of the erosion rates as a function of the impingement velocity of diamond erodents is plotted on a log-log scale in figs.4.15 to 4.17 for the impingement angles of 90^0, 60^0 and 30^0 respectively. It is noted that the erosion rate increases with increasing impingement velocity and particle size.

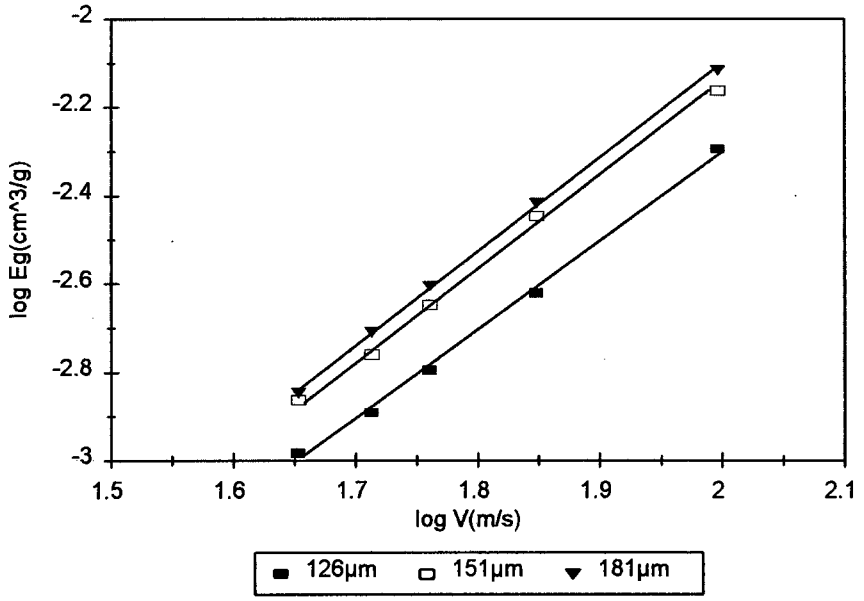

Figure 4. 15 Graph of the erosion rate (Eg) of as received glass versus velocity of diamond erodents using different sizes at an impingement angle of 90^0 incidence.

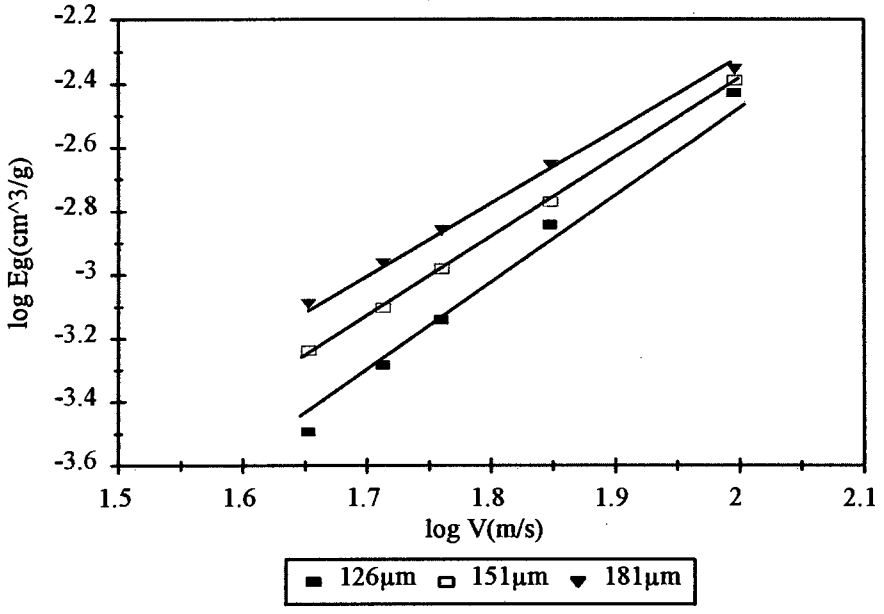

Figure 4. 16 Graph of the erosion rate (Eg) of as received glass versus velocity of diamond erodents using different sizes at an impingement angle of 60° incidence.

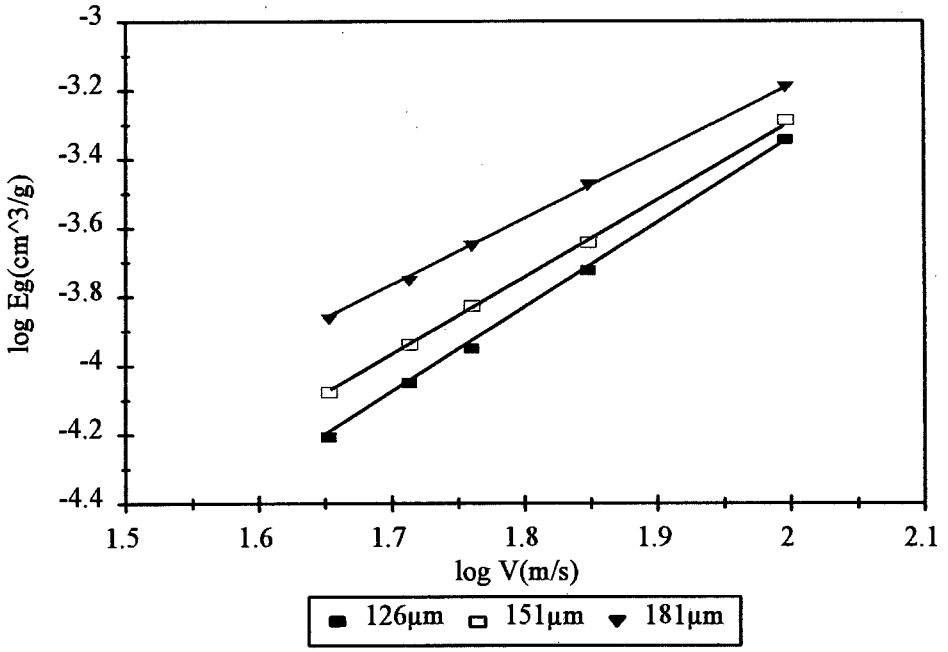

Figure 4. 17 Graph of the erosion rate (Eg) of as received glass versus velocity of diamond erodents using different sizes at an impingement angle of 30° incidence.

4.1.2. Tempered glass

4.1.2.1. Tempered glass impacted by glass beads

The variation of erosion rate of the tempered glass and as received glass with velocity at 90^0 incidence for different sizes of glass beads is presented in Table 4. 1. The erosion rate for as received glass is greater than that for the tempered glass eroded by glass beads over all the velocities and particle sizes used.

Table 4. 1 Variation of erosion rate of as received glass and tempered glass with velocity for different sizes of glass bead erodent impact at 90^0 incidence.

Glass bead size(μm)	Velocity($m.s^{-1}$)	As-rec.-glass Erosion rate (cm^3 x 10e-4/g)	Tem.-glass Erosion rate (cm^3 x 10e-4/g)
63-106	57	0.09	0.03
	71	0.69	0.35
	99	5.60	4.58
	119	10.38	9.89
	131	13.16	11.49
106-125	57	0.12	0.04
	71	0.73	0.43
	99	5.93	4.62
	119	12.09	11.02
	131	22.01	21.71
180-250	45	1.65	1.29
	51	2.91	2.45
	57	4.15	3.64
	71	9.41	8.81
	99	23.07	21.62
	119	31.08	30.19
400-500	33	3.99	3.63
	39	9.20	7.80
	45	17.72	16.12
	51	21.33	20.01
	57	26.86	26.62
600-700	33	5.84	5.05
	39	11.13	10.07
	45	17.88	16.30
	51	26.34	23.70
	57	33.36	30.35
800-1000	33	10.26	10.07
	39	22.64	19.59
	45	30.74	28.41
	51	37.85	36.55
	57	46.63	44.17

4.1.2.2. Tempered glass impacted by silicon carbide erodents

Table 4. 2 represents the variation of erosion rate of as received glass and the tempered glass with velocity at 90^0 incidence for different sizes of silicon carbide erodents. The erosion rate is slightly lower for the tempered glass than for as received glass. However, the difference

in erosion rates between as received glass and the tempered glass impacted by glass beads is greater than that between as received glass and the tempered glass impacted by silicon carbide erodent particles.

Table 4. 2 Variation of erosion rate of as -received glass and the tempered glass with velocity for different sizes of silicon carbide erodent impact at 90^0 incidence.

SiC size(μm)	Velocity(ms^{-1})	As-rec.glass Erosion rate (cm^3x10e-4/g)	Tem.-glass Erosion rate (cm^3x10e-4/g)	As-rec.glass Velocity exponent	Tem.-glass Velocity exponent
63-106	45	5.24	4.95	2.2	2.2
	51	6.73	6.45		
	57	8.995	8.78		
	71	14.53	13.73		
	99	28.36	28.05		
106-125	45	6.63	6.58	2.3	2.3
	51	9.59	9.47		
	57	12.47	12.25		
	71	21.55	20.98		
	99	41.05	40.47		
180-250	45	12.40	12.30	2.2	2.2
	51	18.83	18.40		
	57	24.34	23.54		
	71	41.10	40.61		
	99	74.27	73.62		
400-500	33	11.87	11.54	2.7	2.7
	39	21.06	20.68		
	45	30.35	29.75		
	51	41.82	41.08		
	57	50.60	50.21		
600-700	33	17.36	17.25	2.2	2.2
	39	26.23	25.73		
	45	35.93	34.95		
	51	45.75	44.31		
	57	58.51	57.59		
800-1000	33	22.82	22.36	2.1	2.1
	39	32.57	32.29		
	45	46.24	45.42		
	51	56.89	56.35		
	57	69.23	67.75		

4.1.3. Stainless steel

4.1.3.1. Test results

Systematic measurements of the steady state erosion rate of 304 stainless steel have been made for a range of different velocities at 90^0 and 30^0 incidence angles. Five erodent particles (180-250 μm) used for erosion tests are silica, alumina, tungsten carbide, silicon carbide

The variation of erosion rate (Eg) as a function of the impingement velocity of various erodent particles at 90^0 and 30^0 incidence is plotted on log-log scale as shown in figs.4.18 and 4.19 for impingement angles of 90^0 and 30^0 respectively. At 90^0 impact, the 304 stainless steel eroded by diamond erodents surprisingly exhibits the lowest erosion rate as shown in fig.4.18, followed by WC, silica, alumina and SiC erodents. It is also noted that the erosion rates of 304 stainless steel by silica, alumina and SiC tend to be similar. At 30^0 impact, the erosion rate for 304 stainless steel with diamond erodent impact tends to be close to that impacted by SiC, alumina and silica erodent particles although it is still lower than them. The 304 stainless steel eroded by WC erodents exhibits by far the highest erosion resistance as shown in fig.4.19. The variation of erosion rate (Eg) of 304 stainless steel with impingement velocity of SiC erodents and alumina erodents for different particle size is shown in figs. 4.20 to 4.23. It is noted that the erosion rates (Eg) show only a slight variation with the change in

Particle size.

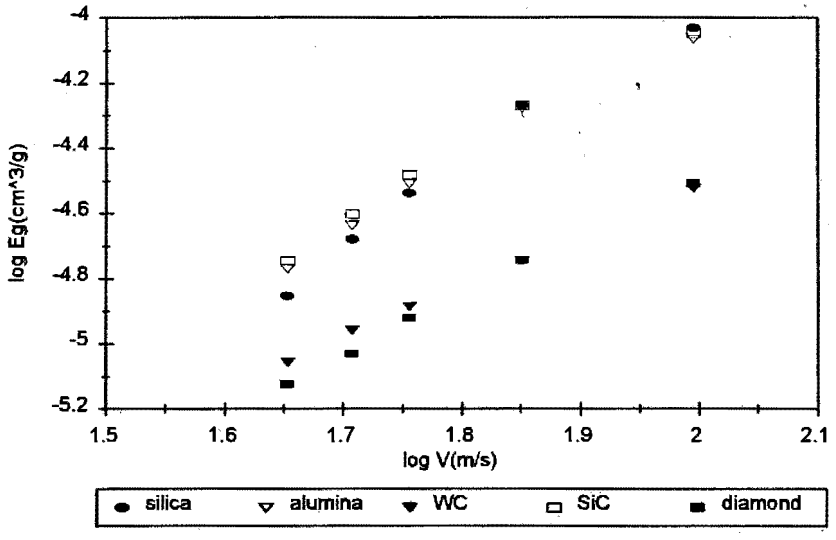

Figure 4. 18 Graph of erosion rate (Eg) of 304 stainless steel versus impingement velocity of indicated erodent particles(180-250 μm) at 90^0 incidence.

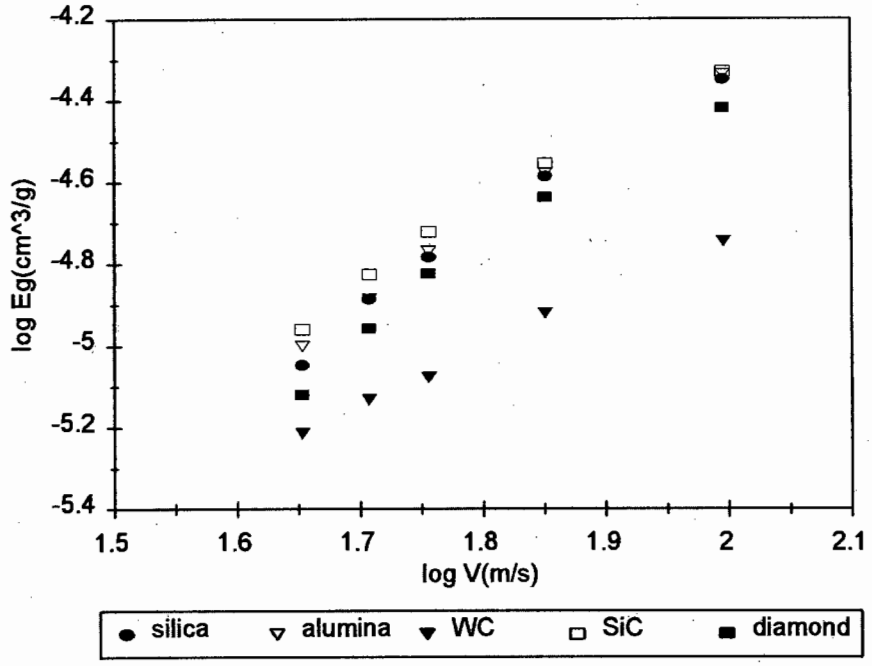

Figure 4. 19 Graph of erosion rate (Eg) of 304 stainless steel versus impingement velocity of indicated erodent particles(180-250 μm) at 30° incidence.

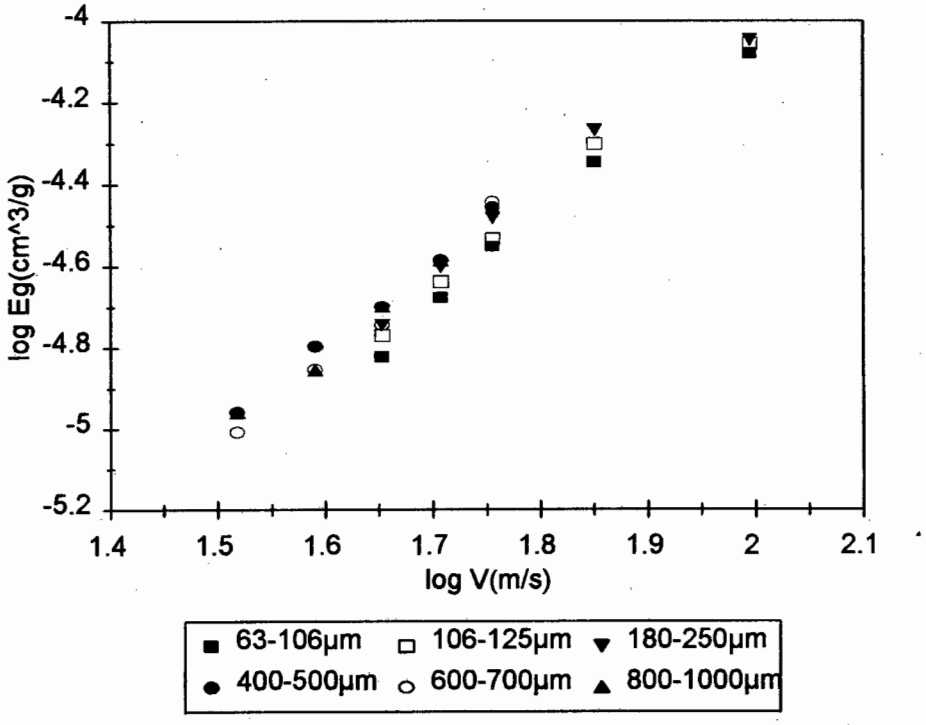

Figure 4. 20 Graph of the steady state erosion rate (Eg) of 304 stainless steel versus velocity of silicon carbide erodents and at an impingement angle of 90° incidence.

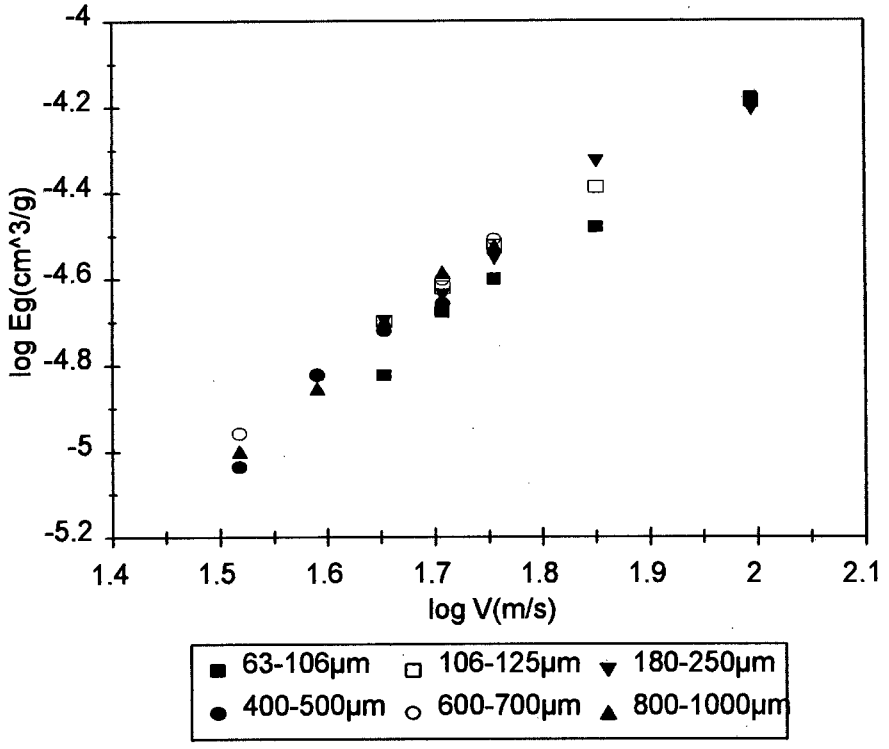

Figure 4. 21 Graph of erosion rate (Eg) of 304 stainless steel versus impingement velocity of SiC erodents at 60° incidence.

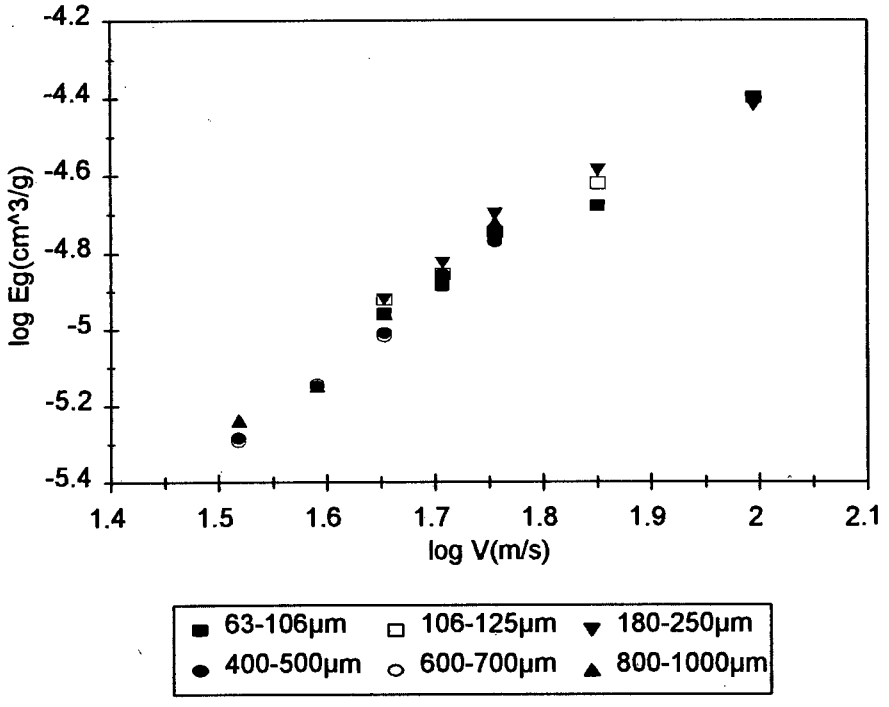

Figure 4. 22 Graph of erosion rate (Eg) of 304 stainless steel versus impingement velocity of SiC erodents at 30^0 incidence.

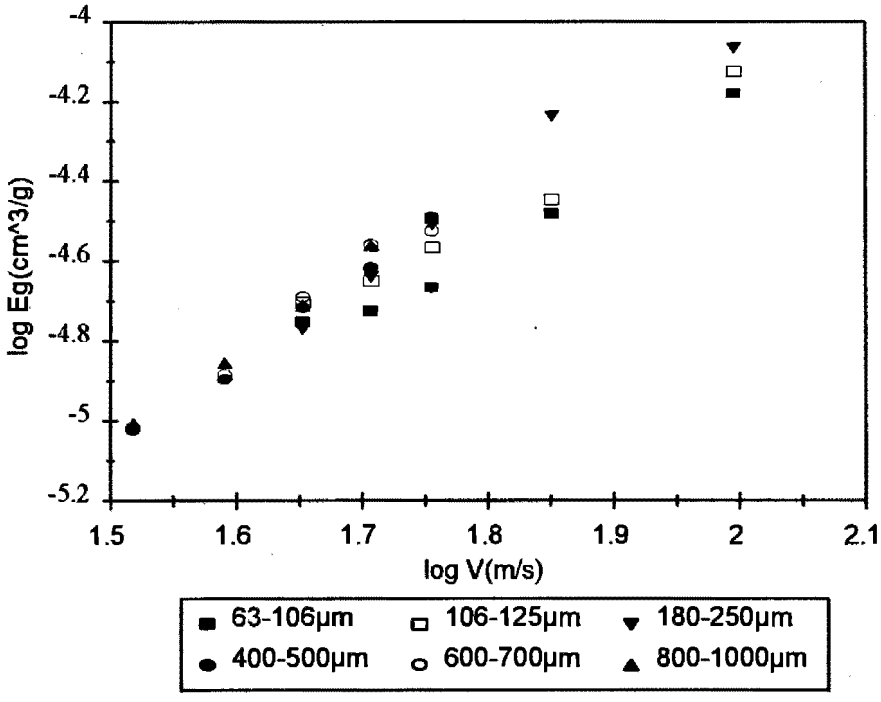

Figure 4. 23 Graph of erosion rate (Eg) of 304 stainless steel versus impingement velocity of alumina erodents at 90^0 incidence.

4.1.3.2. Subsurface hardness

Microhardness measurement was carried out at 25g load on the cross sectioned eroded specimens of 304 stainless steel at regular intervals from the eroded surface up to certain depth where the original microstructure occurs. The variation of Vickers microhardness tests on a cross section of 304 stainless steel after steady state particle erosion at 90^0 and 30^0 incidence is shown in figs. 4.24 and 4.25 respectively. The surface and subsurface hardness after erosion is considerably higher than the initial hardness. This implies a higher flow stress gradient in the near surface region of 304 stainless steel. It is generally noted that the microhardness decreases with increasing depth below the subsurface. The Vickers microhardness of 304 stainless steel is between 470 HV and 280 HV at width of 150 μm for 90^0 incidence as shown in fig. 4.24 and between 360 HV and 280 HV in the near surface region of 70 μm in width for 30^0 incidence as shown in fig. 4.25. The microhardness for diamond erodent impacting at 90^0 incidence is greater than that for the other particle impact. The microhardness of 304 stainless steel is between 470 HV and 320 HV at depth region of 200 μm for diamond erodent impact and between 420 HV and 320 HV at depth region of approximately 50 μm for the other particle impact. However, at 30° impact, there is no significant difference in the microhardness of 304 stainless steel for all particle impact.

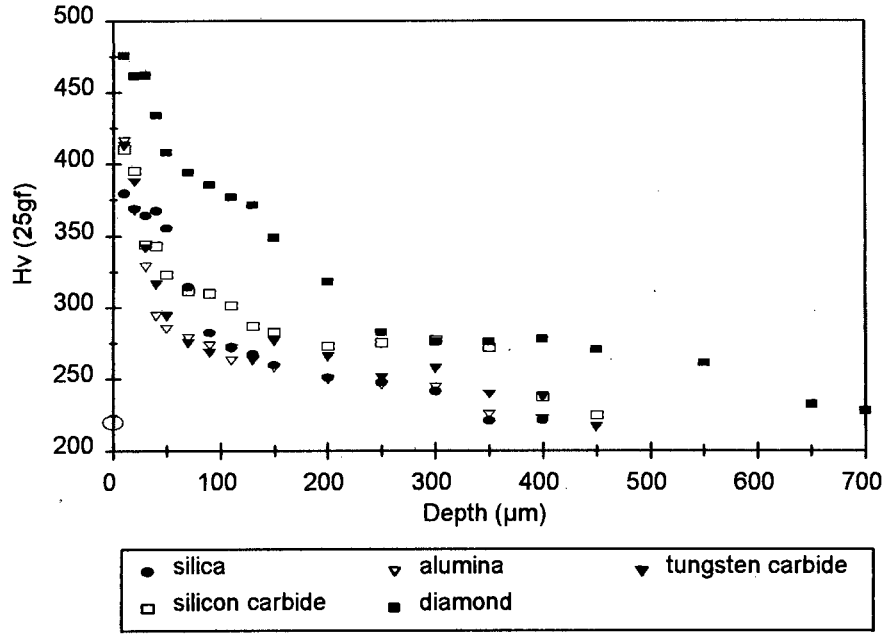

Figure 4. 24 Graph of hardness as a function of depth beneath the eroded surface of 304 stainless steel with 40 g mass of indicated erodents (180-250 μm) impacting at 90^0 incidence.

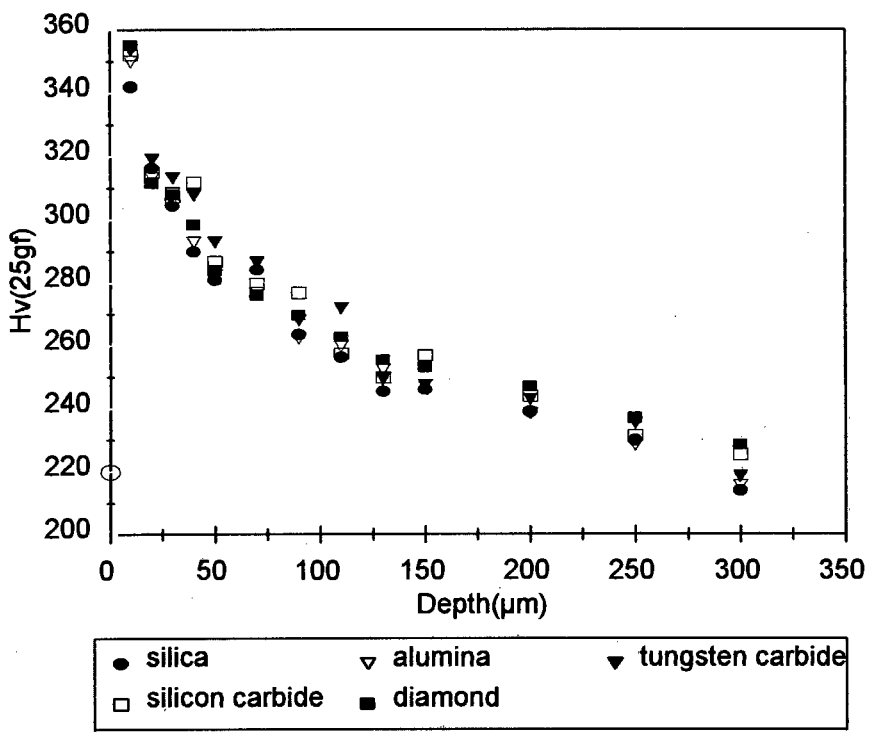

Figure 4. 25 Graph of hardness as a function of depth beneath the eroded surface of 304 stainless steel with 40 g mass of indicated erodents (180-250 μm) impacting at 30^0 incidence.

4.1.3.3. EDS results

A Cambridge Stereoscan 440 scanning electron microscope with energy dispersive x-ray microanalysis system was used for examination of any change in chemical composition after impact. The analyses presented in Table 4. **3** confirmed the presence of elements that are in the silica, alumina, WC and diamond erodent particles respectively. Thus the analysis gives information concerning the embedding of erodent particles in the 304 stainless steel. The extent of embedding for all erodent impact is greater at 90^0 than at 30^0 incidence. Within the sensitivity of the EDS apparatus in this study, carbon from diamond could not be detected.

Table 4. 3 EDS data of 304 stainless steel surface before and after impact with different erodent particle at impingement angles of 30^0 and 90^0 respectively.

Materials	Angle	Chemical Element (wt%)						
		Fe	Cr	Mn	Si	Ni	Al	W
304ss		71.7	18.4	1.8	0.4	7.8	-	-
Silica	30°	65.8	17.4	1.8	4.5	7.1	-	-
	90°	61.5	16.4	1.4	8.9	6.6	-	-
Alumina	30°	70.5	16.4	1.5	0.1	8.0	1.3	-
	90°	69.2	16.4	1.8	0.1	8.1	3.3	-
WC	30°	55.1	15.9	1.4	1.0	5.2	-	21.4
	90°	43.5	12.1	1.1	1.6	4.0	-	37.7
SiC	30°	69.8	16.0	1.7	1.8	8.3	-	-
	90°	65.6	15.2	1.6	6.5	7.4	-	-
Diamond	30°	71.3	18.8	1.7	0.3	7.8	-	-
	90°	71.5	18.5	1.7	0.5	7.8	-	-

4.1.4. Tungsten carbide - cobalt

4.1.4.1. Test results

Variation of the steady state erosion rate (Eg) of tungsten carbide-cobalt with velocity of different erodents (180-250 μm) at an impingement angle of 90^0 incidence is shown in fig. 4.26. It shows that the WC-7% Co exhibits the highest erosion rate for diamond erodents and the lowest erosion rate for silica erodents. The graph of the logarithm of the erosion rate (Eg) versus the logarithm of velocity for silicon carbide in six particle size ranges is shown in fig. 4.27. It is noted that the erosion rate (Eg) increases with increasing impingement velocity.

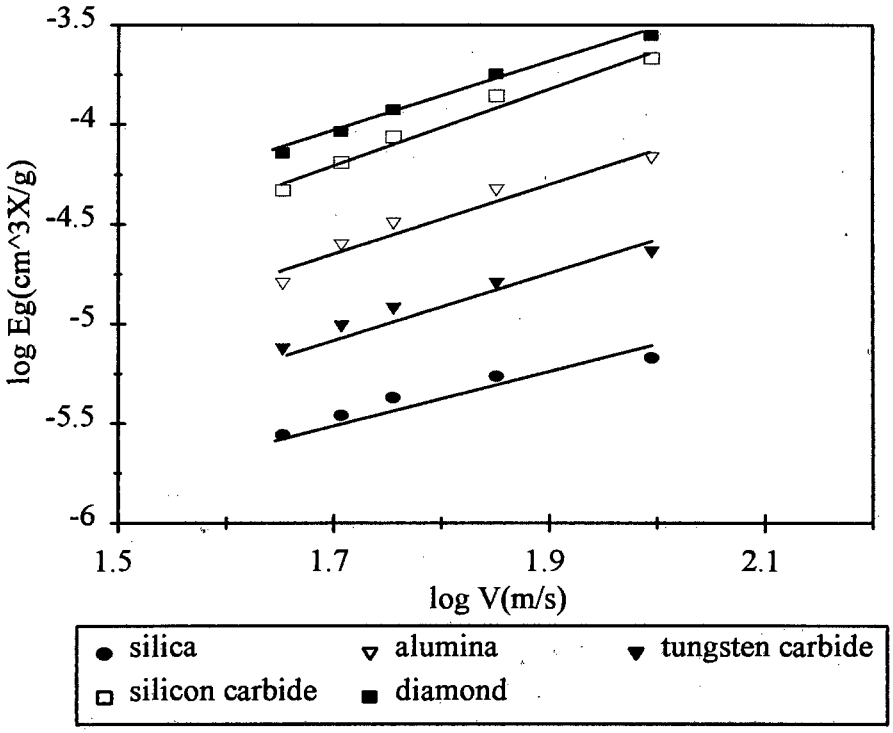

Figure 4. 26 Graph of erosion rate(Eg) of WC-7%Co versus impingement velocity of indicated erodent particles at 90^0 incidence.

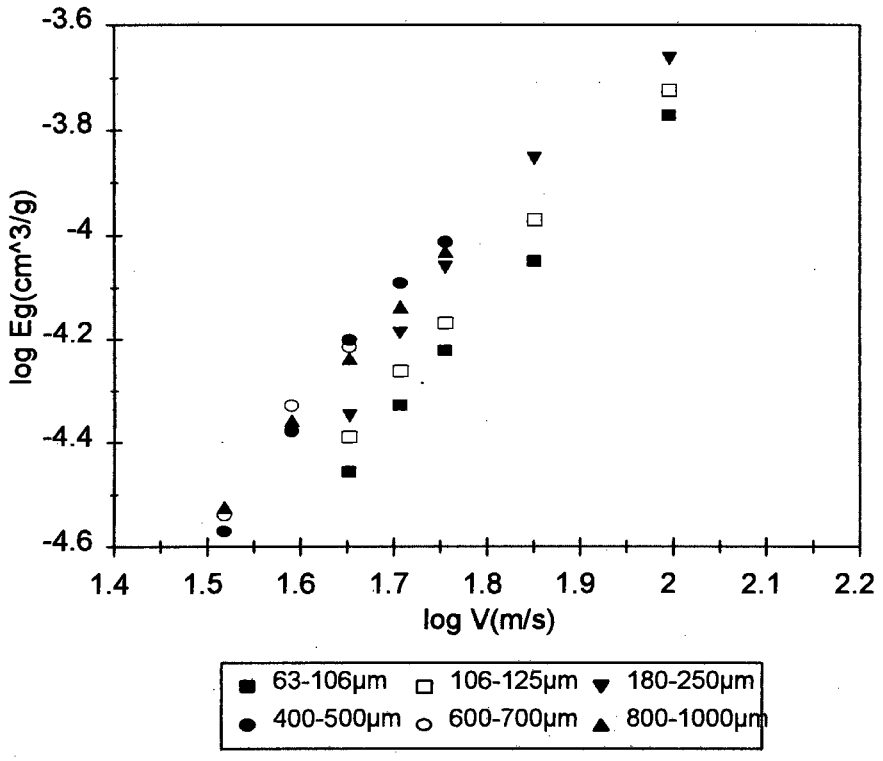

Figure 4. 27 Graph of erosion rate (Eg) of WC-7%Co versus impingement velocity of silicon carbide erodent particles with different size at 90^0 incidence.

4.1.4.2. Measurement of fragmentation of erodents

The micrographs of erodents before and after impact on WC-7%Co targets are shown in fig. 4.28. The graphs of size distribution of erodents (180-250 μm) before and after impact are shown in figs. 4.29 to 4.33 for an impingement angle of 90^0 incidence and at a velocity of 99 $m.s^{-1}$. It is noted that diamond erodents after impact show almost no fragmentation. The ranking of fragmentation of erodents in decreasing severity is silica, alumina, SiC and WC erodents. Fig. 4.28 (c) shows the fragmentation of WC erodents. However, fig. 4.31 does not show the fragmentation distribution of WC after impact as the WC particles with high density are too heavy to be stirred properly. Thus a Malvern Mastersizer apparatus hardly detects the fragmentation of WC erodents.

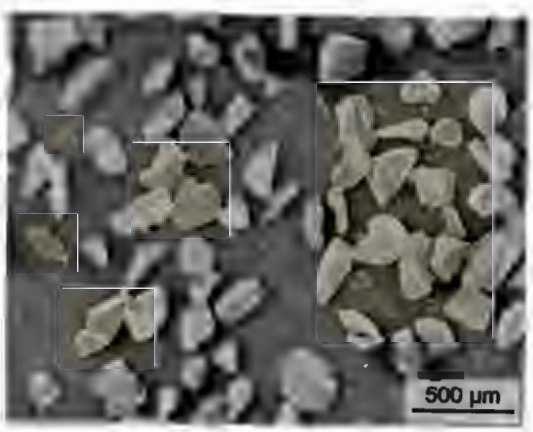

before impact
(a)

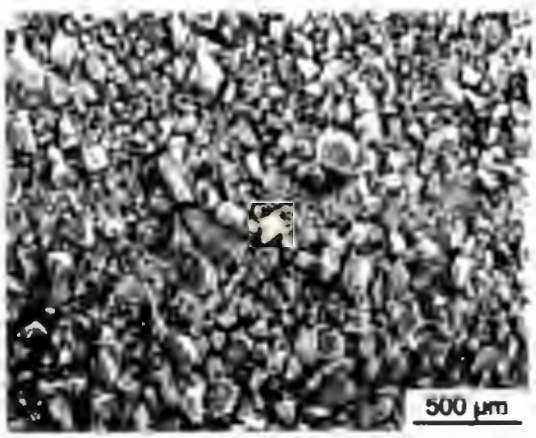

after impact
(a)

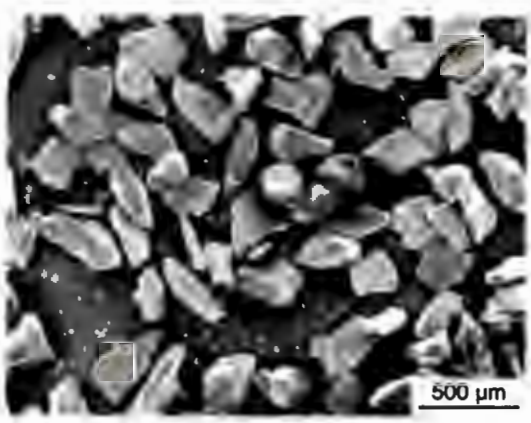

before impact
(b)

after impact
(b)

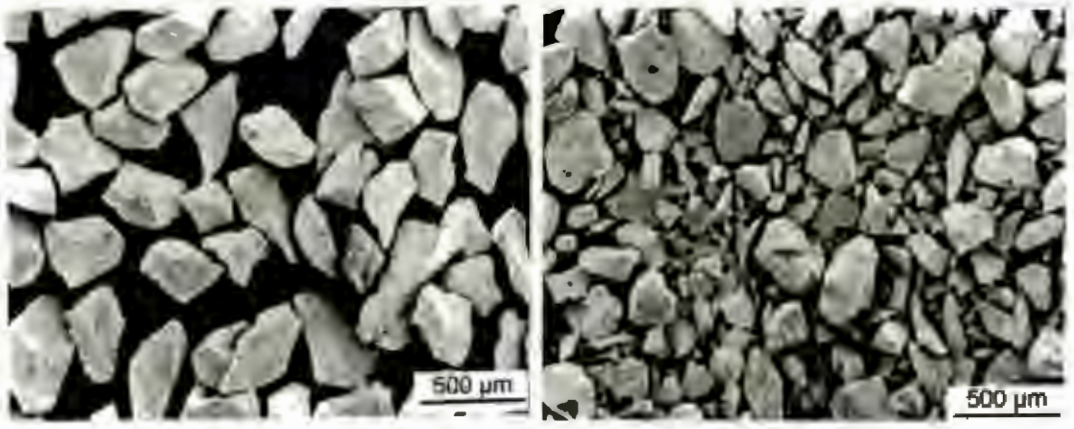

before impact (c) after impact (c)

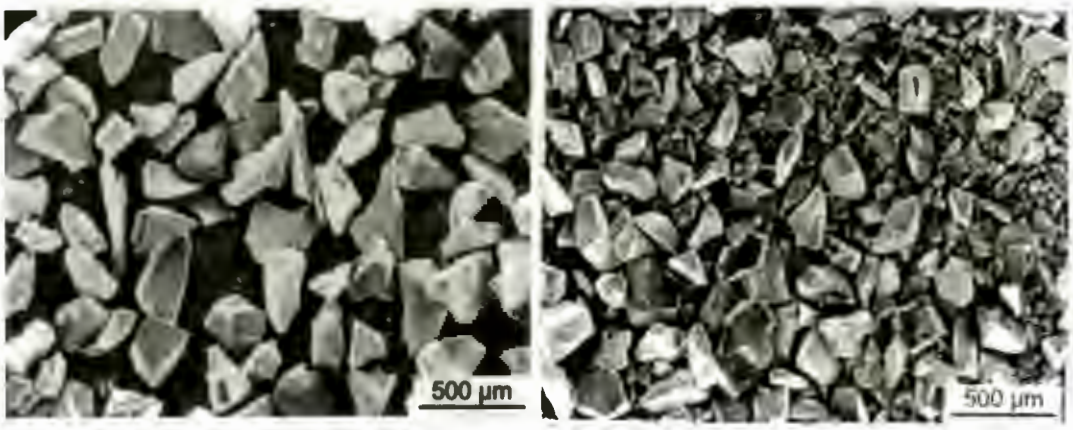

before impact (d) after impact (d)

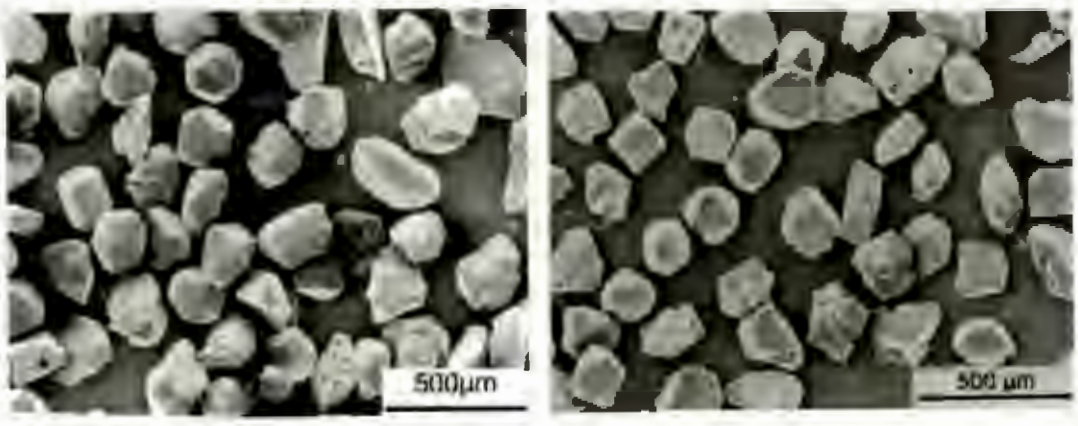

before impact (e) after impact (e)

Figure 4. 28 SEM micrographs of erodent particles (180-250 µm) before and after impacting WC-7%Co surface at 90^0 incidence and at an average velocity of 99 $m.s^{-1}$. (a) silica (b) alumina (c) WC (d) SiC (e) diamond.

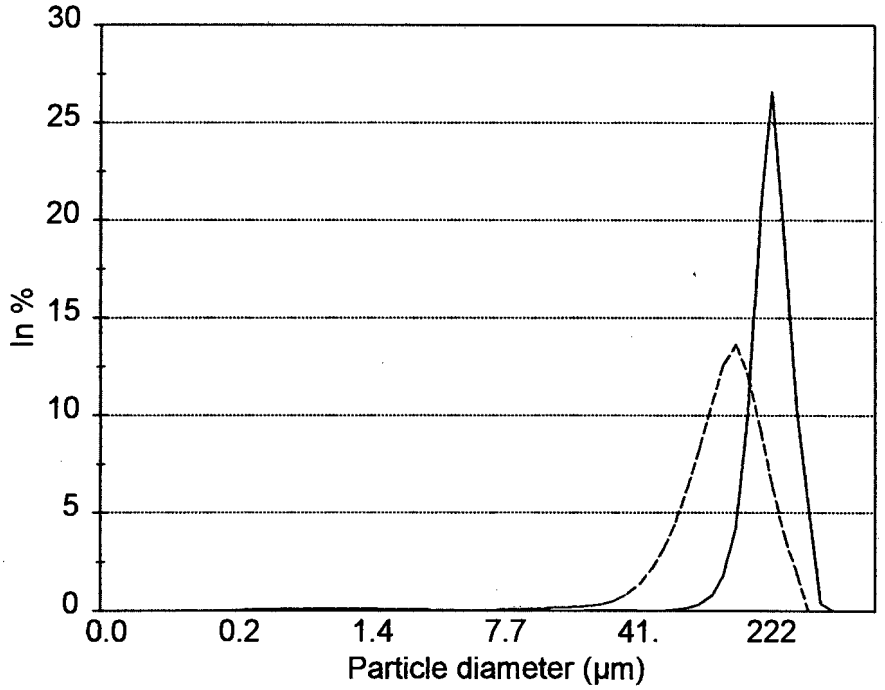

Figure 4. 29 Size distribution of silica erodents before and after impact of WC-7%Co. Solid line: before impact, dashed line: after impact.

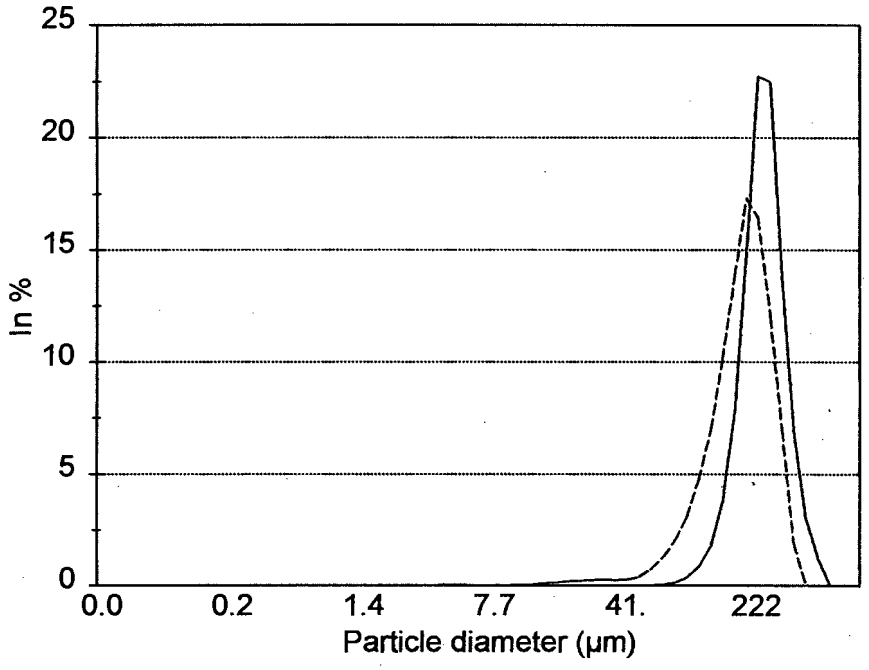

Figure 4. 30 Size distribution of alumina erodents before and after impact of WC-7%Co. Solid line: before impact, dashed line: after impact.

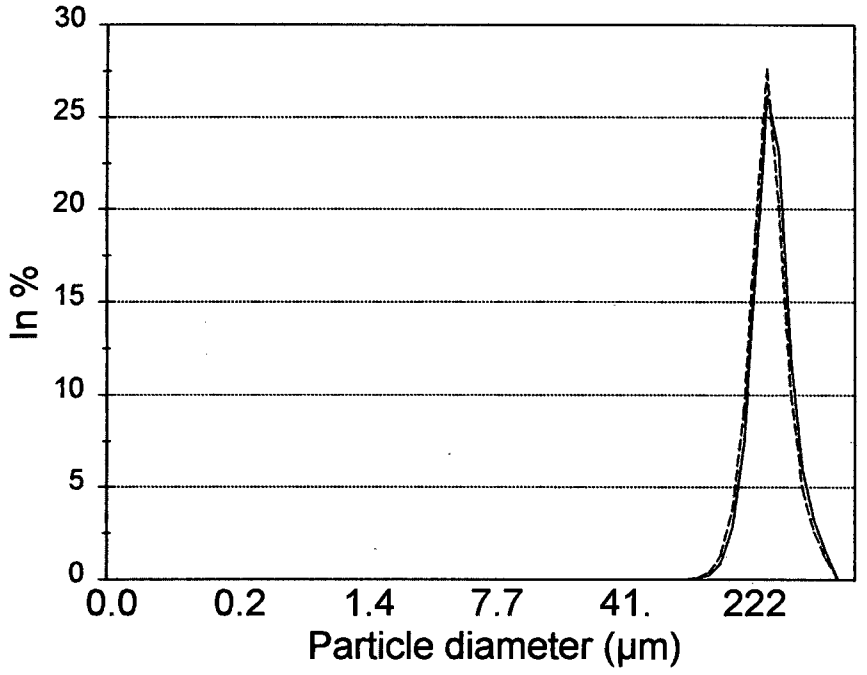

Figure 4. 31 Size distribution of WC erodents before and after impact of WC-7%Co. Solid line: before impact, dashed line: after impact.

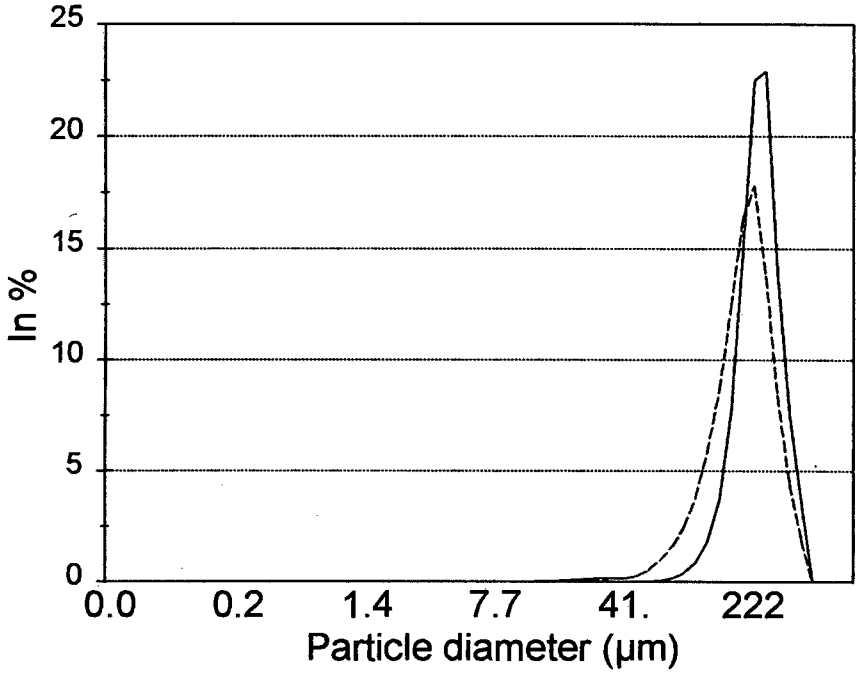

Figure 4. 32 Size distribution of SiC erodents before and after impact of WC-7%Co. Solid line: before impact, dashed line: after impact.

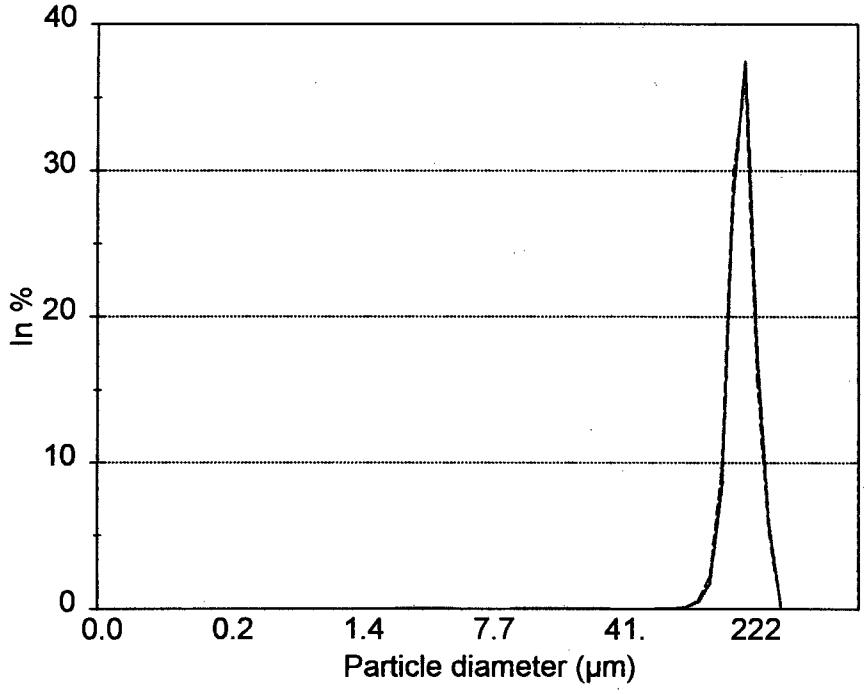

Figure 4. 33 Size distribution of diamond erodents before and after impact of WC-7%Co. Solid line: before impact, dashed line: after impact

4.1.5. Alumina

4.1.5.1. Test results

The erosion rate (Eg) is the highest for diamond erodents, followed by SiC, alumina, WC and silica as shown in fig. 4.34. The variation of the erosion rate (Eg) as a function of the impingement velocity of silica, alumina, SiC and diamond erodents is plotted on log-log scale in figs. 4.35 to 4.38 respectively for an impingement angle of 90° incidence. These figures show that the erosion rate (Eg) increases with increasing impingement velocity. The erosion rate (Eg) by silica erodents impact increases with particle size up to 180-250 μm and then decreases with further increasing particle size while the erosion rate continuously increases with increasing particle size for the other particles.

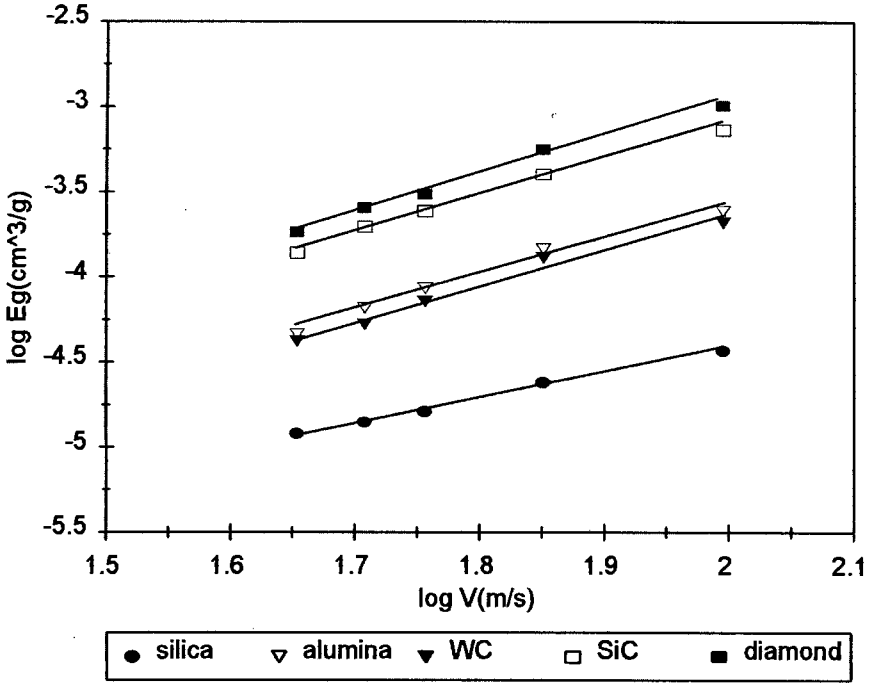

Figure 4. 34 Graph of erosion rate (Eg) of alumina versus impingement velocity of indicated erodent particles(180-250 μm) at 90^0 incidence.

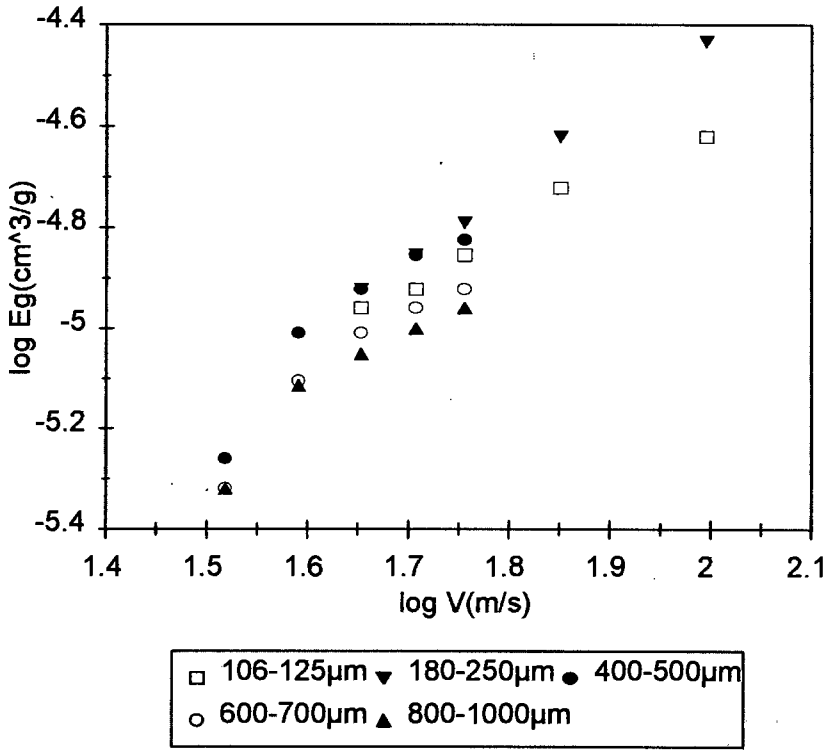

Figure 4. 35 Graph of the erosion rate (Eg) of alumina versus velocity of silica erodents using different sizes at an impingement angle of 90^0 incidence.

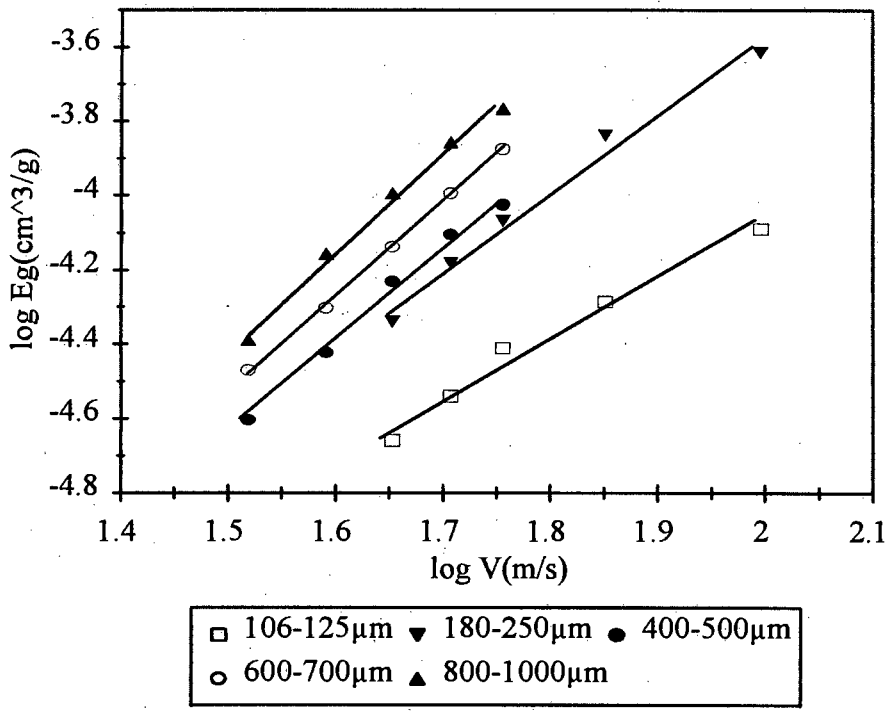

Figure 4. 36 Graph of the erosion rate (Eg) of alumina versus velocity of alumina erodents using different sizes at an impingement angle of 90^0 incidence.

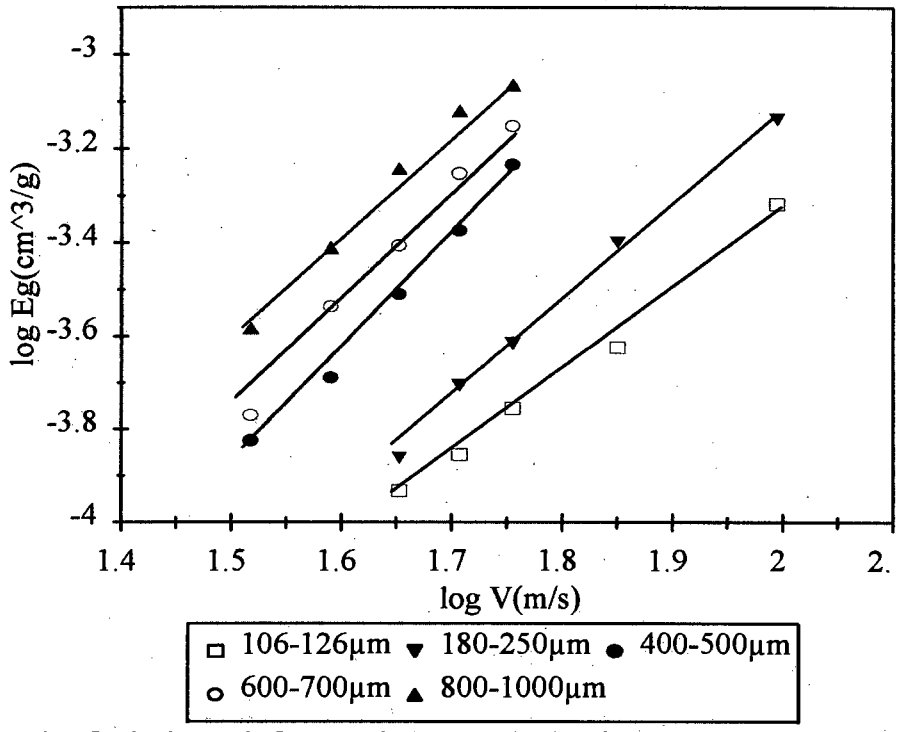

Figure 4. 37 Variation of the erosion rate (Eg) of alumina with velocity of silicon carbide erodents using different size ranges and at an impingement angle of 90^0 incidence.

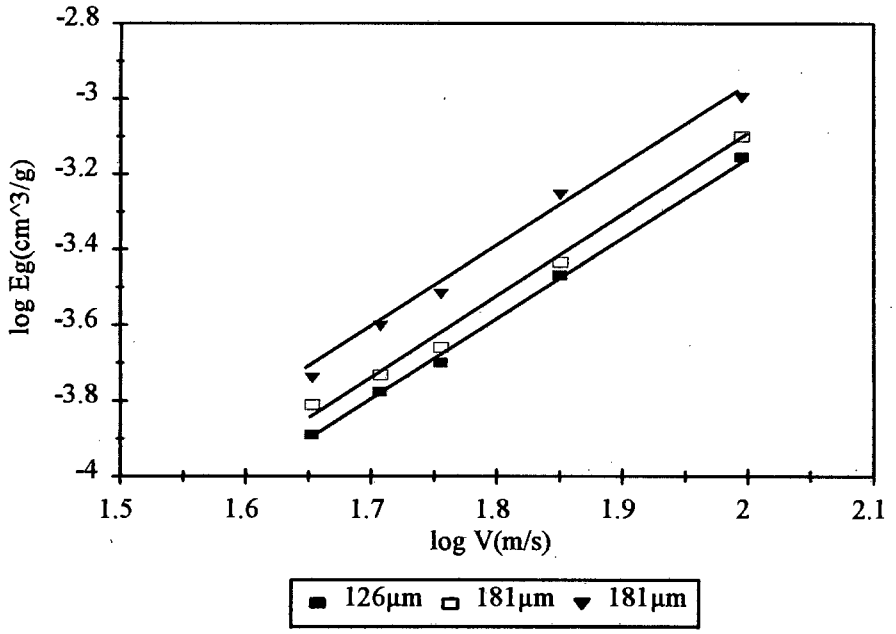

Figure 4. 38 Variation of the erosion rate (Eg) of alumina with velocity of diamond erodents using different size ranges and at an impingement angle of 90^0 incidence.

4.2. Analysis of solid particle erosion results

4.2.1. As received glass

4.2.1.1. Empirical correlation of erosion rate with particle velocity and size

In order to understand the effect of an individual particle on erosion process, the erosion rate per gram (Eg) is converted to the erosion rate per particle (Ep). The erosion rate (Ep), defined as a volume loss per particle of erodent, was estimated by measuring the weight loss after the erosion test as described in section 3.3. Fig. 4.39 represents data pertaining to 180-250 μm in diameter for glass beads, silica, alumina, tungsten carbide, silicon carbide and diamond at an impingement angle of 90°. It shows that the erosion rate (Ep) increases as the impingement velocity increases. The erosion rate (Ep) is the greatest for the tungsten carbide erodents, followed by diamond, silicon carbide, alumina, silica and glass beads. Information on the erosion mechanism could usually be obtained from the velocity exponent that is the slope of straight lines shown in figs. 4.5 to 4.17. Tables 4.4 and 4.5 present the variation of velocity exponents with particle size at 90° and 30° impact respectively.

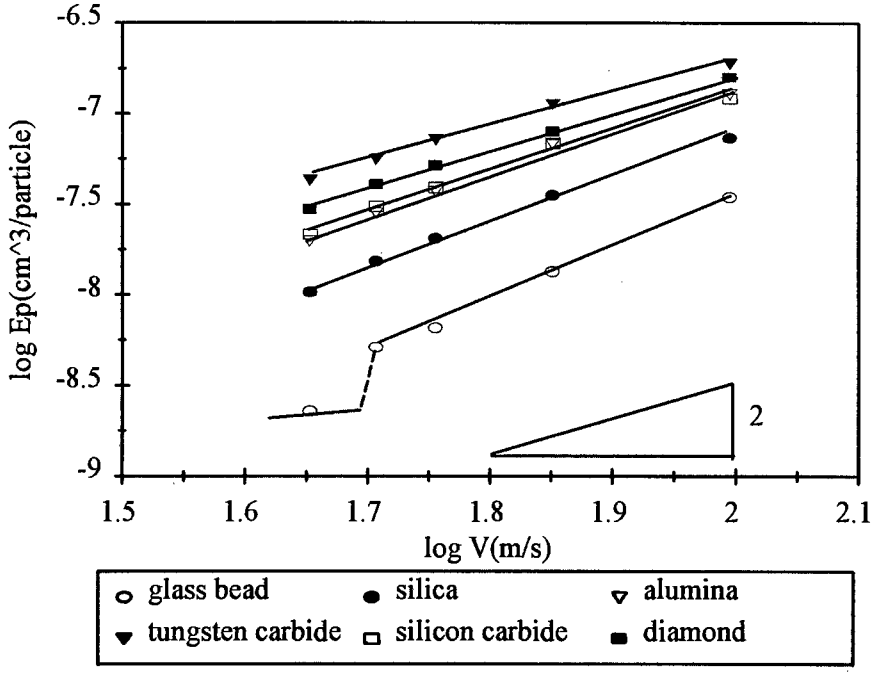

Figure 4. 39. Graph of erosion rate (Ep) of as received glass as a function of the impingement velocity of indicated erodents (180-250 μm) at 90° incidence.

The data presented in Tables 4.4 and 4.5 show that the velocity exponents range from 1.9 to 2.8 and 2.0 to 3.6 for impingement angles of 90° and 30° respectively. There is no clear correlation of velocity exponent with the change in impingement angle. The values of velocity exponents appear to decrease for particle sizes above 400-500 μm in diameter.

Table 4. 4. Variation of velocity exponent for erosion of as received glass with particle size at 90° incidence

size(μm)	silica	alumina	WC	SiC	diamond
63-106	2.5± 0.1	2.5± 0.1		2.2±0.1	
106-125	2.9± 0.1	2.5± 0.1		2.3±0.3	2.0±0.1
151					2.1±0.1
181					2.1±0.1
125-180			1.9±0.1		
212			2.0±0.1		
180-250	2.5± 0.2	2.4± 0.2		2.1±0.2	
400-500	2.8± 0.2	2.5± 0.1		2.7±0.1	
600-700	2.6± 0.1	2.3 ± 0.1		2.4±0.1	
800-1000	2.5± 0.1	2.2 ± 0.1		2.1±0.1	

Table 4. 5. Variation of velocity exponent for erosion of as received glass with particle size at 30° incidence

Size(μm)	Silica	Alumina	SiC	Diamond
63-106	2.5± 0.1	2.5± 0.1	2.3±0.1	
106-125	2.7± 0.1	2.2± 0.1	2.1±0.1	2.5±0.1
151				2.2±0.1
181				2.0±0.1
180-250	2.9± 0.1	2.3± 0.1	2.3±0.1	
400-500	3.6± 0.2	3.0± 0.1	2.6±0.1	
600-700	2.9± 0.1	2.7 ± 0.2	2.2±0.1	
800-1000	2.8± 0.1	2.6 ± 0.2	2.0±0.1	

Fig. 4.40 presents the erosion rate (Ep) of as received glass as a function of particle size for different erodents at a velocity of 57 $m.s^{-1}$ and an impingement angle of 90°. It is noted that the erosion rate increases with increasing particle size. Only the graph at particle velocities of 57 $m.s^{-1}$ and 90° incidence, from which the particle size exponents were calculated, is shown for simplicity (fig.4.40). The exponents at other velocities were calculated from similar graphs and are shown in Table 4.6. It is noted that the values of size exponent are nearly 4.

A multivariate, linear regression analysis was used to analyse the data (figs. 4.5, 4.8, 4.12, 4.15) in order to obtain the empirical correlation of erosion rate with particle velocity and size. The detail of a multivariate, linear regression analysis is presented in Appendix A. Since for spherical glass beads the slope of trend lines as shown in figs. 4.39 and 4.40 is not constant, the empirical correlations of erosion rate versus velocity and size can not be obtained in this case. Likewise, the empirical correlations can not be deduced for WC erodents and steel shot due to lack of sufficient variation in particle sizes.

The empirical relationships of erosion rate (Ep) as a function of velocity (V) and particle size (D) for silica, alumina, silicon carbide and diamond at 90° incidence are detailed below.

Silica: $Ep \propto V^{2.7}D^{4.0}$ (4.1)

Alumina: $Ep \propto V^{2.4}D^{4.0}$ (4.2)

Silicon carbide: $Ep \propto V^{2.2}D^{4.0}$ (4.3)

Diamond: $Ep \propto V^{2.0}D^{4.0}$ (4.4)

Good correlation coefficients (R^2) of 0.998, 0.999, 0.999 and 0.998 were obtained for silica, alumina, SiC and diamond, respectively. The ranking of the value of velocity exponent is as follows: silica > alumina > SiC > diamond.

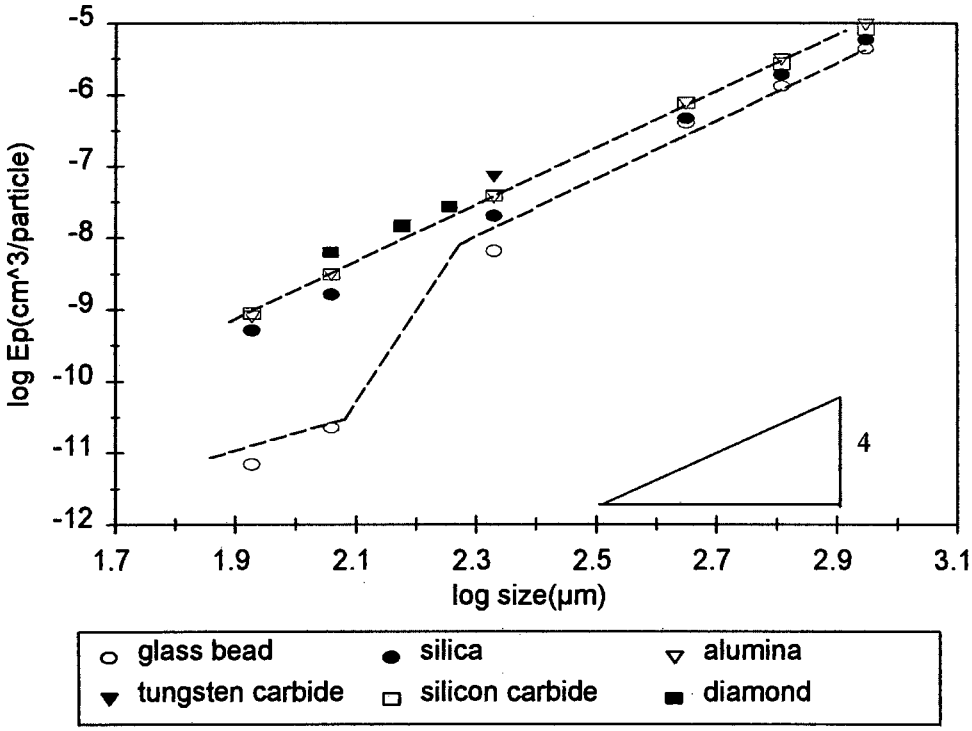

Figure 4. 40. Graph of erosion rate (Ep) of as received glass versus particle size for indicated particles at a velocity of 57 m. s^{-1} and an impingement angle of 90^0.

Table 4. 6. Variation of particle size exponent with velocity at 90^0 incidence for as received glass

velocity($m.s^{-1}$)	SiO_2	Al_2O_3	SiC	Diamond
33	4.6±0.5	4.0±0.1	4.0±0.0	
39	4.2±0.4	4.1±0.1	3.8±0.1	
45	4.1±0.2	4.1±0.0	4.0±0.1	3.8±0.3
51	3.8±0.2	3.9±0.1	3.6±0.0	4.0±0.2
57	3.8±0.0	3.8±0.1	3.5±0.0	4.2±0.4
71	4.0±0.1	4.0±0.1	4.1±0.1	4.0±0.3
99	3.9±0.2	3.8±0.0	4.0±0.0	3.9±0.3

4.2.1.2. The effect of impingement angle

Fig. 4.41 shows graph of the normalised erosion rate (NEp) versus impingement angle for glass eroded by all irregularly shaped erodents (106-125 μm). It is noted that the maximum erosion rate occurs at an impingement angle of 90°. With spherical glass bead impacts, there is a sharp increase in erosion rate at specific threshold angles as shown in figs. 4.42 and 4.43. Above 70 $m.s^{-1}$ impact, the erosion rate exhibited a sharp increase above an impingement angle of 30°. Below 70$m.s^{-1}$ impact, a sharp increase in erosion rate occurs above 60°. The threshold angle transition shifts from low angle regime to high angle regime with decreasing impingement velocity and particle size.

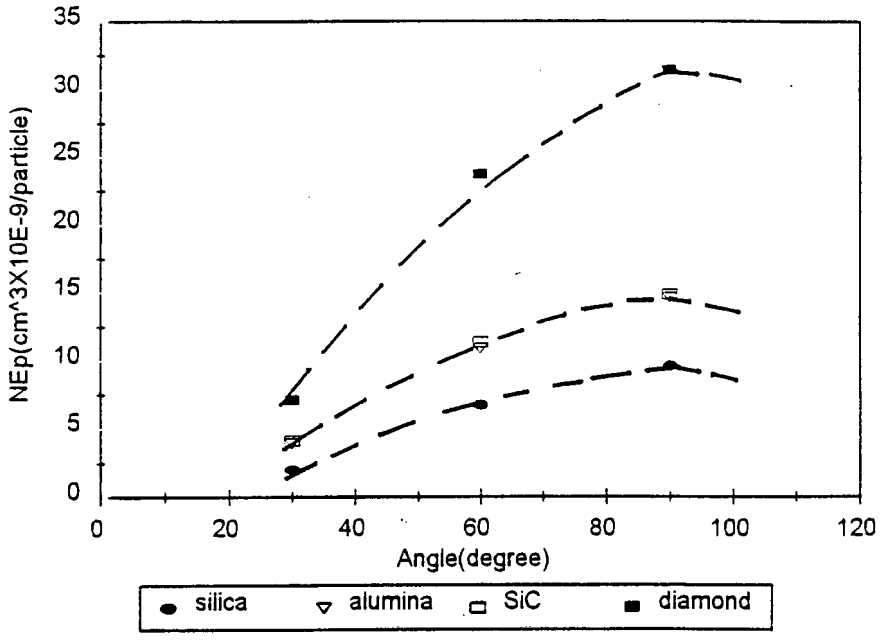

Figure 4. 41. Graph of erosion rate of glass versus impingement angle using the indicated erodents (106-125 μm) at an impingement velocity of 99 $m.s^{-1}$.

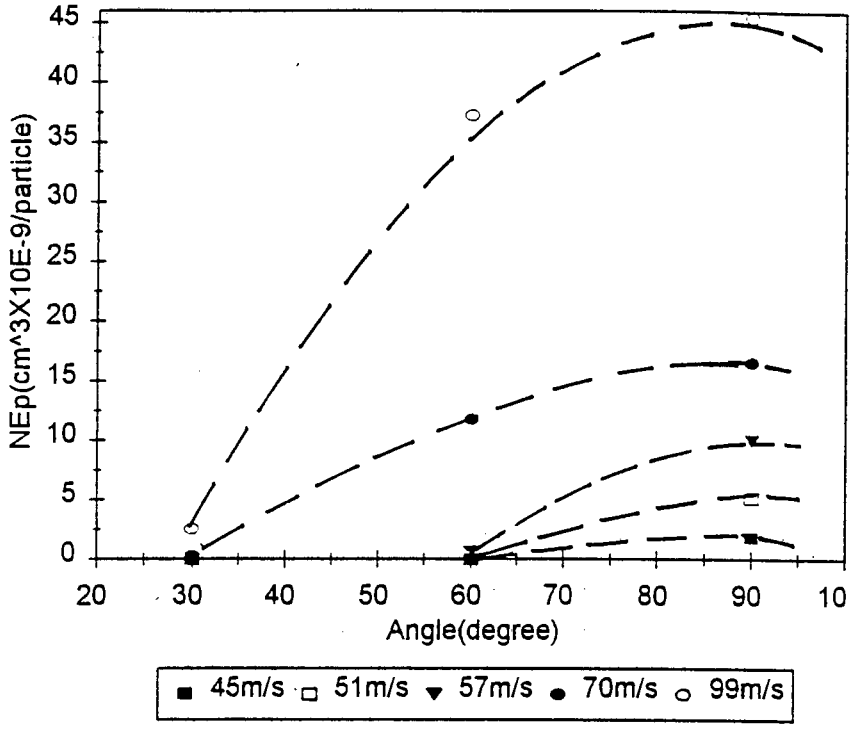

Figure 4. 42. Graph of erosion rate of glass versus impingement angle using glass beads (180-250 μm) with different velocities.

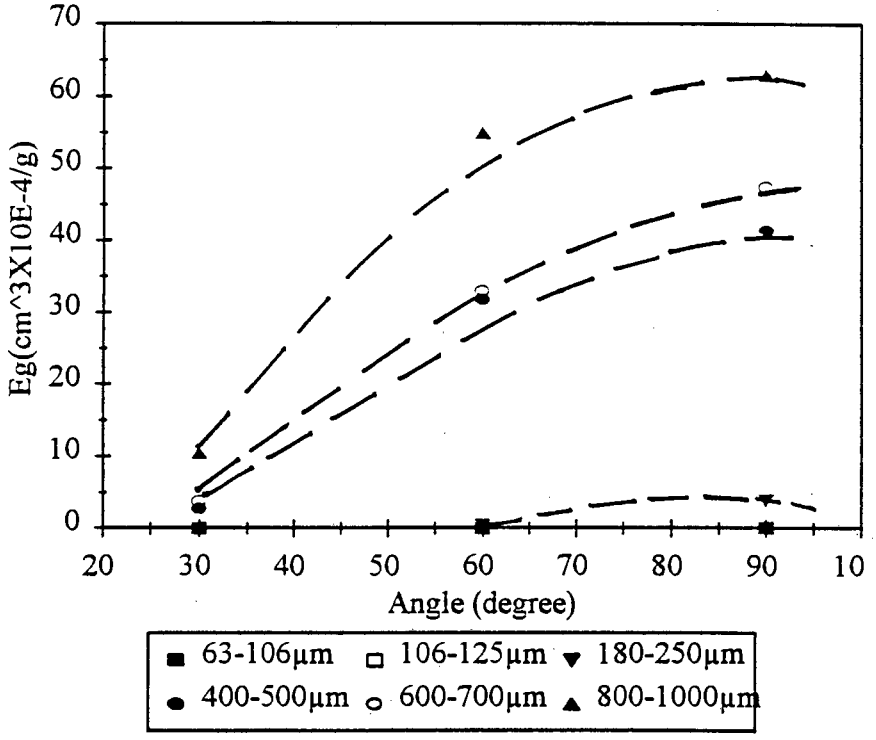

Figure 4. 43. Graph of erosion rate of glass versus impingement angle using glass beads with different sizes.

4.2.1.3. The effect of erodent properties

Fig. 4.44 shows the bar graph of erosion rate (Ep) of glass versus the ratio of particle to target hardness (Hp/Ht). The y axis scale on the left corresponds to dark shaded bar graphs which represents tests at 57 $m.s^{-1}$ with particle sizes ranging between 180-250 μm. It is noted that the erosion rate increases when the ratio of particle to target hardness increases for particles of similar densities such as glass beads, silica, alumina, silicon carbide and diamond erodents. However, WC erodent causes maximum erosion loss. The y axis scale on the right corresponds to striped bar graph which represents tests at 45 $m.s^{-1}$ with particle sizes ranging between 400-500 μm. The erosion rate for glass eroded by steel shots is greater than that for glass eroded by glass beads, silica, alumina and silicon carbide. It suggested that the erosion rate is related not only to the ratio of particle to target hardness but also to the toughness and density of the particles as shown in figs.4.45 and 4.46. Figs.4.45 and 4.46 show that the erosion rates are not directly proportional to the Kp/Kt and density. They illustrate that the erosion rate is determined by the combination of hardness, toughness and density of erodents.

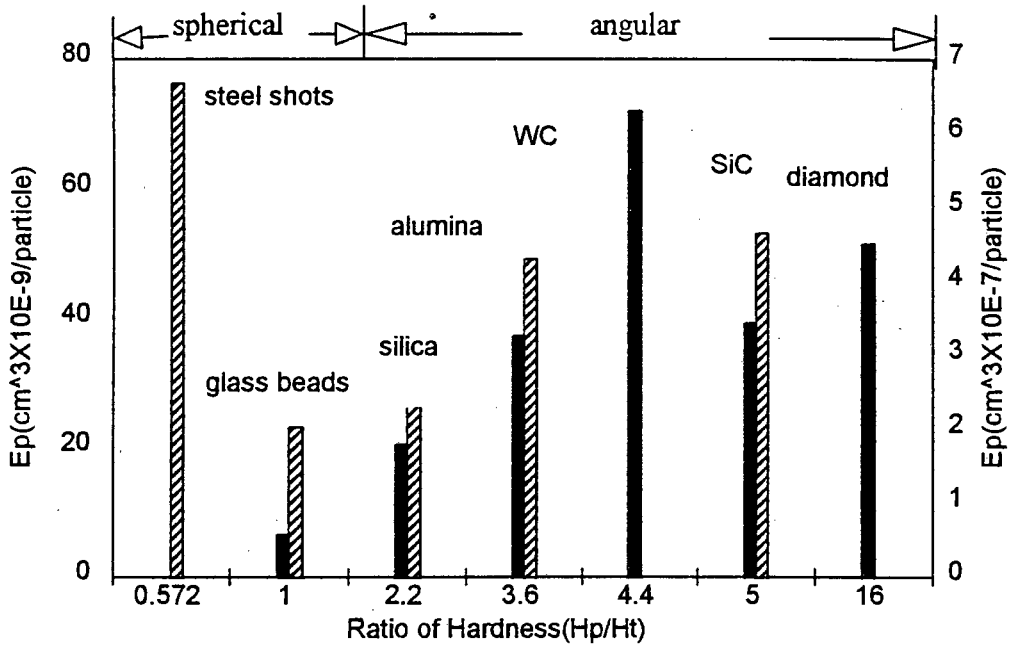

Figure 4. 44. Bar graph of erosion rate (Ep) of glass as a function of Hp/Ht at an impingement angle of 90^0. The y axis scale on the left corresponds to dark shaded bar graph which represents testing at 57 $m.s^{-1}$ with particle size ranging between 180-250 μm. The y axis scale on the right corresponds to striped bar graph which represents testing at 45 $m.s^{-1}$ with particle size ranging between 400-500 μm.

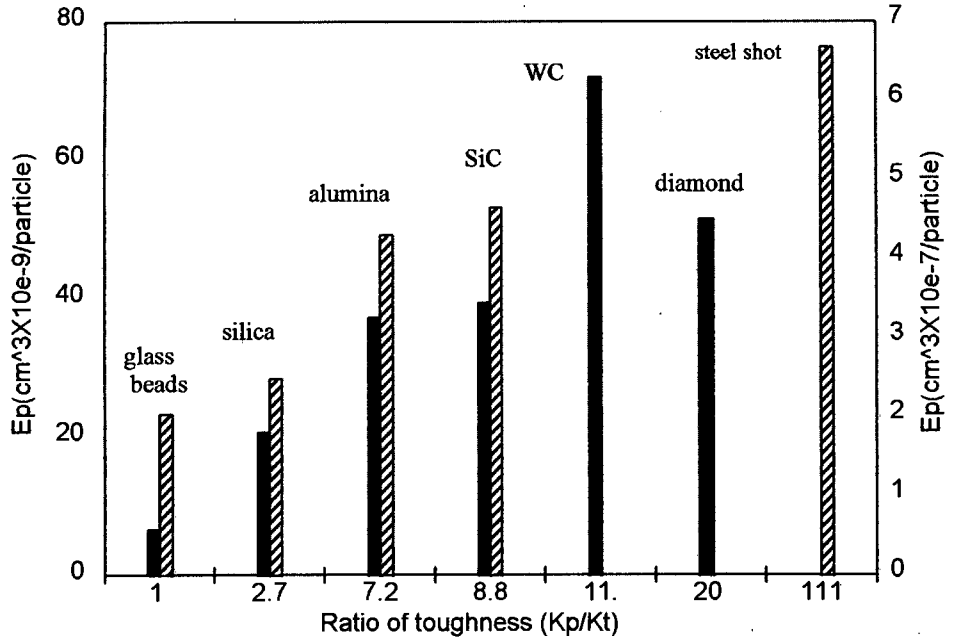

Figure 4. 45. Bar graph of erosion rate (Ep) of as received glass as a function of Kp/Kt at an impingement angle of 90°. The y axis scale on the left corresponds to dark shaded bar graph which represents testing at 57m. s^{-1} with particle size ranging between 180-250μm. The y axis scale on the right corresponds to striped bar graph which represents testing at 45m.s^{-1} with particle size ranging between 400-500μm

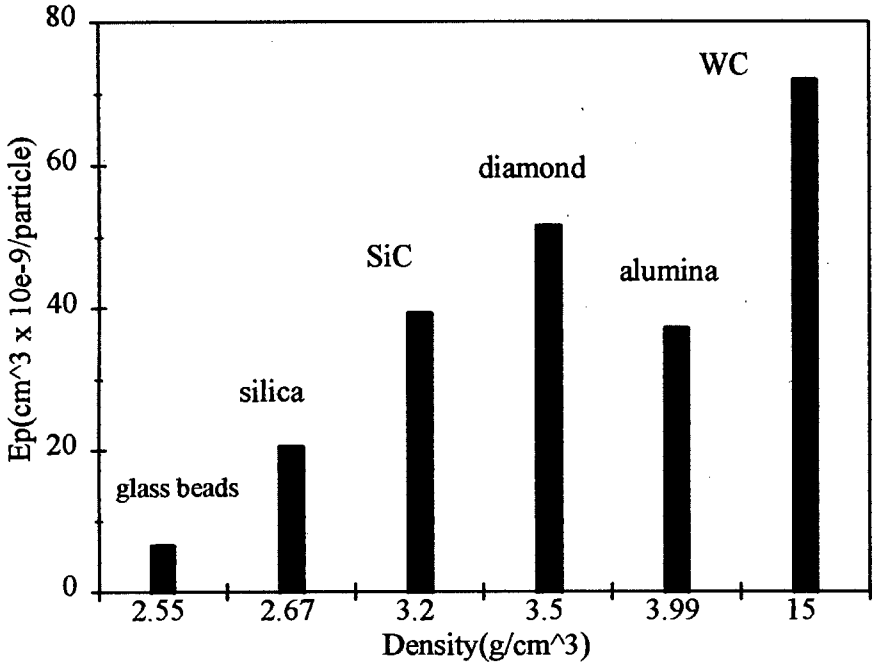

Figure 4. 46. Bar graph of erosion rate (Ep) of as received glass as a function of density of erodents (180-250μm) at an impingement angle of 90° incidence and at a velocity of 57m.s^{-1}

4.2.2. 304 Stainless steel

4.2.2.1. Empirical correlation of erosion rate with particle velocity and size

The variation of the erosion rate (Ep) of 304 stainless steel as a function of the impingement velocity of the erodent particles is plotted on log-log scale as shown in figs. 4.47 and 4.48 for both impingement angles of 90° and 30°, respectively. The least-squares fit of the data presented is in the velocity exponent of nearly 2.0±0.2 for silica, alumina, WC, SiC and diamond erodents at both 90^0 and 30^0 incidence angle respectively. The values of velocity exponent are calculated from figs.4.20 to 4.23 and shown in Table 4.7. It is noted that there is no clear correlation of velocity exponent with different particle size and impingement angle. Figs. 4.49 and 4.50 show the graph of erosion rate (Ep) as a function of particle size of silicon carbide and alumina erodents respectively. It shows that the erosion rate (Ep) increases with increasing particle size. The particle size exponent for silicon carbide and alumina is nearly 3.0. The least square fit of the data presented in figs. 4.47 and 4.48 was used to calculate velocity exponent of 2.0 ± 0.2 which is then used in the following equations.

The empirical correlations of erosion rate per particle (Ep) at 90° incidence are detailed below. It is noted that the value of velocity and size exponent is nearly 2.0 and 3.0 respectively.

For alumina: $$Ep \propto V^{2.0 \pm 0.2} D^{3.0 \pm 0.1} \quad (4.5)$$

For SiC: $$Ep \propto V^{2.1 \pm 0..1} D^{3.0 \pm 0.1} \quad (4.6)$$

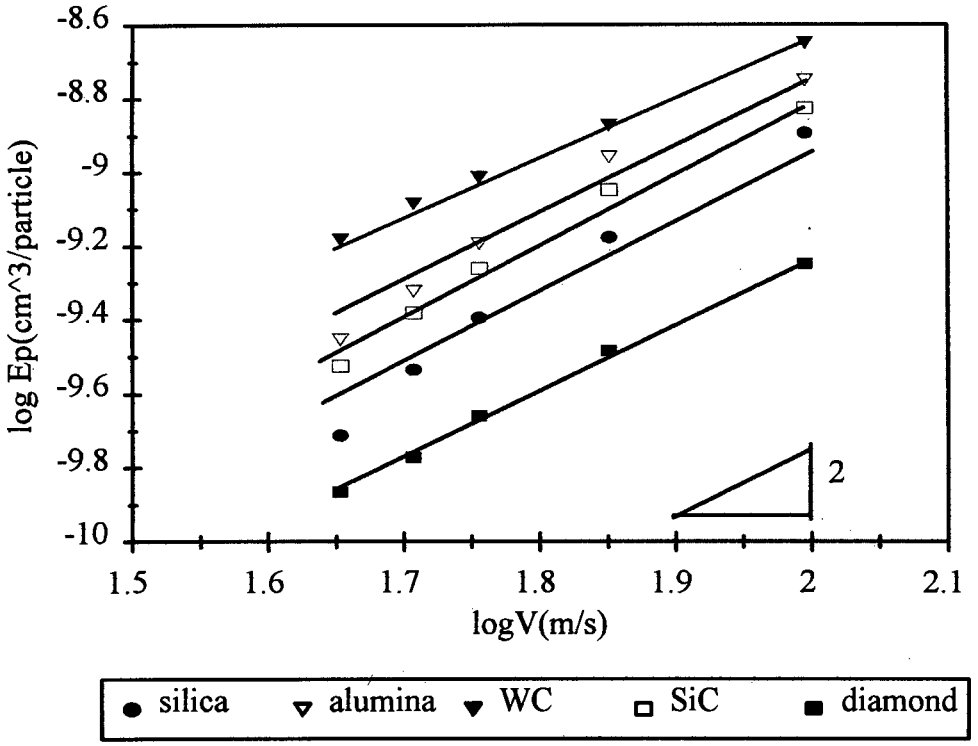

Figure 4. 47. Graph of erosion rate (Ep) of 304 stainless steel versus impingement velocity of indicated erodent particles (180-250 μm) at 90^0 incidence.

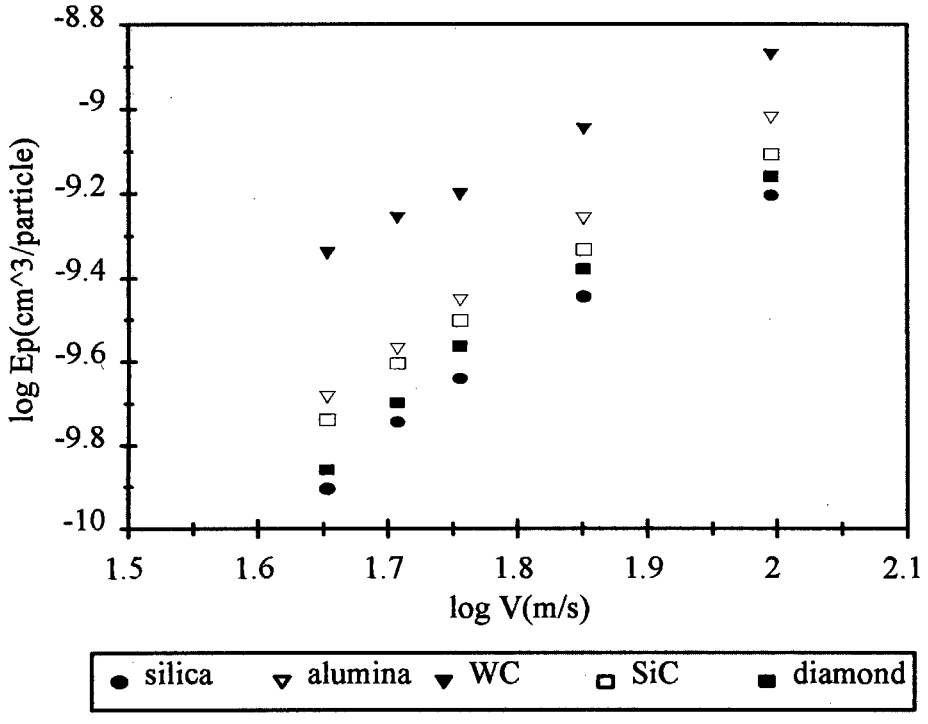

Figure 4. 48 Graph of erosion rate (Ep) of 304 stainless steel versus impingement velocity of indicated erodent particles (180-250 μm) at 30^0 incidence.

Table 4. 7 Variation of velocity exponent for 304 stainless steel with particle size at different angle impact

	alumina	SiC		
size(μm)	90°	90°	60°	30°
63-106	1.7 + 0.3	2.1+0.1	1.8+0.1	1.6+0.1
106-125	1.7 + 0.3	2.1+0.1	1.5+0.1	1.5+0.1
180-250	2.1 + 0.2	2.0+0.1	1.5+0.2	1.4+0.2
400-500	2.1 + 0.1	2.1+0.1	1.9+0.2	2.2+0.1
600-700	2.4 + 0.3	2.3+0.2	1.8+0.1	2.2+0.1
800-1000	2.2 + 0.2	2.1+0.1	2.0+0.1	2.1+0.1

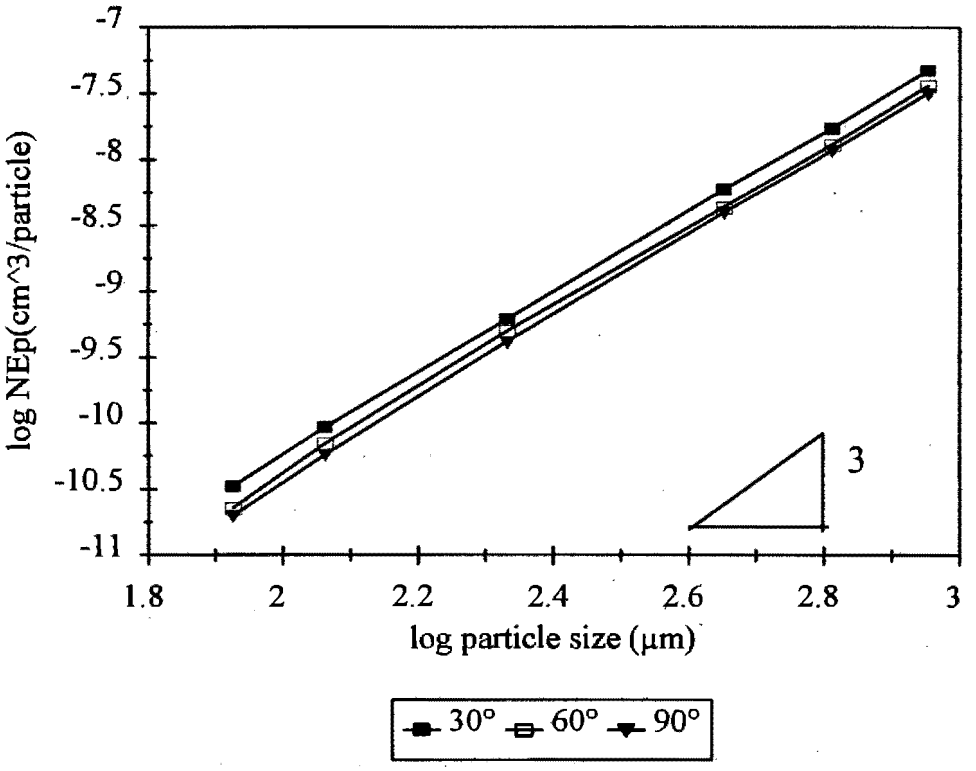

Figure 4. 49. Graph of erosion rate (Ep) of 304 stainless steel versus particle size of silicon carbide at different velocities.

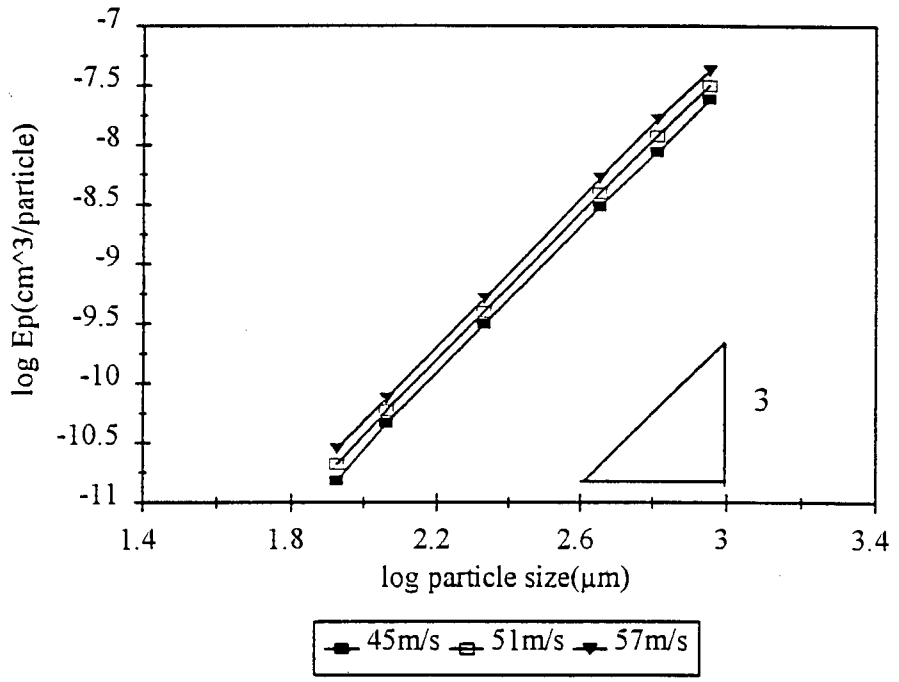

Figure 4. 50 Graph of erosion rate (Ep) of 304 stainless steel versus particle size of alumina erodents at different velocities.

4.2.2.2. The effect of impingement angle

The graph of erosion rate of 304 stainless steel versus impingement angles is shown in fig. 4.51. It shows that the higher erosion rate occurs at oblique angle.

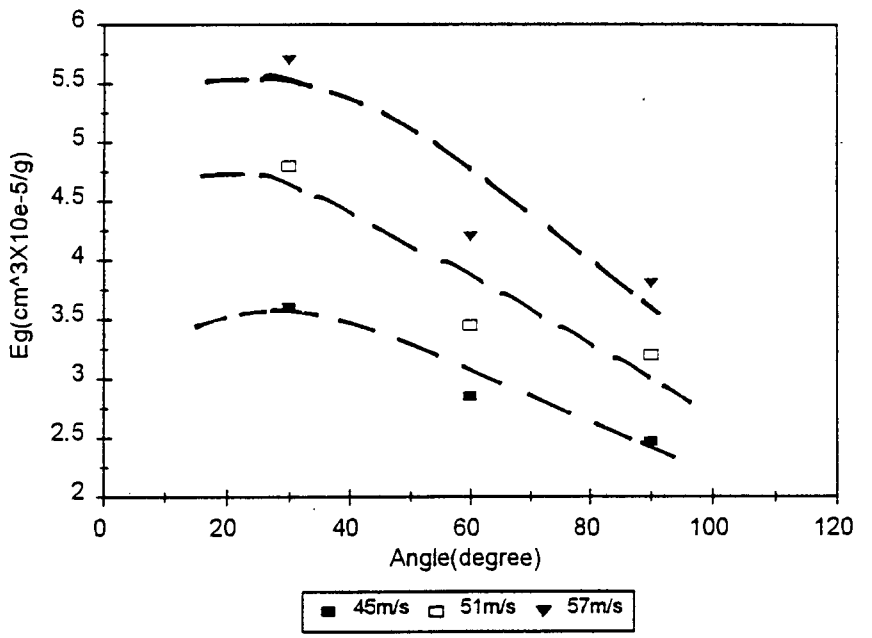

Figure 4. 51. Graph of erosion rate of 304 stainless steel as a function of impingement angle of SiC (180-250 μm) at the indicated velocities.

4.2.2.3. *The effect of erodent properties*

The bar graph of erosion rate of 304 stainless steel as a function of the ratio of hardness is shown in fig.4.52 for impingement angles of 90° and 30° incidence. The bar graph of erosion rate as a function of the ratio of toughness is shown in fig.4.53. It is noted that there is no correlation between the erosion rate and the hardness or toughness of erodents. The bar graph of erosion rate as a function of density of erodent is shown in fig. 4.54. It shows that the erosion rate increases with increasing density of erodent except diamond erodent. This means that the erosion rate is not only related to the density but also to the shape of erodents.

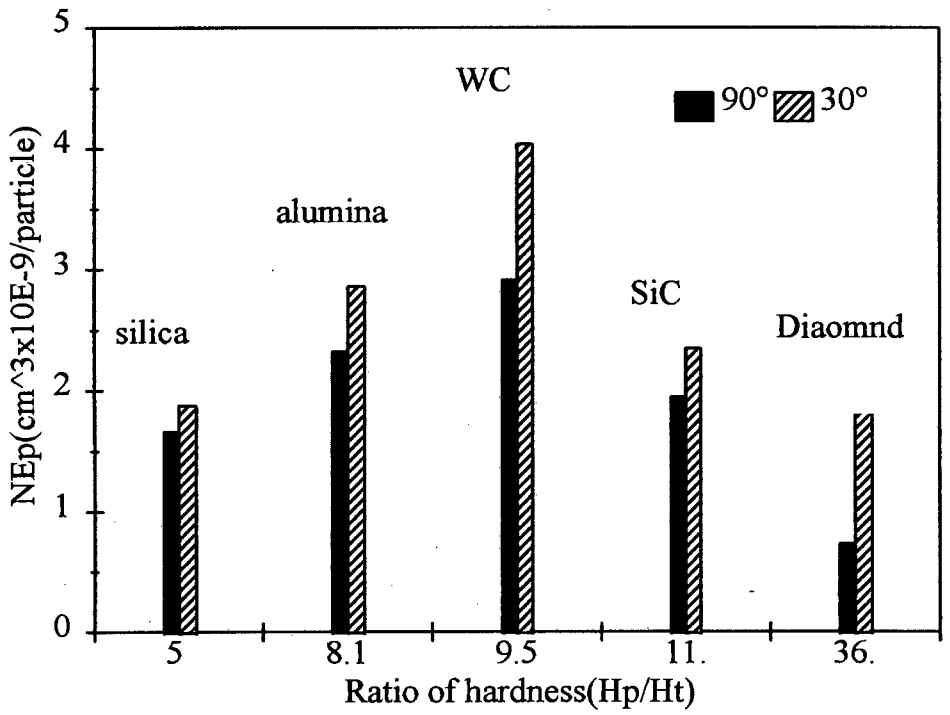

Figure 4. 52. Bar graph of erosion rate (Ep) of 304 stainless steel against ratio of hardness of erodents at a velocity of 99 m.s^{-1} and at impingement angles of 90° and 30° incidence.

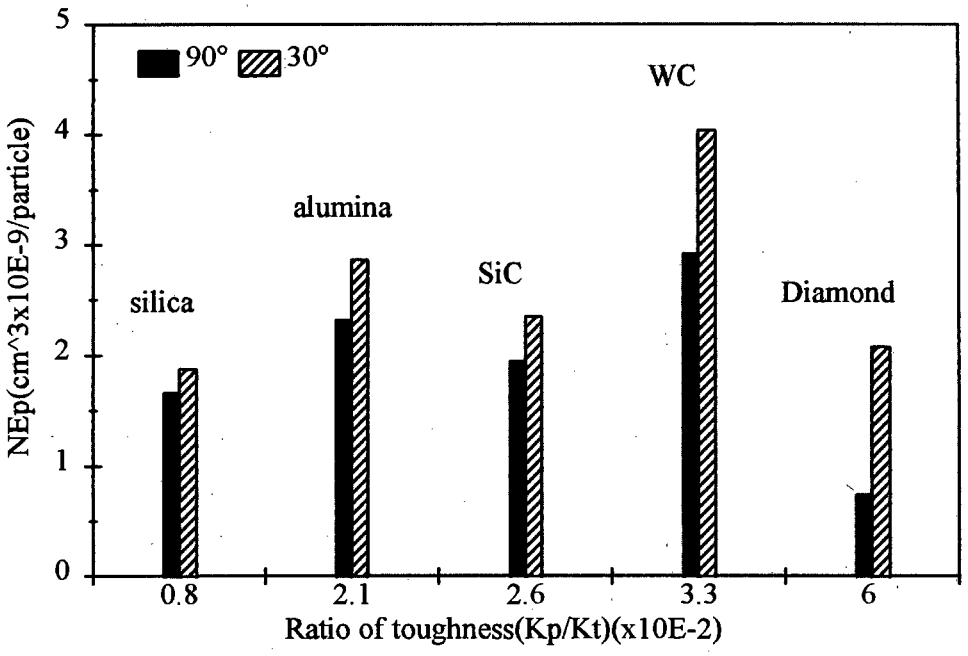

Figure 4. 53. Bar graph of erosion rate (Ep) of 304 stainless steel against ratio of toughness with a velocity of 99 m.s^{-1} and at impingement angles of 90° and 30° incidence.

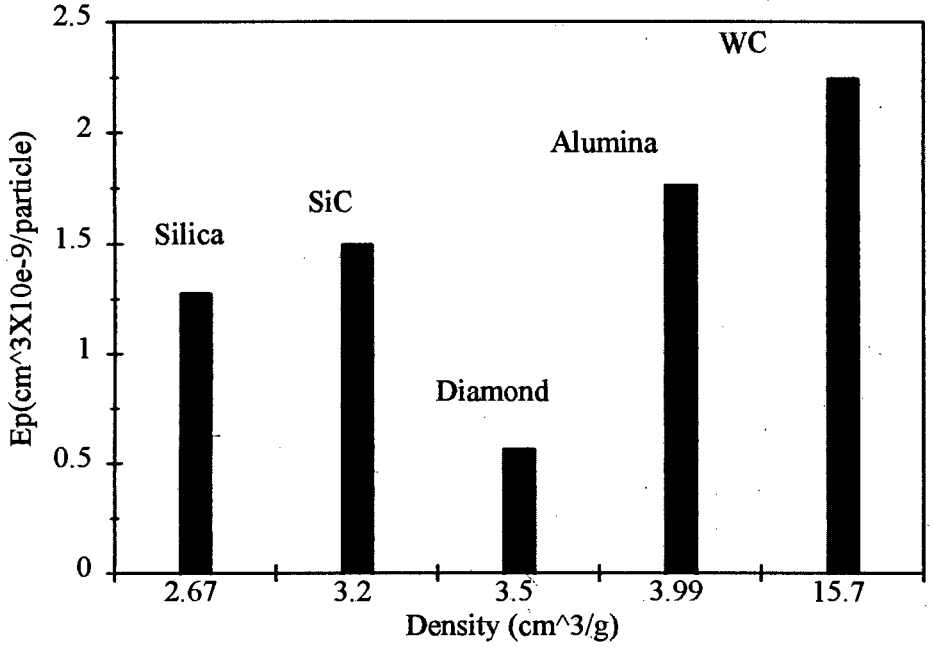

Figure 4. 54. Bar graph of erosion rate (Ep) of 304 stainless steel against density of erodent with a velocity of 99 m.s^{-1} and at an impingement angle of 90°.

4.2.3. Tungsten carbide – cobalt

4.2.3.1. Empirical correlation of erosion rate with particle velocity and size

Variation of the steady state erosion rate (Ep) of WC-7%Co with velocity of different erodents (180-250 μm) at an impingement angle of 90° incidence is shown in fig. 4.55. It shows that the WC-7% Co exhibits the highest erosion rate for diamond erodents and the lowest rate for silica erodents. The value of velocity exponent derived from fig. 4.55 is 1.1 ± 0.2, 1.5 ± 0.2, 1.6 ± 0.1, 1.9 ± 0.2 and 1.9 ± 0.1 for silica, alumina, WC, SiC and diamond erodents respectively. Fig. 4.56 shows the graph of erosion rate (Ep) as a function of particle size of SiC particles. The erosion rate increased with increasing particle size. The value of size exponent for erosion per particle is nearly 3.0 over all the ranges of velocities.

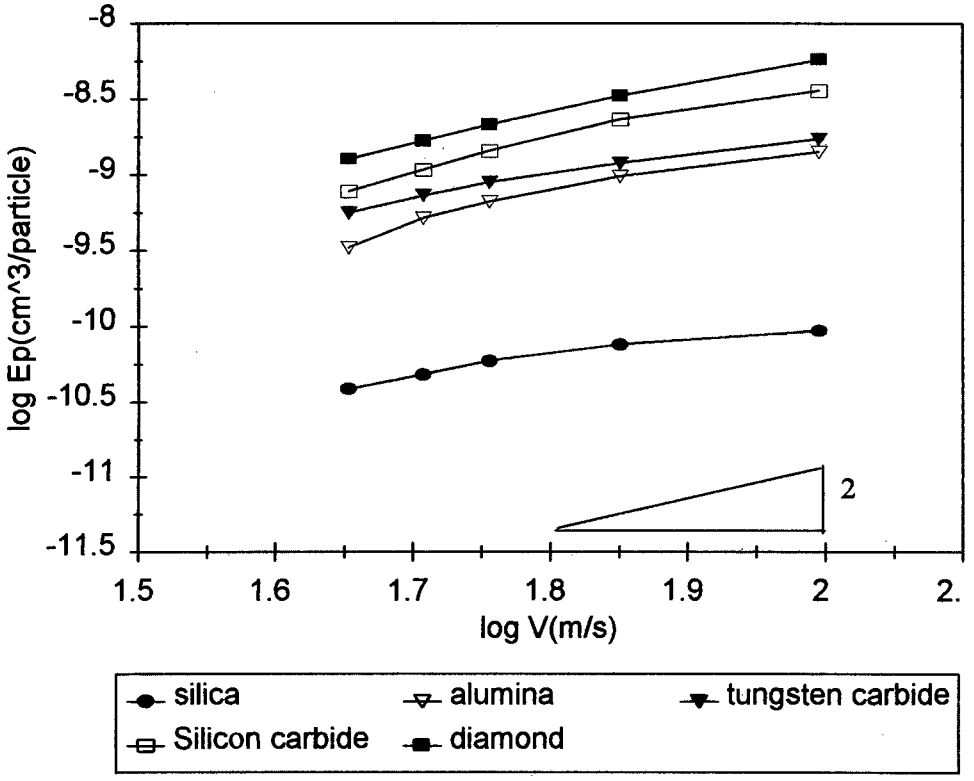

Figure 4. 55. Graph of erosion rate (Ep) of WC-7%Co against impingement velocity of indicated erodent particles (180-250 μm) at 90^0 incidence.

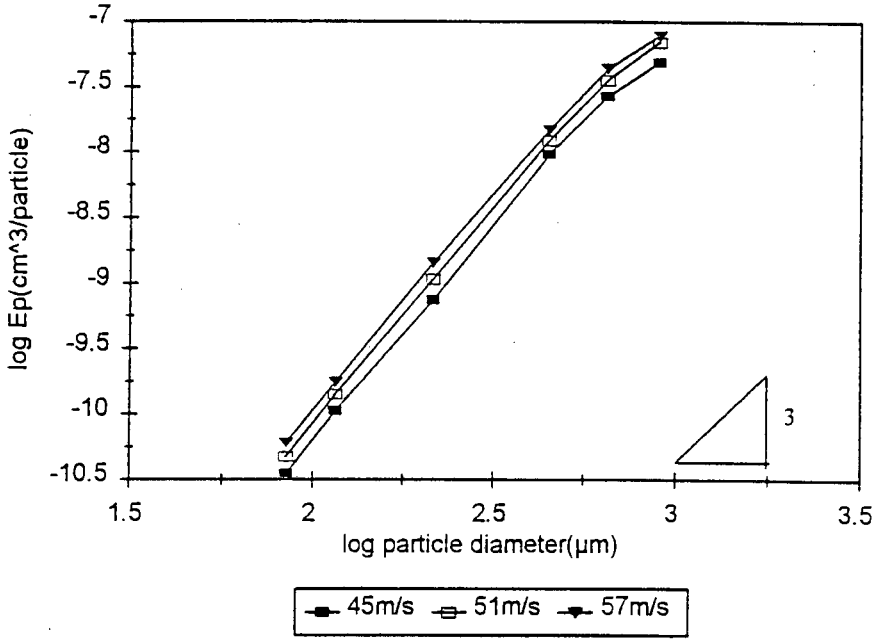

Figure 4. 56. Graph of erosion rate (Ep) of WC-7%Co as a function of particle size of SiC with indicated velocity at 90° incidence.

4.2.3.2. The effect of impingement angle

The effect of impingement angle on the erosion of the WC-7%Co was investigated for SiC erodent particles impacting at 30°, 60° and 90° respectively. Fig.4.57 shows the graph of the erosion rate as a function of impingement angle. It is noted that a maximum erosion rate occurs at an impingement angle of 90°.

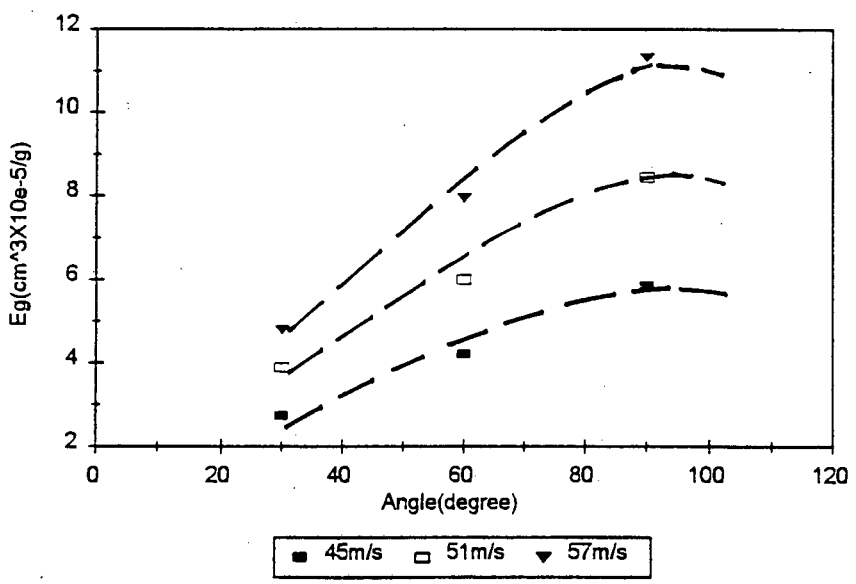

***Figure* 4. 57. Graph of erosion rate (Eg) of WC-7%Co as a function of impingement angle of SiC erodent particles (180-250 μm) with indicated velocity.**

4.2.3.3. The effect of erodent properties

The bar graphs of erosion rate as a function of the ratio of hardness and toughness are shown in figs. 4.58 and 4.59 respectively. It is noted that erosion rate (Ep) increases with increasing the hardness of erodents. There is no direct relationship between the toughness of erodents and the erosion rate. In addition, the erosion rate is not directly related to the density of erodent as shown in fig. 4.60

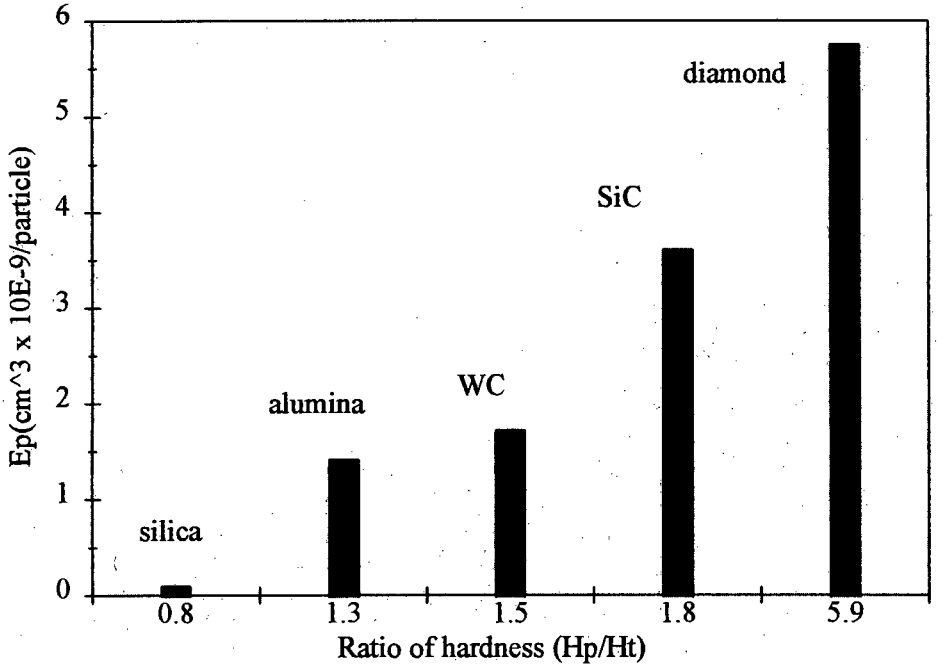

Figure 4. 58. Bar graph of erosion rate (Ep) of WC-7%Co as a function of the ratio of hardness (Hp/Ht) at an impingement angle of 90^0

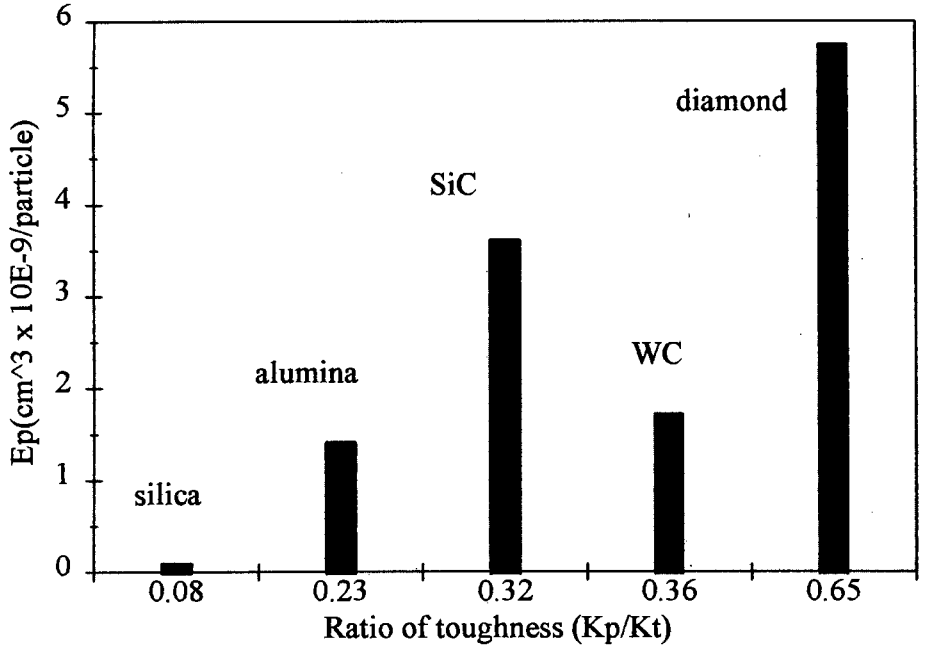

Figure 4. 59. Bar graph of erosion rate (Ep) of WC-7%Co as a function of the ratio of toughness (Kp/Kt) at an impingement angle of 90^0.

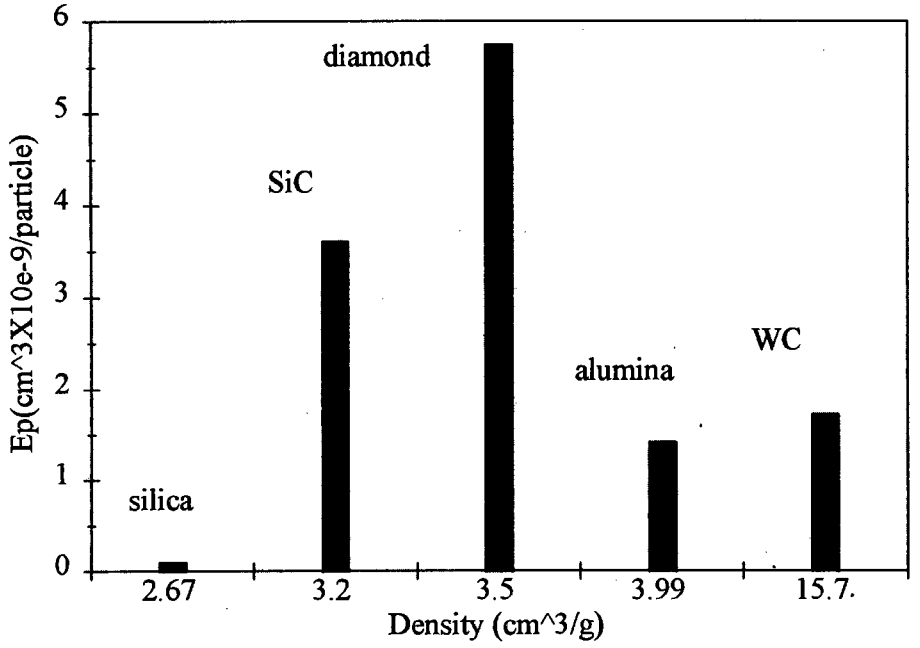

Figure 4. 60. Bar graph of erosion rate (Ep) of WC-7%Co as a function of the density of erodent at an impingement angle of 90° and at a velocity of 99m.s^{-1}.

4.2.4. Alumina

4.2.4.1. Empirical correlation of erosion rate with particle velocity and size

The dependence of erosion rate per particle (Ep) on velocity for alumina eroded by different erodents at 90° incidence is shown in fig. 4.61. It is noted that the erosion rate increases with increasing impingement velocity. The erosion rate of alumina eroded by diamond is the highest, followed by tungsten carbide, silicon carbide, alumina and silica. Velocity exponents presented in Table 4.8 were obtained from plotting logarithmically the erosion rate against particle velocity for different erodents with various particle sizes. It is noted that the velocity exponents increase with increasing particle size up to 400-500 μm in diameter and then decrease with further increasing particle size.

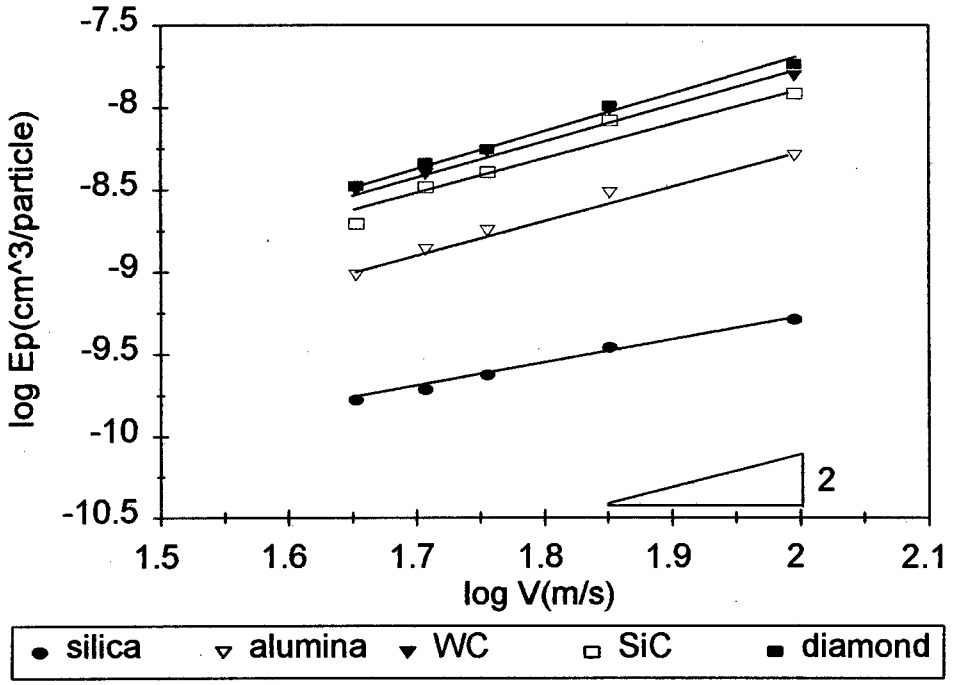

Figure 4. 61. Graph of erosion rate (Ep) of alumina vs impingement velocity of the indicated erodents (180-250μm) at 90° incidence.

Table 4. 8. Variation of velocity exponent with particle size at 90^0 incidence for alumina

size(μm)	silica	alumina	WC	SiC	diamond
106-125	1.0± 0.1	1.6± 0.1		1.8±0.1	2.0 ± 0.1
151					2.1 ± 0.1
181					2.1 ± 0.1
180-250	1.5± 0.1	2.1± 0.2	2.1 ± 0.1	2.2±0.2	
400-500	1.8± 0.3	2.5± 0.2		2.8±0.1	
600-700	1.6± 0.3	2.4 ± 0.1		2.5±0.1	
800-1000	1.4± 0.3	2.4 ± 0.1		2.2±0.1	

The variation of erosion rate (Ep) with particle size for different erodents is shown in fig. 4.62 in log-log scale. The erosion rate increases with increasing particle size. The alumina impacted with silica particles shows a significantly different erosion dependency on particle size compared with the alumina target impacted with the other particles. A slope of straight line (particle size exponent) is nearly 3.0 for silica erodents and nearly 4.0 for the other erodents. The variation of size exponent with velocity at 90° incidence for alumina target is shown in Table 4.9. It appears that the particle size exponents decrease with decreasing the hardness and toughness of erodents.

The empirical particle size-velocity relationships for erosion rate (Ep) are detailed below.

For silica: $Ep \propto V^{1.5} D^{2.6}$ (4.7)

For alumina: $Ep \propto V^{2.2} D^{3.7}$ (4.8)

For SiC: $Ep \propto V^{2.2} D^{3.9}$ (4.9)

For diamond: $Ep \propto V^{2.1} D^{4.0}$ (4.10)

It appears that the particle size exponents decrease with decreasing the hardness and toughness of erodents.

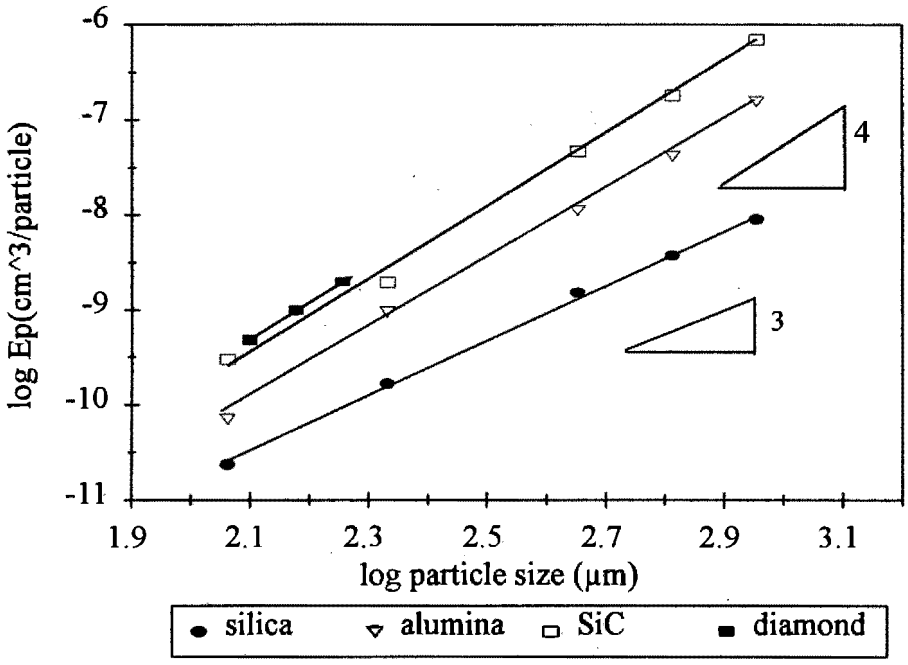

Figure 4. 62. Graph of erosion rate (Ep) of alumina vs particle size at a velocity of 45 $m.s^{-1}$ and at an impingement angle of 90°.

Table 4. 9. Variation of size exponent with velocity at 90^0 incidence for alumina

velocity($m.s^{-1}$)	SiO_2	Al_2O_3	SiC	Diamond
33	2.8±0.1	3.7±0.1	4.1±0.1	
39	2.6±0.2	3.9±0.1	3.9±0.1	
45	2.6±0.1	3.7±0.1	3.6±0.2	3.9±0.0
51	2.7±0.2	3.7±0.1	3.7±0.1	4.0 ±0.3
57	2.5±0.1	3.6±0.1	3.7±0.1	4.1±0.3
71				4.4 ±0.5
99				3.9±0.2

4.2.4.2. *The effect of impingement angle*

Fig. 4.63 shows the graph of the erosion rate versus impingement angle for alumina eroded by silicon carbide. It shows that maximum erosion rate occurs at around an impingement angle of 90°.

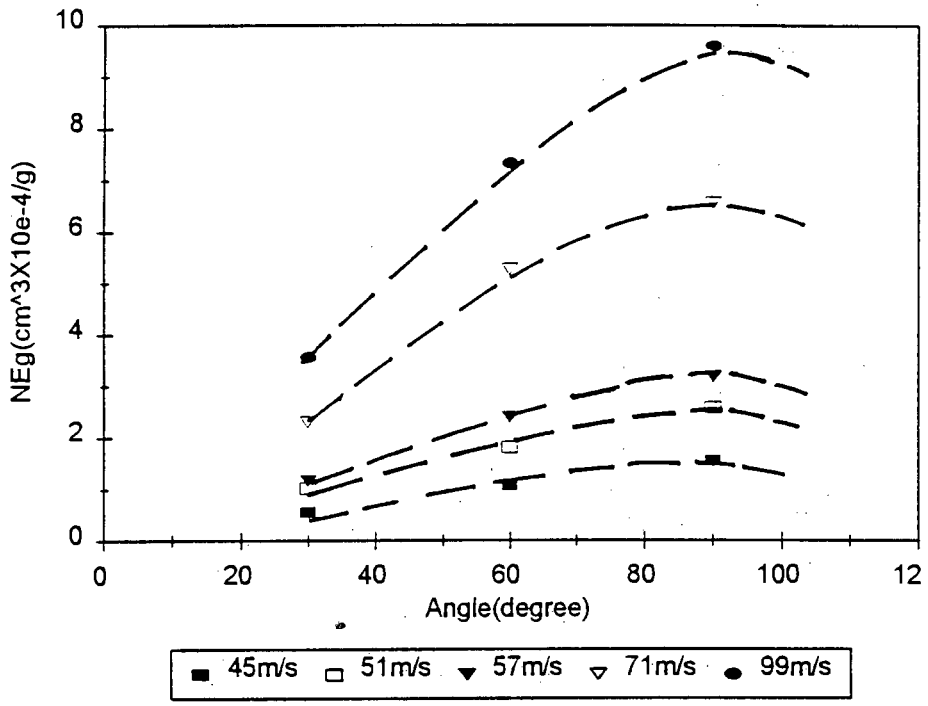

Figure 4. 63. Graph of erosion rate (Eg) of alumina as a function of impingement angle of SiC erodent particles(180-250μm) with indicated velocity.

4.2.4.3. *The effect of erodent properties*

The bar graphs of erosion rate as a function of the ratio of hardness and toughness are shown in figs. 4.64 and 4.65 respectively. There is no direct relationship between the hardness of erodents and the erosion rate (Ep). However, there is an increase in erosion rate (Ep) with increasing the toughness of erodents as shown in fig. 4.65. There is no direct relationship between erosion rate and density of erodent as shown in fig. 4.66.

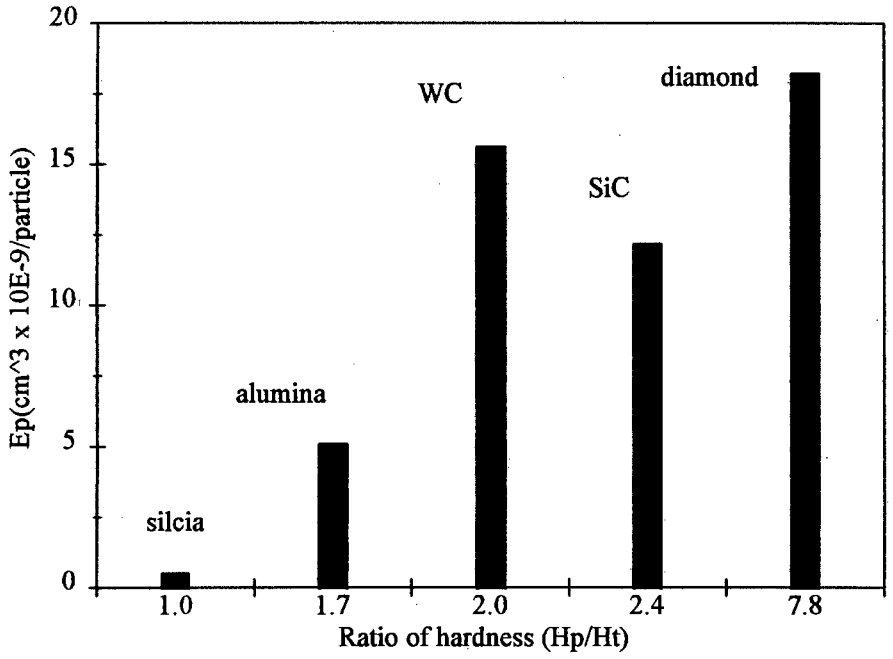

Figure 4. 64. Bar graph of erosion rate (Ep) of alumina against ratio of hardness of erodent to target for erodent particles (180-250 μm) with a velocity of 99 m.s^{-1} and at an impingement angle of 90^0.

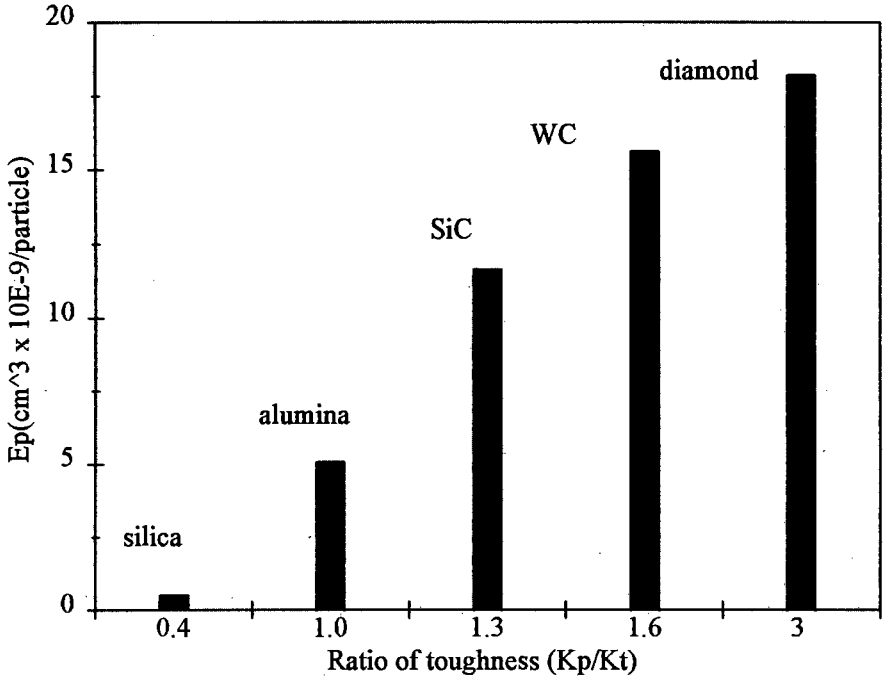

Figure 4. 65. Bar graph of erosion rate (Ep) of alumina against ratio of toughness of erodent to target for erodent particles (180-250 μm) with a velocity of 99 m.s^{-1} and at an impingement angle of 90^0

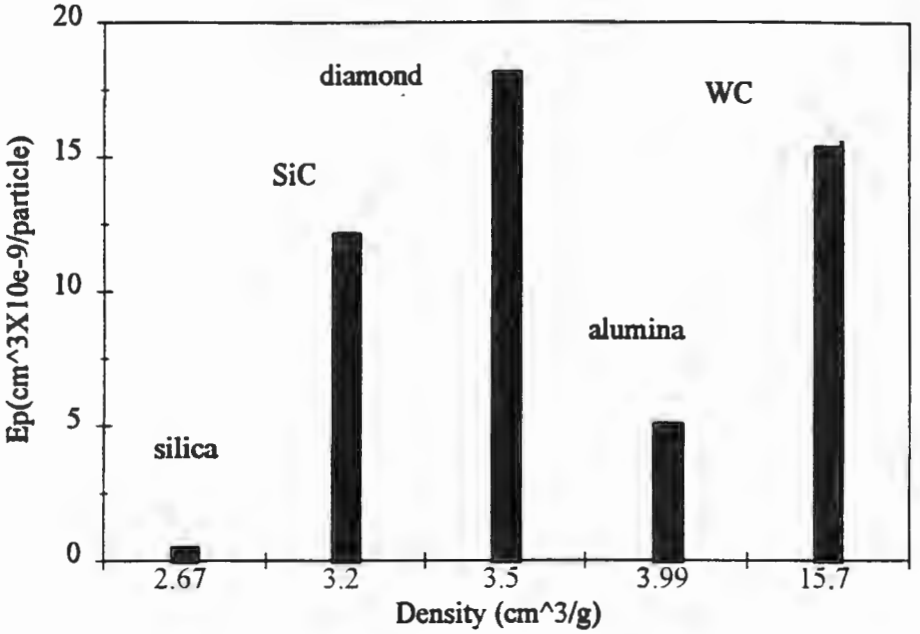

Figure 4. 66. Bar graph of erosion rate (Ep) of alumina against density of erodent(180-250μm) with a velocity of 99 m.s^{-1} and at an impingement angle of 90°

4.3. SCANNING ELECTRON MICROGRAPHS

4.3.1. As received glass impacted by steel shot

4.3.1.1. Steady state eroded surface

The morphology of the eroded surface by steel shot at 90^0 is shown in fig. 4.67. The eroded surfaces exhibit the formation and interaction of Hertzian cracks.

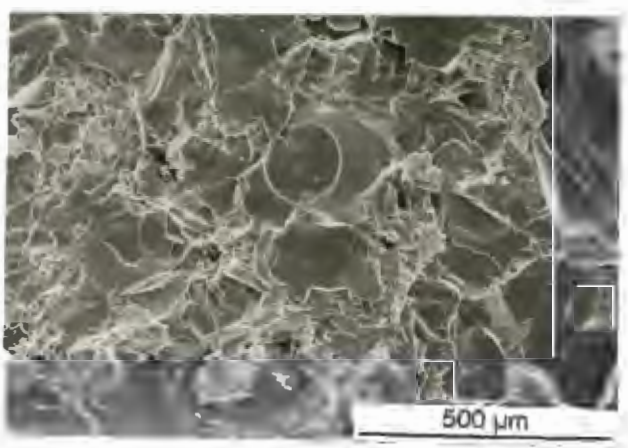

Figure 4. 67 S.E.M. images of eroded surface produced on as received glass using steel shots (400-500 μm) at an average particle velocity of 45 m.s^{-1} and at 90° impact, Hertzian cracks are observed as the dominant mode of erosion

4.3.2. As received glass impacted by glass beads

4.3.2.1. Single impact site examination

The morphology of the eroded surface by a single particle with different angles of impact is shown in figs. 4.68 to 4.70. There exists a particle size effect. With small particle impact, the formation of radial cracks shown in fig. 4.68(a) is associated with the impact at 90^0 incidence at an impingement velocity of 71 $m.s^{-1}$. With further increasing velocity (99 $m.s^{-1}$) crushed region is in the centre of impact site from which lateral cracks emanate as shown in fig. 4.69(a). The evidence of plastic impression or particle debris is noted at 30^0 angle as shown in figs. 4.68(b) and 4.69(b). For particles above or equivalent to the size range of 400-500 μm, Hertzian cracks can be observed for 90^0 incidence as shown in fig. 4.70(a). At 30^0 incidence, Hertzian cracks and smear scar along the direction of impact angle are noted as shown in fig. 4.70(b).

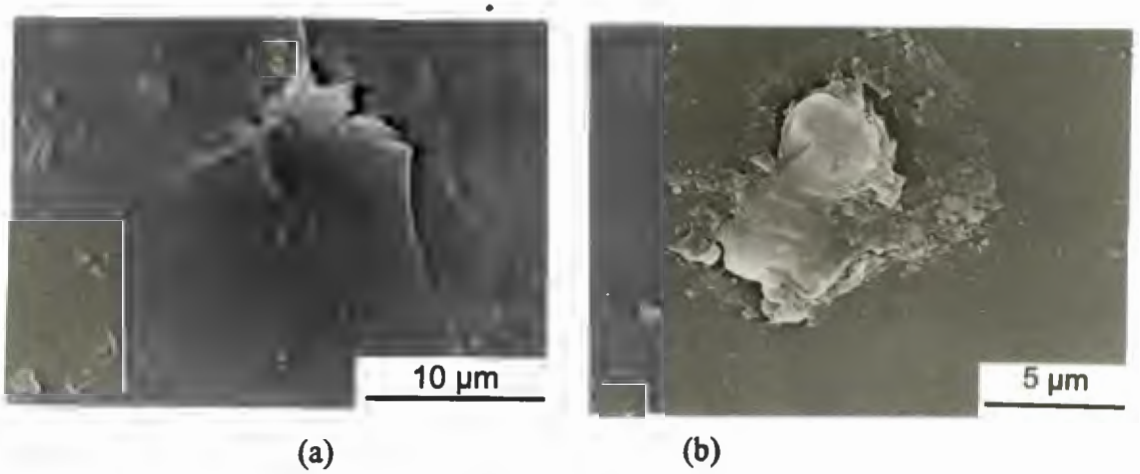

Figure 4. 68 S.E.M. images of single impact sites produced on as received glass using glass beads (106-125 μm) and at an average particle velocity of 71 $m.s^{-1}$ (a) At 90^0 impact, radial cracks emanate from the impact site. (b) At 30^0 impact, fracture surfaces are produced by plastic impression.

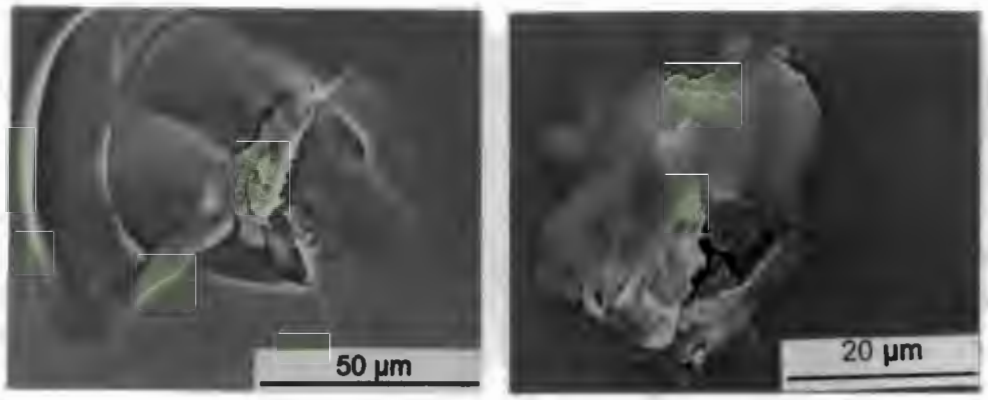

(a) (b)

Figure 4. 69 S.E.M. images of single impact sites produced on as received glass using glass beads (106-125 µm) and at an average particle velocity of 99 m.s^{-1} (a) At 90^0 impact, saucer-shaped fracture surfaces are produced by lateral cracking (b) At 30^0 impact, fracture surfaces are produced by inelastic crushing.

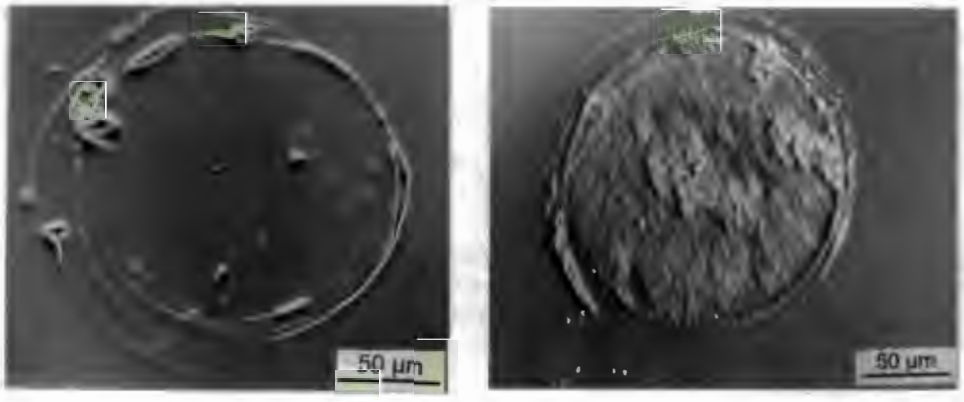

(a) (b)

Figure 4. 70. S.E.M. images of single impact sites produced on as received glass using glass beads (400-500 µm) and at an average particle velocity of 57 m.s^{-1}. (a) At 90^0 impact, Hertzian cracks occur. (b) At 30^0 impact, Hertzian crack and smear scar along the direction of impact is noted.

4.3.2.2. Steady state eroded surface examination

The steady state eroded surfaces of as received glass with six sizes of glass beads at an impingement angle of 90^0 are shown in figs. 4.71 to 4.76. With glass beads below 180-250 μm and impacting at 57 $m.s^{-1}$ and at 90^0 incidence, the material removal involved no fractures associated with Hertzian cone cracks and lateral cracks. All impact sites are plastically deformed as shown in figs. 4.71(a) and 72(a). With an average velocity of 71 $m.s^{-1}$ impact, the evidence of inelastic deformation and lateral cracks is noted as shown in fig. 4.72(b). With further increasing impingement velocity up to 99$m.s^{-1}$ the material removal is associated with lateral cracks as shown in fig. 4.72(c).

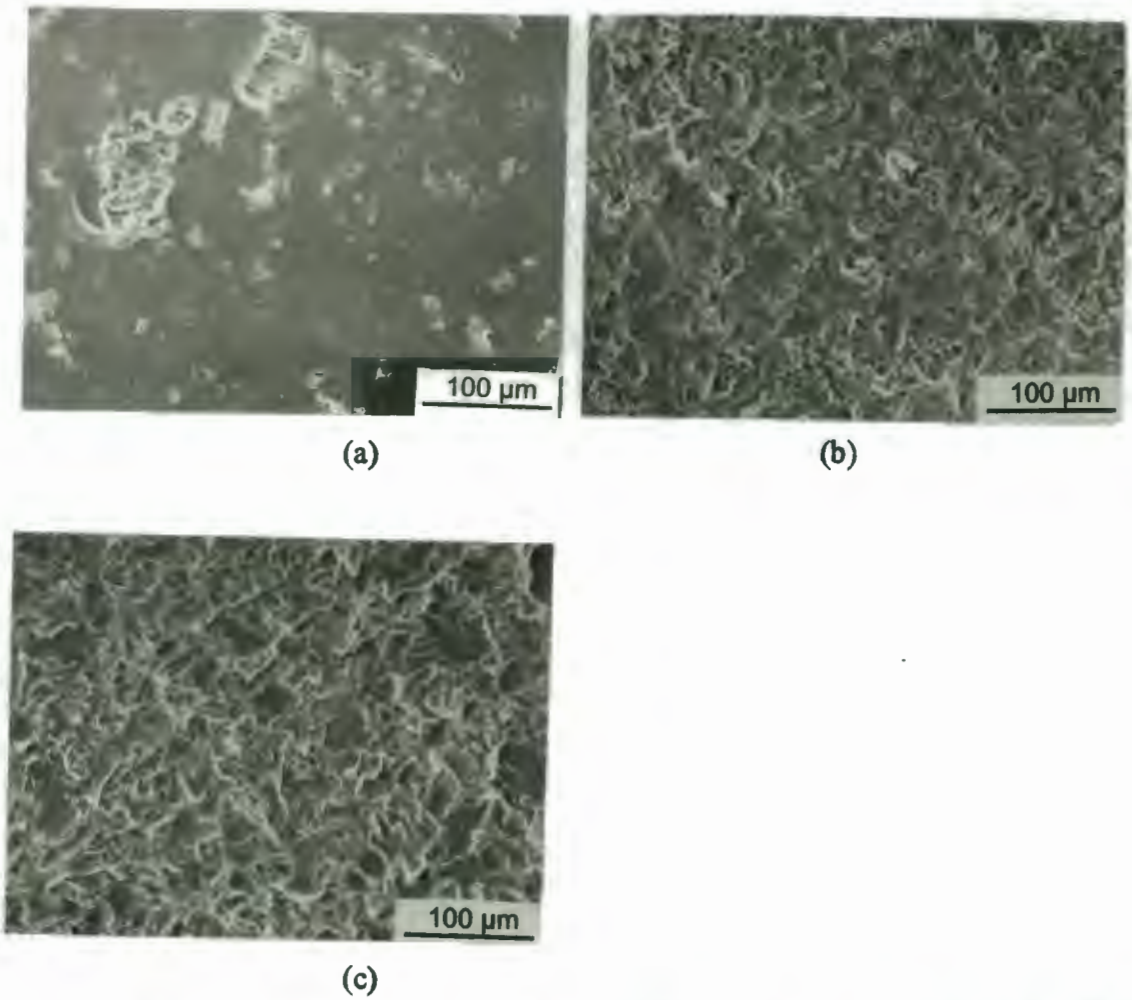

(a) (b)

(c)

Figure 4. 71 S.E.M. images of the steady state eroded surfaces of as received glass after erosion with glass beads (63-106μm) at 90^0 incidence. (a) Erodent mass of 30g with a velocity of 57 $m.s^{-1}$, fracture surfaces are produced by accumulated inelastic deformation. (b) Erodent mass of 30g with a velocity of 71 $m.s^{-1}$, (c) Erodent mass of 30 g with a velocity of 99 $m.s^{-1}$, fracture surfaces (c) are associated with inelastic deformation and the lateral cracks.

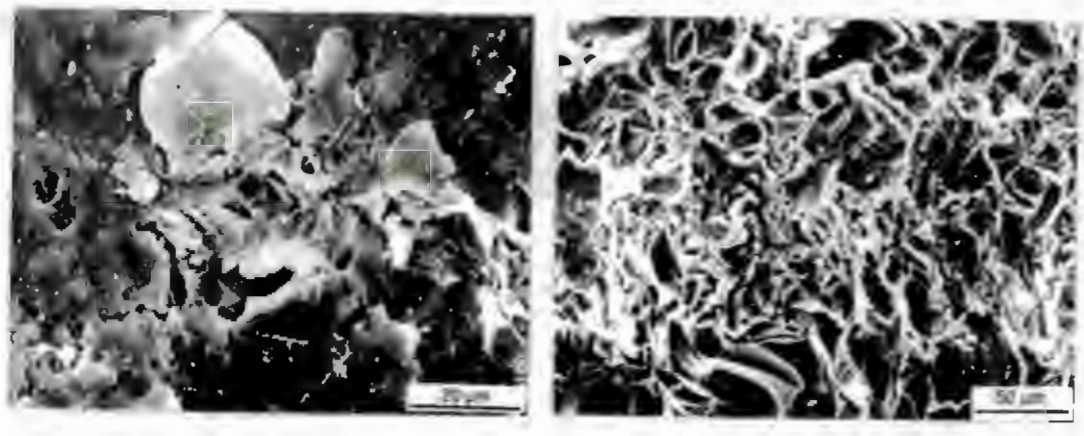

(a) (b)

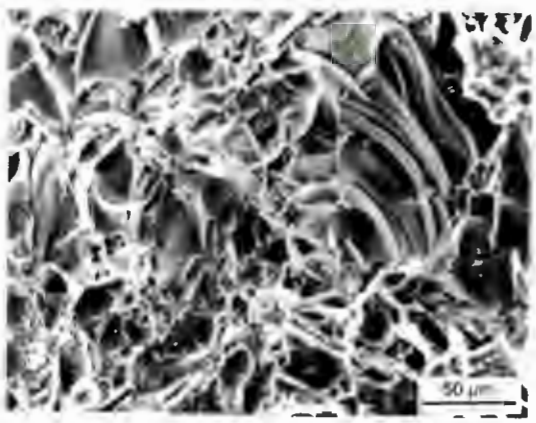

(c)

Figure 4. 72 S.E.M. images of the steady state eroded surfaces of as received glass after erosion with glass beads (106-125 μm) at 90^0 incidence. (a) Erodent mass of 30g with a velocity of 57 $m.s^{-1}$, fracture surfaces are produced by accumulated inelastic deformation (b) Erodent mass of 30g with a velocity of 71 $m.s^{-1}$, fracture surfaces are produced by lateral cracking and plastic deformation (c) Erodent mass of 30 g with a velocity of 99 $m.s^{-1}$, fracture surfaces are associated with the interaction of lateral cracks

With glass beads in the size range of 180-250 μm, the evidence of interaction of lateral cracks is noted for both 51 $m.s^{-1}$ and 99 $m.s^{-1}$ impact as shown in fig. 4.73. With glass beads above or in the size range of 400-500 μm, material removal is associated with the formation and interaction of Hertzian cone cracks over velocities ranging from 33 $m.s^{-1}$ to 57 $m.s^{-1}$ as shown in figs. 4.74, 4.75, and 4.76.

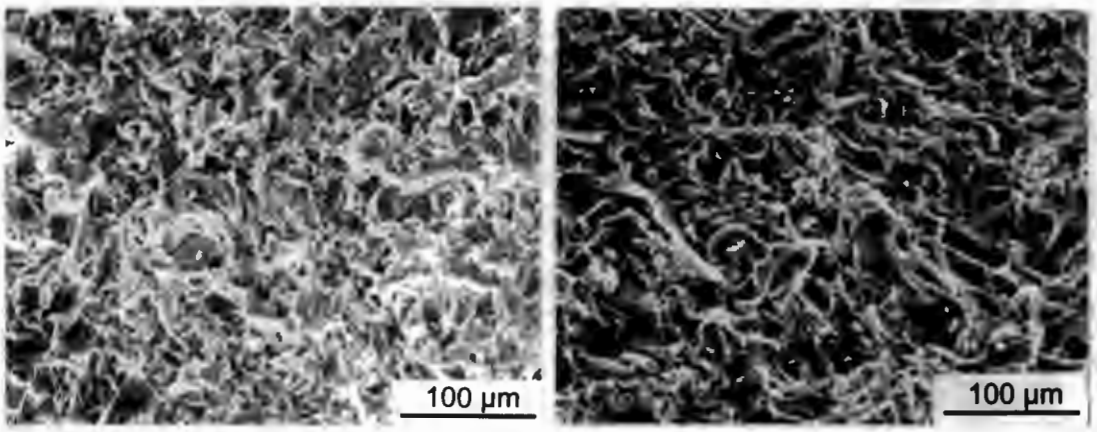

(a) (b)

Figure 4. 73. S.E.M. images of the steady state eroded surfaces of as received glass after erosion with glass beads (180-250 µm) at 90^0 incidence. (a) Erodent mass of 30g with a velocity of 51 $m.s^{-1}$ (b) Erodent mass of 30 g with a velocity of 99 $m.s^{-1}$. All damage patterns are associated with the interaction of lateral cracks.

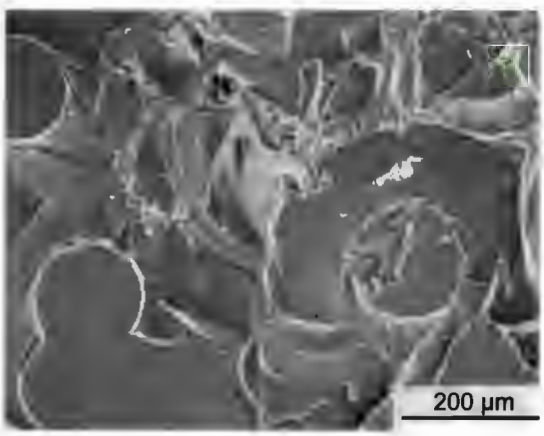

(a)

Figure 4. 74 S.E.M. images of the steady state eroded surfaces of as received glass after erosion with glass beads (400-500 µm) at 90^0 incidence. (a) Erodent mass of 1g with a velocity of 57 $m.s^{-1}$. The damage pattern shows the formation and interaction of Hertzian cracks.

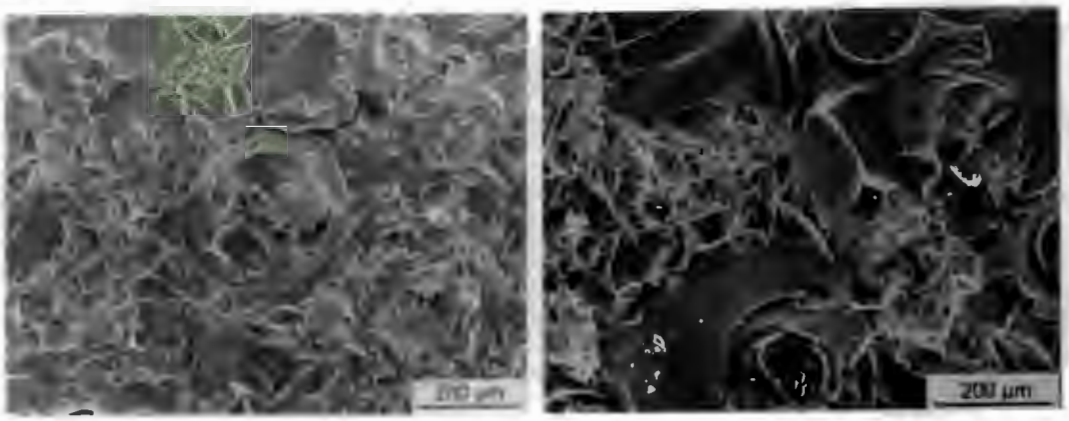

(a) (b)

Figure 4. 75 S.E.M. images of the steady state eroded surfaces of as received glass after erosion with glass beads (600-700 µm) at 90^0 incidence. (a) Erodent mass of 2g with a velocity of 33 m.s^{-1}. (b) Erodent mass of 2 g with a velocity of 57 m.s^{-1}. Note that the damage patterns are associated with the formation and interaction of Hertzian cracks

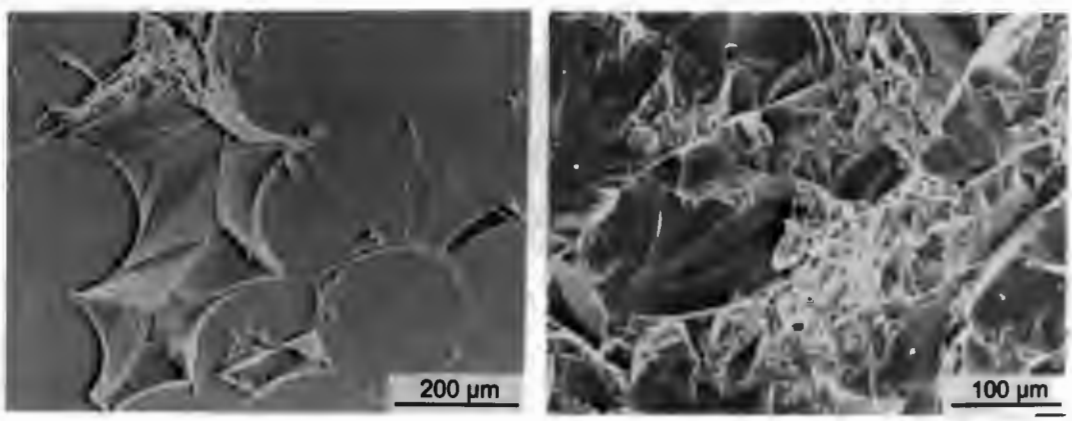

(a) (b)

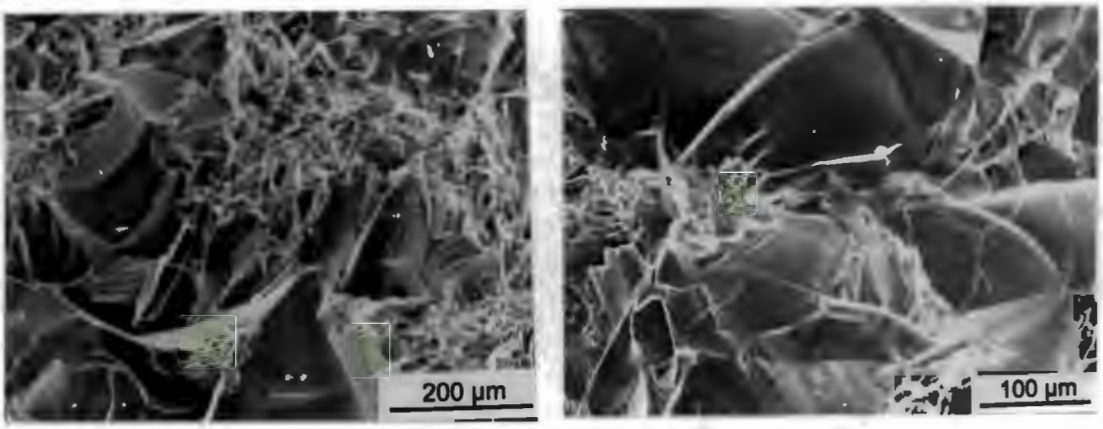

(c) (d)

Figure 4. 76 S.E.M. images of the steady state eroded surfaces of as received glass after erosion with glass beads (800-1000 µm) at 90⁰ incidence. (a) Erodent mass of 2g with a velocity of 33 m.s^{-1} (b) Erodent mass of 20g with a velocity of 33 m.s^{-1} (c) Erodent mass of 1 g with a velocity of 57 m.s^{-1} (d) Erodent mass of 20 g with a velocity of 57 m.s^{-1}. Note that Hertzian cracks occur at both velocities of 33 m.s^{-1} and 57 m.s^{-1}. Material removal is associated with the formation and interaction of Hertzian cone cracks

4.3.3. As received glass impacted by silica erodents

4.3.3.1. Single impact site examination

Single impact sites produced by 90⁰ impact of silica on glass exhibit a crushed region in the centre of the impact site from which radial and lateral cracks emanate as shown in fig. 4.77 (a). The shape of the damage zone for 30⁰ impact angles is in one direction relative to the impact site as shown in fig. 4.77(b). This observation indicates that the direction and extent of the crack propagation from the crack initiation site is dependent on the impact angle. The scale of damage pattern at oblique impact is smaller than that of the pattern at normal angle.

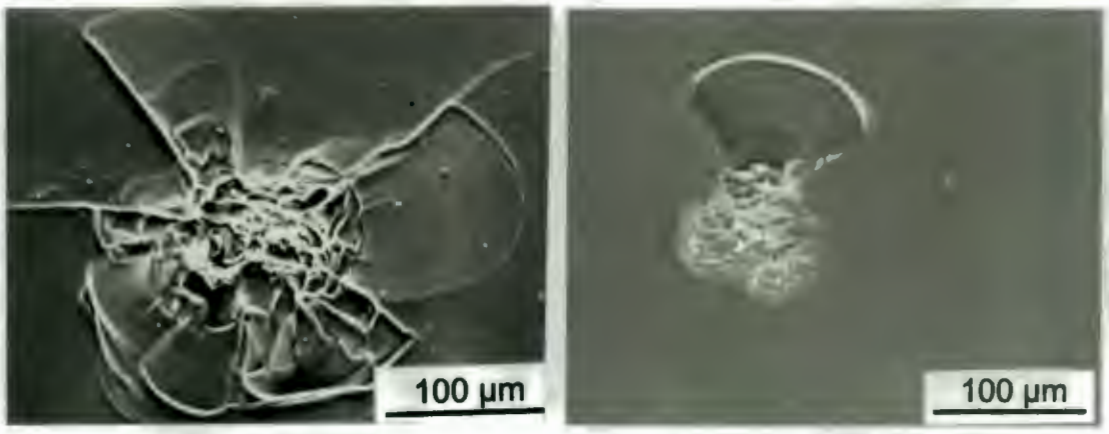

(a) (b)

Figure 4. 77 S.E.M. images of single impact sites produced on as received glass using silica erodents (400-500 µm) and at an average particle velocity of 57 m.s^{-1}. (a) At 90^0 impact, saucer-shaped fracture surfaces are produced by extensive lateral cracking. (b) At 30^0 impact, cracks emanate from the one direction relative to the impact site.

4.3.3.2. Steady state eroded surface examination

The steady state eroded surfaces of as received glass with silica erodents impacting (106-125µm) at an average particle velocity of 99 m.s^{-1} are shown in fig. 4.78 for impingement angles of 30^0 and 90^0. It is noted that the evidence of lateral cracks controlled fracture processes where multiple impacts are needed to produce lateral crack events.

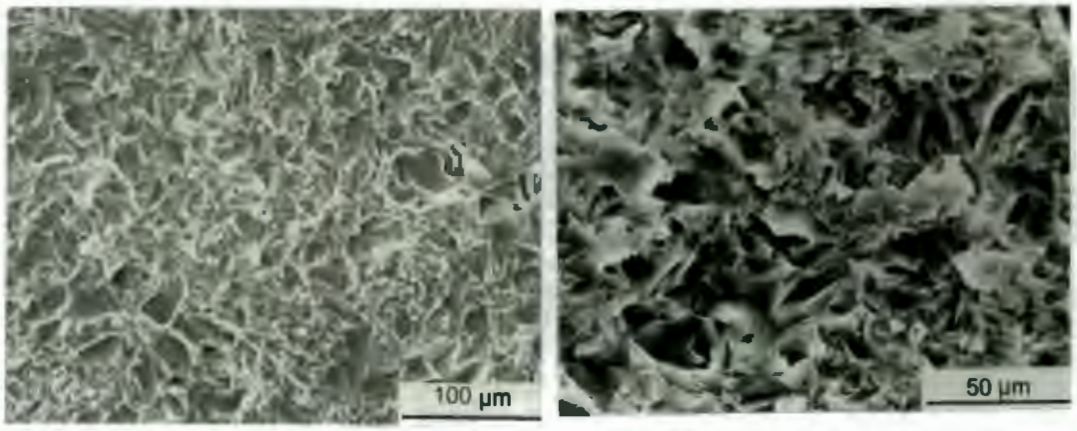

(a) (b)

Figure 4. 78 S.E.M. images of the steady state eroded surface of as received glass after erosion with silica erodents (106-125 µm) at an average particle velocity of 99 m.s^{-1} for (a) 90^0 and (b) 30^0 incidence angle. The fracture surfaces are produced by extensive interaction of lateral cracking for both angles.

4.3.4. As received glass impacted by alumina erodents

4.3.4.1. Single impact site examination

The micrograph of the eroded surface by a single alumina particle is shown in fig. 4.79 for impingement angles of 90^0 and 30^0. The fracture patterns indicate that lateral fracture originates from the boundary of the central crushed material. The scale of the damage pattern at 30^0 incidence is smaller than that of the pattern at 90^0 incidence.

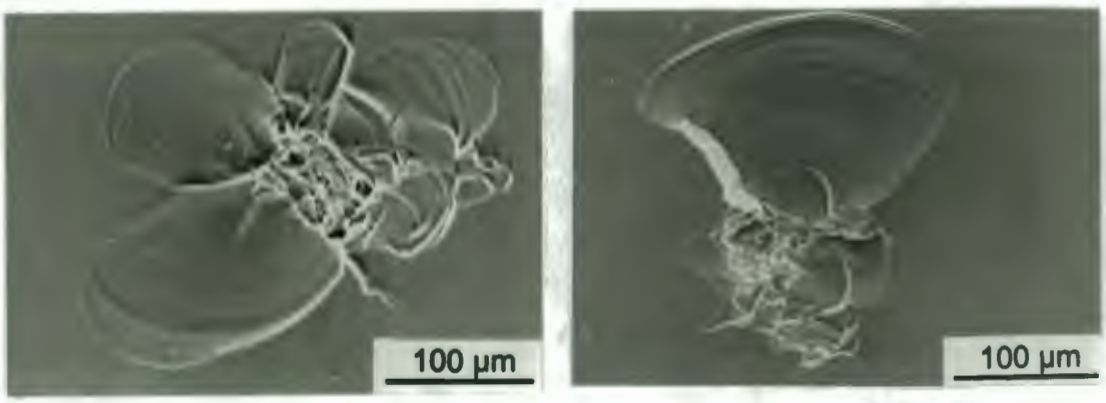

(a) (b)

Figure 4. 79 S.E.M. images of single impact sites produced on as received glass using alumina erodents (400-500 µm) and at an average particle velocity of 57 $m.s^{-1}$. (a) At 90^0 impact, cracks emanate from the central crushed zone. (b) At 30^0 impact, cracks emanate from the impact site.

4.3.4.2. Steady state eroded surface examination

The steady state eroded surfaces of as received glass with alumina erodents impacting (106-125 µm) at an average particle velocity of 99 $m.s^{-1}$ are shown in fig. 4.80 for impingement angles of 90^0 and 30^0. It is noted that the material removal is associated with the formation and interaction of lateral cracks.

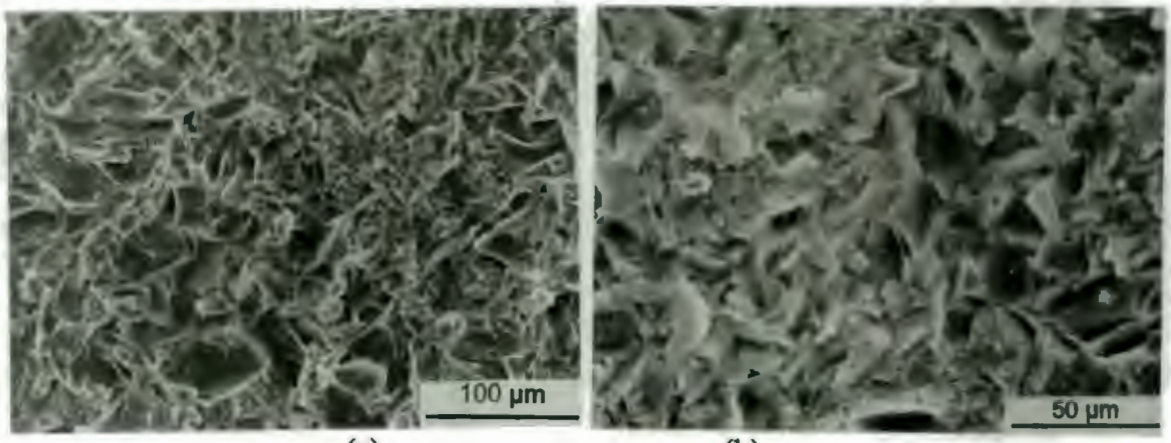

(a) (b)

Figure 4. 80 S.E.M. images of the steady state eroded surface of as received glass after erosion with alumina erodents (106-125 µm) at an average particle velocity of 99 m.s^{-1} for (a) 90^0 and (b) 30^0 incidence angle. The fracture surfaces are produced by extensive interaction of lateral cracking for both impingement angles.

4.3.5. As received glass impacted by tungsten carbide erodent particles

4.3.5.1. Single impact site examination

The micrographs of the eroded surface by a single WC particle are shown in fig. 4.81 for impingement angles of 90^0 and 30^0. It is noted that complete lateral cracks occur at 90^0 incidence impact. At 30^0 impact, the lateral cracks propagate along the direction of impact. The scale of the damage pattern at 30^0 incidence is smaller than that of the pattern at 90^0 incidence.

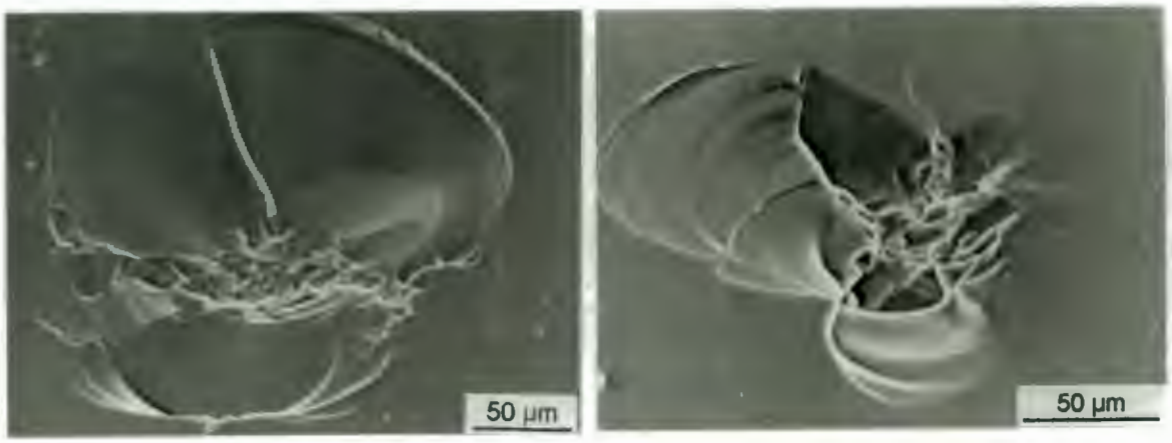

(a) (b)

Figure 4. 81 S.E.M. images of single impact sites produced on as received glass using tungsten carbide erodents (212 µm) and at an average particle velocity of 99 m.s^{-1}. (a) At 90^0 impact, cracks emanate from the central crushed zone. (b) At 30^0 impact, cracks emanate from one direction of impact site.

4.3.5.2. Steady state eroded surface examination

The steady state eroded surfaces of as received glass with tungsten carbide erodents impacting (212 μm) at an average particle velocity of 99 $m.s^{-1}$ are shown in fig. 4.82 for impingement angles of 90^0 and 30^0. The impact sites are produced by the formation and interaction of lateral cracks for both impingement angles.

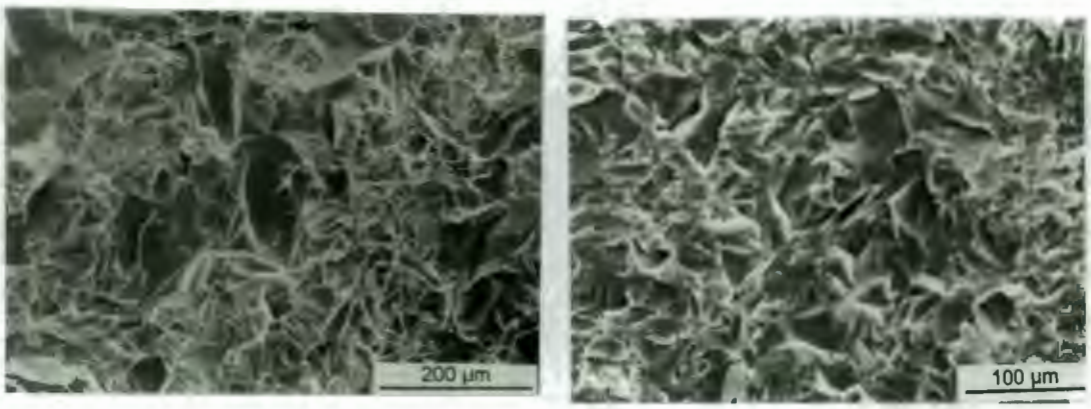

(a) (b)

Figure 4. 82 S.E.M. images of the steady state eroded surface of as received glass after erosion with tungsten carbide erodents (212 μm) at an average particle velocity of 99 $m.s^{-1}$ for (a) 90^0 and (b) 30^0 incidence angles. The fracture surfaces are produced by extensive interaction of lateral cracking for both impingement angles.

4.3.6. As received glass impacted by silicon carbide erodent particles

4.3.6.1. Single impact site examination

The micrographs of the eroded surface by a single SiC particle are shown in fig. 4.83 for impingement angles of 90^0 and 30^0. It is noted that symmetrical lateral cracks occur at 90^0 incidence impact. At 30^0 impact, the lateral cracks propagate along one direction of impact. The scale of the damage pattern at 30^0 incidence is smaller than that of the pattern at 90^0 incidence.

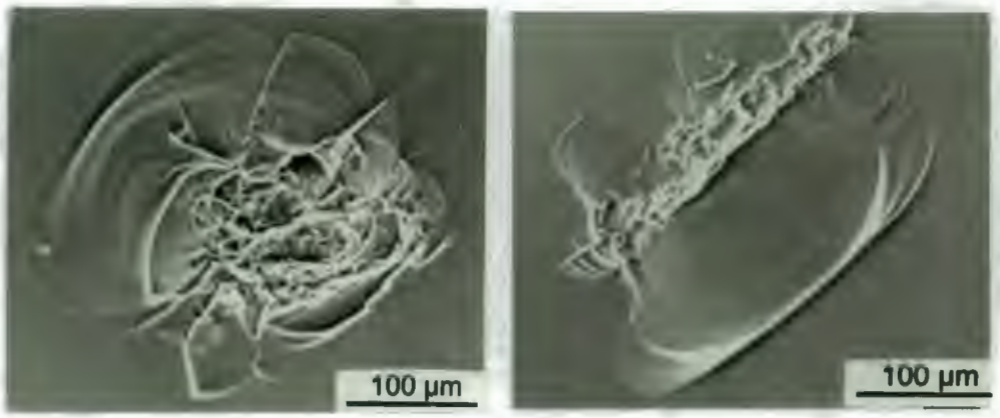

(a) (b)

Figure 4. 83 S.E.M. images of single impact sites produced on as received glass using silicon carbide erodents (400-500 µm) and at an average particle velocity of 57 $m.s^{-1}$ (a) At 90° impact, symmetrical lateral cracks are noted (b) At 30° impact, fracture surfaces are produced by unsymmetrical lateral cracking.

4.3.6.2. Steady state eroded surface examination

The steady state eroded surfaces of as received glass with silicon carbide erodents impacting (106-125 µm) at an average particle velocity of 99 $m.s^{-1}$ are shown in fig. 4.84 for impingement angles of 90° and 30°. The impact sites are produced by the formation and interaction of lateral cracking.

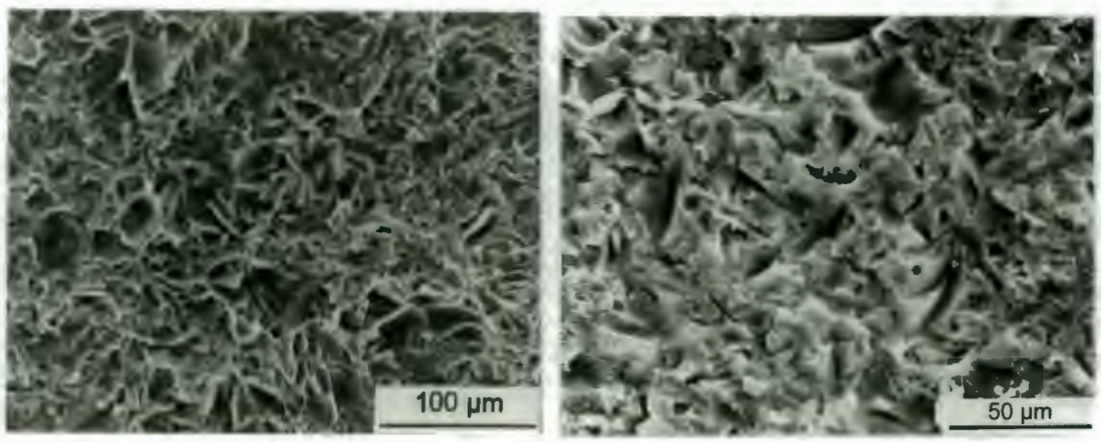

(a) (b)

Figure 4. 84 S.E.M. images of the steady state eroded surface of as received glass after erosion with silicon carbide erodents (106-125 µm) at an average particle velocity of 99 $m.s^{-1}$ for (a) 90° and (b) 30° incidence angles. The damage patterns are associated with the formation and interaction of lateral cracks where multiple impacts are needed to produce.

4.3.7. As received glass impacted by diamond erodent particles

4.3.7.1. Single impact site examination

The micrographs of the eroded surface by a single diamond particle with different impingement angles are shown in fig. 4.85. It is noted that symmetrical lateral cracks occur at 90° incidence impact. At 30° impact, the lateral cracks propagate along one direction of impact. The size of the damage pattern at 30° incidence is smaller than that of the pattern at 90° incidence.

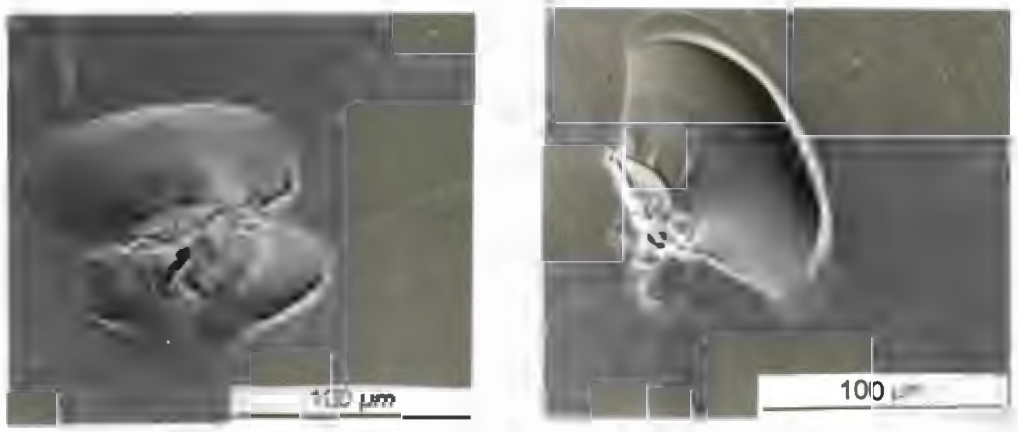

(a) (b)

Figure 4. 85 S.E.M. images of single impact sites produced on as received glass using diamond erodents (151 µm) and at an average particle velocity of 57 m.s^{-1}. (a) At 90° impact, fracture surfaces are produced by complete lateral cracking. (b) At 30° impact, cracks emanate from one direction of impact.

4.3.7.2. Steady state eroded surface examination

The steady state eroded surfaces of as received glass with diamond erodents (126 µm) impacting at an average particle velocity of 99 m.s^{-1} are shown in fig. 4.86 for impingement angles of 90° and 30°. The impact sites are produced by the formation and interaction of lateral cracks

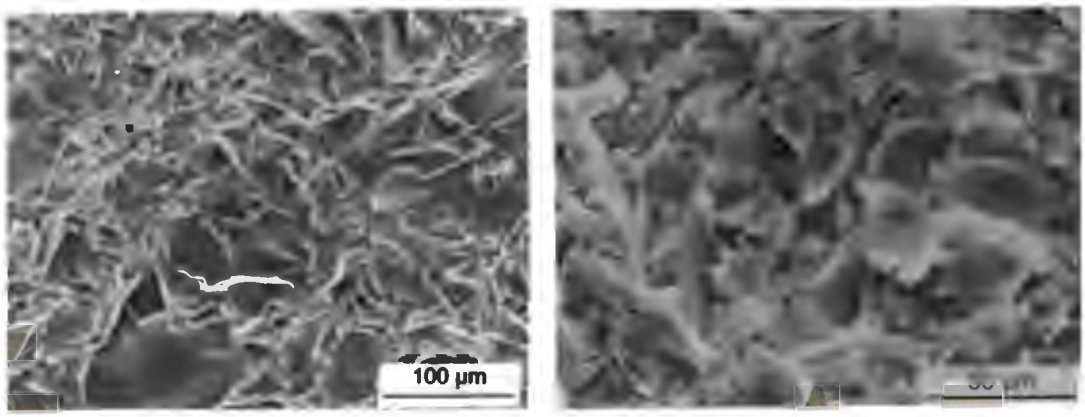

(a) (b)

Figure 4. 86 S.E.M. images of the steady state eroded surface of as received glass after erosion with diamond erodents (126 µm) at an average particle velocity of 99 m.s^{-1} for (a) 90^0 and (b) 30^0 incidence angles. There is evidence that lateral crack propagation and interaction control erosion process.

4.3.8. 304 stainless steel impacted by different erodent particles

4.3.8.1. Single impact site examination

The types of craters produced on the surface of 304 stainless steel for the different erodents impacting at 90° and 30° are shown in fig. 4.87. Single impact sites on the surface of 304 stainless steel exhibit gross plastic deformation. Each strike causes material flow or extrusion up from the surface around some portion of the crater. At 90^0 impact, the craters are formed primarily by the extrusion of erodent particle to form a raised lip adjacent to the impact site. The sets of slip and twin lines adjacent to impact are observed as shown in figs. 4.87(c) and (e). Embedded erodent particles of WC and diamond in the surfaces are shown in figs.4.87 (c) and (e). The craters frequently show features which are imprints from the surface of the erodent particles. This is particularly in the case of diamond erodents where growth features and cleavage steps are imprinted into the soft stainless steel as shown in fig. 4.87(g). At 30^0 impact, the displacement of surface materials is more pronounced due to the more efficient ploughing, cutting and lip formation action at oblique angle. The material is ploughed ahead of the impacting particle and forms a lip of raised material.

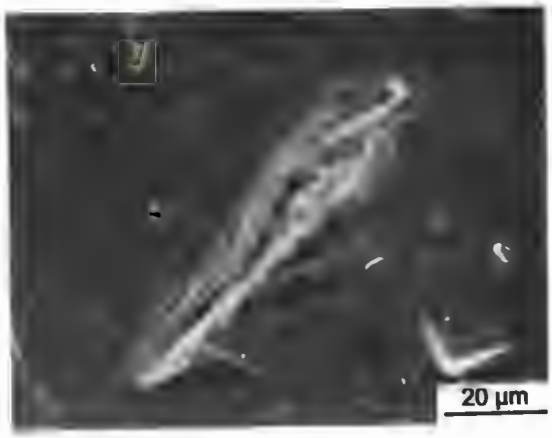

α=90°
(a)

α=30°
(a)

α=90°
(b)

α=30°
(b)

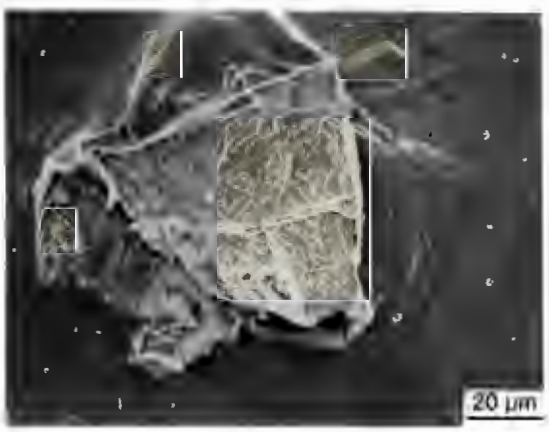

α=90°
(c)

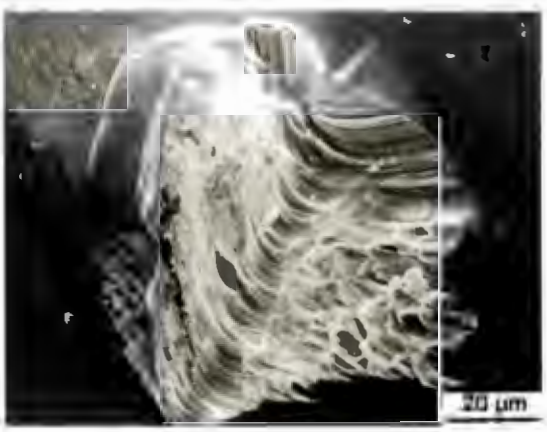

α=30°
(c)

4.3.8.2. Steady state eroded surface examination

The steady state eroded surfaces of 304 stainless steel produced by different erodent particles are shown in fig.4.88. At 90^0 impact, the fracture surface contains deep grooves and prominent lips of materials that are fractured and flattened by successive particle impacts. At 30^0 impact, cutting and ploughing produce large lips which undergo substantial plastic deformation and are flattened by successive impacts and eventually fracture in a ductile manner.

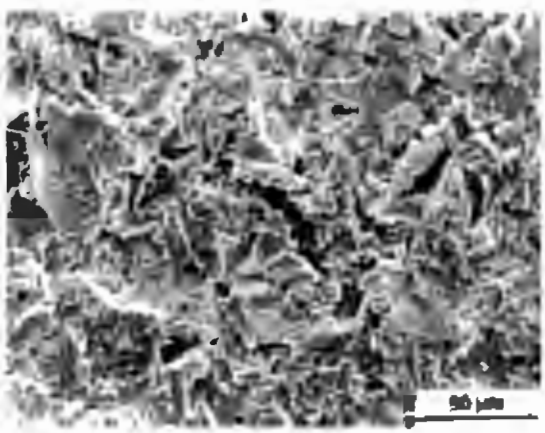

$\alpha=90^0$
(a)

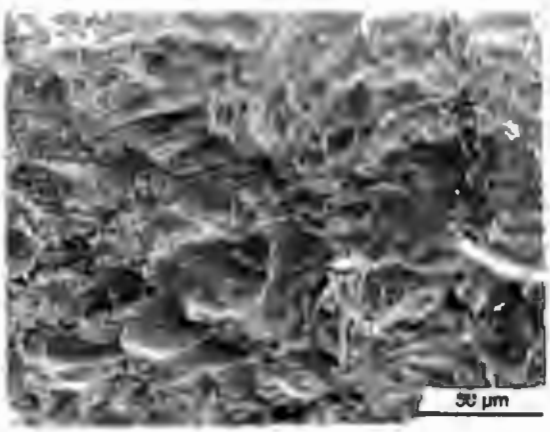

$\alpha=30^0$
(a)

$\alpha=90^0$
(b)

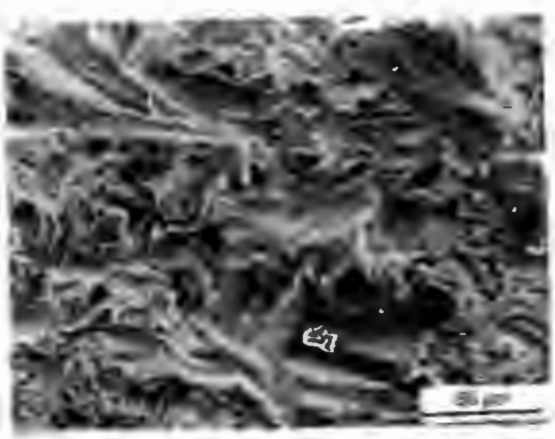

$\alpha=30^0$
(b)

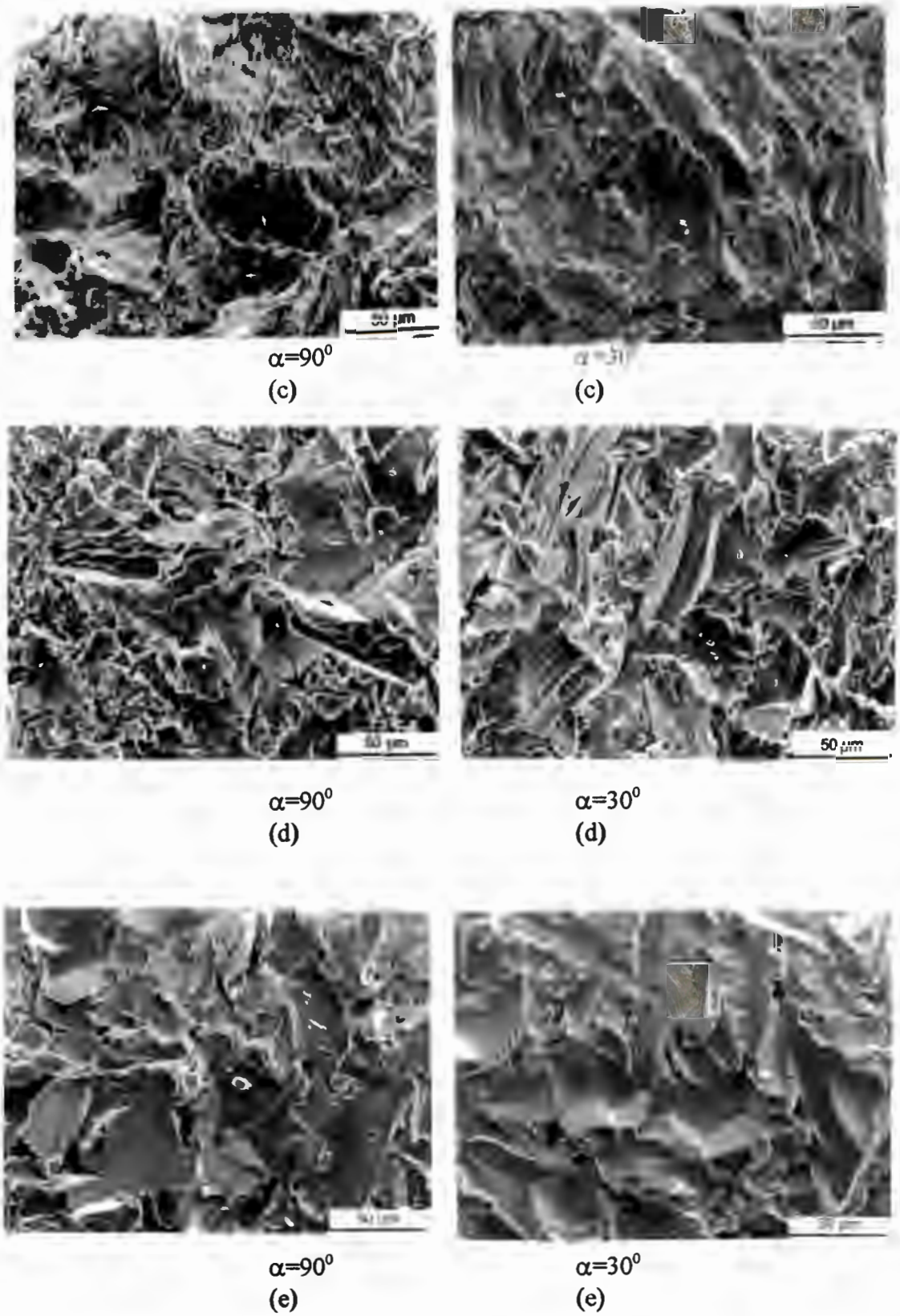

Figure 4. 88 S.E.M. images of the steady state eroded surface of 304 stainless steel with erodent particles(180-250 μm) and an average velocity of 99 $m.s^{-1}$. (a) silica (b) alumina (c) WC (d) SiC (e) diamond. At 90^0 impact, craters are surrounded by flattened and fractured lips. At 30^0 impact, ploughing and cutting produce highly strained lips of material which are subsequently flattened and eventually fracture. Note the gross deformation rupture shown in fig.(e).

4.3.9. WC-7%Co impacted by different erodent particles

4.3.9.1. Single impact site examination

The types of craters produced on the surface of WC-7%Co with different erodent particles impacting at 90^0 incidence are shown in fig. 4.89. Each strike causes a cobalt extrusion and tungsten carbide grain uplift and displacement. It also shows the deformation and fracture of tungsten carbide grains. Particularly the crater formed by diamond impact is heavily deformed and fractured as shown in fig. 4.89(e). At 30^0 impact, the ploughing causes the extrusion of cobalt and tungsten carbide grain uplifted at the exit side as shown in fig. 4.89(f).

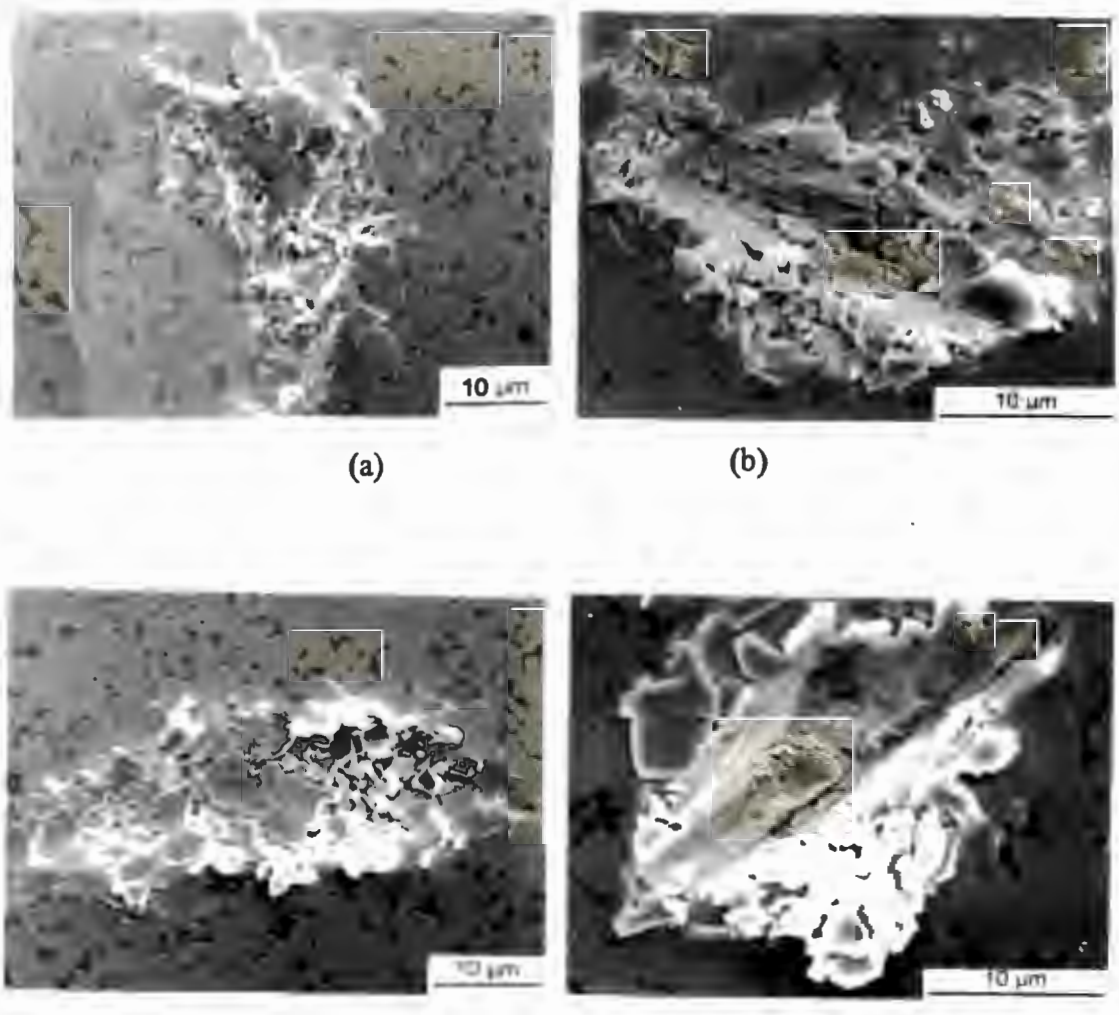

(a) (b)

(c) (d)

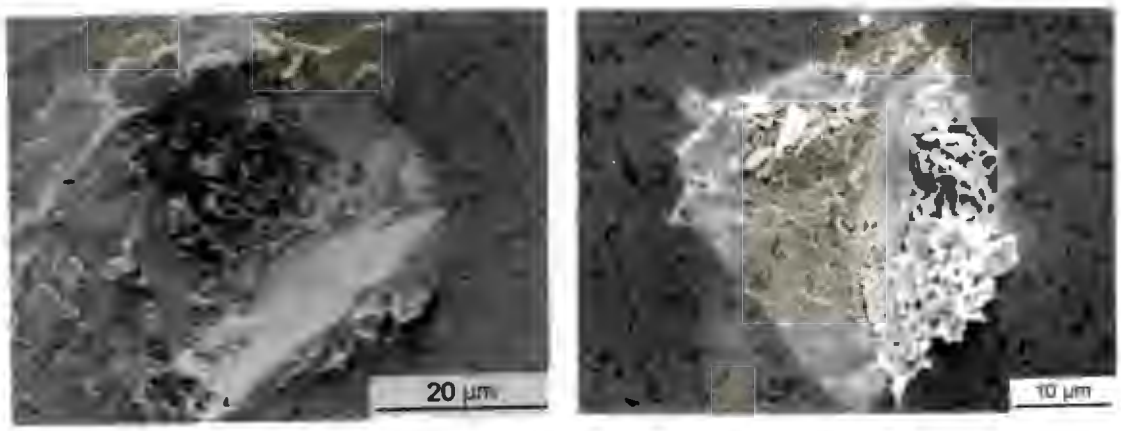

(e) (f)

Figure 4. 89 S.E.M. images of single impact site of WC-7%Co with erodent particles (180-250µm) at an average impingement velocity of 99m.s^{-1} and at 90^0 incidence using (a) silica (b) alumina (c) tungsten carbide (d) silicon carbide (e) diamond erodent particle and (f) silicon carbide particle at an impingement angle of 30^0 incidence. Note the uplifting of the WC grains as well as the extruded cobalt from the binder region.

4.3.9.2. Steady state eroded surface examination

The steady state eroded surfaces of WC-7%Co produced by 90^0 and 30^0 incidence as shown in fig. 4.90. In general, the preferential loss of the cobalt phase is visible. It is noted that all tungsten carbide grains eroded with higher hardness particles appear to be deformed and fractured while no fractures of tungsten carbide grains are noted for the silica erodent impact as shown in fig. 4.90(a). The erosion mode of WC-7% Co eroded with silica erodent at both angles of 90^0 and 30^0 incidence is that the cobalt phase is preferentially removed and then followed by " pull out" of the carbide grains. The indents generated by diamond erodent impact shows the evidence of gross plastic deformation of cobalt.

α=90^0 α=30^0

(a) (a)

α=90°
(b)

α=30°
(b)

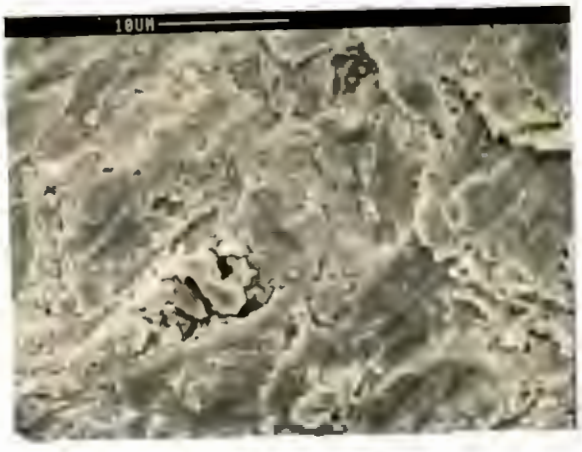

α=90°
(c)

α=30°
(c)

α=90°
(d)

α=30°
(d)

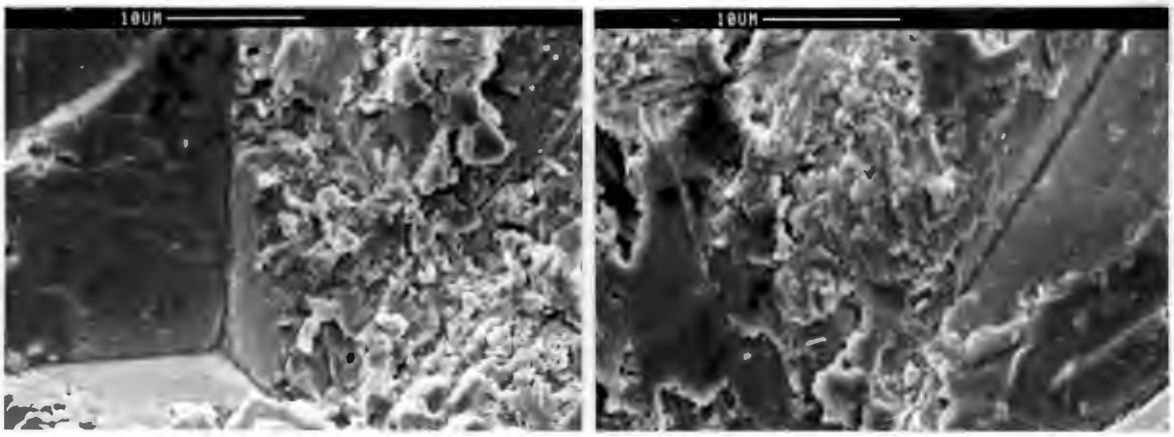

$\alpha=90^0$ $\alpha=30^0$

(e) (e)

Figure 4. 90 S.E.M. images of steady state eroded surface of WC-7%Co after erosion with erodent particles (180-250 μm) and an average impingement velocity of 99 $m.s^{-1}$ for particles (a)silica (b) alumina (c) tungsten carbide (d) silicon carbide (e) diamond at an impingement angle of 90^0 and 30^0 respectively. Note fracture surfaces are produced by the preferential removal of cobalt and then followed by unpullout WC grain.

4.3.10. Alumina impacted by different erodent particles

4.3.10.1. Single impact site examination

The morphology of the eroded surface by a single different particle is shown in fig. 4.91 for an impingement angle of 90^0. Porosity can be seen in the surface. Pores in alumina are sites where crack growth during erosion occurs without the need for crack initiation. It is noted that the damage zones are characterised by a relatively deep pit formed primarily through intergranular chipping with no evidence of any radial or lateral cracking around this zone.

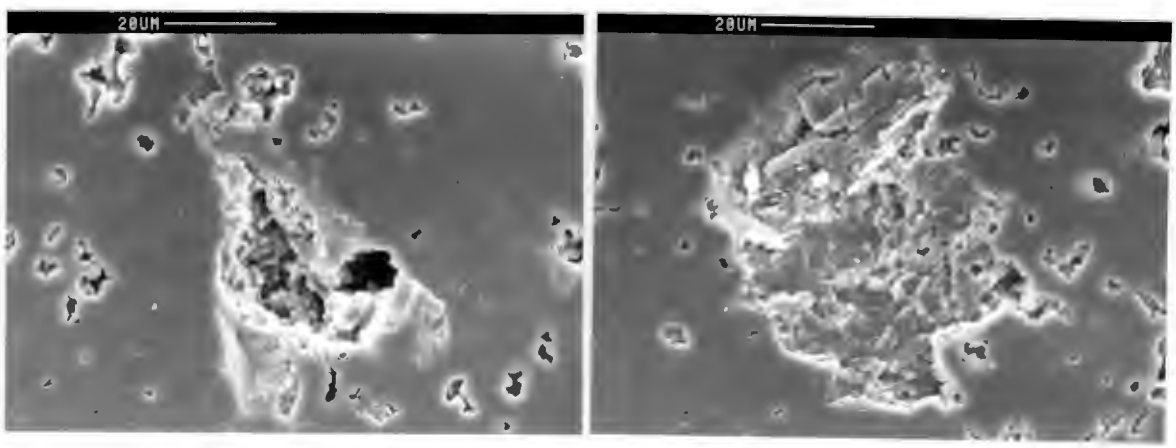

(a) (b)

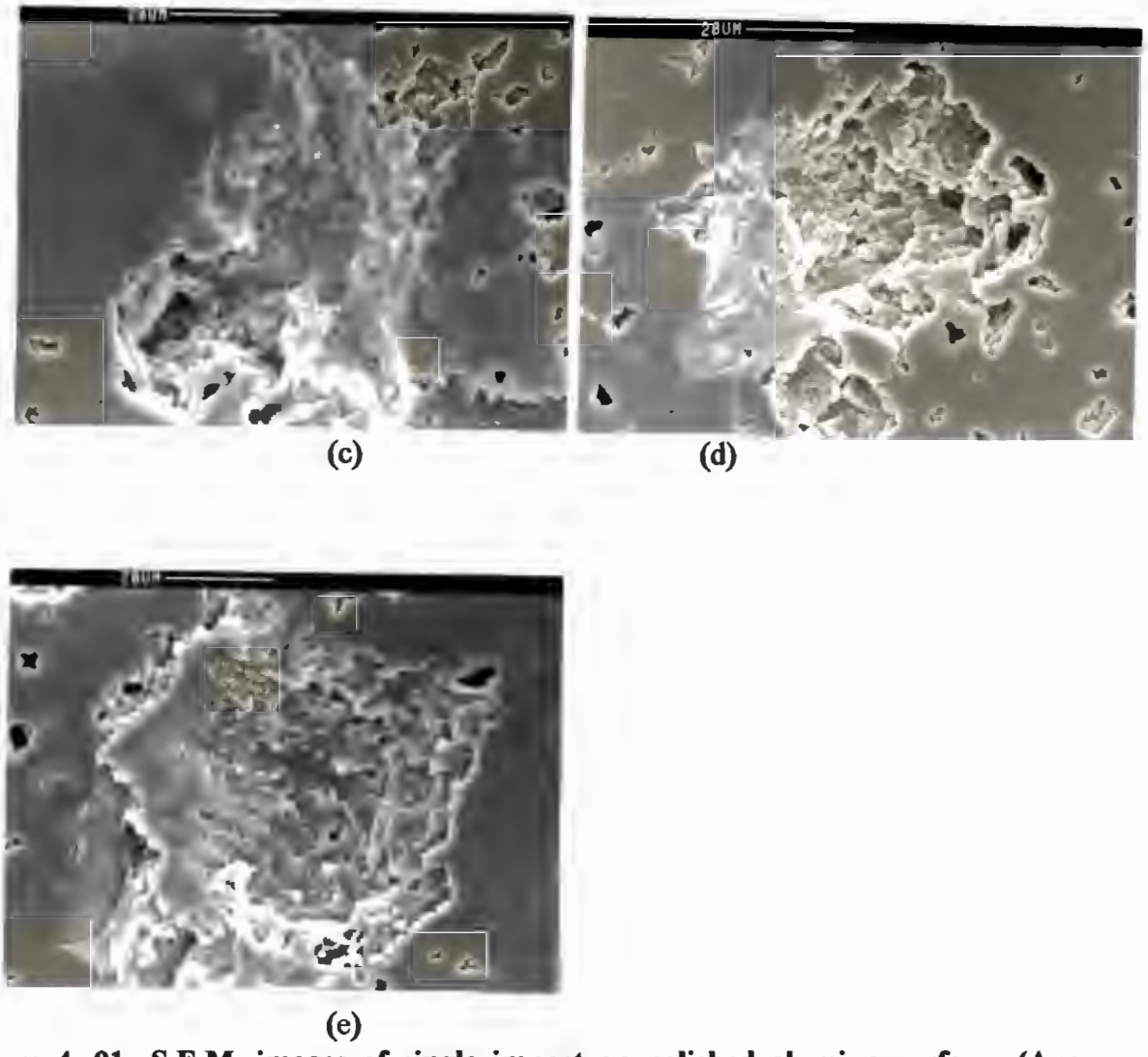

(c) (d)

(e)

Figure 4. 91 S.E.M. images of single impact on polished alumina surfaces (Arrow shows the porosity of alumina) result from the impact of (a) silica (b) alumina (c) tungsten carbide (d) silicon carbide (e) diamond erodents. Note extensive intergranular spallation and fractured grains.

4.3.10.2. *Steady state eroded surface*

The morphology of steady state eroded surface of alumina is shown in fig. 4.92. The impact of silica erodents on alumina results in less grain ejection. The impact of the other particles results in crushed region in the central impact site surrounded by extensive grain ejection.

4.3.10.2. *Steady state eroded surface*

The morphology of steady state eroded surface of alumina is shown in fig. 4.92. The impact of silica erodents on alumina results in less grain ejection. The impact of the other particles results in crushed region in the central impact site surrounded by extensive grain ejection.

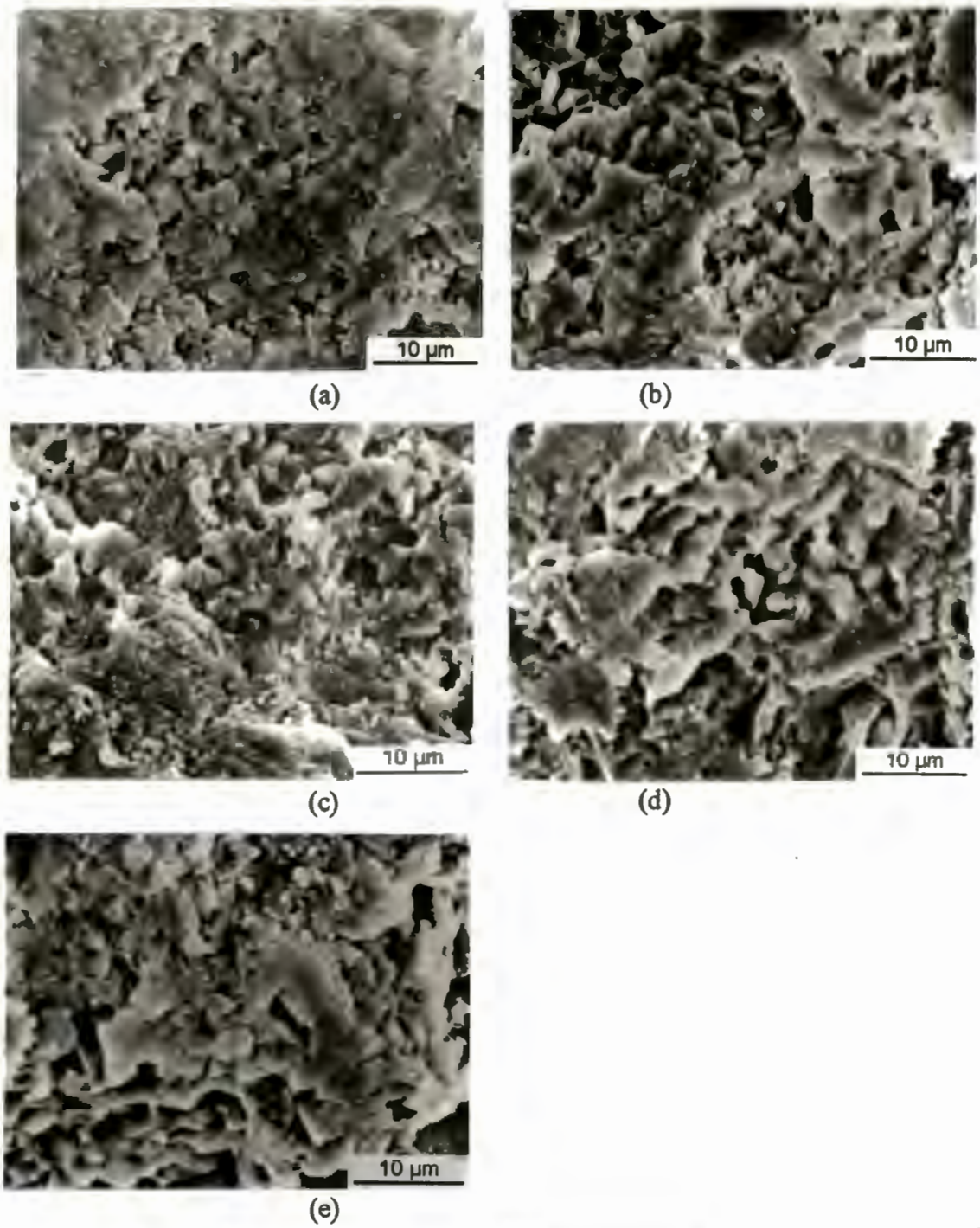

Figure 4. 92 S.E.M. images of steady state eroded surfaces of polished alumina surfaces result from the impact of (a) silica (b) alumina (c) tungsten carbide (d) silicon carbide (e) diamond erodents.

4.4. Cavitation Erosion

4.4.1. Test results

The results of cavitation erosion tests and hardness measurement are shown in Table 4. 10. The steady state erosion rate of as received glass is greater than that of the tempered glass. The incubation period for the tempered glass is longer than that of as received glass. The high nitrogen stainless steel (Cromanite™) exhibits the highest erosion resistance and longest incubation period. The erosion resistance of cobalt based tungsten carbides increases with increasing cobalt content.

Table 4. 10 Results of cavitation erosion tests and hardness measurements.

Materials	Hardness (HV_{25g})	Steady state erosion rate ($10^{-5}cm^3$/hour)	Incubation period (hours)
304 stainless steel	220	17.80	2.50
Cromanite	286	5.50	4.70
As received glass	420	264.00	0.31
As tempered glass	465	228.00	0.33
alumina	1023	15.80	0.90
WC-15Co(wt%)	1070	13.40	2.40
WC-10Co(wt%)	1230	16.20	1.30
WC-8Co(wt%)	1300	22.70	0.91
WC-7Co(wt%)	1350	24.40	0.84

4.4.1.1. Glass

The cumulative volume loss of glass versus time of erosion in the as received and thermally tempered conditions is shown in fig. 4.93. The as received glass exhibits greater cavitation erosion rates than the thermally tempered glass.

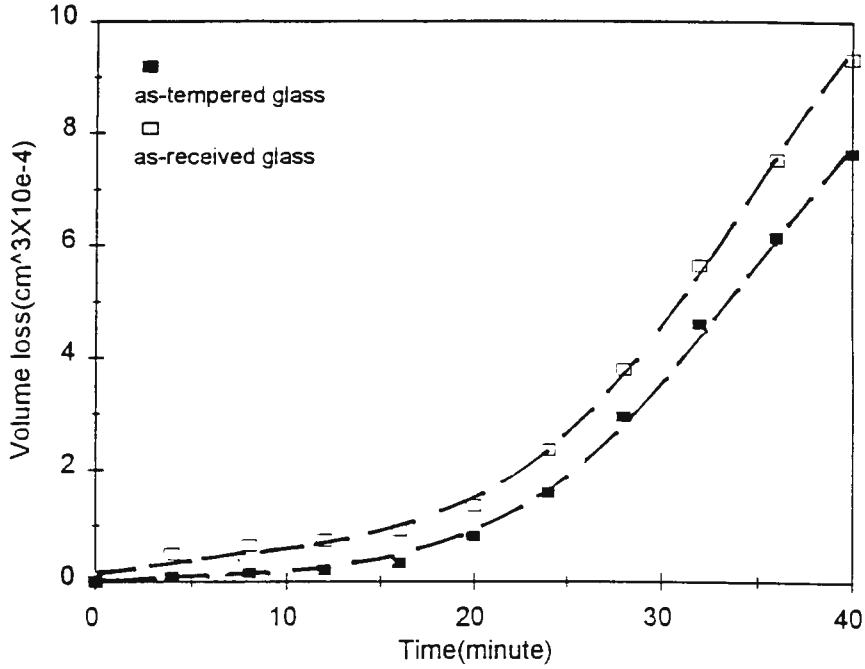

Figure 4. 93 Graph of cumulative volume loss versus time of cavitation erosion for glass in as received and thermally tempered conditions.

4.4.1.1.1. Eroded surface examination

The scanning electron micrographs of the eroded surface of as received glass and the tempered glass are shown in fig. 4.94. After exposure to erosion for 12 minutes the eroded surface of the glass exhibits cracking between the pre-existing flaws. The fracture surfaces of the enlarged flaws are brittle and the enlarged flaws and cracks form a continuous network. By contrast, the severity of damaged surface for the tempered glass is less than that of damaged surface for as received glass after exposure to erosion for 12 minutes. The steady state cavitation eroded surface of glass after 40 minutes of erosion is shown in fig. 4.95. The surface exhibits completely brittle fracture and radial striations near the perimeter of the disc-shaped fracture surface are a common fracture.

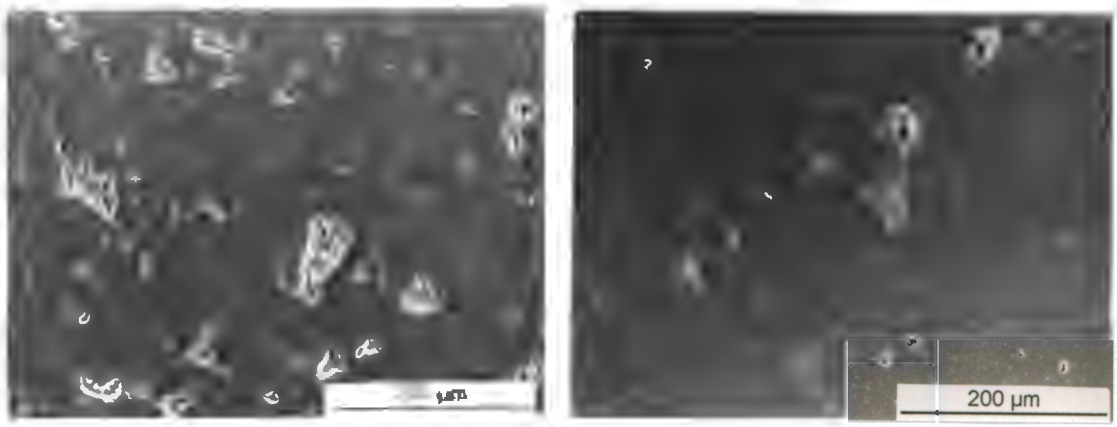

(a) (b)

Figure 4. 94 S.E.M. images of the eroded surface after cavitation erosion for 12 minutes. (a) as received glass (b) the tempered glass.

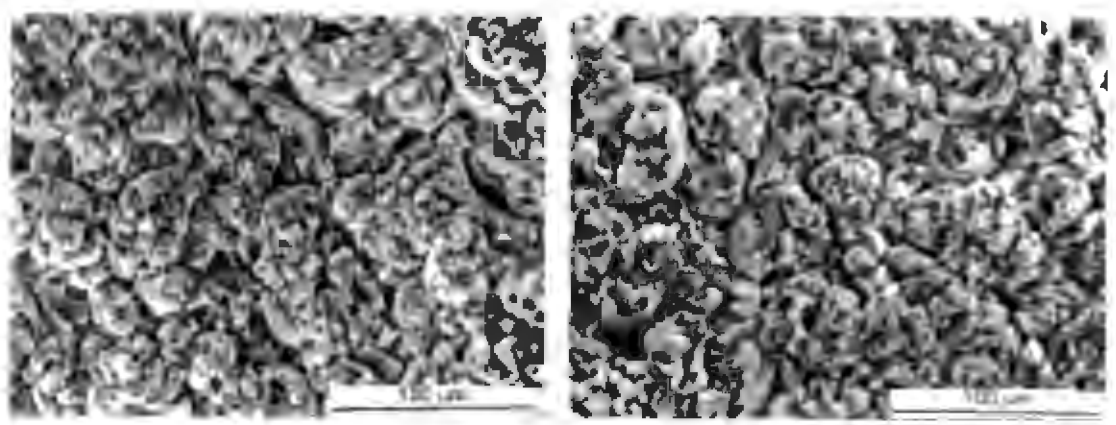

(a) (b)

Figure 4. 95. S.E.M. images of the eroded surface after cavitation erosion for 40 minutes showing the fracture surfaces are brittle. (a) as received glass (b) the tempered glass

4.4.1.2. Stainless steel

The graph of cumulative mass loss versus time of cavitation erosion are shown in fig. 4.96 for 304 stainless and Cromanite™. The Cromanite™ exhibits the better erosion resistance than the 304 stainless steel.

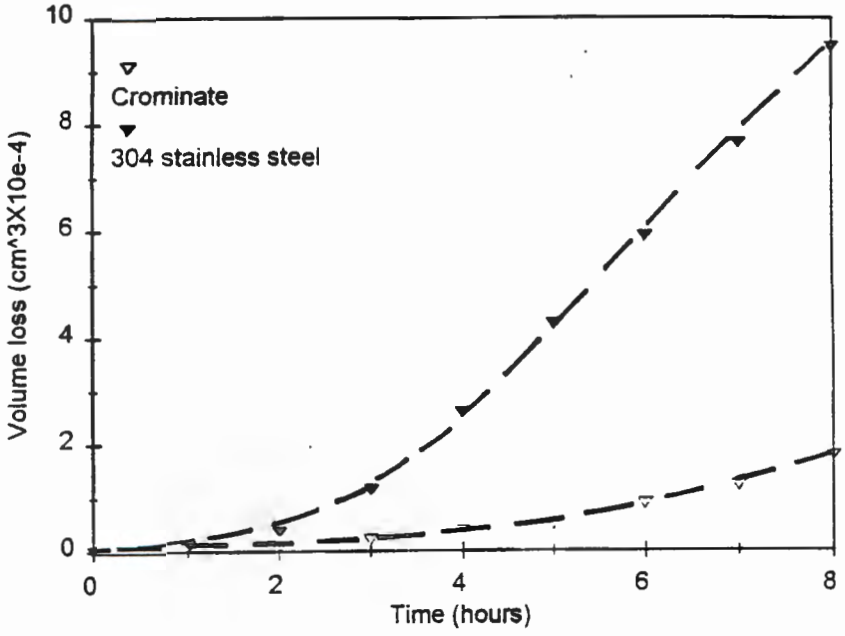

Figure 4. 96 Graph of cumulative volume loss versus time of cavitation erosion for 304 stainless and Cromanite.

4.4.1.2.1. Eroded surface examination

The micrographs of the eroded surface of 304 stainless and Cromanite are shown in fig. 4.97. For 304 stainless steel, an area near the edge of the eroded area shows deformation twins or persistent slip lines. Material is removed by the joining of surface cracks. For Cromanite cavitated for two hours, it shows that the grain boundaries are raised and larger pieces of material removed from the grain boundaries. Note that the micrographs were taken without being etched.

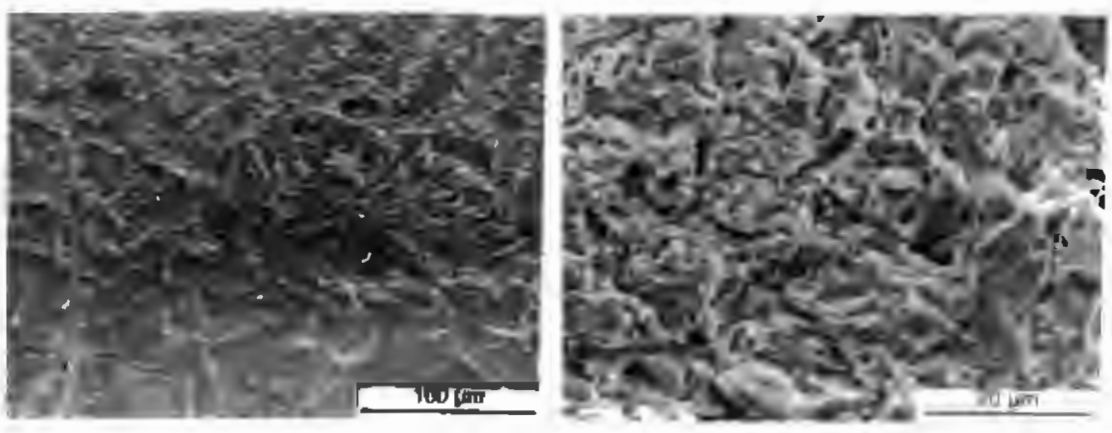

(a) (b)

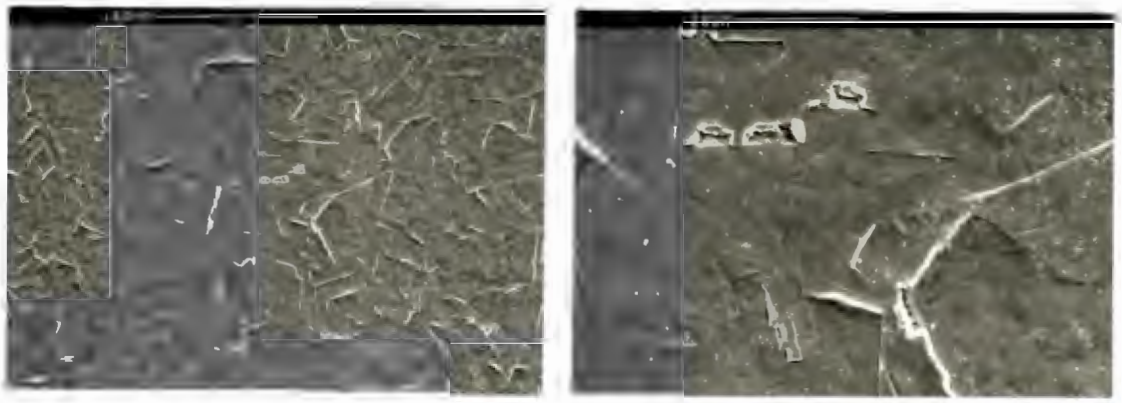

(c) (d)

Figure 4. 97 S.E.M. images of cavitation eroded surface after 2 hours of cavitation. (a) an area near the edge of the eroded area of 304 stainless steel. (b) an area in the middle of the eroded area of 304 stainless steel. (c) The eroded area of Cromanite (d) A high magnification of a section of (c).

4.4.1.3. Tungsten carbide cobalt

The graphs of cumulative mass loss of WC-Co versus time of cavitation erosion are shown in fig. 4.98. The erosion rate increases with increasing the content of cobalt.

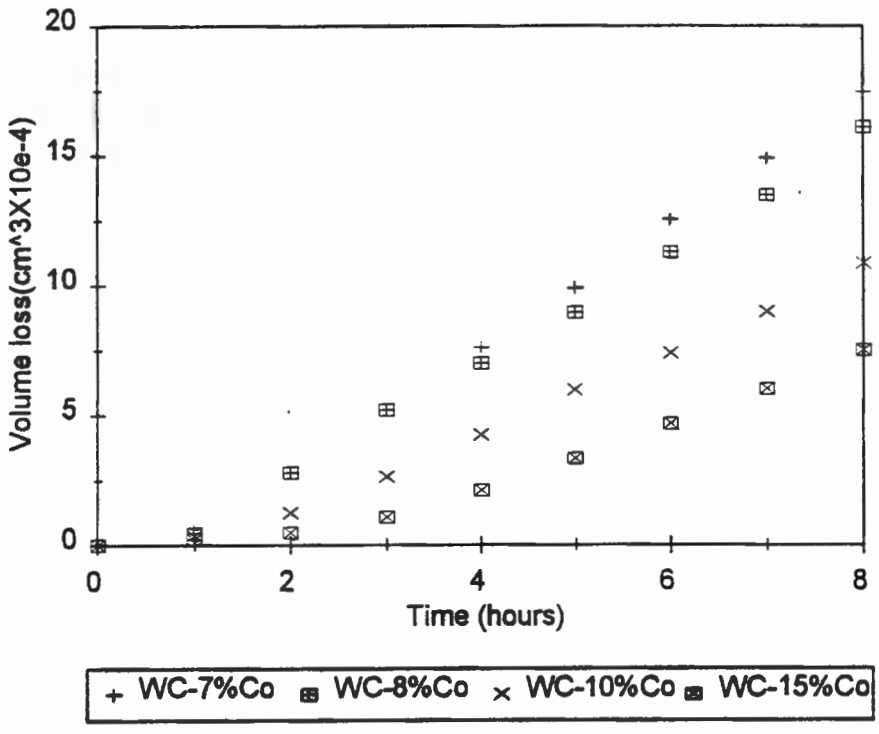

Figure 4. 98 Graph of cumulative volume loss versus time of cavitation erosion for WC-Co.

4.4.1.3.1. Eroded surface examination

The micrographs of the eroded surface of WC-Co are shown in fig. 4.99. The cobalt binder is preferentially eroded followed by removal of carbide particles when there is no longer sufficient cobalt binder to retain these tungsten carbide grains.

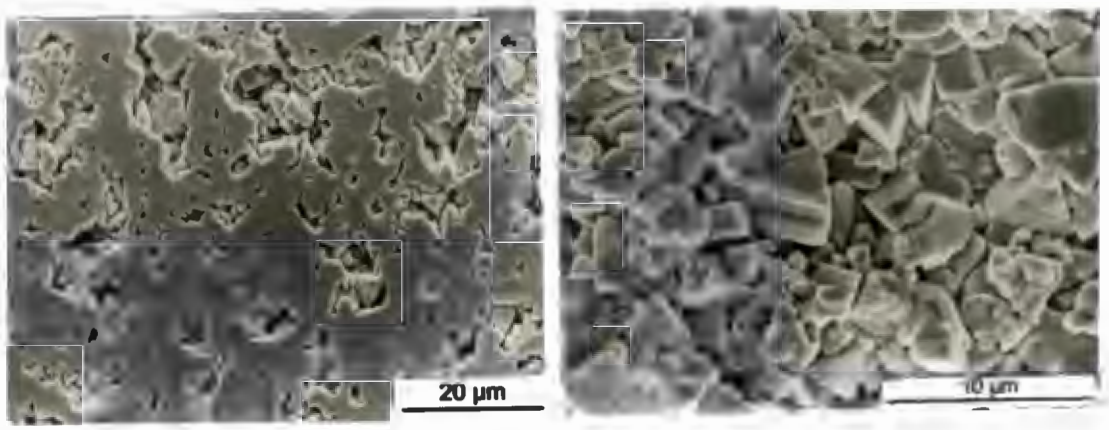

(a) (b)

Figure 4. 99 S.E.M. images of cavitation eroded surface of WC-7%Co after 8 hours of cavitation. (a) an area near the edge of the eroded area. (b) an area in the middle of the eroded area.

4.4.1.4. Alumina

The graph of cumulative mass loss of alumina versus time of cavitation erosion is shown in fig. 4.100. It is noted that erosion rate increases with increasing the time of cavitation erosion.

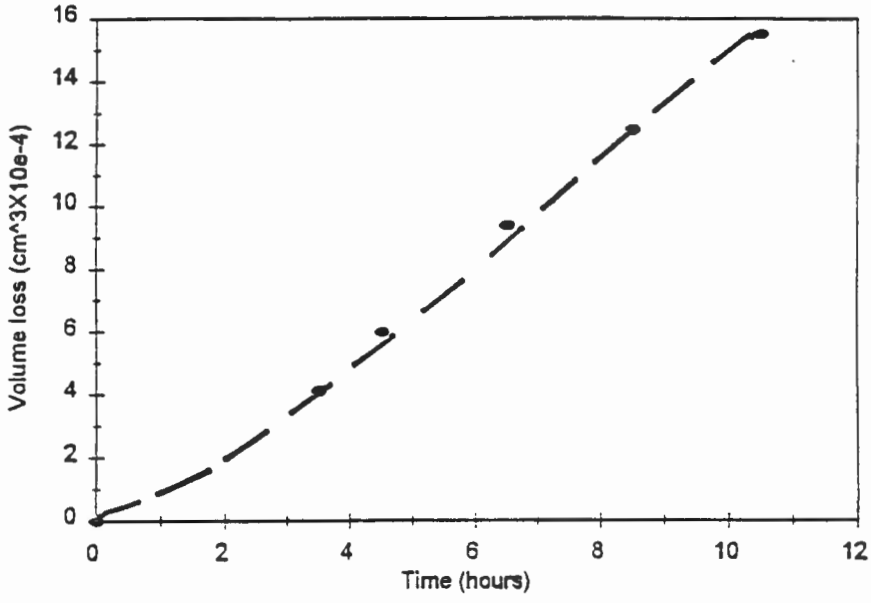

Figure 4. 100 Graph of cumulative volume loss versus time of cavitation erosion for alumina.

4.4.1.4.1. Eroded surface examination

The micrographs of the eroded surface of alumina are shown in fig. 4.101. No evidence of plastic deformation was noted. Microcracking was initiated at grain boundaries and propagated, until grains which were not well constrained by their neighbours were spalled off the surface. Little or no evidence of transgranular fracture was noted. Removal of single grains of the material by microcracking of the weak grain boundaries results in the formation of pits in the surface of the material. These spread until the whole surface is damaged.

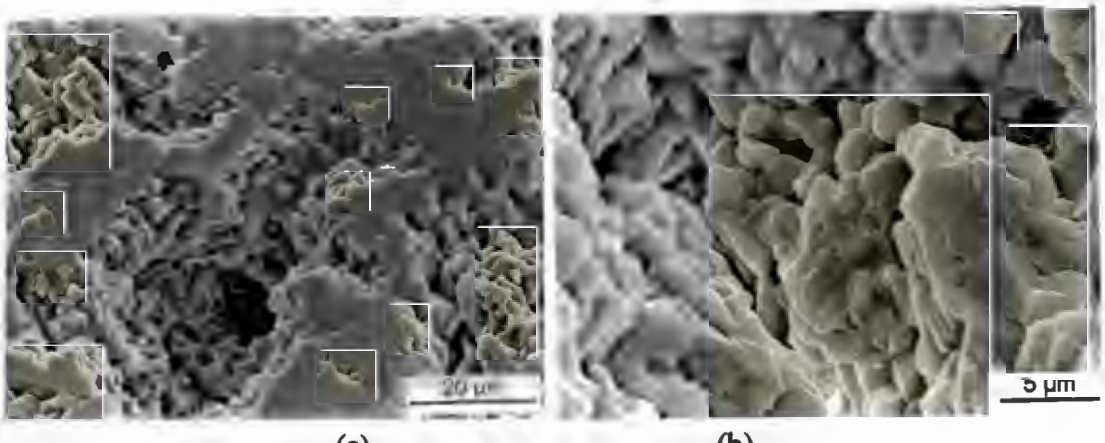

(a) (b)

Figure 4. 101 S.E.M. images of cavitation eroded surface of alumina after 8 hours of cavitation. (a) an area near the edge of the eroded area. (b) an area in the middle of the eroded area.

5. DISCUSSION

5.1. Solid particle erosion

5.1.1. Glass

5.1.1.1. Examination of eroded surface

An examination of single impact sites produced by irregularly shaped particles at 90^0 incidence on glass shows a crushed region in the centre of the impact site from which radial and lateral cracks emanate. The shape of the damage zone for 30^0 incidence is in one direction relative to the impact site. The scale of the damage pattern at 30^0 incidence is smaller than that at 90^0 incidence. The damage patterns produced by irregularly shaped particles on glass have in general crack patterns that resemble those produced during quasi-static indentation using sharp diamond indenters[16]. The damage patterns produced during steady state erosion are very similar for all irregularly shaped particles in spite of a large difference in erosion rates and show evidence of lateral crack controlled fracture processes where multiple impacts are needed to produce lateral crack events. The interpretation for such similarities is that a single mechanism of material removal, which is the formation of lateral fracture and the formation and removal of chips, is operative for all irregularly shaped particles.

The damage patterns by spherical glass beads are determined by the particle size, impingement velocity and angle. The experimental erosion map shown in fig. 5.1, with coordinates of particle velocity and the average diameter of particles, is constructed to categorise the types of damage observed in the as received glass. The solid and dashed lines represent tests at impingement angles of 90° and 30°, respectively. The standard deviation of the data used in this map is approximately 15%. The horizontal line in this figure represents the transition from elastic to inelastic deformation. At 90° impact, the fracture pattern for small spherical glass beads impacting at 90^0 incidence shifts from the inelastic deformation regime (II) to the radial and lateral crack regime (IV) with increasing impingement velocity. The fracture pattern for large spherical glass bead impacts shifts

from an inelastic deformation regime (III) to the Hertzian cone crack regime (V) with increasing impingement velocity. These phenomena can be explained as follows:

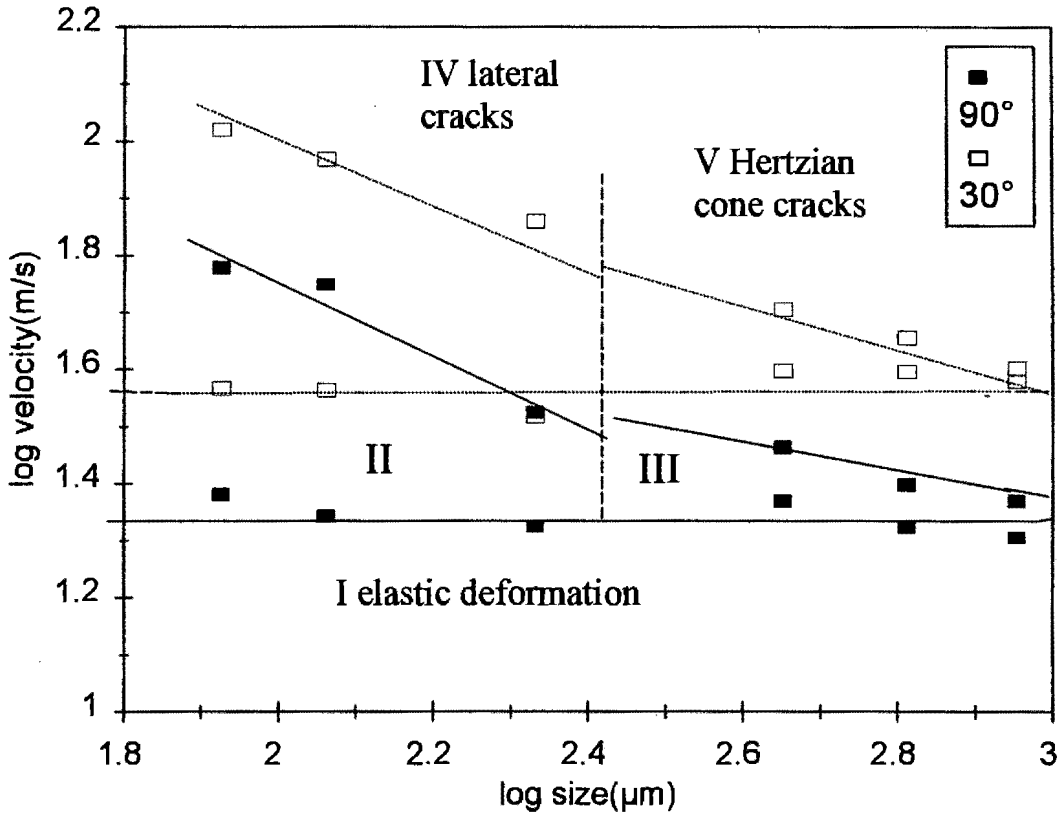

Figure 5. 1. The experimental erosion map of as received glass with spherical glass bead impacts. Solid line: 90^0 incidence; Dashed line: 30^0 incidence

Since the strength of glass is governed by pre-existing micro-cracks in the surface, the ring crack is assumed to initiate from a pre-existing flaw when the stress to which it is subjected reaches a critical value[164]. Timoshenko and Goodier[85] indicated that for the purely elastic case, the radius a of the circle of contact between the indenter of radius, R, and the flat solid surface is given by

$$a^3 = 4kPR/3E \qquad (2.14)$$

$$z = [4k/3E]^{2/3} P^{2/3} R^{-2/3} \qquad (2.15)$$

where

$k = (9/16)[(1-\gamma^2)+(1-\gamma'^2)E/E']$

γ and γ' are the Poisson's ratios of the target materials and the indenter

E and E′ are the Young's moduli of the target and the indenter

P is the load

z is the distance of mutual approach of the deforming solids.

Chaudhri and Walley[165] assume that the maximum elastic strain energy during the impact is equal to the kinetic energy of the impingement particle, that is

$$0.5\,[4\pi R^3\,\rho/3]\,V^2 = \int_0^z P(z)\,dz \qquad (2.13)$$

where

ρ is the density of the particle

V is the impact velocity

P(z) is the load corresponding to the distance of approach z

Integration of equation (5.3) gives the maximum load,

$$P_m = [5\pi\rho/3]^{3/5}\,[4k/3E]^{-2/5}\,R^2\,V^{6/5} \qquad (2.16)$$

The maximum mean pressure is given by $F_m = P_m/\pi a^2 = 1/\pi(5\pi\rho/3)^{1/5}\,(3k/4)^{-4/5}\,V^{2/5}$. The maximum mean pressure and radial tensile stress are dependent on the impingement velocity and the density of the particle. The maximum contact radius between the particle and target is given by:

$$a_m = (P_m/\pi F_m)^{1/2} \qquad (5.1)$$

The duration of the elastic impact[165] is given by

$$T = 2.94(5\rho\pi k/4)^{2/5}R/V^{1/5} \qquad (5.2)$$

The experimental contact radii and contact time can be obtained from the equations (5.1) and (5.2) respectively. When the impact load and contact radius reach a critical value, a ring

crack appears at the surface of the specimen. On increasing the load, plastic deformation of the target and/or erodent will occur. Estimates of the maximum pressures, contact radii and duration of the particle impacts can be made by modelling for glass beads. The values for these parameters used in the experiments are presented in Appendix B. With increasing velocity, the contact radius increases and the contact time decreases as shown in figs. 5.2 and 5.3. Small particles produce smaller stresses over smaller areas[166, 167, 168] and have a lower probability of activating suitable nucleating flaws in the contact zone; thus Hertzian cracking is less likely to occur. Similar results are observed by Marshall and Lawn[169]. The damage deformation of the surface is associated with inelastic deformation controlled processes which may eventually lead to crack propagation under multi-impact processes as shown in figs. 4.71(a) and 4.72(a). With the velocity increasing, there is a sharp increase in erosion rate at a certain critical velocity as shown in figs. 4.2 to 4.4. The threshold velocity shifts from a high velocity regime to a low velocity regime with increasing particle size and impingement angle. This is ascribed to a change in mode of erosion.

The maximum penetration load at higher velocity is so great that lateral cracks are developed by the residual indentation stress that arises from mismatch of the plastic zone and the surrounding elastic matrix. Material removal at critical velocity is associated with the combined mechanism of multi-inelastic deformation and lateral fracture, which operate on a comparable scale. The fact that no Hertzian crack was observed for small particle impact may be attributed to two combined factors: the scarcity of nucleating cracks and insufficient contact time (Fig. 5.3 shows that small particles have very low contact time) for crack propagation in the system even when the applied force is great enough to produce the critical tension at the rim of the area of contact. This is also ascribed to the dependence of the growth of Hertzian fracture on the value of the strain energy density in the target relative to the energy required to form new surfaces[170]. Material removal above the critical velocity is associated with the formation and interaction of lateral cracks as shown in figs. 4.71(c) and 4.72(c).

With particle size range above 400-500 μm in diameter, Hertzian cracks were formed and developed further into Hertzian cone cracks with increasing velocity. This is consistent with the work done by Ball and Mckenzie[171]. Material removal is attributed to the interaction of Hertzian cone cracks as shown in figs. 4.74, 4.75 and 4.76. For 30° impact,

the boundaries of the zone move to higher velocities as shown in fig. 5.1. This is due to a reduced normal component of velocity. A detailed explanation of the effect of impingement angle will be discussed in Section 5.1.1.3.

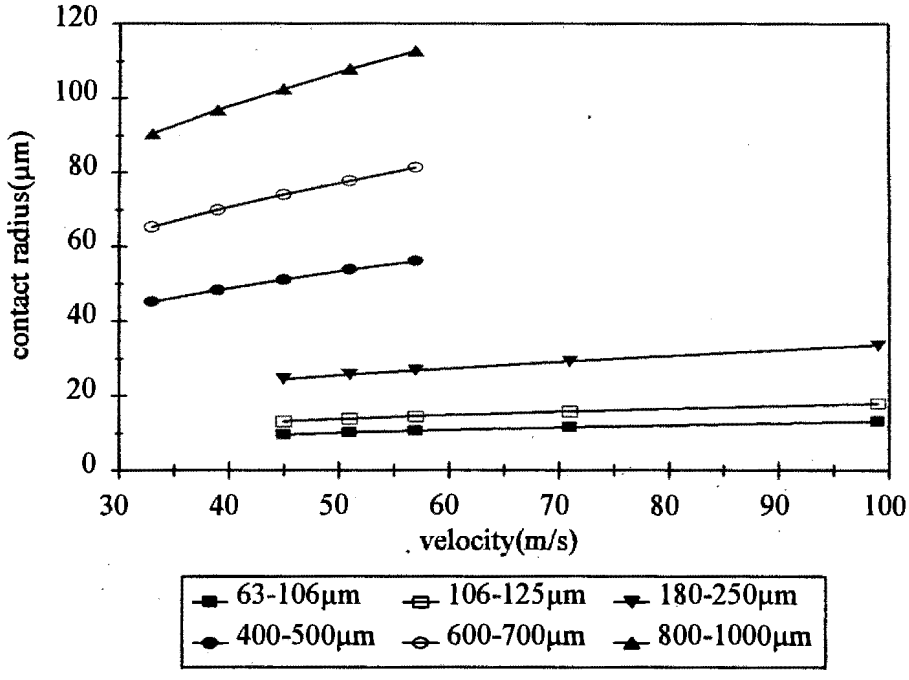

Figure 5. 2. Graph of the theoretical contact radius of glass beads versus the velocity of glass beads.

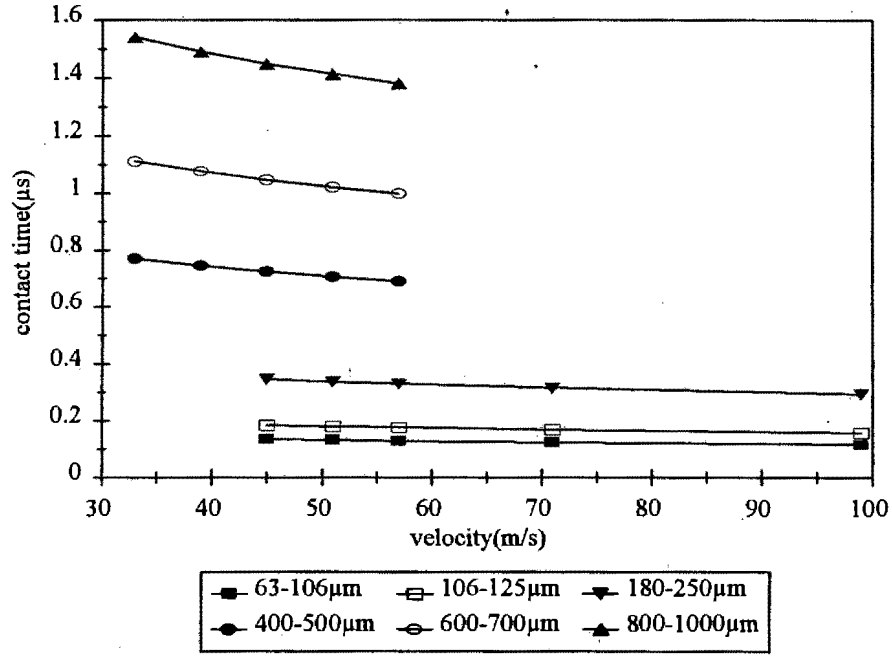

Figure 5. 3. Graph of the theoretical contact time of glass beads versus the velocity of glass beads.

5.1.1.2. Empirical correlation of erosion rate with particle velocity and size

The erosion rate of glass increases with increasing impingement velocity as shown in fig. 4.39. The high velocities result in high kinetic energies and loading pressures, which have the potential to do more damage. The erosion rate increases with increasing particle size as shown in fig. 4.40. The larger particles have high kinetic energy which leads to more erosion loss. This is also ascribed to greater contact area and contact time for larger erodents, which have a higher probability for encountering larger flaws on the surface of glass. These results are supported by Goodwin et al.[121] who eroded glass with quartz particles. In the case of spherical glass beads there is a sharp increase in erosion rate at a certain particle size. This is due to a change in the mode of erosion as shown in fig. 5.1

As described in Section 4.2.1.1, the empirical correlations of erosion rate (Ep) of glass with particle velocity and size for silica, alumina, silicon carbide and diamond at 90° incidence are detailed below:

Silica:	$Ep \propto V^{2.7}D^{4.0}$	(4.1)
Alumina:	$Ep \propto V^{2.4}D^{4.0}$	(4.2)
Silicon carbide:	$Ep \propto V^{2.2}D^{4.0}$	(4.3)
Diamond:	$Ep \propto V^{2.0}D^{4.0}$	(4.4)

The ranking of the value of velocity exponent is as follows: silica > alumina > SiC > diamond. In order to understand these empirical correlations shown in equations (4.1) to (4.4), the reasonable assumption is made that the erosion rate is proportional to the kinetic energy ($0.5MV^2$) and contact time (T) for critical condition where a limited amount of plastic deformation occurs. High kinetic energy results in high damage on the surface[11, 12, 172]. The contact time is required for initiation and propagation of fractures. So the following correlation could be obtained for :

$$Ep \propto 0.5MV^2T \tag{5.3}$$

The contact time of elastic impact is given by reference[85]

$$T = 1.46(5\rho\pi k/4)^{2/5}DV^{-0.2} \tag{5.4}$$

Where

$k = (1-\gamma_1^2)/E_1+(1-\gamma_2^2)/E_2$

E_1, and γ_1 are Young's moduli and Poisson's ratio of target respectively

E_2, and γ_2 are Young's moduli and Poisson's ratio of erodent respectively

ρ is the density of erodent.

Substituting for T, the equation (5.3) can be expressed as

$$Ep \propto V^{1.8}D^{4.0} \qquad (5.5)$$

A comparison of empirical equations (4.1) to (4.4) and theoretical correlation (5.5) indicates that the particle size exponent is the same. However, the values of the velocity exponent in empirical correlation are greater than that in theoretical equation (5.5). The departure of value of velocity exponent from 1.8 in equation (5.5) results from the efficiency of crack initiation and propagation. At low velocity, the erodents have low kinetic energy and low ability to concentrate stresses so that zones of irreversible deformation are small and shallow and lateral cracks are less extensive. With increasing velocity, the effect of erodent hardness is negligible since the high kinetic energy results in irreversible change and lateral cracking for all erodents. Thus the velocity exponent in empirical correlation is greater than 1.8. The velocity exponent increases with decreasing hardness of erodent as seen in equations 4.1-4.4. This is because the relatively softer erodents at low velocity have a lower ability to damage surface than that of the harder erodent.

In order to obtain the exponent values for density and hardness, a multivariate, linear analysis (see Appendix A) was used to analyse the data for all irregularly shaped particles. The empirical relationship between erosion rate and the parameters of irregularly shaped particles and target is as follows:

$$Ep \propto \rho^{1.0\pm0.2}V^{2.4\pm0.1}D^{4\pm0.0}(Hp/Ht)^{0.5\pm0.1}(Kp/Kt)^{0.0} \qquad (5.6)$$

Where

ρ is density of particle

V is velocity

D is the diameter of particle

Ht and Hp are the hardness of target and erodents respectively.

The validity of equation (5.6) can be assessed by plotting the erosion rate as a function of particle and target properties as shown in fig. 5.4. The slope of the line through these data points is nearly 1.

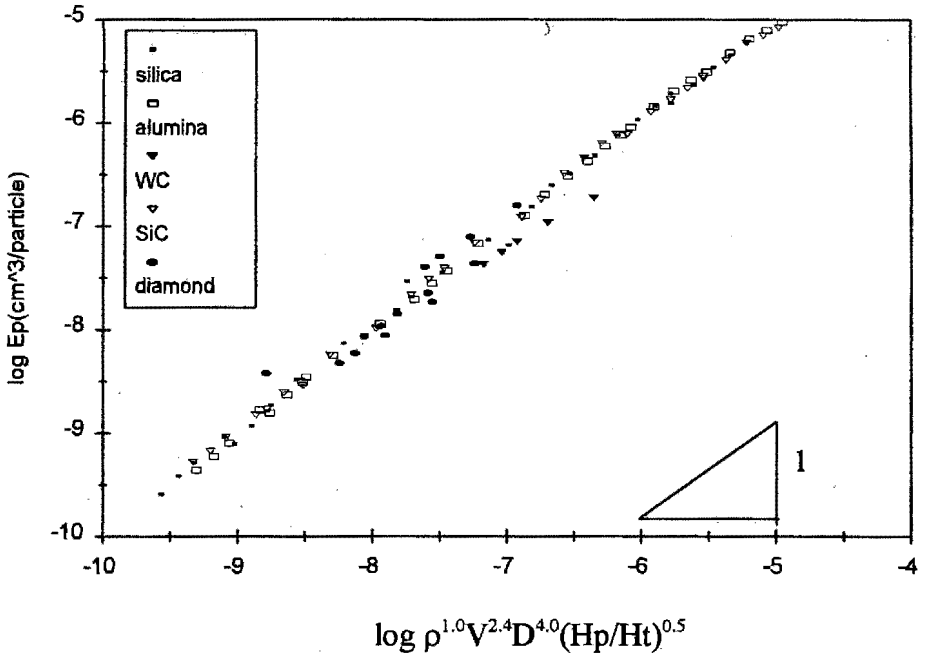

Figure 5. 4. Graph showing the relation between Ep of as received glass and $\rho^{1.0}V^{2.4}D^{4.0}(Hp/Ht)^{0.5}$

The values of exponents are compared with these existing theories in order to evaluate the applicability of these theories to erosion as shown in Table 5.1. It shows that the value of velocity exponent in equation (5.6) is the same as the value of 2.4 predicted by quasi-static model[16] ($Ep \propto \rho^{1.2}V^{2.4}D^{3.7}Ht^{0.1}K_t^{-1.3}$) but lower than the value of 3.2 predicted by dynamic model[15] ($Ep \propto \rho^{1.3}V^{3.2}D^{3.7}Ht^{-1.2}K_t^{-1.3}$). The value of toughness exponent is zero. This means that the toughness of erodents in this case plays a minor role in determining the erosion rate as the hardness of erodents is much higher than that of the target and thus little fragmentation of erodents occurs. The values of other exponents are different from the values that were derived by these two models. These two existing theories are based on the assumption that lateral cracks grow in a quasi-static manner as a result of residual stresses introduced by the impact event. It reveals that these existing theories do not exactly predict the experimental results and the lateral crack models may have certain limitations due to erosion complications in crack interaction effects and variability of the depth of lateral cracking. The basic assumption in these models may be oversimplified. The link-up of

lateral cracks at the average depth of particle penetration may not accurately describe the actual impact crater formation. So an additional study on a mechanics of crack initiation is needed in order to fully comprehend and modify these erosion models. However, a more realistic fracture analysis is admittedly a very difficult problem for impact loading conditions. In addition, the size distribution of the particles used was probably broad enough to affect the accuracy of results.

Table 5.1. A comparison of parameter exponent between existing equation and empirical correlation

	ρ	V	D	Ht	Kt	Hp/Ht	Kp/Kt
Evans, Gulden and Rosenblatt[15]	1.3	3.2	3.7	-1.3	-1.3		
Wiederhorn and Lawn[16]	1.2	2.4	3.7	0.1	-1.3		
Evans and Wilshaw[77]	1.2	2.4	4.0	-0.5	-1.5		
Empirical correlation in this thesis	1.0	2.4	4.0			0.5	0.0

Particular attention is drawn to the paper written by Evans and Wilshaw[77]. They proposed another correlation between the erosion rate and the parameters of erodents and target, that is,

$$E \propto \rho^{1.2} V^{2.4} D^{4.0} Ht^{-0.5} K_t^{-1.5} \qquad (5.7)$$

The only discrepancy between this model and the quasi-static model[16] is that the assumption of relationship between P/C (P: point load, C: crack length) and K_t differs. In the former model the relationship is $P/C^{3/2} \propto K_t$. In the latter model the empirical relationship is $P/C^{4/3} \propto K_t$. It further indicates that a more realistic fracture analysis is needed to modify these erosion models.

In fact, the most important factor in determining the erosion rate is the combined effect of density, velocity, particle size, hardness and toughness of erodents. Particularly, the erodent density is the most important factor in determining the material loss by erosion because the density of erodents is related to the kinetic energy of impingement. As shown in fig.5.5, the sets of data fit the functional dependency of U_k reasonably well, i.e. the slope of trend line is

1.23. The standard deviation is about 10%. This is consistent with the work done by Slikkerveer et al.[32]. Eqs. (4.1)-(4.4) are consistent with the data in Fig.5.5 with consideration of experimental deviation. They plot the erosion per particle against the kinetic energy per particle over a wide range of particle size (9-200μm) and particle velocities (20-300m/s). They observed that the erosion rate is proportional to the kinetic energy raised to power 1.23.

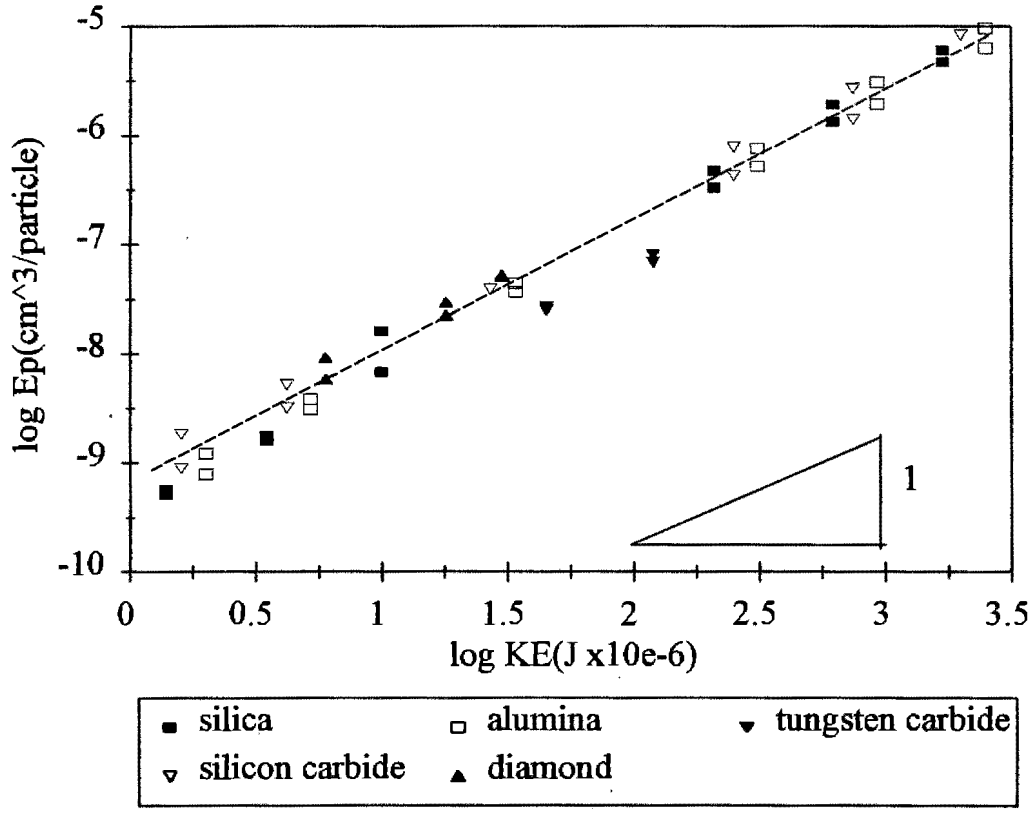

Figure 5. 5 Graph of erosion rate (Ep) of as received glass versus kinetic energy as indicated particles with different sizes at 90^0 incidence and at different impact velocities

5.1.1.3. The effect of impingement angle

The maximum erosion rate of glass at an impingement angle of 90^0 is observed as shown in figs. 4.41 to 4.43, which is a typical brittle mode of erosion. Single particle damage for glass impacted by an irregularly shaped particle is characterised by a highly deformed surface crater and radial and lateral cracks propagating from the contact area. Erosion of glass impacted with these particles at low angles occurs by minor chipping that is an order of

magnitude less than that at high angles as shown in figs. 4.77, 4.79, 4.81, 4.83 and 4.85. Fig. 5.6 shows a comparison between experimental results and theoretical consideration using Ep at 90° incidence times sin α ($Ep_{90°}$ X sin α). It indicates that over the range of impact angles, the theoretical curve has high values of erosion rate in comparison to the experimental curve. This is attributed to the maximum normal load available at 90^0 incidence for the propagation of surface or subsurface flaws. This is also consistent with a reduced component of normal velocity and is due to the strength degradation of glass diminishing as the impact occurs more obliquely[16].

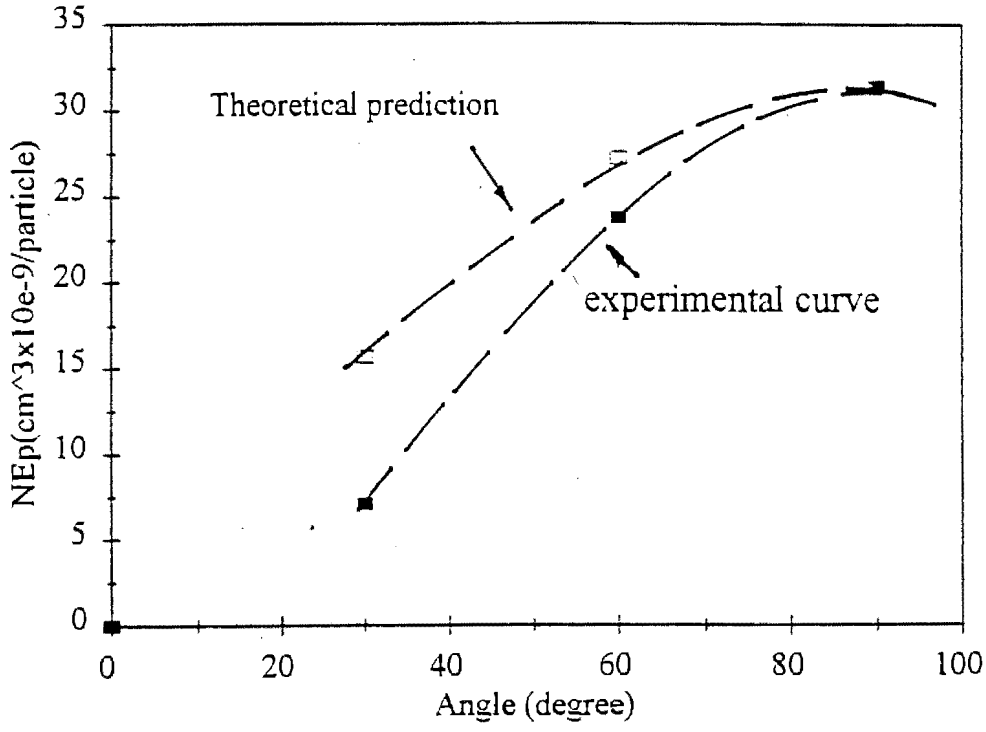

Figure 5. 6 Graph of erosion rate (NEp) of as received glass with diamond impact against impingement angles for a comparison between experimental results and theoretical prediction using Ep at 90° incidence times sin α

With spherical glass bead impact, there is a sharp increase in erosion rate at threshold angle as shown in figs. 4.42 to 4.43. The threshold angle transition shifts from the low angle regime to the high angle regime with decreasing impingement velocity and particle size. This is attributed to low impact load caused by a reduced normal velocity. At low angle impact, the erosion rate is less measurable, associated with plastic deformation controlled process by multi-particle impact. The material removal at high angle impact is related to the

mechanism of lateral cracks for small particles and related to the mechanism of Hertzian cone cracks for bigger particles at high impingement velocity. This is consistent with the graph shown in fig. 5.1.

5.1.1.4. The effect of erodent properties

The as received glass eroded by different erodents exhibits the difference of erosion rate in terms of the efficiency of crack initiation in the target by the erodents as shown in fig. 4.44. The as received glass eroded by nearly spherical steel shot exhibits the poorest erosion resistance. This may be ascribed to high kinetic energy dissipated by steel shot into the target due to its high density and toughness, which offsets the lower hardness of steel shot compared to the other erodents. In addition, the maximum mean pressure and duration of the elastic impact are 3.73 GPa and 0.724 μs for glass beads with a velocity of 45 $m.s^{-1}$. For steel shot, the maximum mean pressure and duration of the elastic impact are 9.44 GPa and 0.965 μs, which are higher than these found for glass beads. This generates a greater scale of Hertzian cracks and causes more damage.

For as rec.- glass eroded with angular particles (180-250μm), as shown in fig. 4.44, the glass eroded with tungsten carbide erodent exhibits the highest erosion rate since the tungsten carbide particles, having the highest density, have more kinetic energy to dissipate into the target. The erosion rate increases with increasing the ratio of erodent to target hardness for particles with similar density such as silica, alumina, silicon carbide and diamond erodents. This is due to the higher hardness and toughness of erodents, which gives them the larger ability to penetrate into target. The erodents with high toughness need more stress to be fragmented and thus cause more erosive wear than the friable erodents. This leads to higher residual crack driving forces for the initiation and propagation of micro-cracks.

Similar results to those obtained here are observed by Ballout et al.[30]. When impacting a glass target with alumina erodents and glass beads, lower erosion rates are found with glass beads than with alumina. They interpreted this result as being due to the shape of erodents. The spherical glass beads cause no cutting and less ploughing on impact than the sharp alumina particles. The results discussed above contradict those reported by Gulden[68]. They found little difference in erosion rate when impacting glass target with silicon carbide and quartz. They attributed this phenomenon to the fact that the ratio of hardness of erodent to

target is greater than 1. However, the experimental results in this study show that glass eroded with steel shot exhibits the highest erosion rate (Ep) although the steel shot is spherical and has the lowest hardness. This is because steel shot has higher maximum mean pressure (9.44 GPa) and duration (0.965μs) of the elastic impact.

Overall, the most important factor in determining the erosion rate for given impact conditions is the combined effect of density, hardness and toughness of erodents. The toughness of erodent is irrelevant when the hardness of erodent is much higher than that of target. The shape and kinetic energy of the particle determine the mode of erosion. However, the shape (spherical or angular) of erodents is not a major parameter in determining the erosion rate if the mode of erosion for spherical erodents is associated with Hertzian cracks.

5.1.2. Thermally tempered glass

The erosion rate for the tempered glass eroded by glass beads and SiC erodents is lower than that for as received glass. This is attributed to the introduction of residual compressive stresses into the surface by the tempering process[143]. The existence of the surface compressive stress effectively reduces the magnitude of the stress intensity factor at the tip of a median/radial crack due to an externally applied tensile stress due to impact[173]. However, ref. 173 did not fully understand the difference in residual stress as measured by Vickers vs.Hertzian indentation but believed it was due to in part to median/radial cracks grow into a region of decreasing compressive stress whereas the initiation of the Hertzian cracking is dependent upon the surface stress. The critical load required to cause the crack formation is higher for the tempered glass than that for the annealed glass. In addition, the compression imposes a net closure force on all pre-existing surface flaws and inhibits the initial extension of cracks as shown in fig. 5.7 so that the load required to nucleate a radial crack in the tempered glass is higher than that in the as-received glass, which therefore improves resistance to degradation.

The ratio of erosion rate between as received glass and the tempered glass was greater for glass bead impact than SiC impact. It is suggested that there is different cracking behaviour

of glass when impacted with spherical and irregular erodents. The spherical glass beads set up elastic Hertzian stress fields in the target which initiate cone cracking. The angular SiC particles produce inelastic deformation zones and initiate median and lateral cracking. Wiederhorn and Lawn[16] observed that the fracture strength of glass is higher with spherical glass bead impact than with angular silicon carbide erodent impact. It is also estimated the residual surface compressive stress in the thermally tempered glass with spherical indenters is 280 +/-180MPa, whereas the estimated value from the Vickers indentation cracking is 60 +/- 5 MPa[173]. The discrepancy is that the cracking caused by spherical indenters is controlled by the surface flaws, whereas the median/radial cracking under a pyramidal indenter is affected by the compressive stress distribution over the entire surface area of the crack. It is concluded that the compressive stresses are more effective in negating the increase of Hertzian stresses which have a maximum value in the radial direction around the periphery of the contact area and produce ring cracks.

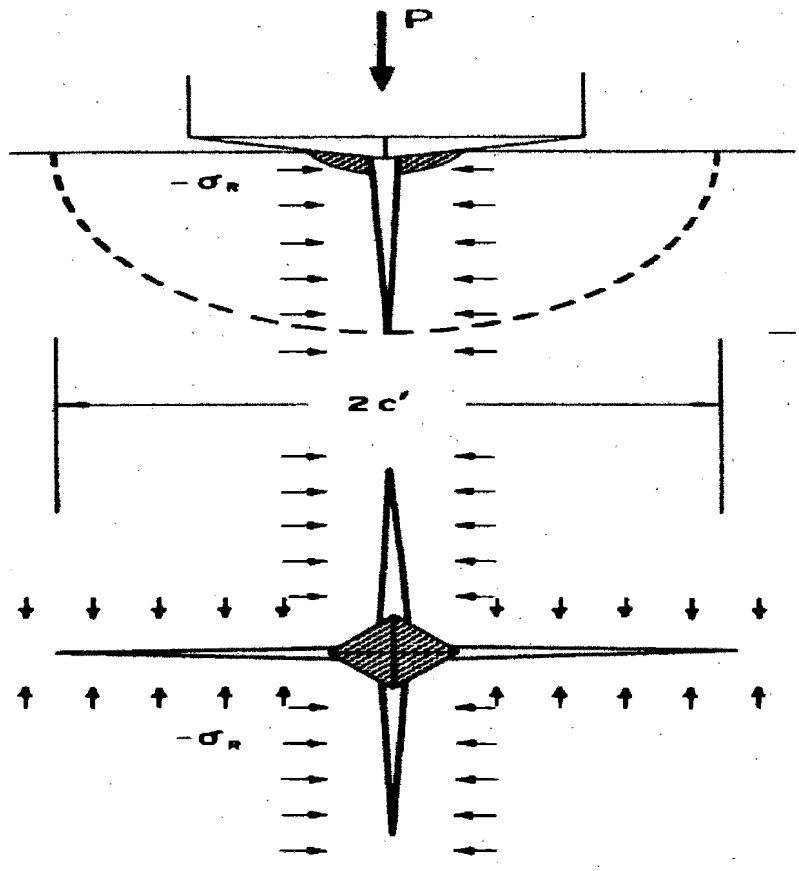

Figure 5. 7. Fracture pattern associated with Vickers diamond pyramid indentation on tempered glass surface, showing views in section (top) and plane (bottom). "Median" cracks initiate from central deformation zone (shaded region) and develop as half-pennies along indentation diagonals. Indentation field drives the cracks, residual tempering field opposes them. (after Marshall et al.[169]).

5.1.3. 304 Stainless steel

5.1.3.1. Examination of eroded surface

Detailed examination of S.E.M. images reveals that the mode of material removal for the 304 stainless steel eroded by irregular shaped particles (shown in figs. 4.87 and 4.88) is ductile. This is shown by the presence of extruded material in the form of lips along the crater rims which are then removed by subsequent impacts. At 30^0 incidence, the material removal occurs from ploughing and cutting type craters, which is in agreement with the work done by Finnie[11] and Hutchings[13]; the erosion of ductile metal by irregularly shaped particles at grazing angle of incidence is generally accepted as being due to a cutting or shear mechanism. At 90^0 impact, the fracture surface contains deep grooves and lips of materials that are fractured and flattened by successive particle impact. The deformation of the surface layer is more pronounced for 90° incidence than 30° incidence as shown in figs 4.24 and 4.25. The work hardening of the surface layer reduces the ability of the target material to deform during impact, thereby favouring fracture. Material will be removed once cracks have formed and propagate in the severe plastic zone during successive impacts[12]. In addition, the surface roughness after multiple impact enhances the probability of material removal by cutting and shear fracture. Once the surface is roughened, particles strike the surface locally at a variety of angles and at grazing angles volume is removed[38]. Particularly for the diamond erodent, the indentation type craters are most frequent at 90° incidence as shown in fig. 4.88(e). The eroded surface exhibits the heavily deformed and ruptured characteristic of this mode of erosion.

EDS analyses of the eroded surface indicate the presence of elements that are in the erodents. This means that a tip or edge of an erodent particle that causes a crater and fracture remains in the 304 stainless steel surface. It also could be that complete particles of erodent bury themselves in the ductile 304 stainless steel. The tip or edge (debris) is pressed down into the surface during subsequent impact and bonded mechanically to the surface. This surface could easily nucleate a large number of subsurface cracks at the boundary between the debris and matrix. This erosion is promoted by the preferential crack growth between the debris and matrix[127].

5.1.3.2. Empirical correlation of erosion rate with particle velocity and size

The empirical correlation of erosion rate (Ep) of 304 stainless steel by alumina and SiC erodent impact with particle size and velocity can be expressed as $Ep = K'V^xD^y$ (presented in equations 4.5 and 4.6), where x is nearly 2.0 and y is nearly 3.0, which conforms with the value in the energy balance theory ($Ep \propto U_k (=0.5MV^2) = K' V^2 D^3$). This means that the erosion rate is mainly determined by the kinetic energy of the eroding particle. The experimental observations have shown that the velocity exponent for bigger particles is normally greater than 2.0 as shown in Table 4.7. This is consistent with the experimental observations by other researchers[12, 37]. Finnie et al.[27] found that a velocity exponent greater than 2.0 could be expected if the cutting depth of the particle is assumed as a function of the material strength. They indicated that flow stress (σ) is inversely proportional to depths (d') of cut of target ($\sigma \propto d'^{-1/2}$). Since $Ep \propto d'^3$ and $d'^3 \propto MV^2/d'^{-1/2}$, the erosion rate per particle (Ep) can be expressed as $Ep \propto V^{2.4}$. This means the velocity exponent is greater than 2.0.

The effect of velocity on the erosion rate for various particle sizes as shown in Table 4.7 shows a lower velocity exponent for smaller particles. This may be ascribed to the particle – fluid interaction and particle-material interaction. Firstly, the particle-fluid interaction. As the free stream velocity is increased, the particles tend to move out of the streamlines as their Reynolds number increases. These larger particles follow more closely straight-line trajectories. The small particles are more easily deflected away from the specimen because of their low inertia/drag ratio[27, 174, 175] and therefore fewer particles will strike on the target. Thus the material loss will be reduced for smaller particles, implying a lower velocity exponent for smaller particles. The second effect is the particle – material interaction. Hutchings[39] reports that during impact, the strain rate increases as the particle size decreases. Thus the target's flow stress is increased for small particles and they remove less material. Increasing impact velocity results in decreasing loading time and hence increasing the strain rate. Thus the smaller particles at high velocities will remove relatively less material which explains the lower velocity exponent.

In order to compare the constant K′ between the theoretical equation and empirical correlation, the constant K′ is calculated below. According to Finnie's theoretical equation[11, 12], the erosion rate per particle of 304 stainless steel can be expressed as

$$Ep \approx (MV^2/2)\ X\ (1/12\sigma)\ \cos^2\alpha \qquad \alpha > 18.5°$$

In this case, 304 stainless steel is impacted with SiC erodents at 30° incidence.
Assuming $\sigma = \sigma_y = 265M\ Pa = 265\ X\ 10^6 g/s^2\ cm$, thus Ep can have the following form

$$Ep \approx 0.0625\ (MV^2/2)\ X\ 1/\sigma = 1.97\ X\ 10^{-10}\ D^{3.0}V^{2.0} \qquad (5.8)$$

For alumina erodents impacting at 30°, the Ep can be expressed below:

$$Ep \approx 0.0625\ (MV^2/2)\ X\ 1/\sigma = 2.46\ X\ 10^{-10}\ D^{3.0}V^{2.0} \qquad (5.9)$$

Where the units of Ep, D and V are cm^3/particle, cm, cm/s respectively. According to theory proposed by Finnie et al.[38], the erosion rate at 90° will be approximately 25% of that at 20° -30°. Thus it is reasonably estimated that at 90° incidence, the erosion rate per particle for SiC and alumina impact may be expressed below:

For SiC erodent at 90° impact,

$$Ep = 1.97\ X\ 10^{-10}\ D^{3.0}V^{2.0} X\ 25\% = 5\ X\ 10^{-11}\ D^{3.0}V^{2.0} \qquad (5.10)$$

For Al_2O_3 erodent at 90° impact,

$$Ep = 2.46\ X\ 10^{-10}\ D^{3.0}V^{2.0}\ X\ 25\% = 6\ X\ 10^{-11}\ D^{3.0}V^{2.0} \qquad (5.11)$$

But the constant K′ for empirical correlation is the slope of straight line as shown in Appendix C and D. A comparison of the constant K′ between theoretical value and empirical correlation is presented in Table 5.2

Table 5.2. A comparison of the constant K′ between theoretical value and empirical correlation for 304 stainless steel

Erodent	Alumina (30°)	SiC(30°)	Alumina (90°)	SiC(90°)
Theoretical value (K′)	2.5×10^{-10}	2.0×10^{-10}	6.0×10^{-11}	5.0×10^{-11}
Empirical value (K′)		1.3×10^{-11}	3.2×10^{-12}	1.5×10^{-12}

By contrast, the constant K′ for 90° in empirical correlation is one order magnitudes less than that in theoretical equation. This is in agreement with the results obtained by Sarkar[176]. He performed the single impact tests on aluminium target and found that the crater volumes calculated from the diameter of the indentation and those calculated from the theory of the impact energy together with the shear stress do not correlate well. The actual erosion rate shows one orders of magnitude less than the calculated erosion rate. This discrepancy may be ascribed to the following effects. Firstly, not all the impact energy is dissipated in producing the crater. A great deal of the kinetic energy is dissipated in the deformation of the target without causing material removal. It is noted that the constant K′ at 30° incidence is one order of magnitude less for empirical correlation than theoretical prediction as shown in Table 5.2. The difference presented in Table 5.2 is bigger for 90° than 30°. This is due to less kinetic energy dissipated to work hardening at 30° incidence than at 90° incidence as shown in figs 4.24 and 4.25. Thus the empirical K′ for 30° incidence is more close to the theoretical K′. Secondly, the interaction of an individual particle is ignored during impact and all particles are assumed to impact the surface in the calculation of actual erosion rate per particle. The number of particles impacting a given target is estimated from the mass of SiC particles used, the mean particle size and density of the particles. Thirdly, the shape of ngular SiC particles is assumed spherical in the calculation of its volume. The fourth effect is that the mass of the small fraction of the embeddment of erodent is not considered in the calculation of the mass loss of target. Thus the constant K′ is lower for empirical correlation than in the theoretical equation.

Overall, the constant K′ is a parameter that is determined by an impingement angle, density of erodents and shape of erodents. The angular erodents with high density and impacting at an oblique angle have high K′. Erosion rate is higher for oblique angles than that for normal angles. This is because a tangential component of velocity is more available for cutting mode of material removal and is confirmed by Finnie[11, 12]. High-density erodents exhibit higher erosion rate due to higher kinetic energy. The erodent shape is one of the most important factors in determining erosion rate. The fact that angular erodents result in higher erosion rate than blunt particles is confirmed by Hutchings[39].

The erosion rate (Ep) increases with increasing particle size as shown in figs. 4.49 - 4.50. The particle size exponent is 3.0, suggesting that the erosion rate (Ep) is mainly determined by the kinetic energy of the eroding particle. However for consideration of erosion rate per gram (Eg), the erosion rate (Eg) increases with increasing particle up to certain size above which the erosion rate is not significantly influenced by particle size as shown in fig. 5.8. These results conform with many other results[177, 178, 179]. Our interpretation for size effect is as follows. The cutting model of erosion developed by Finnie[11] indicated that for the same amount of erodent mass, the total kinetic energy is the same provided that other conditions are the same during erosion. This should result in the same volume loss of the target. However, small particles do not possess sufficient momentum to follow the original direction of the gas movement when nearing the target, i.e. significant numbers of particles are deflected away from the specimen[174, 175]. This means small particles do not have enough kinetic energy due to their low mass, thus showing their size effect. In addition, the particle size affects the strike process through increased strain rate for smaller particles[39]. Hutchings[39] performed the single impact studies of low – carbon steel target using a very hard steel projectile. He found that the strain rate is increased above $10^5 - 10^7$ sec^{-1}. Thus the material's flow stress is increased for small particles, suggesting less material loss.

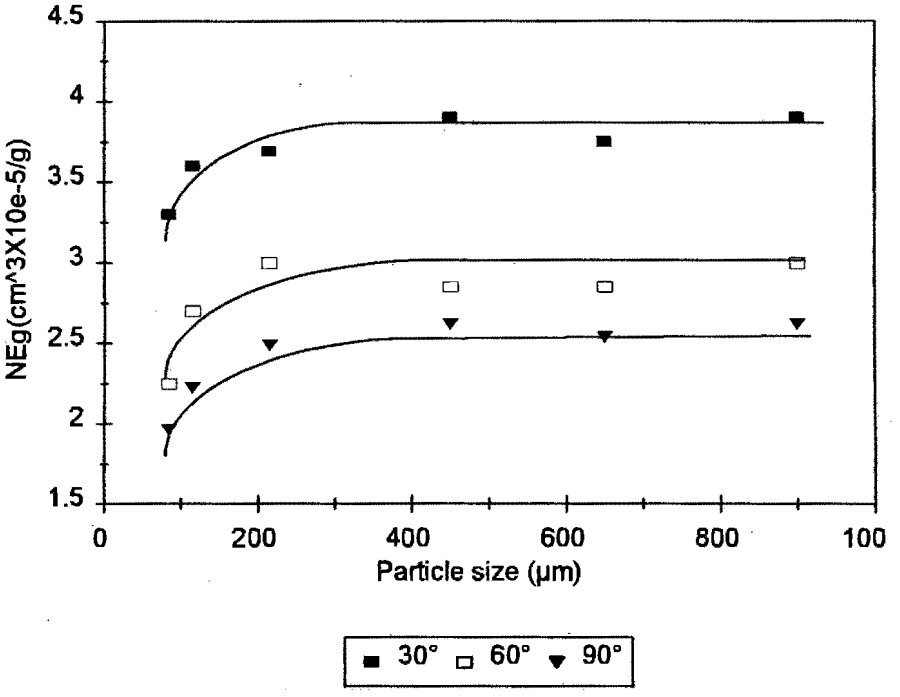

Figure 5. 8 Graph of erosion rate (NEg) per gram of 304 stainless steel as a function of particle size for SiC erodent impacting at different angles and at an impingement velocity of 45 $m.s^{-1}$

5.1.3.3. The effect of impingement angle

For 304 stainless steel, maximum erosion rate occurs at oblique angle shown in fig. 4.51, which is a typical ductile mode of erosion. This is consistent with the work done by Hutchings et al.[114] and Finnie et al.[37]. Finnie et al.[37] has modelled the angle effect for ductile materials. Good agreement was found between theory (based on metal cutting theory) and experiment for impingement angles up to 75°. They indicated that for ductile materials, the maximum erosion rate occurs at an angle of 15-20°. The micrographs of eroded surface of 304 stainless steel show that at an oblique angle impact, a ploughing or shearing action is most pronounced as shown in fig. 4.87 and 4.88. Normal incidence gives more of indentation deformation due to an intense deposition of kinetic energy. The deformation generally causes strain hardening of the surface. Material will be removed once cracks have formed and propagate in the severe plastic zone during successive impacts[12]. In addition, a particle directed towards a surface at 90° may impact with an actual impingement angle that is much less once the surface is roughened. The surface roughness after multiple impact enhances the probability of material removal by cutting and shear fracture. In fact, a single mechanism (cutting mechanism) cannot fully account for the material removal at 90°

incidence. Cutting mechanism and accumulated plastic deformation is operative during erosion at 90^0 incidence[3, 47, 48, 49, 50, 62].

5.1.3.4. The effect of erodent properties

The most interesting result of this investigation is the fact that a low erosion rate of 304 stainless steel eroded by diamond erodents is observed at 90^0 incidence over all velocities as shown in fig. 4.47. It is noted that the diamond erodents are of high hardness and toughness as shown in Table 3.3. The erosion rate increases with increasing density of erodents except diamond erodent as shown in fig.4.54. Based on the energy balance theory ($Ep \propto U_k \propto 0.5MV^2$), high density results in high kinetic energy which causes more material loss. The density of diamond is greater than that of silica and silicon carbide erodents. However, the erosion rate of 304 stainless steel impacted with diamond shows lower erosion loss than that of silica and silicon carbide erodents. These results therefore confirm that density of erodents is not the sole criterion which determines the erosion resistance of materials. The lower erosion rate may result from the blocky shape of diamond, i.e. the shape of erodents plays an important role during erosion, which is consistent with the work done by Hutchings[39]. He indicated that the angular particles cause more erosion than spherical particles since the different effect of "rake angle" (the angle between the front face of the particle to the normal to the target surface) caused by angular and spherical particles. A difference in rake angle caused a change in erosion mechanism from a ploughing or smearing type of impact crater with large rake angles to a micro-cutting mechanism at small rake angles. For spherical particles, the rake angle is always large and negative. In this case, the fracture pattern of 304 stainless steel eroded by diamond erodents show heavily deformed rupture but less effective cutting due to its blocky shape.

In addition, it is observed that the surface is work-hardened to a very high degree by erosion. The formation of a work-hardened surface layer as a result of impact by particles is evaluated as shown in figs. 4.24 and 4.25. It is noted that the 304 stainless steel with all the erodents' impact exhibits work hardening and develops successively work-hardened subsurface layers. Particularly, the erosion of 304 stainless steel with diamond at 90^0 impact causes greater degree of work-hardening as compared to the other erodent impact. The

diamond erodents dissipate more kinetic energy to work hardening the surface of 304 stainless steel and do little cutting or ploughing during impact. The successive impact on the surface will deform the crater around the indentation up to a level where that of the next impact exceeds the strain required for fracture or chip formation and eventually leads to the material removal. In other words, a significant amount of subsurface deformation can be experienced for diamond erodent impact prior to the commencement of the loss of material compared to the other erodents. Thus the steady state erosion rate is low. The erosion resistance at 90^0 incidence is also determined by the extent of work hardening and the hardness that its surface attains as a result of the repeated impact by the eroding particles. It is therefore concluded that erosion rate is strongly dependent on the particle shape and the extent of surface deformation. This is in disagreement with Talia, Ballout and Scatergood[180]. They investigated the erosion of pure Al and Al-12Si alloy surface with sharp angular alumina and spherical glass bead impact and found that the lower erosion rate for glass beads than alumina may be attributed to the differences in hardness and density.

It is noted that at 30° impact, the erosion rate of 304 stainless steel is greater for diamond erodent impact than for silica erodent impact. It indicates that the effect of erodent shape at 30^0 incidence on erosion rate decreases compared to at 90^0 incidence. The material removal will occur when the target reaches a critical strain, which is in agreement with the results observed by Hutchings[13] and Sundararajan et al.[14]. They assume that once the lip forms its fracture occurs easily during subsequent impacts and hence lip formation controls the erosion rate.

When the target surface hardness is much less than the particle hardness, the hardness and toughness of erodents have little effect on the erosive behaviour of 304 stainless steel as shown in figs.4.52 and 4.53. This is in agreement with the work done by Raask[181]. The independence of erosion rate on hardness difference has been explained by the high strain rate of the erosive process[34] (10^5 - 10^7 sec^{-1}) and by the degree of work-hardening achieved by the erosive process. However, Levy et al.[117] found an increase in erosion rate for particles up to 700 HV hardness but for particles harder than this the erosion rates remain constant. Goodwin et. al.[121] found a linear increase of erosion rate with particle hardness up to 2150 HV. The experimental results in this study indicate that the erosion rate is mainly determined by the shape of erodent and then is determined by the erodent density for all

irregularly shaped particles. The hardness and toughness of erodents have little effect on the erosive behaviour of 304 stainless steel.

5.1.4. WC-7%Co

5.1.4.1. Examination of eroded surface

The mode of erosion loss of WC-7%Co is generally associated with impact craters found on eroded surface. The surface morphologies of WC-7%Co indicate that the areas of cobalt between the WC grains render the material susceptible to loss by impacting erodents. The material removal for silica impact initiates by extrusion of the cobalt phase. Removal of the exposed carbide grains occurs when there is no longer sufficient cobalt to retain them. Little WC grain fracture is noted, thus indicating that a ductile mode of erosion predominates for silica erodent impact. However, the occurrence of brittle fracture of the WC grains increases with increasing the hardness of erodent particles as shown in fig. 4.90. The SEM examination of the eroded surface revealed the fractured WC grains and the cobalt material forming "ploughing" and "cutting" craters as described by Hutchings[39] for ductile material erosion mechanism. Similar observations were made by Ball et al.[96] and other researchers[97, 98, 99] for erosion of several different WC-Co grades. Much of the cobalt deforms plastically and work hardens as it is subjected to increasingly higher stresses, eventually the preferential removal of cobalt followed by pullout of the unsupported and fractured WC grains. The eroded surface suggested that the transition from the "ductile" to "brittle" mode of erosion for WC grains was found with increasing the hardness of erodent particles as shown in fig.4.90 and that both ductile and brittle modes contribute to the overall response.

5.1.4.2. Empirical correlation of erosion rate with particle velocity and size

The empirical relationship between erosion rate per particle (Ep) of WC-7%Co impacted with SiC and particle velocity and size has the form $Ep = K' V^x D^y$, where x is nearly 2.0, y is 3.0, and K′ is 2.4×10^{-12} obtained from Appendix D. Using the similar methods described

in Section 5.1.3.2, the theoretical correlation for erosion rate per particle of WC-7%Co can have this form: $Ep=14.8X10^{-12}V^2D^3$. This means that the erosion rate is mainly determined by the kinetic energy of the eroding particle. The discrepancy is the same as that discussed in Section 5.1.3.2.

If erosion is viewed to vary simply as a phenomenon involving transfer of kinetic energy of the erodent particles, one would logically expect a velocity exponent of 2.0. However, The values of velocity exponents for other erodents (180-250μm) derived from fig. 4.55 are 1.1 $\pm$ 0.2, 1.5 $\pm$ 0.2, 1.6 $\pm$ 0.1, 1.9 $\pm$ 0.2 and 1.9 $\pm$ 0.1 for silica, alumina, WC, SiC and diamond erodents respectively. It shows that velocity exponent decreases with decreasing relative hardness and relative toughness of erodents. This is ascribed to the fragmentation of erodents as shown in figs. 4.29 to 4.33. Fragmentation of erodents leads to less kinetic energy to dissipate into the target so that the velocity exponent is less than 2.0. In fact a velocity exponent less than 2 has also been observed in WC-Co, ceramics as well as metallic materials[100].

The slopes of erosion rate per particle (Ep) increase with increasing particle size and then tend to decrease with further increasing particle size as shown in fig. 4.56. This may be due to severe fragmentation of the very large erodents. Large particles are statistically more likely to contain flaws than small particles, which will increase the probability of the large particles shattering on impact with the target surface. Less energy is dissipated into the target so that the slopes of erosion rate per particle decrease with further increasing particle size.

5.1.4.3. The effect of impingement angle

For WC-7%Co, maximum erosion rate occurs at 90^0 angles as shown in fig. 4.57, which is in agreement with the work done by Ball et al.[96] and Conard et al.[98]. They observed that the maximum erosion occurred at normal impact angle for all cobalt content (4.5-11.3% wt). The experimental results suggest that the erosion is predominately brittle. However, the erosion rate (Ep) for WC-7%Co has the form $Ep \propto V^2D^3$. This means that the ductile erosion of cobalt controls the process of erosion. The material removal mechanism is

microcutting as shown in fig. 4.89. Many of tungsten carbide grains are contained entirely in the volume of microcutting chips with dimensions exceeding the carbide size. The formation of the impact site is due mainly to the extrusion of cobalt and the displacement of the WC grains. Once sufficient cobalt has been removed from between the WC grains, the fracture strength of the surface layers decreases. This eventually results in pullout of the unsupported and fractured WC grains. Since the fraction of cobalt is much smaller than that of WC, a large amount of pullout of unsupported and fractured WC results in the occurrence of maximum erosion rate at 90° impact. In fact, the mode of erosion of WC-Co alloys is associated with a combination of ductile and brittle mode.

5.1.4.4. The effect of erodent properties

The erosion rate decreases in the order of erodents diamond, SiC, alumina, WC and silica as shown in figs 4.58 and 4.59. This suggests that erosion rate increases with increasing the hardness of erodents. The examination of eroded surface also indicates that the mode of fracture surfaces vary with the hardness of erodents. With increasing hardness of erodent, the eroded surface of WC-7%Co exhibits increasing evidence of fractured WC grains as shown in fig. 4.90, suggesting that the brittle fracture of the WC grains is dominant. Erodent with high hardness and toughness have less fragmentation as shown in Figs. 4.28-4.33. This indicates that the relative hardness of erodents and targets play a significant role in determining the erosive loss.

Softer erodents are prone to plastic deformation during impact and the amount of energy available for erosion of target is decreased. Thus the erosion rate is relatively lower. When the erodent hardness is similar to that of target, the ease of fracture initiation and propagation is a rate controlling factor of erosion and repeated impacts are required for material removal. For example, the silica and WC erodents have lower ability to penetrate into the WC-Co than SiC and diamond erodents as their hardness are lower than that of SiC and diamond erodents as shown in fig. 4.58. This leads to less material removal for softer erodents. The higher the hardness and toughness of the erodents, the more efficient they are at initiating cracks in the target. This effect is similar to the findings of Wada et al.[110] who have shown that the properties of erodent particles affect the erosion rates and that the

erosion rates increase with increasing particle hardness. According to the energy balance theory ($Ep \propto U_k \propto \rho V^2 D^3$), the erosion rate increased with increasing the density of particles. However, the experimental results show that the erosion rate is not directly proportional to the density of erodents as shown in fig 4.60. The erosion loss of WC-7%Co impacted with WC is less than that of WC-7%Co impacted by SiC and diamond although the WC erodent with high density has high kinetic energy. This is because the WC erodent has similar hardness of WC grain in the WC-7%Co alloy and thus result in lower ability to penetrate into the surface of WC-7%Co.

It is concluded that the relative hardness of particles plays an important role in determining the mode and mechanism of material removal for WC-7%Co alloy.

5.1.5. Alumina

5.1.5.1. Examination of eroded surface

The SEM micrograph of a polished surface of alumina shows the extent of porosity in fig. 3.1(d). In general, fracture can originate from inhomogeneous regions such as pores and grain boundaries when a sample is eroded. Pores in alumina are sites where cracks can initiate during erosion. Damage there occurs without the need for crack initiation. From single impact site shown in fig. 4.91, it is noted that the damage zones are characterised by a relatively deep pit formed primarily through plastic deformation and intergranular cracking with no evidence of any radial or lateral cracking around this zone. This is due to the weakness of the grain boundaries. The stress pulse loosens grains in the region of the contact and is not concentrated sufficiently to nucleate and propagate lateral and radial cracks, i.e. the contact stresses at the impact site did not exceed the threshold for indentation fracture. Ritter et al.[103] and Srinivasan[182] et al. report similar intergranular fracture of eroded sintered alumina.

The steady state eroded surface of alumina eroded by silica erodents shows plastic and intergranular spallation as shown in fig. 4.92(a). The steady state erosion surfaces of alumina eroded by alumina, WC, SiC and diamond exhibited more extensive intergranular spallation and grain ejection as shown in fig. 4.92(b)-4.92(e). It is concluded that the steady state eroded surface of alumina after erosion by different erodents were very similar.

differing only in the ratio of plastic deformation to fracture. The severity of damage pattern is dependent upon each erodent/target combination.

5.1.5.2. Empirical correlation of erosion rate with particle velocity and size

The empirical correlation (equations 4.7 to 4.10) between erosion rate (Ep) of alumina and particle velocity and size has the form: $Ep = K' V^x D^y$, where x is 1.5, 2.2, 2.2 2.1 for silica, alumina, SiC and diamond respectively, y is 2.6, 3.7 3.9 and 4.0 for silica, alumina, SiC and diamond respectively. The value of the size exponent decreases with decreasing the hardness and toughness of erodents. The size exponent for diamond is 4, which is consistent with the value derived in equation 5.5. This indicates that no fragmentation of diamond erodents occurs.

There are two cases where the velocity exponent is greater than 2 and less than 2 as shown in fig. 5.9. When the hardness and toughness of erodents are less than that of target, like silica erodents, the value of velocity exponent is less than 2. This is due to severe fragmentation of silica erodents. When the hardness and toughness of erodents are greater than that of target, like the other erodents, the values of velocity exponent are greater than 2. This is because the efficiency of intergranular spallation is a controlling factor of erosion. At low velocity, the erodents have low ability to concentrate stresses and zones of irreversible deformation are small and shallow. Thus the damage zone is small and erosion rate is low. In other words, the effect of efficiency of intergranular spallation decreases with increasing particle velocity. This effect becomes relatively insensitive at higher velocity due to the high kinetic energy. Thus the velocity exponent is greater than 2.

The velocity exponent increases with increasing particle size up to 450 μm in diameter as shown in Table 4.8, which is in agreement with the results observed by Goodwin et al.[121]. This may be explained by particle - fluid interaction. As the free stream velocity is increased, the small particles are more easily deflected away from the specimen[27, 174, 175] and therefore fewer particles will impact on the target, thus the material loss will be reduced for smaller particles at a high velocity, implying a lower velocity exponent for smaller particles.

The velocity exponent decreases with further increasing particle size above 450 μm in terms of erodent fragmentation. The fragmentation of the larger particles is much more severe than that of the smaller particles. This results in less kinetic energy being transferred to the target per unit volume of erodent so that the velocity exponents are smaller for bigger erodents. This is in agreement with the works done by Scattergood et al[86].

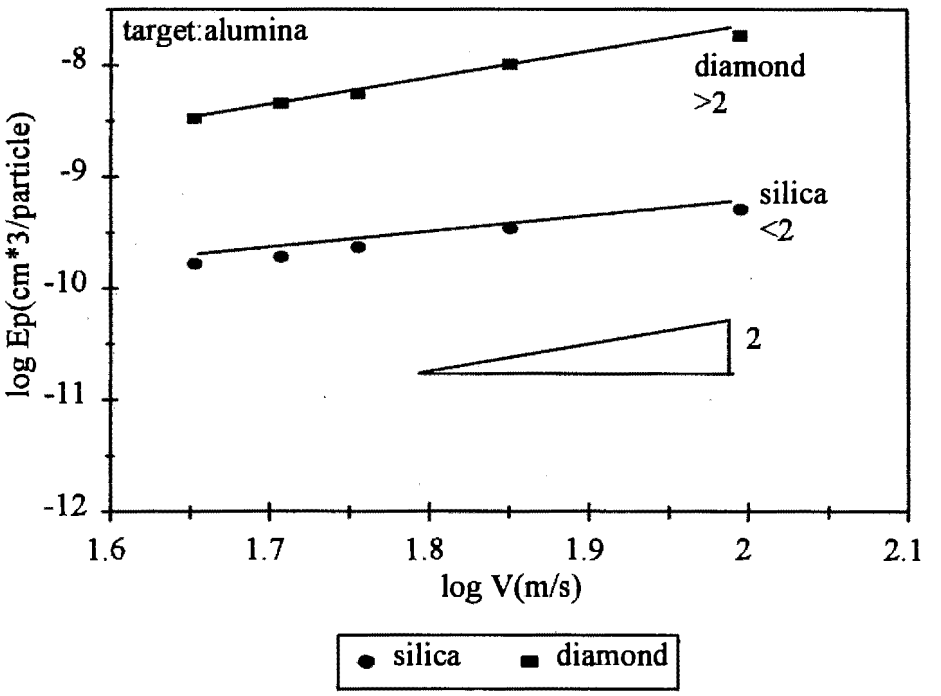

Figure 5.9. Graph of erosion rate (Ep) of alumina against impingement velocity of silica erodents and diamond respectively

5.1.5.3. The effect of impingement angle

Maximum erosion rate of alumina occurs at an impingement angle of 90° as shown in fig. 4.63. This is typical for a brittle mode of erosion. This is in agreement with the observation by Routbort, Scattergood and Key[183]. For oblique impact angles, the velocity V can be resolved into a normal component Vsinα and a tangential component Vcosα. Since the effect of the tangential component of the impact force is negligible, only the normal component Vsinα contributes to the erosion damage[15, 16]. Thus it is valid by incorporating the normal component Vsinα of velocity in place of V for the energy balance theory ($Ep \propto 0.5MV^2$). The erodents impacted at oblique angle have lower kinetic energy dissipated to

the target compared to at normal angle impact. Therefore, it is not surprising that they cause less erosion loss on the target materials.

5.1.5.4. The effect of erodent properties

The erosion rate (Ep) of alumina eroded by diamond is the highest, followed by WC, SiC, alumina and silica as shown in fig. 4.65. It suggests that the erosion rate increases with increasing the toughness of erodents. This is ascribed to the efficiency of intergranular spallation in the target by the erodent.

Since the toughness of erodent particles cannot be measured, the toughness values are based on bulk materials presented in Table 3.3. The lower hardness and toughness silica particles striking alumina target are themselves prone to plastic deformation and fracture on impact and the initial kinetic energy is apportioned between the target and the erodent particles so that less energy is available for erosion. Repeated impacts are required to build up sufficient residual stress to initiate fracture. This leads to less material removal. When the erodent hardness is similar to the target hardness, such as alumina eroded by alumina erodents, the ease of intergranular spallation is a rate controlling factor of erosion. Harder and tougher erodents like WC, SiC and diamond are less prone to plastic deformation and fracture on impact, which leads to high ability to concentrate stress and initiate fracture and crack propagation on surface. Thus the erosion rates are higher. From the energy balance standpoint, the erodents with high density will result in high kinetic energy which leads to more erosion loss. However, the erosion rate (Ep) is not directly proportional to the density of erodents as shown in fig. 4.66. It is noted that the WC erodent with high density does not cause highest erosion loss. This is because the toughness and hardness of erodents play an important role on impact. The toughness and hardness of WC erodents is less than that of diamond erodents. This means that less kinetic energy for WC erodent will transfer to the target due to its more plastic deformation or fragmentation compared to diamond erodents. The experimental results therefore indicate that hardness and toughness is of importance during impact.

5.1.6. Evaluation of materials

A comparative evaluation of the relative performance of all the target materials tested is shown in figs. 5.10 and 5.11. They show that the erosion resistance of the relatively softer 304 stainless steel is better than that of alumina and WC-7%Co target for hard erodents like silicon carbide erodents at impact angle greater than 40°. On the other hand the erosion resistance of the harder WC-7%Co and alumina is better than that of 304 stainless steel for soft erodents like silica. This is attributed to the fragmentation of erodents. As received glass always exhibits poor erosion resistance.

It is concluded that when the hardness of erodents is greater than that of target, stainless steel may be attractive candidate materials for the erosive wear problem at impact angle greater than 40°. WC-7%Co is better than 304 stainless steel at impact angle less than 40°. On the other hand, brittle materials and WC-7%Co are recommended for use when the hardness of erodent is lower than that of target.

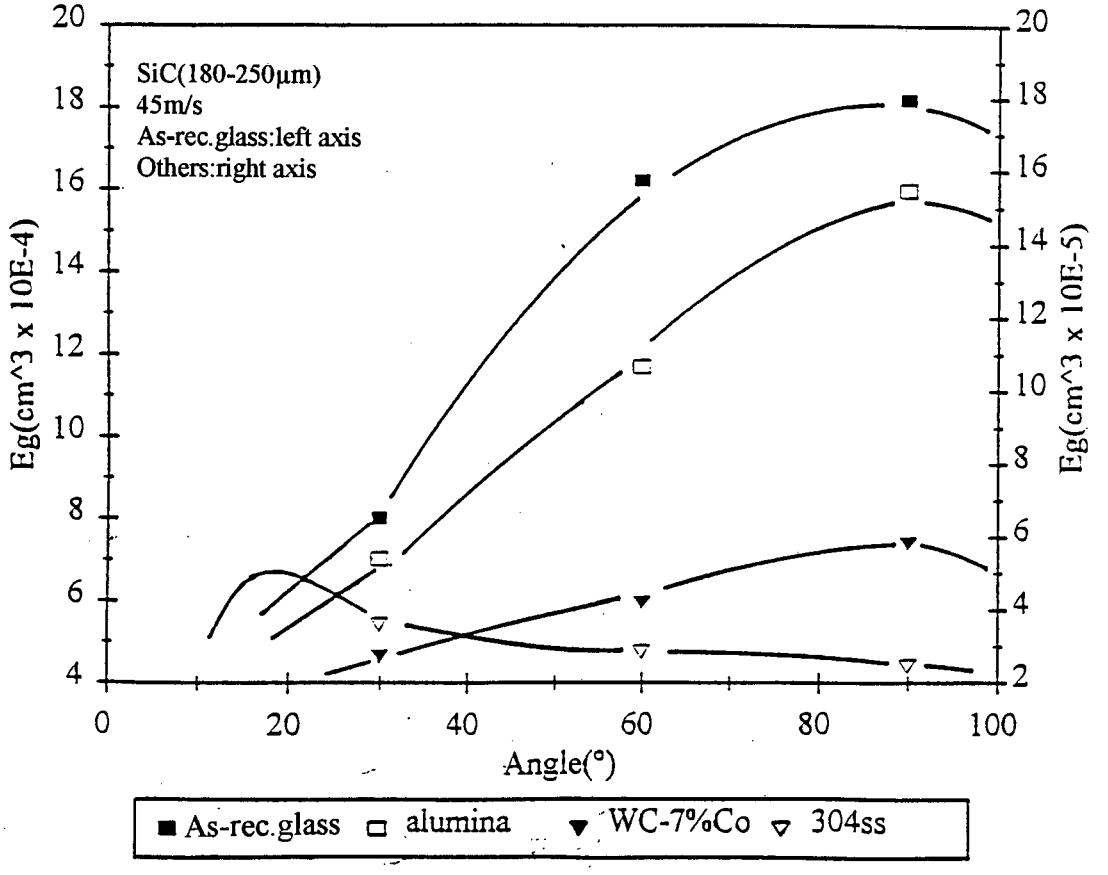

Figure 5.10. Graph of erosion rate (Eg) of materials versus impingement angle using SiC erodents.

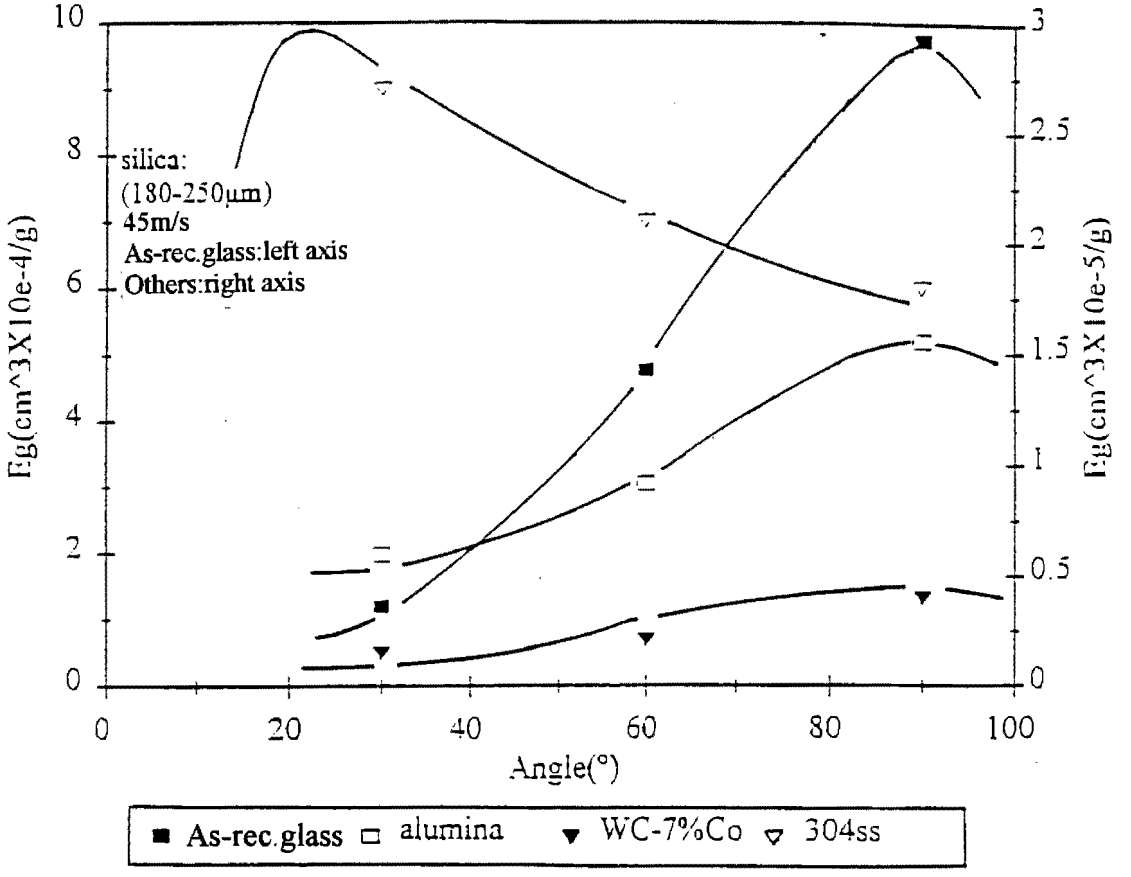

Figure 5.11. Graph of erosion rate (Eg) of materials versus impingement angle using silica erodents.

5.2. Cavitation erosion

The fracture surface during the cavitation erosion of glass is initiated at pre-existing microscopic surface flaws, which are enlarged by the removal of material as shown in fig. 4.94. After exposure to erosion for 12 minutes, the damage surface exhibits formation of cracks. In contrast, the amount and scale of surface damage of the tempered glass are less than that of as received glass. This is attributed to introduction of residual compressive stresses into the surface by tempering process. Such compression imposes a net closure force on all existing surface flaws and inhibits the initial extension of cracks. The compressive stresses in the tempered glass counteract the biaxial stress imposed by cavitation. With increasing time of cavitation, the fracture process is associated with the formation and interaction of enlarged flaws and cracks, which contrasts the Hertzian and lateral fracture produced by solid particle erosion.

The worn surfaces of WC-Co produced by cavitation erosion exhibit the mode of material removal. The carbide phase is much harder than the cobalt binder phases and therefore the binder is preferentially eroded followed by removal of carbide particles when there is no longer sufficient binder to retain these particles as shown in fig. 4.99. The cavitation erosion resistance of cobalt based tungsten carbide increases with increasing cobalt content over the range from 7% to 15% in this present study. It is proposed that the state of stress is an important factor in controlling erosion resistance. Residual stresses are considered to exist in the cemented carbides due to the differences in coefficients of thermal contraction[184]. On cooling from high temperature, the carbides are subjected to a triaxial compressive stress and the binders are subjected to a triaxial tensile stress. In addition, the plastic constraint of the cobalt matrix increases rapidly as the mean free path diminishes. With decreasing cobalt content, a rapid increase in the contiguity of WC-Co, which leads to a large increase in the rigidity of the carbide skeleton and the carbide phase has a greater ability to withstand the transition induced stresses which result from $\alpha \rightarrow \varepsilon$ phase transition in the WC-Co cermets[147]. The effect promotes cracking at the carbide-matrix interface and offsets any benefit derived from hardening of the binder due to an increase in plastic constraint. This leads to an increase in erosion rate of cobalt based tungsten carbide with decreasing cobalt content. In addition, corrosive mechanism may also operate during cavitation erosion of WC-Co. A low % of Co means relatively high tensile stresses in the Co phase. The WC grains are in mechanical contact (contiguity) with each other, preventing them from following the contraction of Co. This emphasises stress corrosion. Increased content of Co leads to lower tensile stresses since the contiguity reduces with Co content.

Better performance of stainless steel with respect to cavitation erosion resistance is ascribed to the transformation of austenite to martensite[142]. The erosion mode is one of ductile fractures as shown in fig. 4.97. In contrast, the cavitation erosion rates of Cromanite are lower than those for 304 stainless steel as shown in fig. 4.96. The hardness and work hardening rate of Cromanite™ is higher than that of 304 stainless steel. This may contribute to its superior cavitation erosion resistance. The contribution of work hardening rate to improving cavitation erosion performance has been reported by some workers[62, 142]. Ball[62] indicated that a high work hardening rate provides wear resistance during erosive or abrasive wear. The benefit of a high work hardening rate is that the flow stress increases with increasing strain, thereby prolonging the attainment of the fracture strain.

The alumina ceramic exhibits lower cavitation incubation time as shown in Table 4.10. This is due to its high porosity on the surface. A large number of pores on the surface serve both as initiation sites for cavity nucleation and erosion spreads by intergranular microcracking until the grains which are not well constrained by their neighbours spall off the surface as shown in fig. 4.101.

6. Conclusions

• Solid particle erosion

The mode of erosion for glass eroded by irregularly shaped particles is associated with the formation and interaction of lateral fractures. With spherical particle impact, the material removal is determined by particle size, impingement velocity and angle. The erosion map, where the velocity of spherical particles is depicted versus the average diameter of particles, has been constructed to categorise the types of damage observed in glass for impingement angles of 90° and 30°. WC-7%Co is associated with a combination of ductile and brittle modes of erosion. The erosion behaviour of 304 stainless steel is associated with cutting, ploughing and accumulation of deformation.

The empirical correlations between erosion rate per particle (Ep) impacting at 90° incidence and particle velocity and size have the form $Ep \propto V^x D^y$ where V is the impingement velocity and D is the particle size. The values of x and y are 2 and 3 respectively for materials like 304 stainless steel and WC-7%Co. A comparison of erosion rate between the experimental value and theoretical value shows that they do correlate well except for 304 stainless steel when eroded at 90° incidence. This discrepancy has been discussed. For brittle materials like glass and alumina eroded with diamond, the experimental values of x and y are 2 and 4 respectively. The departure of x and y from 2 and 4 respectively is ascribed to inefficiency of lateral crack initiation and propagation of glass or inefficiency of intergranular spallation of alumina. The semi-quantitive theoretical erosive model has been proposed to understand the empirical correlations.

For brittle materials like glass and alumina, the erosion rate is determined by kinetic energy, particle size and the relative hardness and toughness of the erodents and target. For ductile materials, the shape and kinetic energy of erodents are the most important factors determining the erosion rate. There is no or little effect of toughness and hardness of erodents on erosion rate.

For glass, alumina and WC-7%Co materials, the maximum erosion rate occurs at normal angle. For glass impacted with spherical glass beads, there existed an angle effect. The threshold angle transition shifts from low angle regime to high angle regime with decreasing impingement velocity. The maximum erosion rate for 304 stainless steel occurs at oblique angle.

A comparison of solid particle erosion resistance for these target materials reveals that the as received glass exhibits the highest erosion rate, followed by the tempered glass. The erosion resistance of 304 stainless, alumina and WC-7%Co depends on the ratio of erodent to target hardness. The erosion resistance of the relatively softer 304 stainless steel is better than that of alumina and WC-7%Co for hard erodents, like silicon carbide and diamond with impact angle greater than 40°. On the other hand the erosion resistance of the harder WC-7%Co and alumina is better than that of 304 stainless steel for softer erodents like silica erodents. Particularly, it reveals that compressive stresses are more efficient in preventing the formation and propagation of Hertzian cracks.

- **Cavitation**

The stainless steel exhibits better cavitation erosion resistance compared to glass, alumina and WC-Co in terms of a considerable transformation of austenite to martensite. In contrast, the erosion resistance of Cromanite™ is higher than that of 304 stainless steel due to its higher hardness and work hardening rate. The erosion rate of as received glass is greater than that of the tempered glass. This is attributed to introduction of residual compressive stresses into the surface by tempering process. Such compression counteracts the biaxial stress by cavitation. The cavitation erosion resistance of WC-Co is dependent upon the cobalt content.

- **Future work**

A semi-quantitative theoretical model has been developed to explain the empirical correlations for brittle materials. However, the assumption of model is based on elastic deformation which may be oversimplified. Thus this model needs to be improved based on indentation fracture mechanics although a more inelastic fracture analysis is admittedly a very difficult problem for impacting load.

Toughness of erodent is one of important factors in determining erosion loss of brittle materials. A new method for the measurement of erodent tough is needed. The search for a new method for quantitatively identifying of the shape of erodents is one of challenging subjects.

7. References

1. A.S.T.M., Standard Terminology Relating to Erosion and Wear, ANSI/ASTM G40-77, 1977
2. Hutchings, I M., *Journal of Microscopy*, **130,** 1983, 331
3. Bitter, J. G. A., *Wear*, **6,** 1963, 5
4. Bitter, J. G. A., *Wear*, **6,** 1963, 169
5. Uuemois H. and Kleis, I., *Wear*, **31,** 1975, 359
6. Smeltzer, C. E., Gulden, M. E. and Compton, W. A., *J.Basic Eng.*, **92,** 1970, 639
7. Neilson, J. H. and Gilchrist, A., *Wear,* **11,** 1968, 123
8. Hartung, J, B.and Horz, F.,.*The Moon*, **5**, 1972, 436
9. Mandeville, J. C. and James F. Vedder, *Earth & Planetary Science Letters*, **11**, 1971, 297
10. Secretan, L. and Berg, O. E., *J. Geophys. Res.*, **74**, 1969, 3681
11. Finnie, I., *Wear*, **3,** 1960, 87
12. Finnie, I., *Wear*, **19,** 1972, 81
13. Hutchings, I. M., *Wear*, **70,** 1981, 269
14. Sundararajan, G. and Shewmon, P. G., *Wear*, **84,** 1983, 237
15. Evans, A. G., Gulden, M.E. and Rosenblatt, M., *Proc. R. Soc. London*, **A361,** 1978, 343
16. Wiederhorn, S. M. and Lawn, B. R., *J. Am. Ceram. Soc.*, **62,** 1-2, 1979, 66
17. Verspui, M. A and Slikkerveer, P. J., *Wear*, **215**, 1998, 77
18. Verspui, M. A., With, G.de, Corbijn, A. and Slikkerveer, P.J., Simulation model for the erosion of brittle materials,conference paper ICEAW, September 1998
19. Wada, S. and Watanabe, N., *Yogyo-Kyokai-Shi*, **94**, 1986, 1157
20. Wada, S. and Watanabe, N., *Yogyo-Kyokai-Shi*, **95**, 1987, 468
21 Wada, S. and Watanabe, N., *Yogyo-Kyokai-Shi*, **95**, 1987, 573
22 Wada, S., Tani, T. and Kamigaito, O., *Mrs Int'l Mtg. On Adv. Mats.*, **5**, 1989, 481
23 Wada, S., Watanabe, N. and Tani, T., *Seramikkusu Ronbunshi*, **96**, 1988, 111
24 Wada, S., Watanabe, N. and Tani, T., *Seramikkusu Ronbunshi*, **96**, 1988, 755
25 Wada, S. and Watanabe, N., *Yogyo-Kyokai-Shi*, **95**, 1987, 976

26 Wada, S. Watanabe, N. and Ukyo, Y., *J. Japan Soc. Of Power Mett.*, **37-7**, 1990, 1074

27. Finnie, I., Wolak, J. and Kabil, Y., *J. Mater.*, **2**, 1967, 682

28. Buijs, M. and Pasmans, J. M., *Wear*, **184,** 1995, 61

29. Sheldon, G. L. and Finnie, I., *J. Eng. for Industry*, Trans, ASTM, **B88**, 1966, 387

30. Ballout, Y., Mathis, J. A. and Talia, J. E., *Wear*, **196**, 1996, 263

31. Verspui, M. A., Modelling Abrasive Processes of Glass, Ph.D thesis, Technische Universitieit Eindhoven, 1998

32. Slikkerveer, P.J., Bouten, P.C.P., in't Veld, F.H., Scholten, H., *Wear*, **217**, 1998, 237

33. Sparks, A. J. and Hutchings, I. M., *Wear,* **149,** 1991, 99

34. Hutchings, I. M., *Proc. Conf. on Corrosion/Erosion of Coal Conversion System Materials*, NACE, Houston, 1979, 394

35. Shewmon, P.G. and Sundararajan, G., *Annu. Rev. Mater. Sci.*, **13,** 1983, 303

36. Foley, T. and Levy, A., *Wear*, **91,** 1983, 45

37. Finnie, I. and Mcfadden, D. H., *Wear*, **48,** 1978, 18

38. Finnie, I., Stevick, G. R. and Ridgely, J. R., Wear, 152, 1992, 91

39. Hutchings, I.M., *Erosion: Prevention and Useful Applications*, ed., W. F. Adler, ASTM, STP664, 1979, 59

40. Hutchings, I. M., Winters, R. E. and Field, J. E., *Proc. R. Soc. London,* A**348,** 1976, 379

41. Smelter, C. E., Gulden, M. E., *USAAVLabs Tech. Rept.*, U.S.Army, 1970, 70

42. Christman, T. and Shewmon, P. G., *Wear*, A**52,** 1979, 57

43. Christman T. and Shewmon, P. G. *Wear*. B**54,** 1979, 145

44. Quadir, T. and Shewmon, P., *Metal Trans*, A**12,** 1981, 1163

45. Bellman, R. and Levy, A. V., *Wear*, **70**, 1981, 1

46. Suh, N. P., *Wear*, **25,** 1973, 111

47. Mamoun, M., *Argonne National Laboratory Rep.ANL-75-XX2*, App. I., 1975

48. Salik, J. and Buckley, D. H., *American Society of Mechanical Engineers*, New York, 1981

49. Finnie, I., Levy, A., and McFadden, D. H., *Erosion: Prevention and Useful Applications,* ed., W. F.Adler, 1979, 36

50. Brown, R., and Edington, J. W., *Wear*, **77,** 3, 1982, 347

51. Rao, P. V., Young, S. G., and Buckley, D. H., *Wear*, **85,** 1, 1983, 223

52. Rao, P. V., Young, S. G., and Buckley, D.H., *J.Microscopy*, **135,** 1, 1984, 49

53. Uetz, H. and Gommel, G. *Wear,* **9,** 1966, 282

54. Andrews, D. R. and Field, J. E., *J. Phys. D: Appl. Phys.*, **15,** 1982, 2357

55. Hutchings, I. M. and Winter, R. E., *Wear,* **27,** 1974, 121

56. Hutchings, I. M. and Winter, R. E., *Wear,* A. **34,** 1975, 141

57. Hutchings, I. M. and Levy, A. V., *Wear,* **131,** 1989, 105

58. Doyle R. A. and Ball A., *Wear*, **151**, 1991, 87

59. Levy, A. V., *The platelet mechanism of erosion of ductile metals*, Rep, LBL15240, Lawrence Berkeley Laboratory University of California, 1984

60. Brown, R., Jun, J. E. and Edington, J. W., *Wear*, **70**, 1981, 347

61. Jahanmir, S., *Wear,* **61,** 1980, 309

62. Ball, A., *Wear,* **91,** 1983, 201

63. Tilly, G. P., *Wear*, **14,** 1969, 63

64. Helms,H.E and Thrasher, S.R., *Engineering Applications of Ceramic Materials*, American Society for Metals, Metals Park, OH, 1985, 25

65. North, B., *Mater. Soc.*, 1984, 257

66. Jack, K. H., *Met, Technol.*, 1982, 297

67. Whitney, E. D., *Powder Metall. Int.*, 1983, 201

68. Gulden, M. E., P*revention and Useful Application.* ed., Adler, W. F., **664,** 1979, 101

69. Field, J. E. and Hutchings, I. M., *Proc. 3rd Conf. of Mechanical Properties Under High Rates of Strain*, Oxford, 1984

70 Ritter, J.E. and Jakus, K., Particle impact damage in glass from subthreshold to hypervelocity,(invited paper) World Ceramic Congress, Italy, June, 1998

71. Hertz, H., *Hertz's Miscellaneous Papers*, Chaps. 5 and 6, Macmillan, London, 1896

72. Routbort, J. L., Scattergood, R. O. and Turner, A, P. L., *Wear,* **59,** 1980, 363

73. Lawn, B. R., and Wilshaw, T. R., *J. Mater. Sci.*, **10**, 1975, 1049

74. Wiederhorn, S. M., Hockey, B. J., *Journal of Materials Science,* **18,** 1983, 766

75. Gulden, M. E., *J. Am. Ceram. Soc.*, **64,** 3, 1981,C56

76. Lawn, B. R., Hockey, B. J. and Richter, H., *J. Microsc.*, **130,** 3, 1983, 295

77. Evans, A. G. and Wilshaw, T. R., *Acta Met.*, **24,** 1976, 939

78. Johansson, S., Ericson, F., and Schweitz, J. A., *Wear,* **115,** 1987, 107

79. Breder, K. G., De Portu, G., Ritter, J. E., and Fabriche, D. D., *J. Am. Ceram. Soc.*,**71,** 9, 1988, 770

80. Gochnour, S., Bright, J. D., Shetty, D. K. and Cutler, R. A., *J. Mater. Sci.*, **25,** 1990, 3229

81. Murugesh, L., Srinivasan, S., and Scattergood, R. O., *J. Mater. Eng.*, **13,** 1, 1991, 55

82. Marrero, M., Routbort, J. L., *Wear*, A, **162-164**, 1993, 280

83. Griffith, A. A., *Phil.Trans. Roy. Sic.*, **221**, 1920, 163

84. Lawn, B. R. and Fuller, E. R., *J. Mater. Sci.*, **10**, 1975, 2016

85. Timoshenko, S. P. and Goodier, J. N., "Theory of elasticity" Chapt. 12 (McGraw-Hill, New York) 1970

86. Scattergood, R. O. and Routbort, J. L., *Wear*, **67,** 2, 1981, 227

87 Singh, T., Tiwari, S. N. and Sundararajan, G., *Wear*, **145**, 1991, 77

88. Morrison, C. T. and Scattergood, R. O., *Wear*, **111,** 1986, 1

89 Soderberg, S., Hogmark S. and Swahn, H., *Tribology International*, **12**, 1981, 333

90 Soderberg, S., Hogmark S. and Swahn, H., *Preprint No. 82-AM-4A-1 of the 37th Annual Meeting in Cincinnati*, 5, 1982

91 Hammarsten, A., Soderberg, S. and Hogmark, S., *Proc. of the Wear of Materials Conference*, ed. K.C. Ludema and published by ASME, 1983, 373

92. Larsen-Basse, J., *J. Metals.*, **35,** 11, 1983, 35

93. Fink, J. B., Hoenig, S. A. and Griffith, J. L., *Wear,* **108,** 1986, 97

94. Mohan, G. D. and Klamechi, B. E., *Wear,* **74,** 1981, 85

95. Ball, A., Willmott, S. and Resente, A., *Wear*, **123**, 2, 1987, 753

96. Ball, A. and Paterson, A. W., Microstructural Design of Erosion Resistance Hard Metals, Proceedings of the International Conferece on Recent Developments in Special Steels and Hard Metals, Rhodes Island, 1985, 377

97. Wright, I. G., Shetty, D. K. and Clauer, A. H., Proc. 6th Int. Conf. on Erosion Liquid and Solid Impact, Cambridge, Cavendish laboratory, **63,** 1983, 1

98. Conrad, H., Shin, Y. and Sargent, G. A., Proc. Int. Conf. Recent on Developments in Speciality Steels and Hard materials, Pretoria, South Africa, 1982, 423

99. Shetty, D. K., Wright, I. G., Stropki, J. T., A. S. L. E., Transaction, **28**, 1984, 123

100. Shetty, D.K., Wright, I. G. and Stropki, J. T. ASLE Transactions, **28**, 1, 1985, 123

101. Murugesh, L. and Scattergood, R. O. *Journal of Materials Science*, **26**, 1991, 5456

102. Vaughan, R. A. and Ball, A., *J. Hard Materials*, **2**(3-4) 1991, 257

103. Ritter, J. E., Rosenfeld, L. and Jakus, K., *Wear*, **111**, 1986, 335

104. Finnie, I., Corrosion-Erosion Behaviour of Materials ed., Nateson, K., New York, 1980, 118

105. Levy, A. V., *Wear*, **68**, 1981, 269

106. Shewmon, P. G., *Wear*, **68,** 1981, 253

107. Wilson, S. and Ball, A, Electron Microscopy Society of Southern Africa-Proceedings, **19**, 1989, 171

108. Budinski, K. G., *Wear of materials*, 1983, 311

109. Srinivasan, S. and Scattergood, R. O., *Wear*, **128,** 1988, 139

110. Wada, S., Watanabe, N., and Tani, T., J. Ceram. Soc. Jpn., ed.,Yogyo-kyokai-shi, **96**, 1988, 737

111. Sykes, M. T., Scattergood, R. O. and Routbort, J. L., *Composites*, **18**, 1987, 153

112. Morrison, C. T., Routbort, J. L. and Scattergood, R. O., *Mater. Res. Soc. Symp. Proc.*, **78**, 1987, 207

113. Foley, T. and Levy, A., the Effect of Heat Treatment on the Erosion Behaviour of Steel, Proc. Int. Conf. on Wear of Materials, 1983, 346

114. Hutchings, I. M. and Winter, R. E., *J. Phys. D: Appl. Phys.*, **8** 1975, 8

115. Winter, R. E., and Hutchings, I. M., *Wear,* **34,** 1975, 141

116. Sundararajan, G., *Wear*, **186-187**, 1995, 129

117. Levy, A. V. and Chik, P., *Wear*, **89**, 1983, 151

118. Head, W. J., Lineback, L. D. and Manning C. R., *Wear*, **23**, 1973, 291

119. Winter, R. E. and Hutchings, I. M., *Wear*, 29, 1974, 181

120. Misra A. and Finnie I., *Wear*, **65**, 1981, 359

121. Goodwin, J. E., Sage, W. and Tilly, G. P., *J. Basic Eng.*, **92**, 1970, 619

122. Tilly, G. P. and Sage, W., *Wear*, **16,** 1970, 447

123. Zhou, J. R. and Bahadur, S., *Wear*, **132,** 1989, 235

124. Hutchings, I.M., *J. Phys*, **10**, 1977, 179

125. Routbort, J. L., Helberg, D. A. and Goretta, K. C., *J. Hard Materials*, **1**, 2, 1990, 123

126. Brown, R. and Edington, J. W., *Wear*, **69,** 1981, 369

127. Brown, R. and Edington, J. W., *Wear* , **72,** 1981, 113

128. Levy, A. V., Aghazadeh, M. and Hickey, G., the Effect of Test Variables on the Platelet Mechanism of Erosion, Rep.LBL-17835, Lawrence Berkeley Laboratory, 1984

129. Gulden, M.E., Erosion: Prevention and useful applications, ASTM, STP 664, W. F. Adler Ed., 1979, 101

130. ANSI/ASTM G 32-77, **10**, 1980, 881, Annual Book of ASTM Standards

131. Thiruvengadam, A., ASTM, *Applied Mechanics Reviews*, **3**, 1971, 245

132. Rayleigh, L., *Philips. Mag.*, **34**, 1917, 94

133. Kornfeld, M. and Suvorov, L., *Journal of Applied Physics*, **15**, 1944, 495

134. Karimi, A. and Martin J. L., *International Metals Review*, **31**, 1, 1986

135. Vaidya, S. and Preece, C. M., *Metallurgical Transactions A*, **9A**, 1978, 299

136. Goebel, J. A. and Petit, F. S., *Metallurgical Transactions*, **11**, 1970, 1943

137. Thiruvengadam, A. and Waring, S., *J. Ship. Res.*, **10**, 1. 1966, 1

138. Hobbs, M. J., in erosion by cavitation or impingement, ASTM, STP, **408**, 1967, 159

139. Richman, R. H. and McNaughton, *Wear*, **140**, 1990, 63

140. Ahmed, S. M., Hokkirigawa K. and Oba, R., *Wear*, **177**, 1994, 129

141. Woodford, D. A., *Metallurgical Trans.*, **3**, 1972, 1137

142. Heathcock, C. J., Protheroe B. E. and Ball, A., *Wear*, **80**, 1982, 311

143. Rawson, H., Glasses and Their Application, 1991

144. Holloway, D. G., The Physical properties of Glass, London and Winchester, 1973

145. Luyckx, S. B., *Acta Metallurgical.* **16**, 1970, 535

146. Gurland, J. and Exner, H. E., *Powder Metallurgy*, **13**, 25, 1970, 12

147. Exner, H. E., *International Metals Reviews*, **243**, 4, 1979, 149

148. Roebuck, B., Almond, E. A. and Conttendon, A. M., *Materials Science and Engineering*, **66**, 1984, 363

149. Exner, H. E. and Gurland, J., *Power Metall. Int.*, **13**, 1970, 25

150. Gurland, J., *Trans. Metall.Soc.*, **227**,1146, 1963

151. Chermant, J. L. and Osterstock, F., *J. Mater. Sci.*,**11**, 1979, 1939

152. Roebuck, B. and Almond, E. A., *Int.Met.Rev.*, **33**, 1980, 90

153. Gurland, J., *Int.Met.Rev.*,**33**, 1980, 151

154. Kronberg, M. L., Acta Met., **5**, 1957, 507

155. Davidge, R.W., Mechanical behaviour of ceramics, ed, R. W. Cahn et al, Cambridge, 1979, 81

156. Evans, A. G. and Tappin, G. *Proc. Br. Ceram. Soc.*, **20**, 1972, 275

157. Ritter, J. E., *J. Am. Ceram. Soc.*, **67**, 11, 1984, 769

158. Shipway, P. H. and Hutchings, I., M., *Wear,***174**, 1994, 169

159. Ruff, A. W. and Ives, L. K., *Wear*, **35,** 1975, 195

160. Shipway, P. H. and Hutchings, I. M., *Wear*, **162-164,** 1993, 148

161. Annual book of A. S. T. M. Standards, 03.02, G32, 1993, 115

162. Speidel, M. O., High Nitrogen Steels, HNS 88, Proceeding of the international conference organised by the Metals, 5, 1988, ed. J. Foct and A Hendry, 92

163. Cass, T., Statistical Methods in Management, Cassell, London, 1974, 120

164. Auerbach, F., *Ann. Phys. Chem.*, **43,** 1891, 61

165. Chaudhri, M. M. and Walley, S. M., " Fracture Mechanics of Ceramics", ed. Bradt, R. C. plenum, **3,** 1978

166. Hamilton, B. and Rawson, H., *J. Mech. Phys. Solids,* **18,** 1970, 127

167. Finnie, I., *J. Mech. Phys. Solids,* **15,** 1967, 401

168. Fisher, G. M. C., J. *Appl. Phys.*, **38,** 1967, 1781

169. Marshall, D. B. and Lawn, B. R., *J. Am. Ceram. Soc.*, **16,** 1-2, 1978, 21

170. Griffith, A. A., Phil. *Trans. Roy.Soc.* **221,** 1920, 163

171. Ball, A, and McKenzie, H. W., *J. de Physique,* **4,** C8, 1994, 783

172. Vingsbo, O. and Hogmark, S., *Wear*, **100**, 1984, 489

173. Chaudhri, M. M. and Phillips, M. A., *Phil. Magazine* A, **62**, 1, 1990, 1

174. Laitone, J. A., *Wear*, **56**, 1979, 239

175. Laitone, J. A., *J. of Aircraft*, **16,** 12, 1979, 809

176. Sarkar, A. D., *Wear*, **87**, 1983, 173

177 Misra, A. and Finnie, I., *Wear*, **65**, 1981, 359

178 Sage, W. and Tilly, G. P., *J. Roy. Aer. Soc.*, **73**, 1969, 427

179. Ruff, A. W. and Wiederhorn, S. M. *Treatise Mater. Sci. Technol.*, **16**, 1979, 69

180 . Talia, J. E., Ballout, Y. A. and Scattergood, R. O., Wear, **196**, 1996, 285

181. Raask, E., Proc. 5th Int. Conf. On Erosion by Solid and Liquid Impact, Cambridge, 1979, 1

182. Srinivasan, S. and Scattergood, R. O., *Wear*, **142,** 1991, 115

183. Routbort, J.L., Scattergood, R.O. and Kay, E. W., *J. Amer. Ceram. Soc.*, **63,** 11-12, 1980, 635

184. Gurland, J. and Parikh, N. M., Fracture, Ed. H. Lebowitz, **2**, 1972, 841

Appendix A: A multiple linear regression

(1) Assumption: $Epi \propto V^b D^c$

To obtain the least squares estimates of the parameters of b and c. We minimize

$$Q = \Sigma (Epi - Epi^*)^2$$

where Epi^* is a observed result from experiment.

Setting the derivative of Q with respect to b and c respectively equal to zero gives

$$\partial Q / \partial b = 0$$

$$\partial Q / \partial c = 0$$

then the value of b and c can be obtained by solving the above equations simultaneously.

(2) Assumption : $Ep \propto \rho^a V^b D^c (Hp/Ht)^d (Kp/Kc)^e$

Using the same methods above, setting the derivative of Q with respect to a, b c, d, and e respectively equal to zero gives

$$\partial Q / \partial a = 0$$

$$\partial Q / \partial b = 0$$

$$\partial Q / \partial c = 0$$

$$\partial Q / \partial d = 0$$

$$\partial Q / \partial e = 0$$

then the value of a, b, c, d and e can be obtained by solving the above five equations simultaneously

APPENDIX B- Calculated impact parameters

Impact parameters of as received glass are presented in Table 1. The maximum mean pressure and radial tensile stress increase with increasing velocity of glass beads. The contact radius increases and the contact time decreases with increasing velocity.

Table 1. Calculated impact parameters

Size(μm) (glass beads)	Velocity(m/s)	Maximum mean pressure(GPa)	Radial tensile stress(GPa)	Contact radius(μm)	Contact time(μs)
63-106	45	3.73	1.08	9.60	0.14
	51	3.92	1.14	10.11	0.13
	57	4.10	1.19	10.58	0.13
	71	4.48	1.30	11.55	0.12
	99	5.11	1.48	13.20	0.12
106-125	45	3.73	1.08	13.16	0.19
	51	3.92	1.14	13.83	0.18
	57	4.10	1.19	14.46	0.18
	71	4.48	1.30	15.78	0.17
	99	5.11	1.48	18.00	0.16
180-250	45	3.73	1.08	24.50	0.35
	51	3.92	1.14	25.74	0.34
	57	4.10	1.19	26.90	0.33
	71	4.48	1.30	29.30	0.32
	99	5.11	1.48	33.0	0.30
400-500	33	3.30	0.96	45.30	0.77
	39	3.52	1.02	48.40	0.75
	45	3.73	1.08	51.30	0.72
	51	3.92	1.14	53.90	0.71
	57	4.10	1.19	56.30	0.69
600-700	33	3.30	0.96	65.40	1.11
	39	3.52	1.02	69.90	1.08
	45	3.73	1.08	74.00	1.05
	51	3.92	1.14	77.84	1.02
	57	4.10	1.19	81.40	1.00
800-1000	33	3.30	0.96	90.50	1.54
	39	3.52	1.02	96.80	1.49
	45	3.73	1.08	102.50	1.45
	51	3.92	1.14	107.80	1.41
	57	4.10	1.19	112.70	1.38

Appendix C Graph of erosion rate (Ep) of 304 stainless steel vs V^2D^3 for SiC and alumina erodents at 90° and 30° incidence

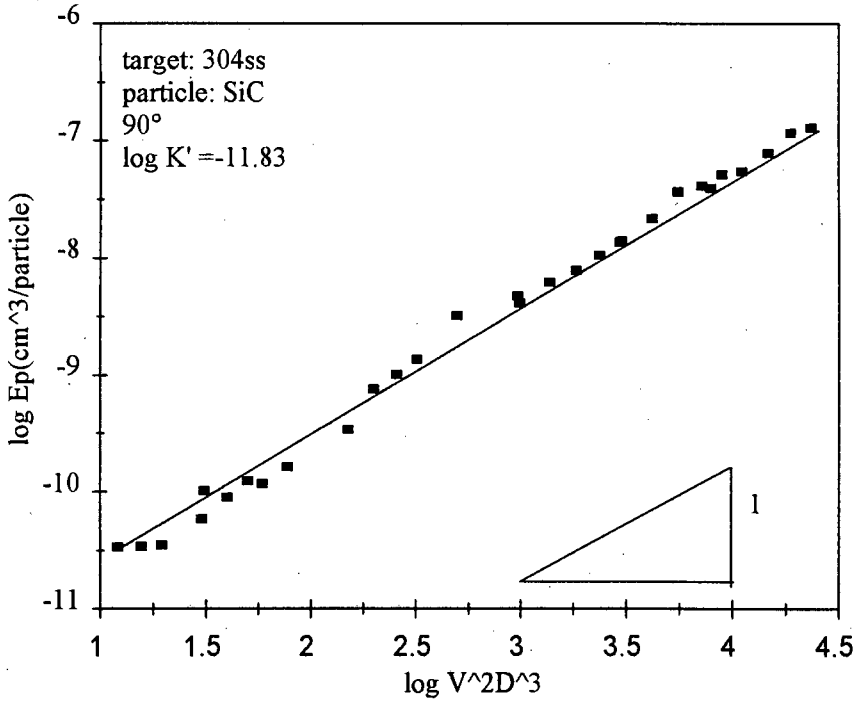

Figure 1. Graph of erosion rate (Ep) of 304 stainless steel vs V^2D^3 for SiC erodent impacting at 90^0

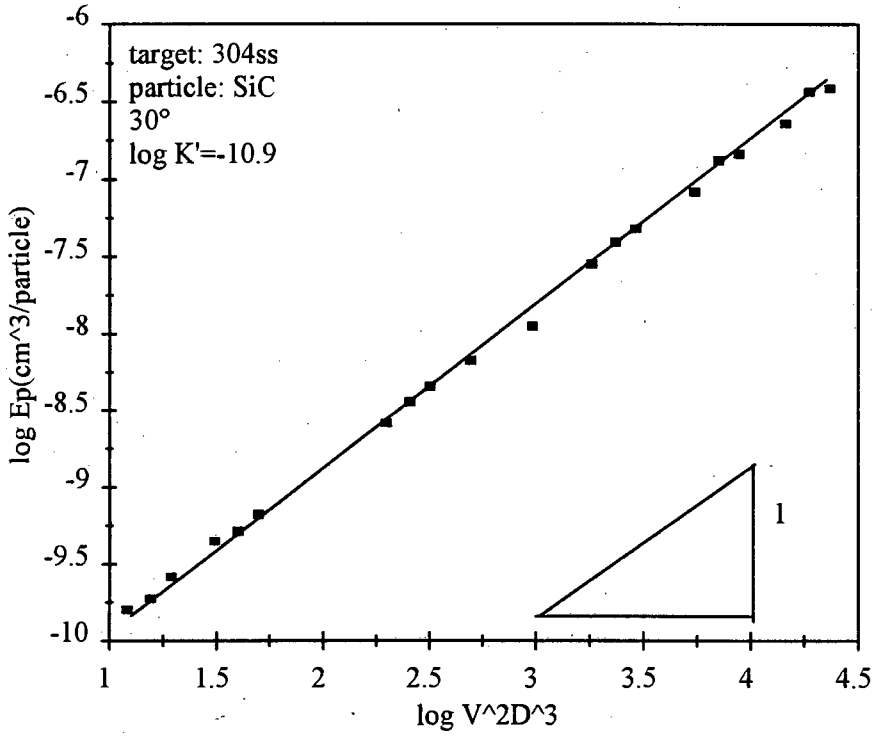

Figure 2. Graph of erosion rate (Ep) of 304 stainless steel vs V^2D^3 for SiC erodent impacting at 30^0

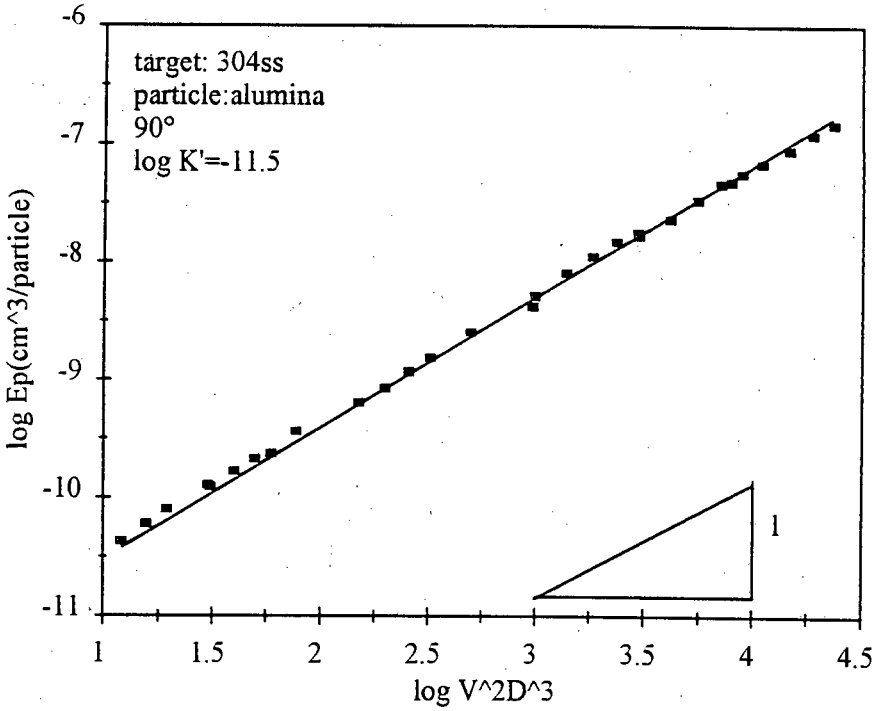

Figure 3. Graph of erosion rate (Ep) of 304 stainless steel vs V^2D^3 for alumina erodent impacting at 30^0

Appendix D. Graph of erosion rate(Ep) of WC-7%Co vs V^2D^3 for SiC erodent impacting at 90°

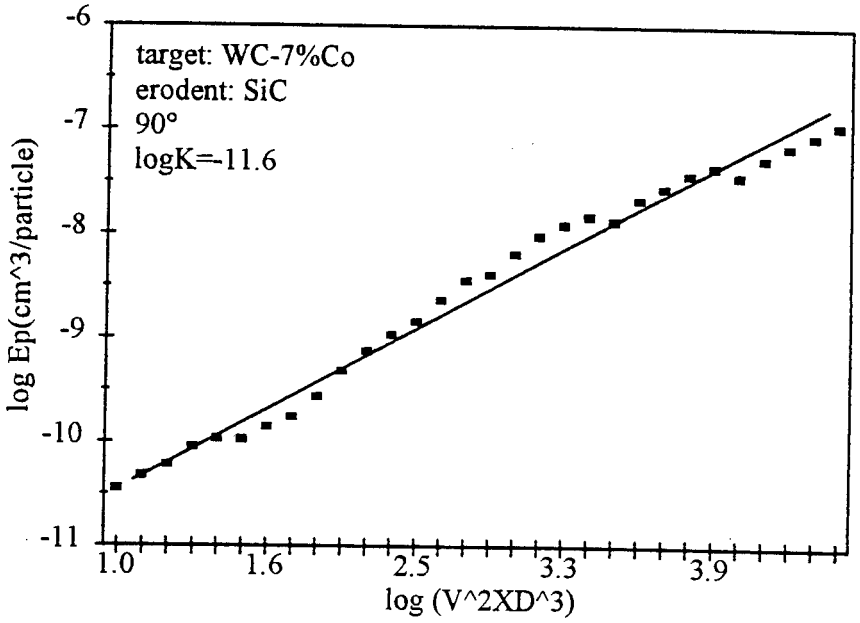

Figure 4 Graph of erosion rate(Ep) of WC-7%Co vs V^2D^3 for SiC erodent impacting at 90°